Fluid effect on wave propagation in heterogeneous porous media

Proefschrift

ter verkrijging van de graad van doctor
aan de Technische Universiteit Delft,
op gezag van de Rector Magnificus prof.dr.ir. J.T. Fokkema,
voorzitter van het College voor Promoties,
in het openbaar te verdedigen op woensdag 18 maart 2009 om 10:00 uur

door

Bouko Barteld Sytze Adriaan VOGELAAR

Geofysicus

geboren te Reimerswaal

Dit proefschrift is goedgekeurd door de promotor:
Prof.dr.ir. C.P.A. Wapenaar

Copromotor:
Dr.ir. D.M.J. Smeulders

Samenstelling promotiecommissie:

Rector Magnificus,	voorzitter
Prof.dr.ir. C.P.A. Wapenaar,	Technische Universiteit Delft, promotor
Dr.ir. D.M.J. Smeulders,	Technische Universiteit Delft, copromotor
Prof.dr. S.M. Luthi,	Technische Universiteit Delft
Prof.dr.ir. M.E.H. van Dongen,	Technische Universiteit Eindhoven
Dr. R.-E. Plessix,	Shell International E&P
Prof.dr. J.M. Harris,	Stanford University, USA
Prof.ir. M. Peeters,	Colorado School of Mines, USA
Prof.dr.ir. P.L.J. Zitha,	Technische Universiteit Delft, reservelid

The research described here was carried out at the Section of Applied Geophysics and Petrophysics, Department of Geotechnology, Faculty of Civil Engineering and Geosciences, Delft University of Technology, The Netherlands and at the Seismic Wave Physics Laboratory, Department of Geophysics, School of Earth Sciences, Stanford University, Unites States of America.

This research is part of the Shell-FOM program 'The physics of fluids and sound propagation'. The work was funded by the Stichting voor Fundamenteel Onderzoek der Materie, Utrecht, The Netherlands.

Copyright © 2009 by B.B.S.A. Vogelaar
ISBN 90-902-????-1
Printed by Delft University Press
Cover: Wingertsbergwand, Germany (Courtesy Geologisch College Miölnir)

Aan Dorien, Rosalie en Olivier

Contents

Summary

Acoustic wave propagation through porous media is affected by the properties of the pore fluid and the matrix material. Acoustic velocity and travel times are extensively used for imaging of subsurface strata, and to predict petrophysical properties such as porosity, fluid type and saturation. In contrast the attenuation (loss of wave energy) is not routinely used for these predictions.
This thesis reports the influence of fluid inhomogeneities (gas bubbles) on wave attenuation in fluid-saturated porous media. It is well-known that the Biot theory accurately predicts velocities at seismic and cross-well frequencies (1-1000 Hz), but largely underestimates attenuation. This discrepancy is mainly due to mesoscopic inhomogeneities in the frame (e.g., interbedded shales) and the fluid (e.g., gas bubbles or layers). The term mesoscopic is to be understood as larger than the typical pore size but smaller than the seismic wavelength. The inhomogeneities can be grouped together and described by local pressure equilibration models. The passing seismic wave causes local pressure differences between the gas and the surrounding liquid. These differences are equilibrated by local, mesoscopic, flow. For frame inhomogeneities, these models are known as double-porosity models, whereas for fluid inhomogeneities they are called patchy saturation models.
Patchy saturation models do incorporate the slow Biot wave on the mesoscale as the pressure equilibration is essentially diffusive. Yet, on the macroscale where the seismic waves propagate and the attenuation is governed by viscous flow induced by pressure differences on the scale of the wavelength, the slow Biot wave is averaged out. The effect of frequency on patchy saturation models was investigated for gas layers in porous media. It was found that for frequencies smaller than the Biot rollover frequency, inertia terms may be neglected, and the dynamic permeability may be approximated by the Darcy permeability. At higher frequencies, system resonances occur. The patchy saturation models describe rollover from low-frequency Wood (iso-stress) behavior, towards high-frequency Hill behavior, where the high frequencies are to be taken lower than the Biot rollover frequency. In this high-frequency limit, gas and liquid act as if they were sealed from each

other because there simply is not enough time for pressure equilibration.
An alternative to the patchy saturation model is the Rayleigh-Plesset-Biot approach, which essentially averages over fluid properties only, thus leaving intact the two-phase fluid-solid concept at the macroscopic level. Here the fluid is to be understood as the liquid-gas mixture. It was found that the Rayleigh-Plesset-Biot model predicts two compressional waves at the seismic scale, whereas patchy saturation models have only one. It was also found that the seismic wave is more attenuated than in the patchy saturation model. Applying the Rayleigh-Plesset-Biot model to literature data of resonant bar experiments on rock samples at frequencies from 0.6 to 6 kHz, a very good match between the reported and predicted attenuation was found.
Using a gas-injection technique, a single bubble was created in an oil-saturated porous sample. The procedure was tested by visualization by means of refractive index matching. At 500 kHz, it was found that in this case the patchy saturation model gives a better prediction than the Rayleigh-Plesset-Biot model. However, so-called squirt flow, describing pressure equilibration on the smaller, microscale, may also contribute to attenuation, at these frequencies. The attenuation measurements were performed using the Spectral Ratio Data Analysis, where two otherwise identical samples of different length were used in the experiments. The phase velocities of 45 natural rocks and artificial porous samples also measured in this way, were calibrated against conventional ultrasonic measurements where first arrival picking was applied. It was also confirmed that for the phase velocities, the Biot theory is accurate. For the attenuation, it is not. At these frequencies, mesoscopic attenuations probably do not play a significant role, but inhomogeneities on a smaller scale (microcracks in the grains or at the grain contacts) may become dominant. This is, however, beyond the scope of this thesis.
The same 45 samples were also used for Differential Acoustic Resonance Spectroscopy (DARS) measurements. In these experiments the compressibility of a sample is determined by the change in the resonance frequency of a tube due to the introduction of the sample. DARS experiments on non-porous samples confirm the perturbation theory by Morse and Ingard. For sealed porous samples, good agreement between Gassmann and DARS moduli was obtained. For open-pore samples the DARS moduli could not be interpreted in terms of frame and fluid moduli, because the compressibility is governed by the relative fluid motion at the outer wall. Another challenge is to quantify the attenuation of porous samples using DARS. Measurements based on more realistic in-situ conditions (pressurized samples with multi-constituent properties) should lead to revisions of the theory, and enhance the use of attenuation for reservoir characterization.

Chapter 1

Introduction

Understanding the physics of acoustic wave propagation in porous materials affects a wide range of applications from the exploration of the Earth's crust to the design of sound-absorbing materials and the nondestructive testing of fractured materials. This research concentrates on wave propagation through porous rocks that are fully or partially filled with liquid and gas. The central point to be inferred from this thesis is that the interpretation of compressional wave propagation provides information about the pore fluids and their presumed mobility in a porous material.

1.1 Background literature

Far more information about the constitution of the Earth is obtained from seismic than from all other geophysical methods combined. Of the two main aspects of wave propagation - velocity and attenuation - knowledge of velocities has provided most of our information about the Earth (Winkler et al., 1979). Attenuation data of seismic waves is of much more limited use, partly because it is difficult to obtain, but mainly because it is so difficult to interpret in terms of rock properties. This is still due primarily to our lack of understanding of the physical processes involved in attenuation.

Attenuation refers to the total loss of energy of a sound wave along its propagation path resulting from all mechanisms responsible for such losses, including but not limited to, absorption, scattering, and diffraction. Absorption refers to the loss of energy of an acoustic wave that results in an increase in temperature in the propagation medium and is associated with relaxation phenomena. Scattering and diffraction result in a redirection of wave energy from the original propagation direction. In this study, we are not considering apparent attenuation caused by

geometrical spreading, partial reflections, multiple scattering and so on, but we are only interested in intrinsic attenuation processes, where seismic wave energy is converted into heat due to the presence of pore fluid(s).
Sound waves are affected by the heterogeneity in the material through which they travel. The major goals of the interpretation of exploration seismic data are the identification of pore fluids and the mapping of hydrocarbon deposits in the geological structure. Predictive knowledge of acoustic properties in natural sandstones is useful in the search for economic natural gas and oil reservoirs. Recent developments in borehole acoustic measurements and subsea geophone arrays make it feasible to conduct high-resolution surveys to detect pockets of unswept reserves and to monitor the progress of enhanced recovery by gas and water injection (Helle et al., 2003). Because the inversion from seismic to petrophysical characteristics is far from unique, this task requires seismic parameters, such as seismic velocity, impedance, and Poisson's ratio.
The inclusion of seismic absorption in this list could add complementary information. For example, absorption may be more sensitive to clay content than seismic velocity (Klimentos and McCann, 1990) and the shear to compressional wave absorption ratio has been found to be a better indicator of fluid saturation than the corresponding velocity ratio (Toksöz et al., 1979; Winkler and Nur, 1982). However, in practice, seismic absorption is difficult to measure, particularly over depth intervals as short as most reservoir intervals.
Understanding the physics of elastic wave propagation in porous rocks partially saturated with liquid and gas is thus important for exploring and exploiting hydrocarbon reserves. Unraveling the intrinsic effects can be a robust tool in the quantitative interpretation of well and seismic data, e.g. for acoustic logging and for computing true-amplitude synthetic seismograms in time-lapse seismic studies. The underlying rock physics controlling intrinsic loss can give us valuable insight into the stratigraphy, lithology, and fluid content of the survey area. Oil, water, and gas commonly coexist in prospective reservoirs, and an accurate assessment of the gas content is needed to assert the economic value of the reservoir. Distinguishing the nature of reservoir fluids by their acoustic signature is a key issue in seismic exploration and reservoir monitoring.
In the past decades, different techniques have been used to study the attenuation of acoustic waves propagation through rock. Although much data have been collected, no well-defined mechanism of energy loss has yet been firmly established on both experimental and theoretical grounds other than those reported by Biot (1956a,b).

Before the eighties, one of the most intuitively appealing and widely discussed

mechanisms proposed for seismic energy loss was based on simple Coulomb friction (Winkler et al., 1979). In this mechanism the passing wave causes sliding at grain boundaries or across crack faces, thereby converting seismic energy into heat. Friction also seems to explain why the introduction of cracks into a crystalline solid increases attenuation. Using both theoretical arguments and experimental results, several authors (Savage and Hasegawa, 1967; Mason et al., 1978) have expressed doubts about the validity of a frictional attenuation mechanism. Despite these criticisms, frictional losses have often been used to interpret experimental observations (Birch, 1975; Lockner et al., 1977; Johnston et al., 1979).

Several other processes have been eliminated as dominant loss mechanisms, including frictional grain sliding (Mavko, 1979), intrinsic shear and structural relaxation in the pore fluid (Hornby and Murphy, 1987), thermo elasticity (Jones and Nur, 1983), and interfacial relaxation (Clark et al., 1980; Tittmann et al., 1980). Other potential sources of attenuation in partially saturated media, e.g. the squeeze film phenomenon (Stoll, 1985) and contact line movement (Miksis, 1988), will not be considered here. No single mechanism nor any combination of these mechanisms can coherently explain the experimental results (Murphy et al., 1986).

1.1.1 Scales of heterogeneities

Most natural porous materials, such as rocks and sediments in the Earth, are heterogeneous in the porous-continuum properties at nearly all scales larger than the typical grain size ℓ. The typical dimension of a sandstone grain is 100 μm. The seismic wavelength λ used for exploration of the Earth's subsurface is typically in the range from 1 to 100 m. There is thus a wide range of length scales that are larger than the microscopic grain size ℓ, but smaller than than the macroscopic acoustic wavelength λ. This typical length scale of a heterogeneity in the porous-continuum properties is the so-called mesoscopic length scale L (Pride et al., 2004). In figure 1.1 we see that $\lambda \gg L \gg \ell$. Examples of heterogeneities in rocks are a sudden transition in: elastic modulus, density, permeability, fluid content, etc.

Recent studies by Pride et al. (2004) have shown that the major cause of attenuation in porous media is wave-induced fluid flow, which occurs at three different spatial scales: macroscopic, mesoscopic, and microscopic.

The first type of intrinsic attenuation takes place on the scale of the wavelength (macro-scale). Local pressure equilibration is obtained between the peaks and troughs of a passing wave by means of viscous pore-fluid flow induced by the macroscopic pressure gradient. This type of attenuation is commonly known as the Biot attenuation (1956a; 1956b; 1962a; 1962b). The original Biot theory is

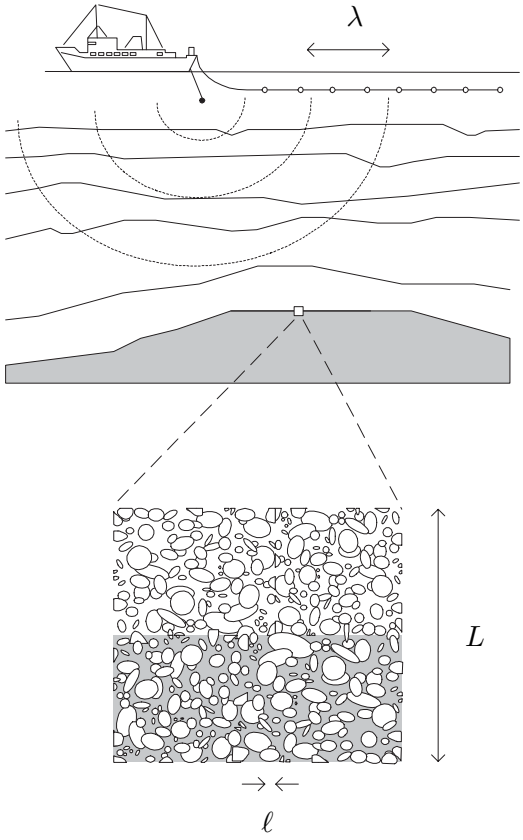

Figure 1.1: Schematic representation of the length-scale relation $\lambda \gg L \gg \ell$, where λ is the wavelength of the acoustic pulse, L is the length-scale containing a mesoscopic-scale heterogeneity in the local porous-continuum properties, and ℓ is a characteristic size of a grain.

applicable to media where a homogeneous porous frame is composed of a single solid phase and saturated by a single fluid. The relaxation time τ of this process is λ^2/D, where λ is the wavelength and D is the pore-pressure diffusivity of Biot's slow wave. In a rigid porous continuum, the diffusivity is well approximated by $k_0 K_\mathrm{f}/\eta\phi$, where k_0 is the Darcy permeability, ϕ the porosity, and η and K_f the viscosity and bulk modulus of the saturating fluid, respectively (Smeulders, 2005). Maximum energy dissipation occurs when the oscillation time $1/\omega_\mathrm{c}$ just equals the relaxation time τ. Interestingly, the frequency ω_c is of the same order of magnitude

as the Biot critical frequency ω_{B}

$$\omega_{\mathrm{c}} \simeq \omega_{\mathrm{B}} = \frac{\eta\phi}{\alpha_\infty \rho_{\mathrm{f}} k_0}, \tag{1.1}$$

which describes the transition from low-frequency viscosity dominated flow to high-frequency inertia dominated flow. Here α_∞ denotes the tortuosity, and ρ_{f} is the fluid density. Equation (1.1) shows that the transition frequency moves toward higher frequencies with increasing viscosity and decreasing permeability. This contradicts the experimental data of Jones (1986). Another apparent drawback of the Biot theory is that the macroscopic flow mechanism underestimates the velocity dispersion and attenuation in rocks (Mochizuki, 1982; Dvorkin et al., 1995; Arntsen and Carcione, 2001).

Several authors extended the Biot theory to include an additional solid or fluid phase (Stoll and Bryan, 1970; Bedford and Stern, 1983; Garg and Nayfeh, 1986; Berryman et al., 1988). Pham et al. (2002) generalized the model of Carcione et al. (2000), based on a Biot-type three-phase theory, that considers the coexistence of two solid phases (sand and clay) and a fluid mixture to include effects of partial saturation by a modified empirical fluid mixing law proposed by Brie et al. (1995). Additional attenuation in their model is described by a constant Q-model (Kjartansson, 1979) and viscodynamic functions obtained by Johnson et al. (1987) for high-frequency behavior. Masson et al. (2006) modeled Biot's poroelastic equations by discretizing a discontinuous medium with small continuous cells. Other approaches to account for the effects of gas bubbles in a liquid, e.g. Brandt (1960); Gregory (1976); Domenico (1976); Toksöz et al. (1976) and Lopatnikov and Gorbachev (1987) assume the porous solid to be saturated by an (effective) single fluid whose properties are determined by averaging the properties of the liquid and the gas constituents.

The second type of intrinsic attenuation takes place on the grain scale (micro-scale). It is common to invoke non-Biot attenuation mechanisms to explain low-frequency (seismic and sonic) attenuation in rocks (Carcione and Picotti, 2006). These mechanisms are the so-called local fluid flow or squirt flow mechanisms, which have been extensively discussed in the literature (O'Connell and Budiansky, 1974; Budiansky and O'Connell, 1976; Mavko and Nur, 1979; Dvorkin and Nur, 1993; Dvorkin et al., 1995; Mavko et al., 2003). When the pore pressure increases due to a passing seismic wave, there will be pressure equilibration between the pore space and the micro cracks in the grains and at the grain contacts. In this mechanism, fluid-filled microcracks respond with greater fluid-pressure changes than the main pore space. Fluid will be squeezed in and out of these cracks.

The resulting flow at this microscopic level is responsible for the energy loss. The equilibration time τ of this process is R^2/D_h, where R is the length of the micro crack. The crack diffusivity D_h is given by $K_\mathrm{f}h^2/\eta$, with h the crack aperture.

Microscale inhomogeneities in the grains have been identified as contributors to dissipate wave energy. For example, Palmer and Traviolia (1980) fitted the measurements of absolute attenuation and saturation dependence at kHz frequencies in undersaturated gas sands by Gardner et al. (1964) assuming squirt flow. Sams et al. (1997) assume squirt flow attenuation to model their seismic-to-ultrasonic attenuation measurements. These models have the proper dependence of viscosity with frequency, however it has been shown that by applying realistic crack aspect ratios, the microscopic squirt flow model of Dvorkin et al. (1995) is not able to predict the observed levels of attenuation in exploration work (Diallo et al., 2003; Pride et al., 2004). The squirt flow attenuation would need quite small crack aspect ratios in the order of $h/R < 10^{-4}$ to predict maximum attenuation lying in the seismic band. However, the attenuation level itself is also influenced by the crack aspect ratio, and these small ratios yield unrealistically low attenuation levels.

The third pressure equilibration process takes place on the scale larger than the grains but smaller than the wavelength (meso-scale). Pride et al. (2004) have shown that attenuation and velocity dispersion measurements can be explained by the combined effect of mesoscopic inhomogeneities and energy transfer between wave modes. They refer to this mechanism as mesoscopic loss. Fixing the mesoscopic scale by the length of the inhomogeneity L, maximum loss occurs at $1/\omega_\mathrm{c} = L^2/D$, where D is again the slow-wave diffusivity. On this scale, there are always heterogeneities in the frame, in the pore fluid, or in both. Inhomogeneities in the frame structure, e.g. interbedded shales and sands or zones or pockets of weakly cemented grains, are analyzed in double-porosity theories, that are - although generalized - completely consistent with Biot's theory of poroelasticity (Berryman and Wang, 1995, 2000; Pride and Berryman, 2003a,b). Inhomogeneities in the fluid, where e.g. gas pockets larger than the grain size are embedded within a liquid host phase, can be modeled by the definition of an effective medium or the definition of an effective pore fluid.

Traditionally, the influence of an inhomogeneity in the fluid (partial gas saturation) on seismic speeds and attenuation in rocks is computed by the approach proposed by White (1975) and White et al. (1975). Patches of non-uniform saturation occur at the gas-oil and gas-water contacts in hydrocarbon reservoirs. Also during production, gas may come out of the solution creating pockets of free gas. As demonstrated theoretically by White (1975) and White et al. (1975), wave velocity and attenuation are substantially affected by the presence of partial gas

saturation, depending mainly on the size of the gas pockets (saturation), frequency, permeability, and porosity.

White's idea of enhanced attenuation in the presence of even small volume fractions of gas in the pore fluid has been experimentally confirmed by, among others, Murphy (1982a,b); Murphy et al. (1984, 1986), Cadoret (1993); Cadoret et al. (1995, 1998), Knight et al. (1998); Knight and Nolen-Hoeksema (1990), and Winkler (1979, 1983, 1985, 1986); Winkler and Murphy (1995); Winkler and Nur (1979, 1982); Winkler et al. (1979). Partial saturation effects on acoustic properties have been observed in the laboratory, among others, by Yin et al. (1992), Gist (1994a,b), Lucet and Zinszner (1992), and Bourbie and Zinszner (1985). The most exciting result from the laboratory measurements from Murphy (1982a) is that attenuation is found to be very sensitive to partial gas saturation. Experimental evidence of the affection of the acoustics in marine sediments by the presence of gas bubbles in the saturating liquid is given by the review of Anderson and Hampton (1980a,b). Recently, Lebedev et al. (2009) performed simultaneous measurements of P-wave velocity and rock sample X-ray computer tomography (CT) imaging during saturation (water imbibition). They showed that the experimental results are consistent with theoretical predictions and numerical simulations.

The relevance for seismic exploration is profound. Seismic low-frequency effects have been noted with reference to reflections from hydrocarbon-saturated rocks by authors such as Goloshubin and Korneev (2000), Korneev et al. (2004), Ebrom (2004), and Chapman et al. (2006). Castagna et al. (2003) showed that instantaneous spectral analysis (ISA) can be used as a direct hydrocarbon indicator. Turgut and Yamamoto (1988) and Yamamoto and Turgut (1988) modeled loss due to mesoscopic heterogeneities, i.e., the conversion of fast P-wave energy to slow diffusive modes, in 1D numerical computations of finely layered marine sediments. The low-frequency content of bright spots (high amplitude anomalies that can indicate the presence of hydrocarbons) can be caused by mesoscopic loss mechanisms, induced by partial saturation at the gas/oil and gas/water contacts (Rutherford and Williams, 1989). Another effect that could be explained by this mechanism is the presence of gas clouds and gas chimneys (a subsurface leakage of gas from a poorly sealed hydrocarbon accumulation), recorded in offshore seismic sections. The presence of gas, leaked from the reservoir to the overburden, has the effect of lowering seismic velocities and increasing seismic attenuation, producing low signal-to-noise ratio P-wave seismic sections (Carcione, 1998). The explanation is the presence of patchy saturation in the overburden causing losses of mesoscopic nature. The S-wave is not affected, since its energy is mainly transported through the frame of the rocks (Carcione and Picotti, 2006).

Pride et al. (2004) compared the attenuation and dispersion predicted by the double-porosity model of Pride and Berryman (2003a,b) to the dataset of Sams et al. (1997), assuming a well-consolidated sandstone host being embedded by unconsolidated penny-shaped mesoscopic inclusions. The sealed-sample assumption in the patchy saturation model is mathematically equivalent to the assumption that the unit sample is periodically repeated throughout space, as in the initial works of White (1975) and White et al. (1975), as later extended by Dutta and Odé (1979a) for the 3D case, and by Vogelaar and Smeulders (2007) for the 1D case. Johnson (2001) developed an analytical framework for White's model in both dimensions. However, even more realistic modeling geometries than White's configuration, such as a random spatial distribution of a low concentration of spherical inclusions (Gurevich and Lopatnikov, 1995; Gelinsky et al., 1998; Müller and Gurevich, 2004, 2005a,b; Toms et al., 2006, 2007) are unable to accurately explain the strong dependence of extensional attenuation on frequency in Massillon sandstone from the experimental data of Murphy (1982a).

An alternative approach to model the acoustics of partial saturation is by the introduction of an effective fluid instead of an effective medium cell (Smeulders and Van Dongen, 1997). Such effective fluid includes the pressure equilibration effects on the meso-scale as in the White-based models, but it would not fully incorporate the second, solid, phase. Hence, on the macro-scale, there still exists a separate solid phase next to an effective fluid phase, so that all characteristics of Biot's theory remain intact, though modified. This approach is based on the treatment of bubbly liquids, where in first-order approximation the bubbles can be regarded as single scatterers in an infinitely extended liquid host phase (Rayleigh-Plesset approach). It was shown in many experiments (for a review, see e.g. van Wijngaarden (1972)) that even in a cloud of bubbles this approach is remarkably accurate.

1.2 Research challenges

1.2.1 Statement of the problem

The Biot theory is the most general phenomenological theory for wave propagation through two distinct interpenetrating effective media. However, it is well-known that the Biot theory is not capable of simultaneously explaining both the velocity and the attenuation of seismic data measured on many fluid-saturated rocks (Pride et al., 2004). From a fundamental perspective, perhaps the greatest challenge in petrophysics is to understand the way a heterogeneity across all length scales

smaller than the acoustic wavelength affects wave propagation (Pride and Masson, 2006).

1.2.2 Scientific objectives

The aim of this research is to extend the model basis of wave propagation to heterogeneous porous media. It is a combined theoretical and experimental research effort to evaluate the current models and to develop additional visco-poro-elastic ones from low to high frequencies and to design and apply controlled laboratory experiments for the calibration of these models.

The theoretical part of this research aims to determine a physical model that predicts the intrinsic attenuation and velocity of longitudinal waves and their relation to the reservoir properties, such as rock type, porosity, permeability, and saturation, and the fluid properties, such as viscosity, density, and compressibility. In this part of the research, existing discrepancies with alternative approaches will be examined and additional wave damping phenomena will be identified and, if applicable, incorporated in the theory.

The experimental part of this research aims to calibrate the parameters of the developed models and to validate the model's predictive value. Since the phenomena involved are frequency-dependent, and scaling is not trivial, experiments are conducted at ultrasonic and sonic frequencies.

1.2.3 Industrial relevance

There are needs to extract more information from seismic data, especially for reservoir modeling and time lapse interpretation in order to reduce the uncertainties during the exploration, development and production phase of a reservoir. Analysis of seismic data suggests that hydrocarbon deposits are often associated with higher than usual values of attenuation, but this is generally ignored during amplitude-versus-offset (AVO) analysis (Chapman et al., 2006). These rock and fluid properties are only accessible in the vicinity of the well from log and/or core measurements. Seismic data provide three-dimensional information, but generally only structural images are recovered from the data. To extract more information from the seismic data, the dependence of wave propagation on the petrophysical properties is desired. Understanding of the physics that controls wave propagation in the heterogeneous subsurface is an indispensable tool in the search for hydrocarbon deposits.

1.3 Organization of the thesis

The constitution of this dissertation is as follows. After this introductory chapter, the first three chapters evaluate and, if appropriate, extend and modify existing theories on wave propagation in homogeneous and heterogeneous porous media. The following four chapters describe the experimental part of this research.
Chapter two describes the Biot theory. Chapters three and four treat the theory of wave propagation through fluid-saturated rocks in which also gas is present. In chapter three, the original theory and an extended one of patchy saturated rocks are described for a layered geometry of the gas patches filling the pores based on the initial frameworks of White et al. (1975). In chapter four, this 2D model is described in 3D by the theories of White (1975) and Johnson (2001) of which the latter is derived analytically. With basic assumptions, we describe a complimentary model. Also in chapter four, a modified theory of partially saturated media is described based on the initial framework of Smeulders and Van Dongen (1997). The constituent effects on velocity and attenuation are compared.
The first chapter of the experimental part is chapter five, which gives a rock-physical description of the samples of interest. The applicable laboratory equipment is described, together with the data acquisition and processing procedures. The results involve determination of density, porosity, permeability, and bulk and shear modulus of 45 natural and synthetic porous materials. In chapter six the oil-saturated ultrasonic bulk properties are determined by two different laboratory set-ups and by two methods. Measurements of velocity and attenuation on the influence of gas injected in an otherwise liquid-saturated sample are shown in chapter seven. The final experimental chapter, chapter eight, investigates the bulk moduli of the described samples at sonic frequencies by means of a Differential Acoustic Resonance Spectroscopy (DARS) set-up. In chapter nine the conclusions are itemized.

Chapter 2

Biot theory

2.1 Introduction

Despite earlier descriptions by Zwikker and Kosten (1941) and Frenkel (1944), the formulation of a comprehensive theory for the mechanical interaction between the fluid phase and the solid phase in a homogeneous porous material is attributed to Biot (1956a,b).

One of the most prominent results of Biot's theory of wave propagation in porous media is that there are in contrast with the conventional elastic theory three bulk waves: two compressional and one shear wave. It is generally accepted that the first experimental validation of the slow wave was by Plona (1980) on artificial rock composed of glass beads. Since then, important progress has been made in the field of viscous and thermal interaction (equivalent-fluid models) which opened new ways for experimental verification. The slow compressional wave was later also detected in natural rocks, both in air-saturated (Nagy et al., 1990) and water-saturated ones at ultrasonic frequencies (Kelder and Smeulders, 1997). Velocity measurements have proven the very broad predictive power of the Biot theory. Predictions on the damping behavior of these waves, however, are still poor (Smeulders, 2005).

In this chapter, we will briefly present the acoustic bulk properties of the three wave types following from the Biot theory. The low- and high frequency limiting behavior of these waves is given and the Gassmann (1951) theory is discussed, since this helpful for later use in chapters 3, 4, and 8. The stress-strain relations are given here, since these are also the starting equations of the theories in chapter 4. The input parameters of the Biot equations are measured in laboratory experiments in chapter 5. The velocities and quality factor experimentally measured on oil-

saturated rocks are compared with the Biot theory in chapter 6.

2.2 Acoustic bulk properties

Consider a fluid-saturated homogeneous poroelastic rock under loading. The total stress τ_{ij} (solid plus fluid phases) and pore fluid pressure p in terms of the solid and fluid strains, e_{ij} and ϵ_{ij}, are in the case of isotropic materials

$$\begin{aligned} \tau_{ij} &= [(P+Q-2\mu)e_{kk} + (Q+R)\epsilon_{kk}]\delta_{ij} + 2\mu e_{ij}, && (2.1)\\ -\phi p &= Qe_{kk} + R\epsilon_{kk}. && (2.2) \end{aligned}$$

The porosity is ϕ and the shear modulus of the matrix is μ. Explicit expressions of the poroelastic coefficients are given in terms of the bulk moduli of the pore fluid, the solid, and the matrix $K_{\mathrm{f,s,m}}$, respectively as (Biot and Willis, 1957)

$$\begin{aligned} P &= \frac{\phi K_{\mathrm{m}} + (1-\phi)K'}{\phi'} + \frac{4}{3}\mu,\\ Q &= \frac{\phi K'}{\phi'}, && (2.3)\\ R &= \frac{\phi^2 K_{\mathrm{f}}}{\phi'}, \end{aligned}$$

where

$$\begin{aligned} \phi' &= \phi + \frac{K'}{K_{\mathrm{s}}},\\ K' &= K_{\mathrm{f}}(\gamma - \phi), && (2.4) \end{aligned}$$

and $\gamma = 1 - K_{\mathrm{m}}/K_{\mathrm{s}}$ is the so-called Biot coefficient. The bulk modulus of the matrix is derived from the dry rock density ρ_{s} and the dry P- and S-wave velocities, $v_{\mathrm{P\ dry}}$ and $v_{\mathrm{S\ dry}}$:

$$K_{\mathrm{m}} = (1-\phi)\rho_{\mathrm{s}}\left(v^2_{\mathrm{P\ dry}} - \tfrac{4}{3}v^2_{\mathrm{S\ dry}}\right). \quad (2.5)$$

The shear modulus is independent of the pore fluid, and can therefore be determined by the dry shear wave velocity (Berryman, 1999):

$$\mu = (1-\phi)\rho_{\mathrm{s}} v^2_{\mathrm{S\ dry}}. \quad (2.6)$$

Consider, then, the solid and fluid displacements, $\mathbf{u}$ and $\mathbf{U}$, in a saturated homogeneous poroelastic matrix under loading. The fluid can be liquid, gas, or a gas-liquid mixture. Due to the intrinsic frequency-dependent nature of the viscous

interaction, it is useful to consider the Biot equations in the frequency domain. Adopting an $\exp(i\omega t)$ dependence for all relevant quantities, the Biot equations for the solid and the fluid are (Biot, 1956a,b):

$$\begin{aligned} -\omega^2[(\rho_{11}+\rho_{12})\hat{\mathbf{u}}+(\rho_{22}+\rho_{12})\hat{\mathbf{U}}] &= \nabla\cdot\hat{\tau}, \quad (2.7)\\ \omega^2[\rho_{12}\hat{\mathbf{u}}+\rho_{22}\hat{\mathbf{U}}] &= \phi\nabla\hat{p}, \quad (2.8)\end{aligned}$$

where the complex density terms are defined as

$$\begin{aligned} \rho_{11} &= (1-\phi)\rho_{\mathrm{s}}-\rho_{12},\\ \rho_{22} &= \phi\rho_{\mathrm{f}}-\rho_{12}, \quad (2.9)\\ \rho_{12} &= (1-\tilde{\alpha})\phi\rho_{\mathrm{f}}.\end{aligned}$$

The accent circumflex over a field variable (displacements, particle velocities, stresses, and pressures) denotes small variations of that variable. The accent circumflex over the dependencies of these field variables (such as strains, etc) is omitted. The solid and fluid densities are $\rho_{\mathrm{s,f}}$. The dynamic tortuosity, $\tilde{\alpha}$, describing the transition from the viscous to the inertia-dominated regime is given by Johnson et al. (1987):

$$\tilde{\alpha}=\alpha_\infty\left(1-i\sqrt{\frac{\omega_{\mathrm{B}}}{\omega}\left(\frac{\omega_{\mathrm{B}}}{\omega}+\frac{i}{2}\right)}\right), \quad (2.10)$$

where α_∞ is the real-valued tortuosity. The critical Biot frequency, describing this transition, is

$$\omega_{\mathrm{B}}=\frac{\phi\eta}{k_0\alpha_\infty\rho_{\mathrm{f}}}, \quad (2.11)$$

where k_0 is the permeability and η is the fluid viscosity. The dynamic tortuosity is related to the dynamic permeability $\tilde{k}$ (Johnson et al., 1987):

$$\frac{\tilde{\alpha}}{\alpha_\infty}=\frac{k_0}{\tilde{k}}\frac{\omega_{\mathrm{B}}}{i\omega}. \quad (2.12)$$

We substitute equations (2.1) and (2.2) in (2.7) and (2.8) and assume that the solution can be written in the frequency-wavenumber domain using an $\exp(-i\mathbf{k}\cdot\mathbf{r})$ convention. Here, $\mathbf{k}$ is the three-dimensional wavenumber vector, and $\mathbf{r}$ is the three-dimensional position vector. Using standard decomposition techniques (see Wisse (1999)), the dispersion relation for the squared compressional wave velocity $c^2=(\omega/k)^2$ is

$$d_2c^4+d_1c^2+d_0=0, \quad (2.13)$$

with

$$\begin{aligned} d_0 &= PR - Q^2, \\ d_1 &= -(P\rho_{22} - 2Q\rho_{12} + R\rho_{11}), \\ d_2 &= \rho_{11}\rho_{22} - \rho_{12}^2. \end{aligned} \tag{2.14}$$

Solutions of the quadratic equation (2.13) in c^2 yield two complex roots corresponding to the fast and slow compressional waves ($j = 1, 2$):

$$c_j^2 = \frac{-d_1 \pm \sqrt{d_1^2 - 4d_0 d_2}}{2d_2}. \tag{2.15}$$

The phase velocities and intrinsic attenuations[1] are computed from the wavenumbers as

$$c_{\mathrm{P}} = \frac{\omega}{\mathrm{Re}(k)} \tag{2.16}$$

and

$$Q^{-1} = \left| \frac{2\mathrm{Im}(k)}{\mathrm{Re}(k)} \right|. \tag{2.17}$$

The resulting wave modes including limiting behavior are displayed in figure 2.1. The rock and fluid properties are given in table 2.1. The wave type in which the fluid and frame displacements are in-phase has a high velocity and low damping and is called the fast wave, while the one in which they are out-of-phase has a low velocity and high intrinsic damping and is accordingly denoted the slow wave. Fast wave dispersion is minimal. The slow wave velocity, however, increases from zero at low-frequencies to a constant value at high-frequencies. This transition frequency from low-frequency diffusive behavior to a high-frequency propagatory behavior is described by the critical Biot frequency in equation (2.11). In our example $\omega_{\mathrm{B}}/2\pi = 1.3 \cdot 10^5$ Hz, which is where the fast wave attains maximum attenuation. We thus see that for surface seismics and even low-frequency acoustic tools (3 kHz) phase velocity and attenuation are dominated by the viscosity of the fluid. Since viscosity is strongly temperature dependent, in a reservoir, η can be as low as 0.25 mPa·s for water and has therefore a strong effect on the transition frequency.
Equations (2.7) and (2.8) not only give the complex wavenumbers, but also determine the fluid-solid displacement ratios (Kelder, 1998):

$$\beta_j = \frac{Q - \rho_{12}c_j^2}{\rho_{22}c_j^2 - R} = \frac{\rho_{11}c_j^2 - P}{Q - \rho_{12}c_j^2}. \tag{2.18}$$

[1]The quality factor (inverse attenuation) and one of Biot's poroelastic constants are both denoted by symbol Q.

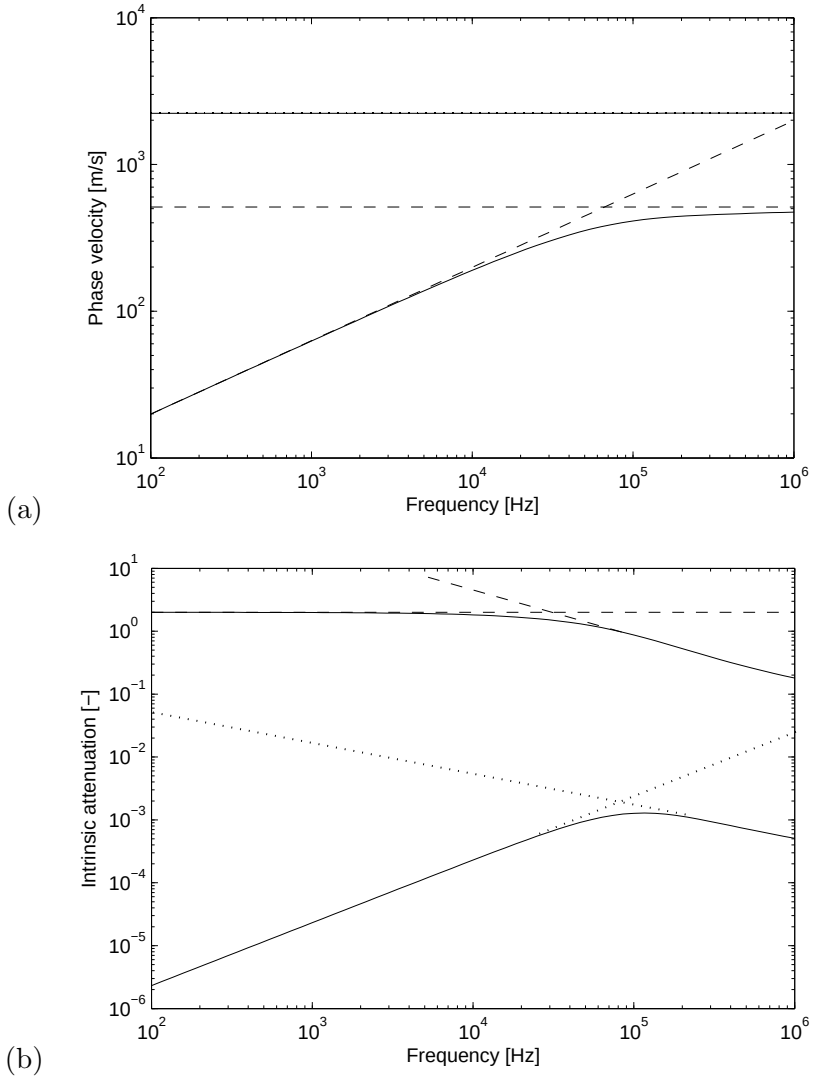

Figure 2.1: Phase velocity (a) and intrinsic attenuation (b) of the compressional waves predicted by the Biot theory. The fast wave is the upper solid curve in figure (a) and the lower solid curve in (b). The dotted lines are the low and high-frequency asymptotes of the fast wave. The slow wave is the lower solid curve in (a) and the upper solid curve in (b). The dashed lines are the low and high-frequency asymptotes of the slow wave. The properties of the fully water-saturated sandstone rock are given in table 2.1.

	Matrix	Grains	Water
Density ρ [kg/m^3]		$2.65 \cdot 10^3$	$1.0 \cdot 10^3$
Bulk modulus K [Pa]	$2.637 \cdot 10^9$	$35.0 \cdot 10^9$	$2.25 \cdot 10^9$
Viscosity η [Pa·s]			$1.0 \cdot 10^{-3}$
Porosity ϕ [-]	0.284		
Permeability k_0 [m^2]	$1.0 \cdot 10^{-13}$		
Shear modulus μ [Pa]	$1.740 \cdot 10^9$		
Tortuosity α_∞ [-]	3.52		

Table 2.1: Constituent properties of a fully water-saturated sandstone rock with a relatively weak frame (Johnson, 2001).

The decomposition techniques also provide the dispersion relation for the shear wave

$$\mu\rho_{22} - d_2 c^2 = 0, \tag{2.19}$$

with the straightforward solution

$$c = \sqrt{\frac{\mu\rho_{22}}{d_2}}. \tag{2.20}$$

The fluid-solid displacement ratio is in this case (Kelder, 1998)

$$\beta_{\mathrm{S}} = -\frac{\rho_{12}}{\rho_{22}}. \tag{2.21}$$

2.3 Limiting behavior

In the high and low-frequency limit, equations (2.7) and (2.8) are identical to respectively Darcy's law and Newton's second law, or in other words dominated by viscosity or inertia.
The low-frequency behavior of the Biot theory follows from equations (2.7) and (2.8) simply by setting to zero all higher-order inertial terms and by taking the dynamic permeability, $\tilde{k}$, equal to its steady-state value, k_0. Using equation (2.12) then gives

$$\nabla \cdot \hat{\tau} = 0, \tag{2.22}$$

$$\frac{k_0}{\eta\phi}\nabla\hat{p} = i\omega(\hat{\mathbf{u}} - \hat{\mathbf{U}}). \tag{2.23}$$

The solutions of equations (2.22) and (2.23) are as follows. There are solutions in which the fluid and solid are locked together: $\hat{\mathbf{u}} = \hat{\mathbf{U}}$. In that case the total stress, equation (2.1), is related to the displacement in the usual way, but with a new constrained modulus H:

$$\hat{\tau}_{ij} = (H - 2\mu)e_{kk}\delta_{ij} + 2\mu e_{ij}, \tag{2.24}$$

where $H = P + 2Q + R$. This modulus was originally derived by Gassmann (1951). Substitution of equations (2.3) in H yields

$$H = K_{\mathrm{m}} + \frac{\gamma^2}{(\gamma - \phi)/K_{\mathrm{s}} + \phi/K_{\mathrm{f}}} + \tfrac{4}{3}\mu. \tag{2.25}$$

For later use, we also define the so-called Biot-Gassmann bulk modulus K_{BG} of the saturated rock

$$K_{\mathrm{BG}} = H - \tfrac{4}{3}\mu. \tag{2.26}$$

These equations (2.24) thus naturally imply that the compressional and shear waves should propagate unattenuated with speeds given by

$$\lim_{\omega \to 0} c_1 = \sqrt{\frac{H}{\rho}}, \tag{2.27}$$

and

$$\lim_{\omega \to 0} c_{\mathrm{S}} = \sqrt{\frac{\mu}{\rho}}, \tag{2.28}$$

with $\rho = (1 - \phi)\rho_{\mathrm{s}} + \phi\rho_{\mathrm{f}}$ the total density. There are also solutions of equations (2.22) and (2.23) in which the fluid and solid move out-of-phase. This is seen by considering plane wave propagation in the x direction, for example. In that case it can be seen that the fluid-solid displacement ratio $\beta = \hat{U}/\hat{u}$, with $\hat{u}$ and $\hat{U}$ the displacements in the x direction, is given by

$$\lim_{\omega \to 0} \beta_2 = -\frac{P + Q}{Q + R}. \tag{2.29}$$

Substitution of β_2 in equation (2.23) yields that all relevant quantities obey a diffusion equation with diffusivity given by

$$D = \frac{k_0}{\eta\phi^2}\frac{PR - Q^2}{H}. \tag{2.30}$$

The slow wave speed is then given by ($\omega \to 0$)

$$c_2 = \sqrt{i\omega D}. \tag{2.31}$$

As seen in equation (2.10), in the high-frequency limit the dynamic tortuosity becomes real-valued, so that the high-frequency limit of the compressional and shear waves are given by equations (2.15) and (2.20) using $\tilde{\alpha} = \alpha_\infty$.
The low and high-frequency asymptotes of the fast and slow compressional waves are also shown in figure 2.1. In agreement with equation (2.31) the low-frequency slow wave velocity is proportional to $\omega^{1/2}$. In the high-frequency limit, the slow wave velocity is independent of frequency, since $\tilde{\alpha} = \alpha_\infty$. The low-frequency asymptote of the fast wave attenuation is linear with frequency, since there $\mathrm{Re}(k_1) \propto \omega$ and $|\mathrm{Im}(k_1)| \propto \omega^2$. The high-frequency asymptotes of both the fast and slow wave attenuation are proportional to $\omega^{-1/2}$, since $\mathrm{Re}(k_j) \propto \omega$ and $|\mathrm{Im}(k_j)| \propto \omega^{1/2}$. The low-frequency attenuation of the slow wave has a constant value of 2, since the absolute values of the imaginary and real part are equal.
We finally notice that the low and high-frequency asymptotes of the fast and slow wave velocities and attenuations intersect at frequencies on the order of magnitude of ω_B.
Clearly, Biot's theory applies to homogeneous porous media. However, if the medium is heterogeneous at meso-scale, it may also be possible to carry out a numerical study by discretizing the heterogeneous medium with small homogeneous cells, but this is expensive (Masson et al., 2006). So, in the following two chapters we investigate macro-models that account for meso-scale heterogeneities.

Chapter 3

Theory of partially saturated rocks with layered patches[1]

Abstract

The low-frequency theory of the White model to predict the dispersion and intrinsic attenuation in a single porous skeleton saturated with periodic layers of two immiscible fluids is extended to the full frequency range using the Biot theory. The extension is similar to the Dutta-Odé model for spherical inhomogeneities. Below the layer resonance frequency, the acoustic bulk properties for several gas-water fractions are in good agreement with the original White model. Deviations start to occur at higher frequencies due to the growing importance of resonance phenomena that were neglected in the original White model. The full model predicts significantly higher damping at sonic frequencies than the original White model. We also show that attenuation is significantly dependent on porosity variations. With realistic rock and fluid properties a maximum attenuation of about 0.3 is found at seismic frequencies.

3.1 Introduction

Information about the subsurface recovered from sonic, cross well, VSP, and seismic data can be retrieved from the physical mechanisms that control attenuation. Intrinsic attenuation is the decreasing of the amplitude of the propagating wavelet

[1]Published in *Geophysical Prospecting 55*(5), 685-695 (2007).

Note that the notation in the present chapter differs from the original publication to make it consistent with the other chapters of this dissertation.

by conversion of its energy into heat. All other loss mechanisms, such as scattering, interference, spherical divergence, receiver to earth coupling, wave conversion, and so forth are termed apparent attenuation, and are essentially due to a limitation in the positioning of the receivers. If we consider the subsurface of interest as a macroscopically homogeneous porous medium composed of elastic grains fully saturated by a single pore fluid, the expansion and contraction of a passing wave will cause relative movements between the individual grains and between the grains and the pore fluid. These movements together with the global flow behavior of the fluid will dissipate energy from the wave as first reckoned by Biot (1956a,b). However, it is well-known that the purely viscosity-based damping predicted by the Biot theory significantly underestimates the level of attenuation observed in field data in the seismic frequency band (e.g. Sams et al. (1997)). Microscale heterogeneities, such as cracks in the individual grains cause squirt flow (Mavko et al., 2003) and can explain the attenuation observed by Jones (1986) in the laboratory. The higher ultrasonic velocities of King et al. (2000), measured on sandstones from hydrocarbon reservoirs with high porosity and a wide range of permeability, support local flow phenomena owing to the presence of open microcracks. It was shown (e.g. Pride et al. (2003)) that this squirt mechanism is unable to explain the attenuation in the seismic frequency band.

Mesoscale heterogeneities larger than the grain size but smaller than the dominant wavelengths have been found to yield additional loss mechanisms (Pride et al., 2003). These may either be due to variations in solid grain properties, such as the grain bulk modulus and solid density, to variations in packing, such as porosity, permeability, frame bulk modulus, or to saturation by fluids with different properties, such as density, compressibility, and viscosity. Lithological mixtures of sand and clay saturated by oil or water and gas are in this way regarded as mesoscale heterogeneities. Among others, Murphy et al. (1986) and Cadoret et al. (1995) observed patchy saturation effects on the acoustic properties at laboratory frequencies between 1 and 500 kHz. Compressional wave velocities and attenuation were measured both *in situ* (0.2-1.5 kHz) and in the laboratory (200-800 kHz) on poorly sorted seafloor sediments by Best et al. (2001). The observations of Best et al. (1994) on water-saturated sandstones and shales with varying amounts of clay and lime mud support local viscous fluid-flow, due to compliant minerals, as the most likely loss mechanism at high effective pressures. Recently, Batzle et al. (2006) measured attenuation from 5 Hz to 800 kHz using forced deformation, resonance, and ultrasonic techniques, and found the influence of fluid mobility as a possible dominant mesoscopic loss process between heterogeneous compliant regions.

Immiscible fluids can be modelled as patches of one fluid surrounded by a second

fluid or by a sequential periodic layering of two pore-fluids within a uniform porous frame. The patches in the model of White (1975) are equidistant spaced fluid spheres, while Johnson (2001) treated wave-induced mesoscopic flow without placing restrictions on the patch geometries. Pride et al. (2004) modelled wave-induced flow for an arbitrary mesoscopic geometry of patchy saturation within each averaging volume. Gei and Carcione (2003) calibrated a modified empirical fluid-mixing law proposed by Brie et al. (1995) with the spherical White model at high frequencies to obtain wave velocities and attenuation of gas-hydrate-bearing sediments as a function of pore-pressure, temperature, frequency and saturation. Müller and Gurevich (2005a,b) modelled wave propagation in an inhomogeneous medium by using the Biot equations with randomly varying coefficients (fluctuations in the solid phase, drained frame and fluid parameters as a function of position) and so analysed the effect of wave-induced flow on attenuation and dispersion. Earlier, one-dimensional results (Gurevich and Lopatnikov, 1995; Gelinsky et al., 1998) showed that attenuation due to fluid-flow in a randomly layered porous medium differs significantly from the attenuation in periodically layered media of White et al. (1975), as homogenized by Norris (1993). Carcione et al. (2003) simulated the relaxation phenomena of the spherical White model with numerical experiments and found comparable trends. Recently, Brajanovski et al. (2005) used White's concept to model the dispersion and attenuation of a porous medium, permeated by aligned fractures, by considering a periodically layered poroelastic bimodal medium. They used the results of Norris (1993) in which one of the two layer thicknesses goes to zero and its porosity essentially goes to one, and the dry bulk modulus of the fracture goes to zero.

The original White (1975) and White et al. (1975) theories of fluid flow effects in porous media containing spherical or layered inhomogeneities are restricted to frequencies ω much lower than the critical Biot frequency

$$\omega \ll \omega_B = \frac{\phi\eta}{k_0\alpha_\infty\rho_\mathrm{f}}, \tag{3.1}$$

where ϕ, α_∞, and k_0 are the porosity, tortuosity, and permeability of the composite, and ρ_f and η denote the density and viscosity of the pore fluid.

This paper on flow-induced attenuation focuses on the layered geometry of White et al. (1975), with either two fluids saturating one solid frame or two solid phases containing a single fluid in all pores. Within this 1D framework, simultaneous variation in both fluid and solid phase is also possible. White et al. (1975) derived expressions for the acoustic bulk properties of low-frequency compressional waves travelling perpendicular to the boundaries of a medium, which consists of

a porous skeleton alternately saturated with two layers of fluids. For wavelengths long compared to the layer thickness, the zones appear macroscopically isotropic and homogeneous. They concluded that for alternate saturation with water and gas, fluid-flow across the boundaries may result in substantial dispersion and attenuation of low-frequency compressional waves. The effects are less significant for a reduction in contrast between the fluid properties, and hence are less noteworthy for alternating liquid-liquid saturation, e.g. oil-water, than for liquid-gas saturation.

Counter-intuitively, no significant dispersion or attenuation was noted by White et al. (1975) for layers with a different porosity and permeability saturated by a single fluid. Indeed, other theoretical treatments, such as the double porosity model (Pride and Berryman, 2003a,b), showed the dependence of dispersion and attenuation on porosity and permeability. Shapiro and Müller (1999) showed that the frequency dependence of the P-wave attenuation coefficients and its anisotropy are sensitive to fluctuations in permeability.

The main purpose of present paper is twofold: (1) the low-frequency layered White model is extended to the full frequency range; and (2) the dependence of attenuation and dispersion on variation in medium properties is examined over the full frequency range and compared with White's layered model.

First, we introduce the basic poroelastic relationships of the Biot theory, followed by a description of the geometry of a periodically layered model with the corresponding boundary conditions. Next, the computational procedure to calculate the forward- and backward-propagating pressure waves of the fast and the slow Biot wave is treated. This gives rise to a new complex plane-wave modulus for the entire frequency range, which is compared with the original low-frequency approximation of White et al. (1975) on attenuation and dispersion. The individual contributions from Biot's fast and slow wave to the pore pressure are analysed throughout the layer, since this will help in understanding the features of the Biot theory as applied to current model.

3.2 Poroelastic relationships

The relationships between the different complex-valued one-dimensional[1] amplitudes of the pore-pressure $\hat{p}$, the intergranular stress $\hat{\sigma}$, the fluid velocity $\hat{w}$ and the solid velocity $\hat{v}$, follow from the stress-strain relationships of the Biot the-

[1]Corrected for the error in Vogelaar and Smeulders (2007).

ory (1956a; 1956b), in the form presented by Jocker et al. (2004)

$$-i\omega\phi\hat{p} = -ik(Q\hat{v} + R\hat{w}), \tag{3.2}$$

$$-i\omega\hat{\sigma} = -ik(P'\hat{v} + Q'\hat{w}), \tag{3.3}$$

where

$$P' = P - \frac{1-\phi}{\phi}Q, \tag{3.4}$$

$$Q' = Q - \frac{1-\phi}{\phi}R, \tag{3.5}$$

and

$$P = A + 2\mu, \tag{3.6}$$

where μ denotes the frame shear modulus. An $e^{i\omega t}$ dependence is implicitly understood. Explicit expressions of the elastic coefficients A, Q and R, are given in terms of the bulk modulus of the fluid K_f, the bulk modulus of the solid K_s and the bulk modulus of the drained matrix K_m, by Biot and Willis (1957) as

$$A = \frac{\phi K_\mathrm{m} + (1-\phi)K'}{\phi'} - \frac{2}{3}\mu, \tag{3.7}$$

$$Q = \frac{\phi K'}{\phi'}, \tag{3.8}$$

$$R = \frac{\phi^2 K_\mathrm{f}}{\phi'}, \tag{3.9}$$

where

$$\phi' = \phi + \frac{K'}{K_\mathrm{s}}, \tag{3.10}$$

is an effective porosity and

$$K' = K_\mathrm{f}\left(1 - \phi - \frac{K_\mathrm{m}}{K_\mathrm{s}}\right), \tag{3.11}$$

is an effective bulk modulus. Combining the stress-strain relationships, equations (3.2) and (3.3), with the momentum balance equations for the fluid and the solid,

it is possible to derive the dispersion relation for compressional waves in porous media. For details we refer the reader to, for example, Smeulders (2005) and references therein. Defining the complex-valued wave velocity c, the dispersion relation can be written as

$$(PR - Q^2) - (P\rho_{22} + R\rho_{11} - 2Q\rho_{12})c^2 + (\rho_{11}\rho_{22} - \rho_{12}^2)c^4 = 0. \tag{3.12}$$

The complex-valued frequency-dependent mass density coefficients ρ_{11}, ρ_{12} and ρ_{22}, are dependent on the solid density ρ_{s}, the fluid density ρ_{f}, the tortuosity α_∞, and the dynamic interaction between the fluid and the solid matrix by Johnson et al. (1987)

$$\rho_{11} = (1-\phi)\rho_{\mathrm{s}} - \rho_{12}' - ib(\omega)/\omega, \tag{3.13}$$

$$\rho_{12} = \rho_{12}' + ib(\omega)/\omega, \tag{3.14}$$

$$\rho_{22} = \phi\rho_{\mathrm{f}} - \rho_{12}' - ib(\omega)/\omega, \tag{3.15}$$

where

$$\rho_{12}' = -(\alpha_\infty - 1)\phi\rho_{\mathrm{f}}. \tag{3.16}$$

The dynamic interaction coefficient $b(\omega)$ is defined as

$$b(\omega) = \frac{\eta\phi^2}{k_0}\sqrt{1 + i\frac{\omega}{2\omega_{\mathrm{B}}}}, \tag{3.17}$$

and ω_{B} is the critical Biot frequency defined in equation (3.1). From equation (3.12), we understand that there are two solutions for the compressional velocity, viz. $c_1 = \omega/k_1$ for the fast Biot wave with wavenumber k_1 and $c_2 = \omega/k_2$ for the slow Biot wave with wavenumber k_2. The Biot theory not only predicts the wave speeds c_j, where $j = 1$ or 2, but also yields the relationships between the complex-valued amplitudes. It is convenient to define the fluid-to-solid amplitude ratio by

$$\beta_j = \frac{\hat{w}_j}{\hat{v}_j} = \frac{\rho_{11}c_j^2 - P}{Q - \rho_{12}c_j^2}. \tag{3.18}$$

From equations (3.2) and (3.3), the ratio of solid stress to pore pressure is

$$\frac{\hat{\sigma}_j}{\hat{p}_j} = \phi\frac{P' + Q'\beta_j}{Q + R\beta_j}, \tag{3.19}$$

and the ratio of the solid velocity to pore pressure is given by

$$\frac{\hat{v}_j}{\hat{p}_j} = \phi\frac{\pm c_j}{Q + R\beta_j}, \tag{3.20}$$

where the $\pm$ sign indicates the propagation direction.

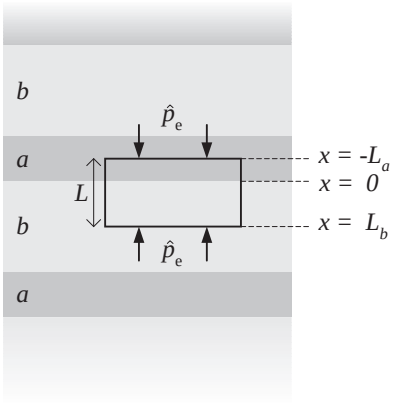

Figure 3.1: Geometry of a stratigraphy of periodic zones with layer properties a and b, including a representative element of length L.

3.3 Model geometry and boundary considerations

Consider a fully saturated poroelastic solid with horizontal periodic zones of two different medium properties. These two different zones are isotropic and homogeneous and can be a result of two different saturating fluids. In figure 3.1, the top of a representative element is chosen in the middle of layer a at $x = -L_a$ and the bottom in the middle of layer b at $x = L_b$, such that $L_a + L_b = L$. By symmetry there is no fluid flow across the middle of any layer. In other words, neither fluid can escape from the 'jacketed' representative element.
When a harmonic pressure wave travels perpendicular to this layering, the layers will expand and contract. From an external pressure $\hat{p}_e$ on the top and bottom of the representative element a resulting total strain ϵ is computed. Their ratio gives the complex plane-wave modulus H^*

$$H^* = -\frac{\hat{p}_e}{\epsilon}, \tag{3.21}$$

which is related to an effective complex wavenumber k_{eff} by $k_{\text{eff}} = \omega\sqrt{\rho_e/H^*}$, with the effective medium density ρ_e, defined as

$$\rho_e = \sum_{m=a,b} \frac{L_m}{L}\rho_m. \tag{3.22}$$

The density of layer m is $\rho_m = (1-\phi_m)\rho_{sm} + \phi_m\rho_{fm}$, where ρ_{sm} and ρ_{fm} are respectively the solid and fluid densities in layer m, which has porosity ϕ_m. The real part of k_{eff} yields the phase velocity $c_{\text{eff}} = \omega/\text{Re}(k_{\text{eff}})$, whereas both real and imaginary parts define the attenuation $Q^{-1} = 2\text{Im}(k_{\text{eff}})/\text{Re}(k_{\text{eff}})$.

The pore fluid pressures in layers a and b are given by

$$\hat{p}_a = A_1^+ e^{-ik_{1a}x} + A_1^- e^{ik_{1a}x} + A_2^+ e^{-ik_{2a}x} + A_2^- e^{ik_{2a}x}, \tag{3.23}$$

$$\hat{p}_b = B_1^+ e^{-ik_{1b}x} + B_1^- e^{ik_{1b}x} + B_2^+ e^{-ik_{2b}x} + B_2^- e^{ik_{2b}x}, \tag{3.24}$$

with complex pressure coefficients $A_1^\pm$ or $B_1^\pm$ for the fast wave and $A_2^\pm$ or $B_2^\pm$ for the slow wave in layer a or b pointing in the $\pm$ x-direction. The unknowns are solved as a boundary value problem using Biot's theory. System equations (3.23) and (3.24) can be solved with eight boundary conditions. Continuity of pore pressure and continuity of intergranular stress at the boundary between media a and b prescribed that

$$\hat{p}_a = \hat{p}_b \qquad \text{at } x = 0, \tag{3.25}$$

$$\hat{\sigma}_a = \hat{\sigma}_b \qquad \text{at } x = 0. \tag{3.26}$$

Continuity of volume flux and continuity of solid particle velocity at the boundary requires that

$$\hat{\overline{w}}_a = \hat{\overline{w}}_b \qquad \text{at } x = 0, \tag{3.27}$$

$$\hat{v}_a = \hat{v}_b \qquad \text{at } x = 0, \tag{3.28}$$

where $\hat{\overline{w}}_m = \phi_m(\hat{w}_m - \hat{v}_m)$. Continuity of total stress at the top and at the bottom of the representative element implies that

$$\hat{p}_a + \hat{\sigma}_a = \hat{p}_\mathrm{e} \qquad \text{at } x = -L_a, \tag{3.29}$$

$$\hat{p}_b + \hat{\sigma}_b = \hat{p}_\mathrm{e} \qquad \text{at } x = L_b. \tag{3.30}$$

Finally, the relative velocity should be zero at the top and at the bottom of the representative element:

$$\hat{\overline{w}}_a = 0 \qquad \text{at } x = -L_a, \tag{3.31}$$

$$\hat{\overline{w}}_b = 0 \qquad \text{at } x = L_b. \tag{3.32}$$

3.4 Full frequency solution

The eight unknowns in equations (3.23) and (3.24) can be found from a linear system in $\hat{p}_\mathrm{e}$ written in matrix form as

$$\sum_{j=1}^{8} H_{ij} y_j = z_i. \tag{3.33}$$

The coefficients of matrix H_{ij} are obtained from equations (3.18), (3.2) and (3.3) applied to the boundaries outlined in equations (3.25)-(3.32), where y_j is a column vector of the unknown elements given by

$$\mathbf{y} = (\ A_1^+,\quad A_1^-,\quad A_2^+,\quad A_2^-,\quad B_1^+,\quad B_1^-,\quad B_2^+,\quad B_2^-\ )^\mathrm{T}, \tag{3.34}$$

and the column vector z_i reads

$$\mathbf{z} = \hat{p}_\mathrm{e}(\ 0,\quad 0,\quad 0,\quad 0,\quad 1,\quad 1,\quad 0,\quad 0\ )^\mathrm{T}. \tag{3.35}$$

Equation (3.33) is solved with the frequency-dependent elements of H_{ij} given in Appendix A. From the matrix computations in Matlab, the pore-pressure amplitudes $A_j^\pm$ and $B_j^\pm$ relative to the effective pressure $\hat{p}_\mathrm{e}$ are obtained. With equations (3.19), (3.20) and (3.23), (3.24), the solid displacements $\hat{u}_a$ at $x = -L_a$ and $\hat{u}_b$ at $x = L_b$ are computed to obtain the complex plane-wave modulus for the full frequency range

$$H^* = \frac{L}{\hat{u}_a|_{x=-L_a} - \hat{u}_b|_{x=L_b}} \hat{p}_\mathrm{e}. \tag{3.36}$$

The absolute and phase values of the reduced complex plane wave modulus are plotted as a function of frequency in figure 3.2 for a medium with material properties as given in table 3.1. The rock and fluid properties correspond to the values of case 5 of White et al. (1975). The skeleton of case 5 is a highly permeable unconsolidated sand, fully saturated with alternate water and gas zones. A gas fraction of 10% is chosen. We observe that for low frequencies, the absolute value of H^* becomes less than the effective plane-wave modulus H_e, owing to the additional compliance because of fluid exchange across $x = 0$. When the wavelength becomes of the same order as the layer thickness, resonance occurs and the medium becomes extremely compliant. These phenomena are comparable to the so-called passing and stopping bands in transmittivity computations (e.g. Jocker et al. (2004)). On increasing the frequency, the medium oscillates out-of-phase with respect to $\hat{p}_\mathrm{e}$ (anti-resonance) and at around 10^4 Hz, relatively high values for H^* are obtained.

Skeleton	Water	Gas
$\rho_{\rm s} = 2650$ kg/m^3	$\rho_{{\rm f}a} = 1000$ kg/m^3	$\rho_{{\rm f}b} = 70$ kg/m^3
$K_{\rm s} = 33.4 \times 10^9$ Pa	$K_{{\rm f}a} = 2.2 \times 10^9$ Pa	$K_{{\rm f}b} = 9.6 \times 10^6$ Pa
$k_0 = 1.0 \times 10^{-12}$ m^2	$\eta_a = 0.6 \times 10^{-3}$ kg/m/s	$\eta_b = 15 \times 10^{-6}$ kg/m/s
$\phi = 0.30$		
$K_{\rm m} = 3.18 \times 10^9$ Pa		
$\mu = 1.40 \times 10^9$		
$L = 0.20$ m		

Table 3.1: Properties of the skeleton and fluids of case 5 from White et al. (1975).

Note that these values fall outside the scale of the figures. The phase values have a maximum around 70 Hz. At high frequency, resonances between 0° and 180° occur. The model solutions of the original White et al. (1975) theory as derived in Appendix B, are also plotted; these will be discussed below.

3.5 Analysis of pore-pressure distribution

We analyse the pore pressure distribution in figure 3.3. The separate contributions of the fast and the slow wave are also plotted. A gas fraction of 20% is chosen. The rock and fluid properties are given in table 3.1. We note that: (1) The discontinuities at the gas-water interface ($x = 0$) observed in the fast and slow waves are exactly equal and opposite in sign, so that the net fluid pressure is continuous. (2) Both the real and imaginary parts of the fluid pressure due to the fast wave are practically constant for all frequencies, except for high frequency. (3) The fluid pressure due to the slow wave in the gas-bearing layer is almost independent of the distance from the interface. However, in the water-bearing layer, it varies significantly, especially at high frequencies. (4) At low frequencies, the net fluid pressure approaches a constant value throughout the medium, while at the highest shown frequencies, the pore-fluid pressure exhibits oscillatory behaviour. Similar features were reported by Dutta and Odé (1979a,b) on the spherical White model.

3.6 Resulting attenuation and dispersion

The phase velocity and attenuation characteristics from the full model and White's model are shown in figure 3.4 for different gas saturations. Different L_b/L ratios are chosen similar to figures 2 and 4 in the original White et al. (1975) paper.

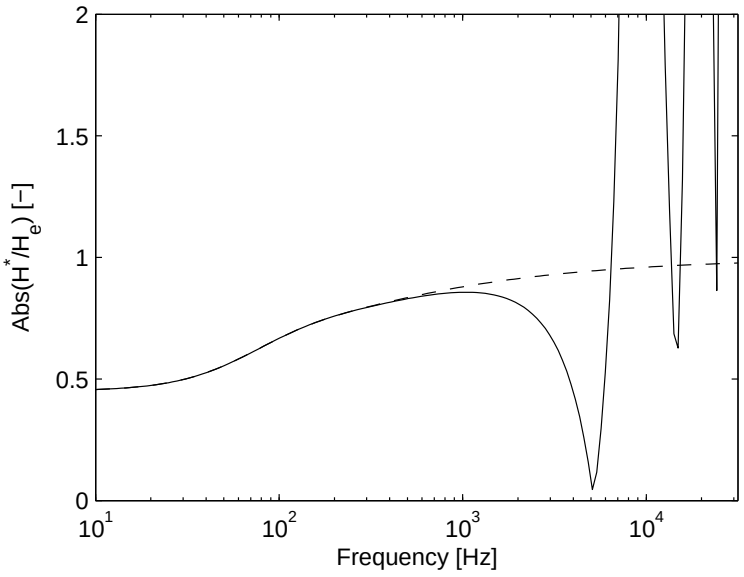

(a)

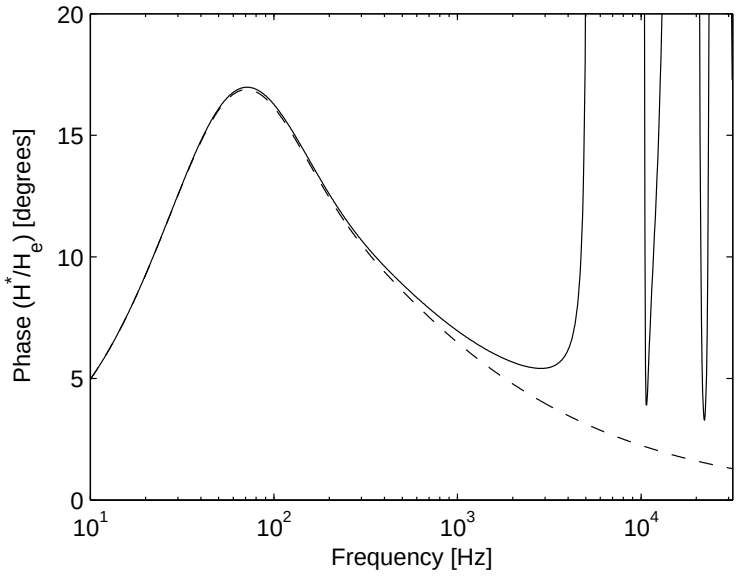

(b)

Figure 3.2: Absolute and phase values of the reduced plane-wave modulus H^*/H_e as a function of frequency for the full model (solid curves) and White's model (dashed curves). The rock and fluid properties are given in table 3.1. The gas fraction is 10%. The absolute value of the first anti-resonance maximum is at approximately 20, while the phase oscillates periodically between zero and 180° (not shown in the figures).

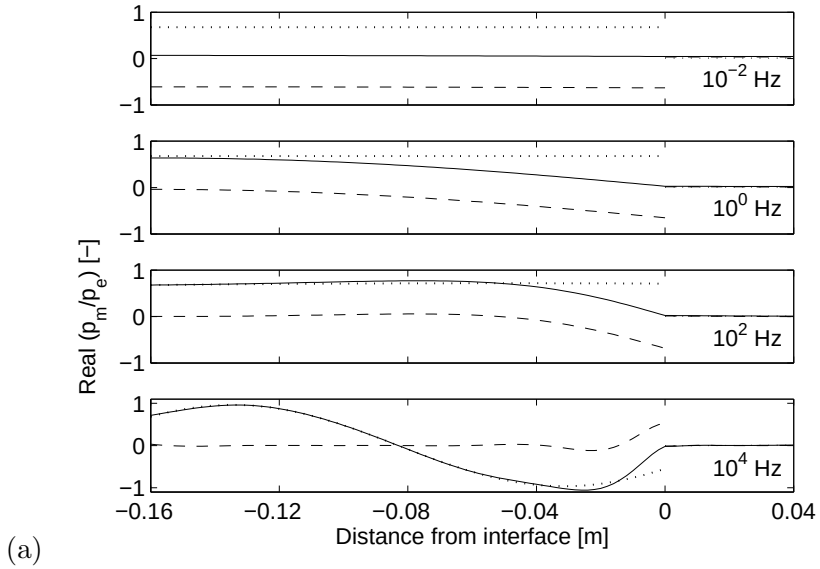

(a)

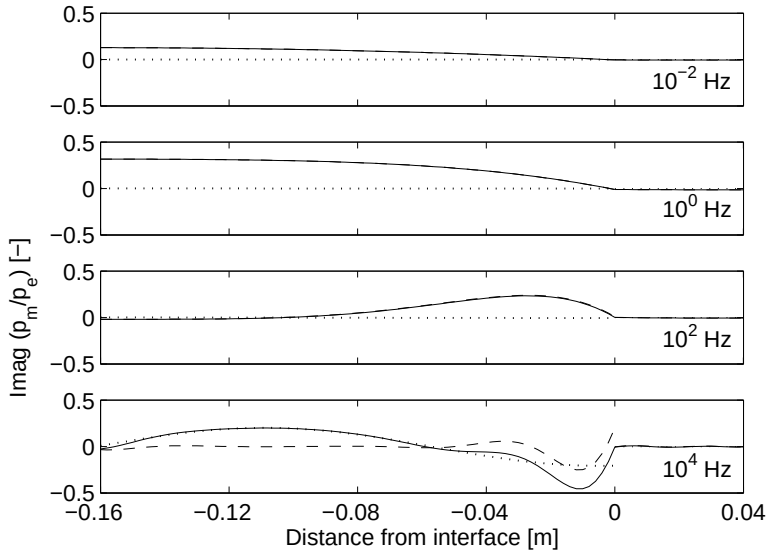

(b)

Figure 3.3: Real and imaginary components of the pore pressure $\hat{p}_m$ relative to the effective pressure $\hat{p}_e$ throughout the layers for four indicated frequency values. The solid curves give the sum of the fast (dotted curves) and the slow (dashed curves) compressional-wave contributions. The skeleton, gas and water properties are given in table 3.1. The gas-filled zone comprises 20% of the stack. Because of symmetry, only the distribution enclosed by the representative element is shown for water between x = -0.16 m and $x = 0$ and for gas between $x = 0$ and 0.04 m.

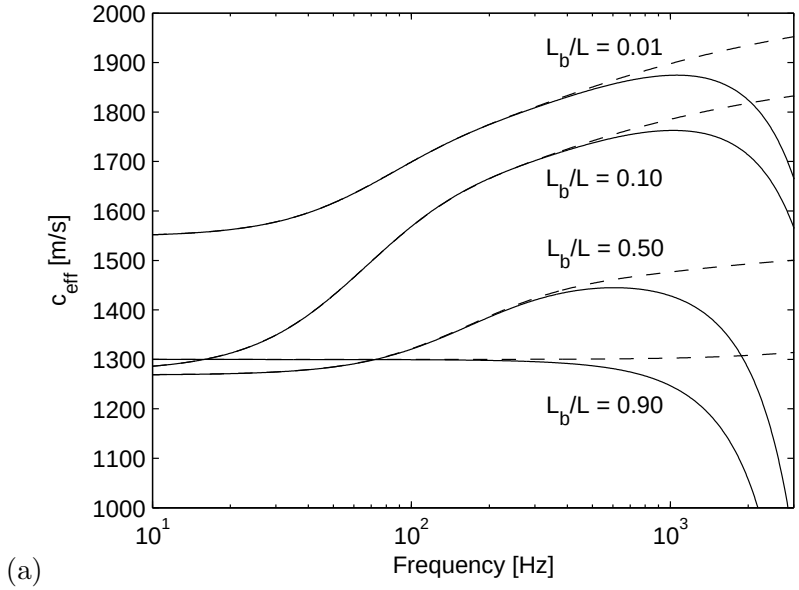

(a)

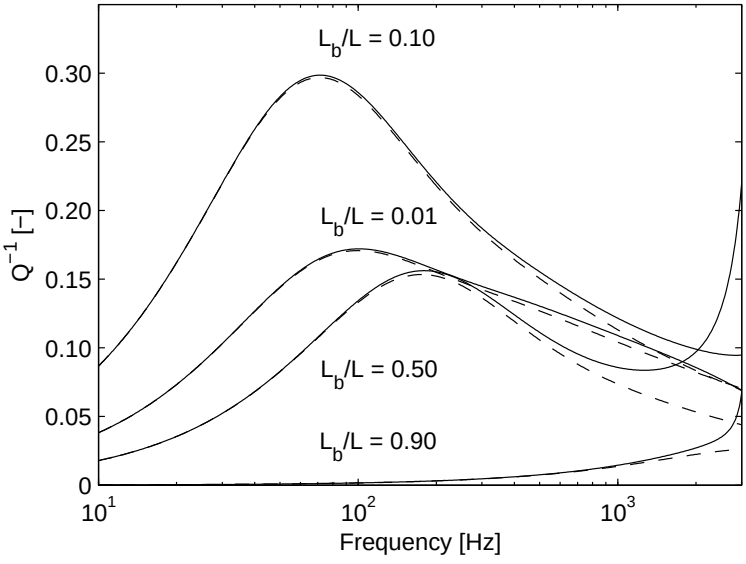

(b)

Figure 3.4: Attenuation Q^{-1} and phase velocity c_{eff} as a function of frequency for the full model (solid curves) and White's model (dashed curves) for several gas fractions L_b/L. The medium properties are given in table 3.1. The data are truncated near resonance frequency.

We observe that for increasing gas fraction, the low-frequency limit of the wave velocity c_{eff} decreases due to the lower stiffness of the system. At very high gas fractions, the velocity at low frequencies increases again due to the density effect becoming dominant in this case. The White model gives an accurate prediction for the velocity in all cases, although for higher frequencies, deviations start to occur. As was noted (Pride et al., 2002), the attenuation peak is largely due to the slow-wave-induced diffusion in order to equilibrate the fluid pressure between the layers. Such attenuation is at a maximum when the penetration length of the diffusion process is of the order of the layer spacing:

$$\omega_{\max} \approx \frac{K_{\text{f}} k_0}{\eta \phi L^2}. \tag{3.37}$$

The peak attenuation increases and shifts toward lower frequencies for a decreasing gas fraction from 90% to 10%. For a gas fraction of 1% the damping is less significant than for 10%, indicating that the maximum effect of fluid-flow is expected to lie around 5% gas saturation. The figures clearly demonstrate that even a small amount of gas trapped in a porous water-saturated rock significantly alters the acoustic properties in the usual seismic frequency band (5-500 Hz). Note that our full model predicts at least 10% higher damping in the sonic range (0.8-3 kHz) than White's model.

The shape of the attenuation curve is typical for a relaxation process, which at low frequencies increases almost linearly with frequency ω up to a maximum value and then decreases as approximately $\omega^{-1/2}$. This low-frequency behaviour has also been reported for 3D periodic structures (White, 1975; Dutta and Seriff, 1979) and 3D random structures (Müller and Gurevich, 2005b). However, the attenuation at low frequencies in periodic layering differs from random layering where it is proportional to $\omega^{1/2}$ (Gurevich and Lopatnikov, 1995). The high-frequency asymptote has also been found in randomly layered structures and 3D periodic and random heterogeneities by the same authors, although the scaling is not universal for any kind of disorder (Müller and Gurevich, 2005b). Moreover, Johnson (2001), Pride and Berryman (2003a,b) and Pride et al. (2004) found the same low- and high-frequency asymptotes for media with regularly distributed identical inhomogeneities of any shape.

The effect of porosity on attenuation for both models is shown in figure 3.5 for three different layer fractions. For this purpose, layer a was chosen to have a porosity $\phi_a = 0.1$ and layer b of $\phi_b = 0.3$, while all other rock parameters remained unaffected. The entire medium is saturated with water. As seen in figure 3.5, non-negligible attenuation is observed for both models with a peak attenuation at about 150

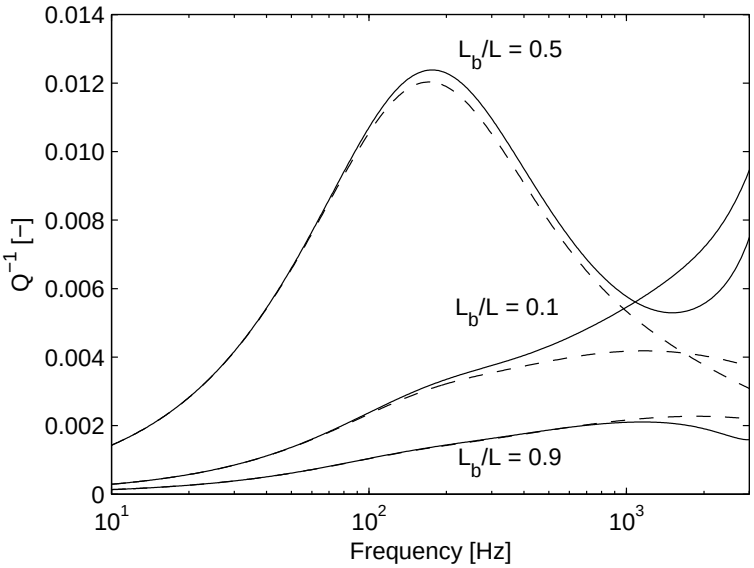

Figure 3.5: Attenuation as a function of frequency for the full model (solid curves) and White's model (dashed curves) for zones with different porosities $\phi_a = 0.1$ and $\phi_b = 0.3$. The remaining skeleton and water properties are given in table 3.1. The fractional thickness of layer b with respect to L indicates the relative amount L_b/L within the stack. The data are truncated near resonance frequency.

Hz when the layers with different porosities have identical thicknesses. Again, we calculate a frequency-dependent underestimation of the intrinsic attenuation for White's model with respect to the full theory. Our analysis of both models does not support the statement of White et al. (1975) that no significant dispersion or attenuation was noted for any of the relative amounts of two media having different porosity.

3.7 Conclusions

Inhomogeneities in fluid-saturated porous rocks are introduced by a periodic sequence of alternating plane-parallel layers with a length scale much larger than the typical pore-size. These inhomogeneities have a considerable effect on seismic-wave propagation and damping. For wavelengths larger than the layer thickness (low frequencies), an effective frequency-dependent plane-wave modulus was defined by White et al. (1975). It was assumed that local pressure differences due

to the passing of a seismic wave are counteracted by mesoscopic fluid-flow from regions of high pore-pressure to regions of low pore pressure. This mesoscopic equilibration causes extra damping with respect to the Biot global-flow model. On the basis of the full Biot theory, we extend this model to the higher frequency range. We compare the extended model with the original White model. When the wavelength becomes of the same order as the layer thickness, resonance occurs and the medium becomes extremely compliant. At even higher frequencies, the medium oscillates out-of-phase with respect to the effective pressure and gives rise to anti-resonance effects.

The influence of fluid-flow on attenuation is considered in two cases for the layered White model: (1) a uniform porous medium saturated with a gas-water layering; and (2) a porous medium having layers of different porosity, but saturated with a uniform liquid. For case 1, fluid-flow across the boundaries results in large attenuation and dispersion in the usual seismic frequency band (5-500 Hz). Maximum attenuation (up to 0.3) occurs at 70 Hz for around 5% gas saturation. In the sonic range (0.8-3 kHz), our full model predicts at least 10% higher intrinsic damping than White's approximate model. Although for case 2 the peak attenuation is less pronounced than for a contrast in fluid properties (i.e. case 1), we still observe a peak attenuation of about 0.013 at 150 Hz when both layers have identical thicknesses. Again, we calculate a frequency-dependent underestimation of the damping from White's model with respect to the full theory. Apparently, at sonic frequencies, resonance effects become more important; these are not taken into account in the original White model.

Appendix A

The elements of H_{ij} in system $\sum_{j=1}^{8} H_{ij} y_j = z_i$ with y_j and z_i specified in equations (3.34) and (3.35) follow from the values at the boundary locations $x = 0, -L_a$, and L_b as listed in equations (3.25)-(3.32). The elements h_{ij} of matrix H_{ij} are

$$\begin{aligned} h_{11} = h_{12} = h_{13} = h_{14} &= 1, \\ h_{15} = h_{16} = h_{17} = h_{18} &= -1; \end{aligned} \tag{3.38}$$

$$\begin{aligned} h_{21} = h_{22} &= \phi_a \frac{P'_a + Q'_a \beta_{1a}}{Q_a + R_a \beta_{1a}}, \\ h_{23} = h_{24} &= \phi_a \frac{P'_a + Q'_a \beta_{2a}}{Q_a + R_a \beta_{2a}}, \\ h_{25} = h_{26} &= -\phi_b \frac{P'_b + Q'_b \beta_{1b}}{Q_b + R_b \beta_{1b}}, \\ h_{27} = h_{28} &= -\phi_b \frac{P'_b + Q'_b \beta_{2b}}{Q_b + R_b \beta_{2b}}; \end{aligned} \tag{3.39}$$

$$\begin{aligned} h_{31} = -h_{32} &= \phi_a^2 \frac{c_{1a}(\beta_{1a} - 1)}{Q_a + R_a \beta_{1a}}, \\ h_{33} = -h_{34} &= \phi_a^2 \frac{c_{2a}(\beta_{2a} - 1)}{Q_a + R_a \beta_{2a}}, \\ h_{35} = -h_{36} &= -\phi_b^2 \frac{c_{1b}(\beta_{1b} - 1)}{Q_b + R_b \beta_{1b}}, \\ h_{37} = -h_{38} &= -\phi_b^2 \frac{c_{2b}(\beta_{2b} - 1)}{Q_b + R_b \beta_{2b}}; \end{aligned} \tag{3.40}$$

$$\begin{aligned} h_{41} = -h_{42} &= \frac{h_{31}}{\phi_a(\beta_{1a} - 1)}, \\ h_{43} = -h_{44} &= \frac{h_{33}}{\phi_a(\beta_{2a} - 1)}, \\ h_{45} = -h_{46} &= \frac{h_{35}}{\phi_b(\beta_{1b} - 1)}, \\ h_{47} = -h_{48} &= \frac{h_{37}}{\phi_b(\beta_{2b} - 1)}; \end{aligned} \tag{3.41}$$

$$
\begin{aligned}
h_{51} &= (1+h_{21})e^{ik_{1a}L_a},\\
h_{52} &= (1+h_{22})e^{-ik_{1a}L_a},\\
h_{53} &= (1+h_{23})e^{ik_{2a}L_a},\\
h_{54} &= (1+h_{24})e^{-ik_{2a}L_a},\\
h_{55} &= h_{56} = h_{57} = h_{58} = 0;
\end{aligned}
\tag{3.42}
$$

$$
\begin{aligned}
h_{61} &= h_{62} = h_{63} = h_{64} = 0,\\
h_{65} &= (1-h_{25})e^{-ik_{1b}L_b},\\
h_{66} &= (1-h_{26})e^{ik_{1b}L_b},\\
h_{67} &= (1-h_{27})e^{-ik_{2b}L_b},\\
h_{68} &= (1-h_{28})e^{ik_{2b}L_b};
\end{aligned}
\tag{3.43}
$$

$$
\begin{aligned}
h_{71} &= h_{31}e^{ik_{1a}L_a},\\
h_{72} &= h_{32}e^{-ik_{1a}L_a},\\
h_{73} &= h_{33}e^{ik_{2a}L_a},\\
h_{74} &= h_{34}e^{-ik_{2a}L_a},\\
h_{75} &= h_{76} = h_{77} = h_{78} = 0;
\end{aligned}
\tag{3.44}
$$

$$
\begin{aligned}
h_{81} &= h_{82} = h_{83} = h_{84} = 0,\\
h_{85} &= -h_{35}e^{-ik_{1b}L_b},\\
h_{86} &= -h_{36}e^{ik_{1b}L_b},\\
h_{87} &= -h_{37}e^{-ik_{2b}L_b},\\
h_{88} &= -h_{38}e^{ik_{2b}L_b}.
\end{aligned}
\tag{3.45}
$$

Appendix B

A low-frequency approximation of H^* was derived by White et al. (1975). It is easy to show that for static compression of a bimodal porous medium an effective plane-wave modulus H_e can be defined by

$$H_\mathrm{e} = \sum_{m=a,b} \left(\frac{L_m}{H_m L} \right)^{-1}. \tag{3.46}$$

The individual moduli H_m are the so-called Gassmann moduli (1951) for layer m, which are related to the Biot parameters via

$$H_m = P_m + R_m + 2Q_m. \tag{3.47}$$

Next, it is assumed that due to the external loading $\hat{p}_\mathrm{e}$, a pore pressure increase $B_m \hat{p}_\mathrm{e}$ is induced, where B_m is the plane-wave Skempton's coefficient, related to the Biot parameters via

$$B_m = \lim_{\omega \to 0} \left(\frac{\hat{p}_m}{\hat{p}_\mathrm{e}} \right)_{2m} = \frac{Q_m + R_m}{H_m \phi_m}, \tag{3.48}$$

where the subscript $2m$ refers to the slow wave. As a consequence of a contrast in the medium properties of layers a and b, there will be a pore-pressure discontinuity $(B_a - B_b)\hat{p}_\mathrm{e}$ at $x = 0$, which is counteracted by fluid-flow across the boundary. Fluid-flow is described by the wall impedances Z_m as derived in Appendix C:

$$\hat{\overline{w}}_m = \frac{\hat{p}_m}{Z_m}. \tag{3.49}$$

Continuity of volume flux at the boundary yields

$$\hat{\overline{w}}_a\big|_{x=0} = \hat{\overline{w}}_b\big|_{x=0} = \hat{\overline{w}}, \tag{3.50}$$

so that the continuity of pore-pressure at the boundary is satisfied by

$$B_a \hat{p}_\mathrm{e} + Z_a \hat{\overline{w}} = B_b \hat{p}_\mathrm{e} - Z_b \hat{\overline{w}}, \tag{3.51}$$

and thus

$$\hat{\overline{w}} = \frac{B_b - B_a}{Z_a + Z_b} \hat{p}_\mathrm{e}. \tag{3.52}$$

With β_{jm} from equation (3.18), the fluid-flow across the boundary creates an extra matrix displacement described by the parameter

$$\chi_{jm} = \frac{\hat{\overline{w}}_m}{\hat{v}_m} = \phi_m(\beta_{jm} - 1), \tag{3.53}$$

which is equal to the negative reciprocal of Skempton's coefficient B_m, i.e.

$$\lim_{\omega\to 0}\chi_{2m} = -\frac{\phi_m H_m}{Q_m + R_m} = -B_m^{-1}. \tag{3.54}$$

Hence, with equation (3.52), the extra displacement is given by

$$\hat{u}_a + \hat{u}_b = \frac{B_b - B_a}{i\omega}\hat{\overline{w}} = \frac{(B_b - B_a)^2}{(Z_a + Z_b)i\omega}\hat{p}_{\mathrm{e}}, \tag{3.55}$$

and the strain due to fluid-flow is derived as

$$\epsilon_{\mathrm{flow}} = \frac{\hat{u}_a + \hat{u}_b}{L_a + L_b} = \frac{(B_b - B_a)^2}{(Z_a + Z_b)i\omega}\frac{\hat{p}_{\mathrm{e}}}{L}. \tag{3.56}$$

Finally with equation (3.21), we find White's plane-wave modulus H_0^* to be

$$H_0^* = H_{\mathrm{e}}\left[1 - \frac{H_{\mathrm{e}}(B_b - B_a)^2}{(Z_a + Z_b)i\omega L}\right]^{-1}. \tag{3.57}$$

The absolute and phase values of H_0^* are also plotted in figure 3.2. As expected, we note that for low frequencies the White approximation is in excellent agreement with the full solution.
The low-frequency limit of Z_m from equations (3.71) and (3.72) is

$$\lim_{\omega\to 0} Z_m = \frac{\eta_m}{k_{0m}k_{2m}^2 L_m}, \tag{3.58}$$

which means, with equation (3.66), that

$$\lim_{\omega\to 0} Z_a + Z_b = \frac{i}{\omega}\left(\frac{\eta_a D_a}{k_{0a}L_a} + \frac{\eta_b D_b}{k_{0b}L_b}\right). \tag{3.59}$$

Substitution into equation (3.57) gives

$$\lim_{\omega\to 0} H_0^* = H_{\mathrm{e}}\left[1 + \frac{H_{\mathrm{e}}(B_b - B_a)^2}{L(\frac{\eta_a D_a}{k_{0a}L_a} + \frac{\eta_b D_b}{k_{0b}L_b})}\right]^{-1}. \tag{3.60}$$

From equation (3.57), it is immediately clear that the high frequency limit of White's solution is given by

$$\lim_{\omega\to\infty} H_0^* = H_{\mathrm{e}}. \tag{3.61}$$

At high frequencies, the fluid has no time to flow and the model obviously reduces to the case of static compression without fluid exchange.

Appendix C

The out-of-phase movement between the solid and the fluid is described by slow Biot waves that propagate in each layer:

$$\hat{p}_a = A_2^+ e^{-ik_{2a}x} + A_2^- e^{ik_{2a}x}, \tag{3.62}$$

$$\hat{p}_b = B_2^+ e^{-ik_{2b}x} + B_2^- e^{ik_{2b}x}. \tag{3.63}$$

For low frequencies, the slow wave satisfies the diffusion equation in terms of pore fluid pressure, i.e.

$$\frac{\partial \hat{p}}{\partial t} - D\nabla^2 \hat{p} = 0, \tag{3.64}$$

where the diffusivity D is related to Biot's phenomenological parameters as (Chandler and Johnson, 1981)

$$D = \frac{PR - Q^2}{b_0 H}, \tag{3.65}$$

in which $b_0 = \eta\phi^2/k_0$ is the viscous damping factor. The solution of equation (3.64) is given by

$$k_2 = \tfrac{1}{2}\sqrt{2}\,(1-i)\sqrt{\frac{\omega}{D}}. \tag{3.66}$$

Fluid flow across the boundary is quantified by the velocity of the fluid relative to the velocity of the solid frame

$$\hat{\overline{w}}_m = \phi_m(\hat{w}_m - \hat{v}_m), \tag{3.67}$$

and depends on the pressure gradient via Darcy's law,

$$\hat{\overline{w}}_m = -\frac{k_{0m}}{\eta_m}\nabla \hat{p}_m, \tag{3.68}$$

so that from equations (3.62) and (3.63), we obtain

$$\hat{\overline{w}}_a = \frac{ik_{2a}k_{0a}}{\eta_a}\left(A_2^+ e^{-ik_{2a}x} - A_2^- e^{ik_{2a}x}\right), \tag{3.69}$$

$$\hat{\overline{w}}_b = \frac{ik_{2b}k_{0b}}{\eta_b}\left(B_2^+ e^{-ik_{2b}x} - B_2^- e^{ik_{2b}x}\right). \tag{3.70}$$

The relative velocity $\hat{\overline{w}}$ should be zero at $x = -L_a$ and $x = L_b$, so that

$$\left.\frac{\hat{p}_a}{\hat{\overline{w}}_a}\right|_{x=0} = \frac{\eta_a}{k_{0a}k_{2a}}\cot(k_{2a}L_a) = Z_a, \tag{3.71}$$

$$\left.\frac{\hat{p}_b}{\hat{\overline{w}}_b}\right|_{x=0} = -\frac{\eta_b}{k_{0b}k_{2b}}\cot(k_{2b}L_b) = -Z_b, \tag{3.72}$$

with the acoustic impedance Z_m, looking into layer m from the boundary between the two layers at $x = 0$.

Chapter 4

Theory of partially saturated rocks with spherical patches

4.1 Introduction

When a poroelastic solid is saturated with a liquid-gas mixture, additional interaction mechanisms than treated in the Biot theory have to be taken into account to describe wave propagation. In chapter 3, we discussed the effects of a periodic layering of gas and liquid saturations. However, other geometric configurations are possible. Here, we model inhomogeneities in the fluid by considering isolated spherical gas patches in the liquid saturating the matrix and focus on mesoscopic loss-mechanisms. Patchy theory is concerned with the class of models first proposed by White (1975) and White et al. (1975).

In section 4.2, we consider the geometry of the gas bubbles surrounded by liquid and formulate an expression to predict its influence on wave propagation. This expression is based on the boundary conditions as formulated by Deresiewicz and Skalak (1963). We first treat patchy saturation in the quasi-static Biot context in section 4.3 and compare this exact solution with a generalized quasi-static theory as suggested by Johnson (2001). The exact solution using the full Biot theory proposed by Dutta and Odé (1979a) is reviewed in section 4.5. For a gas bubble, the acoustic properties are compact over a wide frequency range. This considerably simplifies the computations, and leads to the development of a complimentary model: the Compact Gas Bubble model in section 4.6. The dependence on medium properties is treated in section 4.7 in terms of phase velocity and intrinsic attenuation. Finally, in section 4.8, we apply the Rayleigh-Plesset-Biot theory for linear pressure waves in bubbly liquids to partially saturated porous media and compare

it with predictions of the generalized quasi-static theory.
The purpose of studying these different models is to understand the physical phenomena involved, to define the relevant input parameters of the models (chapter 5), and to interpret the experiments (chapter 7).

4.2 Physical model

Consider a non-rigid porous medium fully saturated by a fluid that contains gas bubbles larger than the typical pore size, see figure 4.1. The interaction among the individual gas bubbles is neglected. When this gas bubble is subjected to the macroscopic pressure field of a compressional seismic wave (i.e., on a length scale much larger than the size of the inhomogeneity), the bubble will contract and expand. These oscillations generate waves on the mesoscale (i.e., on the length scale of the inhomogeneity), which consume energy from the seismic wave, causing intrinsic attenuation. The external pressure field is assumed to be spatially homogeneous at the scale of the inhomogeneity, and the effective (macroscopic) bulk modulus can be obtained by considering a representative volume comprising a single gas bubble (radius a) and a liquid shell (radius b) surrounding the bubble. Radius b is chosen such that the volume of the sphere $\frac{4}{3}\pi b^3$ equals the volume of the unit cell of the cubic lattice (see figure 4.1).
We assume that the porous and permeable solid is describable by the Biot equations. It is saturated with two different Newtonian fluids, having saturations s_a and s_b. At any point in the sample, it is fully saturated with either fluid, so that $s_b = 1 - s_a$. The gas fraction $s_a = (a/b)^3$. Throughout this work, subscript a refers to the gas phase and subscript b to the liquid phase.
The wave-induced pore pressure in the liquid will be different from that in the gas. The pressures will equilibrate via diffusive mechanisms. The characteristic frequency is determined by the diffusion time across a characteristic patch size:

$$\omega_c \sim D/b^2, \tag{4.1}$$

where D is the slow wave diffusivity, cf. equation (2.30), in the region with the liquid.
Solving the Biot equations yields the solid displacement as a function of the applied pressure and hence, the effective bulk modulus of the representative volume. The computation of the effective bulk modulus of the representative volume makes only sense if the frequency is low enough so that the wavelength of the fast compressional and shear waves are large compared to the dimensions of the bubbles and their

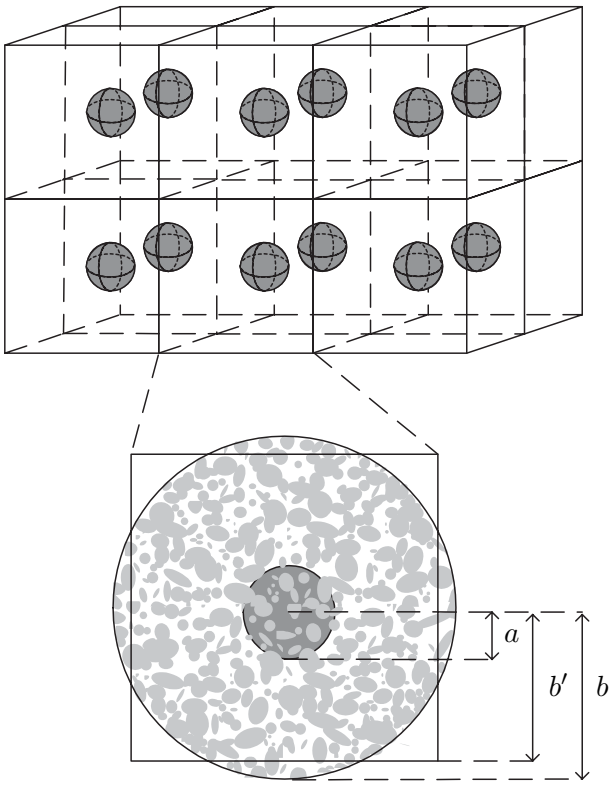

Figure 4.1: Geometry of a cubic lattice of periodic spherical gas bubbles with radius a, separated by distance $2b'$. Each gas bubble is surrounded by a liquid shell with radius b, such that the volume of the cube equals the volume of the sphere $V_{b'} = V_b$.

mutual distance. That is the mesoscopic condition $\omega \ll \omega_L$ should hold where

$$\omega_L \sim c_S/b, \tag{4.2}$$

in which c_S is the speed of the shear wave in the region of the liquid.

In the following, the Biot theory of chapter 2 is solved using the appropriate boundary conditions. These are: continuity of solid displacement $\mathbf{u}$ and fluid displacement $\mathbf{U}$, pressure p and total stress τ at $r = a$ and the condition that at

$r = b$ the external pressure p_{e} is applied at a sealed pore boundary[1]:

$$u_a(a) = u_b(a), \tag{4.3}$$
$$U_a(a) = U_b(a), \tag{4.4}$$
$$p_a(a) = p_b(a), \tag{4.5}$$
$$\tau_a(a) = \tau_b(a), \tag{4.6}$$
$$u_b(b) = U_b(b), \tag{4.7}$$
$$\tau_b(b) = -p_{\mathrm{e}}. \tag{4.8}$$

By solving the above equations, the field variables are determined uniquely everywhere.
The effective bulk modulus, $K(\omega)$, can then be deduced via its definition:

$$K(\omega) = -\frac{b}{3u_b(b)}p_{\mathrm{e}}, \tag{4.9}$$

where $u_b(b)$ is the radial solid displacement at the outer boundary. Once the effective bulk modulus K is obtained, an effective complex wavenumber is computed by

$$k_1 = \omega\sqrt{\frac{\rho}{K + \frac{4}{3}\mu}}, \tag{4.10}$$

where subscript 1 describes the fast wave on the macroscale (the conventional seismic wave). It is assumed that the shear modulus (on the macroscale) is independent of the fluid saturation: $\mu = \mu_a = \mu_b$. The total density ρ is

$$\rho = (1-\phi)\rho_{\mathrm{s}} + \phi(s_b\rho_{\mathrm{f}b} + s_{\mathrm{a}}\rho_{\mathrm{f}a}), \tag{4.11}$$

where $\rho_{\mathrm{f}n}$ denotes the gas (subscript a) or liquid (subscript b) density.

4.3 Exact patchy theory in the quasi-static Biot context

We now consider the response of the representative element to a uniform compressive stress. We presume that the frequency is low enough that the Biot theory is in its low frequency limit. Thus the fast compressional and shear waves are nondispersive and nonattenuating whereas the slow compressional wave is diffusive in character. The requirement is $\omega \ll \omega_{\mathrm{B}}$ where the Biot crossover frequency is given

[1] Corrected for a typo in Johnson (2001).

in equation (2.11). The theory presented here assumes that $\omega_c \ll (\omega_B, \omega_L)$, so that one can investigate the crossover region from $\omega \ll \omega_c$ to $\omega \gg \omega_c$ without violating the low-frequency approximation.

The starting equations are essentially those of the Biot (1956a,b) theory at low-frequencies, equations (2.22)-(2.23). It is relatively simple to solve equations (2.22)-(2.23) if the geometry of the patches is either layered (see chapter 3) or spherical.

The spherically symmetric solutions to equations (2.22)-(2.23) obey the following equations:

$$\frac{\partial}{\partial r}\left[(P+Q)\left(\frac{\partial u}{\partial r}+\frac{2u}{r}\right)+(R+Q)\left(\frac{\partial U}{\partial r}+\frac{2U}{r}\right)\right]=0, \tag{4.12}$$

and

$$-i\omega b_0(U-u)=\frac{\partial}{\partial r}\left[Q\left(\frac{\partial u}{\partial r}+\frac{2u}{r}\right)+R\left(\frac{\partial U}{\partial r}+\frac{2U}{r}\right)\right], \tag{4.13}$$

where u and U are the radial displacements of the solid and the fluid, respectively. The elastic coefficients are given in equations (2.3) and the dissipation term $b_0 = \eta\phi^2/k_0$. The solutions for which the fluid motion is locked-on to the solid's, $u(r)/U(r) = 1$, are linear combinations of r and r^{-2}. These are low-frequency fast wave solutions. The solutions for which $u(r)/U(r) = -(P+Q)/(Q+R)$ are linear combinations of spherical Bessel functions, $j_1(k_2r)$ and $n_1(k_2r)$, where k_2 is the wavenumber of the slow wave, see equation (2.29).

The general solution for the radial direction in each region is therefore written as (Johnson, 2001)

$$\begin{aligned}
u(r) &= Ar+\frac{B}{r^2}+(Q+R)[Fj_1(k_2r)+Gn_1(k_2r)],\\
U(r) &= Ar+\frac{B}{r^2}-(P+Q)[Fj_1(k_2r)+Gn_1(k_2r)],\\
p(r) &= -\frac{3(Q+R)}{\phi}A+\frac{(PR-Q^2)}{\phi}k_2[Fj_0(k_2r)+Gn_0(k_2r)],\\
\tau(r) &= 3K_{BG}A-\frac{4\mu}{r^3}B-\frac{4\mu(Q+R)}{r}[Fj_1(k_2r)+Gn_1(k_2r)].
\end{aligned} \tag{4.14}$$

The quantities P, Q, R, K_{BG}, and $k_2(\omega)$ have different values in the two different regions a and b since they are a function of the pore fluid. Their expressions are given by equations (2.3) and (2.25). The shear modulus μ is identical for both regions, because one homogeneous continuous matrix comprises both regions.

There are eight arbitrary constants: A, B, F, G in each of the two regions. The requirement that the particular solution be finite at $r = 0$ implies $B_a = 0$ and

$G_a = 0$. The remaining six boundary conditions are given by equations (4.3)-(4.8). This set was solved numerically by Johnson (2001), but we show here that an analytical solution is readily available.
The sealed pore condition at the outer boundary, equation (4.7), gives that

$$G_b = -F_b \frac{j_1(k_{2b}b)}{n_1(k_{2b}b)}. \tag{4.15}$$

This means that all expressions (4.14) in the liquid region can be rewritten using the auxiliary parameter

$$f_{\ell ba} = j_\ell(k_{2b}a) - n_\ell(k_{2b}a)\frac{j_1(k_{2b}b)}{n_1(k_{2b}b)}. \tag{4.16}$$

where $\ell = 0, 1$ is the order of the spherical Bessel function. Subtraction of the solid and fluid continuity equations (4.3) and (4.4) at $r = a$ leads to

$$F_a j_1(k_{2a}a) = F_b f_{1ba}\frac{H_b}{H_a}, \tag{4.17}$$

so that the solid continuity equation (4.3) becomes

$$A_a a = A_b a + \frac{B_b}{a^2} + F_b f_{1ba} N, \tag{4.18}$$

with

$$N = (R_b + Q_b) - (R_a + Q_a)\frac{H_b}{H_a}. \tag{4.19}$$

The continuity of total stress and pore pressure at the interface between the regions now yields that

$$\frac{3a}{4\mu}A_a K_{\mathrm{BG}a} = \frac{3a}{4\mu}A_b K_{\mathrm{BG}b} - \frac{B_b}{a^2} - F_b f_{1ba} N, \tag{4.20}$$

$$-3A_a(R_a + Q_a) + 3A_b(R_b + Q_b) = F_b(P_b R_b - Q_b^2)k_{2b} f_{0ba}(1 - f), \tag{4.21}$$

where we introduced another auxiliary parameter

$$f = \frac{P_a R_a - Q_a^2}{P_b R_b - Q_b^2}\frac{k_{2a}}{k_{2b}}\frac{H_b}{H_a}\frac{j_0(k_{2a}a)}{j_1(k_{2a}a)}\frac{f_{1ba}}{f_{0ba}}. \tag{4.22}$$

Adding equations (4.18) and (4.20) yields the surprisingly simple relationship

$$A_a H_a = A_b H_b. \tag{4.23}$$

	Matrix	Grains	Water	Gas
Density ρ [kg/m^3]		$2.65 \cdot 10^3$	$1.0 \cdot 10^3$	1.0
Bulk modulus K [Pa]	$2.637 \cdot 10^9$	$35.0 \cdot 10^9$	$2.25 \cdot 10^9$	$1.0 \cdot 10^5$
Viscosity η [Pa·s]			$1.0 \cdot 10^{-3}$	$1.0 \cdot 10^{-5}$
Porosity ϕ [-]	0.284			
Permeability k_0 [m^2]	$1.0 \cdot 10^{-13}$			
Shear modulus μ [Pa]	$1.740 \cdot 10^9$			
Tortuosity α_∞ [-]	3.52			

Table 4.1: Constituent properties of the partially saturated sandstone rock with a relatively weak frame (Johnson, 2001).

Combination of equations (4.18), (4.21) and (4.23) yields that

$$B_b = -b^3 A_b g, \tag{4.24}$$

with

$$g = s_a \left(1 - \frac{H_b}{H_a} + \frac{3N^2}{P_b R_b - Q_b^2} \frac{f_{1ba}}{f_{0ba}} \frac{1}{k_{2b} a} \frac{1}{1-f}\right). \tag{4.25}$$

The last boundary condition (4.8) finally implies

$$3A_b K_{\mathrm{BG}b} - \frac{4\mu}{b^3} B_b = -p_{\mathrm{e}}, \tag{4.26}$$

so that with equation (4.24) this becomes

$$A_b = -\frac{p_{\mathrm{e}}}{3K_{\mathrm{BG}b} + 4\mu g}. \tag{4.27}$$

The solid displacement at the outer boundary is $u(b) = A_b b(1-g)$ and with equation (4.9), the quasi-static bulk modulus $K(\omega)$ is

$$K(\omega) = \frac{K_{\mathrm{BG}b} + \frac{4}{3}\mu g}{1-g}. \tag{4.28}$$

The parameter set of table 4.1 is chosen to show the effective bulk modulus as a function of frequency in figure 4.2. The gas fraction is 0.1 and $b = 0.1$ m. The results are plotted over a wide frequency range to emphasize the limiting behavior. Analyzing figure 4.2, we infer that the frequency where the slope of $|K|$ and the phase of K are the highest, is the transition frequency $\omega_c \approx D/b^2$, see equation (4.1). According to equation (3.37), this is approximated by (Pride et al., 2004):

$$\omega_c \approx \frac{K_{\mathrm{f}b} k_0}{\eta_b \phi b^2}. \tag{4.29}$$

Using the constituent properties of table 4.1, we obtain $\omega_c/2\pi = 13$ Hz. At this transition frequency, the Biot slow wave diffusion length equals the characteristic length of the inhomogeneity (Gurevich and Lopatnikov, 1995). Equation (4.29) indicates that the mesoscopic loss mechanism moves toward lower frequencies with increasing viscosity and decreasing permeability. This behavior is opposed to the Biot relaxation mechanism, whose critical frequency is given by equation (2.11). Similar behavior is seen in figure 3.2 for the plane wave modulus in the 2D case.

4.3.1 Static limit

In the static limit, the Biot equations of motion reduce to (Dutta and Odé, 1979b)

$$\frac{\partial}{\partial r}(\nabla \cdot \mathbf{u}) = 0, \tag{4.30}$$

$$\frac{\partial}{\partial r}(\nabla \cdot \mathbf{w}) = 0. \tag{4.31}$$

Note that we work here with relative displacement $\mathbf{w} = \phi(\mathbf{U} - \mathbf{u})$. The solutions for spherically symmetric displacements are

$$u(r) = Ar + Br^{-2}, \tag{4.32}$$

$$w(r) = Fr + Gr^{-2}. \tag{4.33}$$

Hence, we have for the pore pressure and total stress from equations (2.1)-(2.2) that:

$$p = -\frac{Q+R}{\phi}\left(\frac{\partial u}{\partial r} + \frac{2u}{r}\right) - \frac{R}{\phi^2}\left(\frac{\partial w}{\partial r} + \frac{2w}{r}\right), \tag{4.34}$$

$$\tau = H\frac{\partial u}{\partial r} + (H - 2\mu)\frac{2u}{r} + \frac{Q+R}{\phi}\left(\frac{\partial w}{\partial r} + \frac{2w}{r}\right), \tag{4.35}$$

and therefore

$$p = -\frac{3(Q+R)}{\phi}A - \frac{3R}{\phi^2}F, \tag{4.36}$$

$$\tau(r) = 3K_{\mathrm{BG}}A + \frac{3(Q+R)}{\phi}F - \frac{4\mu}{r^3}B, \tag{4.37}$$

where we used equation (2.26). We note that the pressure is no longer a function of r as a result of the displacement functions u and w specified in equations (4.32) and (4.33). Again, Q, R, and K_{BG} are elastic constants and A, B, F, and G are yet unknown variables in both regions. A finite solution at $r = 0$ implies $B_a = 0$ and $G_a = 0$. The remaining six unknowns are determined by using the boundary conditions (4.3)-(4.8).

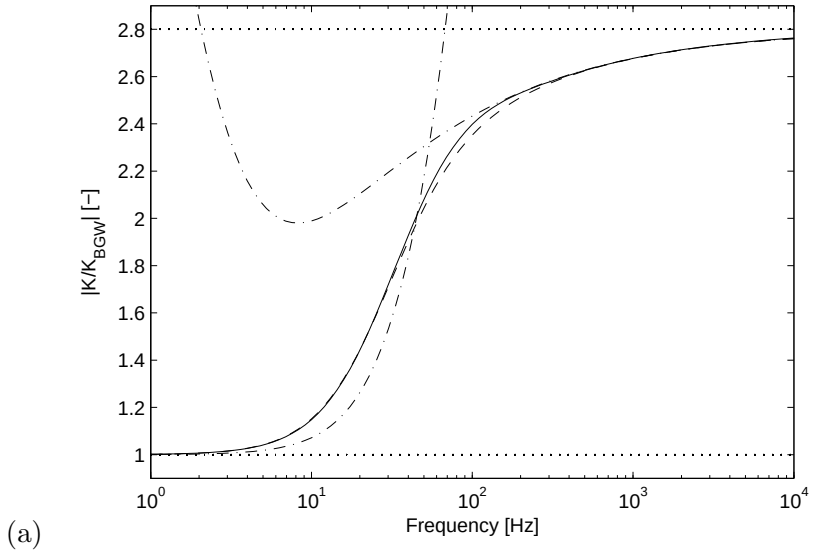

(a)

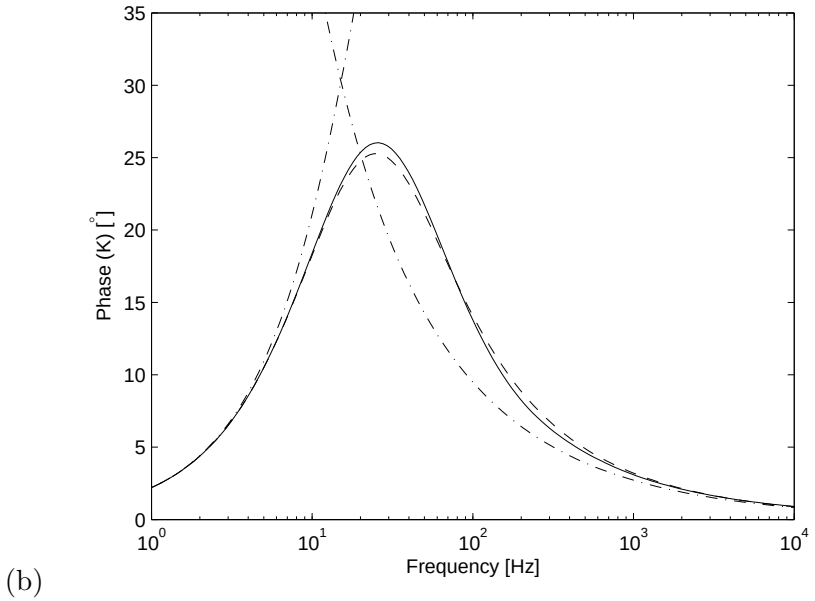

(b)

Figure 4.2: Effective bulk modulus as a function of frequency in the quasi-static Biot context. (a) Absolute value of K/K_{BGW}. (b) Phase value. Exact (solid) and generalized (dashed) quasi-static bulk modulus from equations (4.28) and (4.70), respectively. The lower and upper horizontal dotted lines are the limiting moduli, K_{BGW} and K_{BGH}, equations (4.53) and (4.64). The dashed-dotted curves are low and high-frequency asymptotes, equations (4.68) and (4.69). The input values are from table 4.1, $s_a = 0.1$ and $b = 0.1$ m.

From the continuity of pressure and total stress at the interface, equations (4.5) and (4.6), we have that

$$-\frac{3(Q_a+R_a)}{\phi}A_a-\frac{3R_a}{\phi^2}F_a = -\frac{3(Q_b+R_b)}{\phi}A_b-\frac{3R_b}{\phi^2}F_b, \tag{4.38}$$

$$3K_{\mathrm{BG}a}A_a+\frac{3(Q_a+R_a)}{\phi}F_a = 3K_{\mathrm{BG}b}A_b+\frac{3(Q_b+R_b)}{\phi}F_b-\frac{4\mu}{r^3}B_b. \tag{4.39}$$

We note that (see equation (2.4))

$$\frac{(Q+R)\phi}{R}=1-\frac{K_{\mathrm{m}}}{K_{\mathrm{s}}}=\gamma, \tag{4.40}$$

so that this value is identical in both regions, because it does not depend on the fluid properties. Multiplication of the left and right hand sides of equation (4.38) by $(Q+R)\phi/R$, and subsequent addition to equation (4.39) yields that

$$K_{\mathrm{m}}A_a=K_{\mathrm{m}}A_b-\frac{4}{3}\frac{\mu}{a^3}B_b, \tag{4.41}$$

where we have used that (see equation (2.25))

$$K_{\mathrm{BG}}-\frac{(Q+R)^2}{R}=K_{\mathrm{m}}. \tag{4.42}$$

This expression combined with the continuity of solid displacement, $A_a a = A_b a + B_b/a^2$, gives

$$A_a = A_b \tag{4.43}$$

$$B_b = 0. \tag{4.44}$$

The no-flow condition at the outer boundary, equation (4.7), and the continuity of relative displacement at $r=a$, equation (4.4), combine to

$$G_b = -F_b b^3 \tag{4.45}$$

$$s_a F_a = -s_b F_b. \tag{4.46}$$

The condition of the external stress at the outer boundary, equation (4.8), now yields:

$$3K_{\mathrm{BG}b}A_a-\frac{3s_a}{s_b}\frac{Q_b+R_b}{\phi}F_a=-p_{\mathrm{e}}. \tag{4.47}$$

Combining with the rewritten equation (4.39)

$$3(K_{\mathrm{BG}a}-K_{\mathrm{BG}b})A_a+\frac{3}{\phi}\left[Q_a+R_a+(Q_b+R_b)\frac{s_a}{s_b}\right]F_a=0, \tag{4.48}$$

we find that

$$F_a = \frac{1}{3}\frac{s_b(K_{\mathrm{BG}a}-K_{\mathrm{BG}b})\phi}{s_a(Q_b+R_b)K_{\mathrm{BG}a}+s_b(Q_a+R_a)K_{\mathrm{BG}b}}p_{\mathrm{e}}, \tag{4.49}$$

$$A_a = -\frac{1}{3}\frac{s_a(Q_b+R_b)+s_b(Q_a+R_a)}{s_a(Q_b+R_b)K_{\mathrm{BG}a}+s_b(Q_a+R_a)K_{\mathrm{BG}b}}p_{\mathrm{e}}. \tag{4.50}$$

Using $u_b(b) = A_b b$ in equation (4.9), we have that the effective bulk modulus in the static limit is given by (using equation (4.42))

$$\begin{aligned} K_{\mathrm{BGW}} &= -\frac{b}{3u_b(b)}p_{\mathrm{e}} = -\frac{1}{3A_b}p_{\mathrm{e}} \\ &= \frac{s_a(K_{\mathrm{BG}b}-K_{\mathrm{m}})K_{\mathrm{BG}a}+s_b(K_{\mathrm{BG}a}-K_{\mathrm{m}})K_{\mathrm{BG}b}}{s_a(K_{\mathrm{BG}b}-K_{\mathrm{m}})+s_b(K_{\mathrm{BG}a}-K_{\mathrm{m}})}. \end{aligned} \tag{4.51}$$

Using $s_a + s_b = 1$, this can be rewritten as

$$K_{\mathrm{BGW}} = \frac{K_{\mathrm{BG}b}(K_{\mathrm{BG}a}-K_{\mathrm{m}})+s_aK_{\mathrm{m}}(K_{\mathrm{BG}b}-K_{\mathrm{BG}a})}{(K_{\mathrm{BG}a}-K_{\mathrm{m}})+s_a(K_{\mathrm{BG}b}-K_{\mathrm{BG}a})}. \tag{4.52}$$

Following Johnson (2001), this zero-frequency modulus is called the Biot-Gassmann-Wood modulus. It was also found by Dutta and Odé (1979b)[2]. It is clear from equation (4.52) that in the case of complete liquid saturation, $s_a = 0$, or complete gas saturation, $s_a = 1$, K_{BGW} reduces to $K_{\mathrm{BG}b}$ or $K_{\mathrm{BG}a}$, respectively.
A more accessible form of the modulus K_{BGW} is found if we use the expression for the Biot-Gassmann modulus of equation (2.25):

$$K_{\mathrm{BGW}} \equiv K_{\mathrm{BG}}(K_{\mathrm{W}}) = K_{\mathrm{m}} + \gamma^2\left[\frac{\gamma-\phi}{K_{\mathrm{s}}}+\frac{\phi}{K_{\mathrm{W}}}\right]^{-1}, \tag{4.53}$$

where the fluid modulus K_{f} of equation (2.25) is in this case replaced by the harmonic average K_{W} of the two fluid moduli in regions a and b (Wood's formula):

$$\frac{1}{K_{\mathrm{W}}} = \frac{s_a}{K_{\mathrm{f}a}}+\frac{s_b}{K_{\mathrm{f}b}}. \tag{4.54}$$

This was discussed earlier by Dutta and Odé (1979b) and Norris (1993) explicitly for layered and spherical patches. Johnson (2001) argued that equation (4.53) is an exact result, independent of the spatial distribution of the fluids. Using the input of table 4.1 with $s_a = 0.1$, K_{BGW} is equal to 2.64 GPa. It is the lower bound of the effective bulk modulus in figure 4.2 and is well-approximated by K_{m} in this case.

[2]Corrected for a typo in equation (A-16) of Dutta and Odé (1979b)

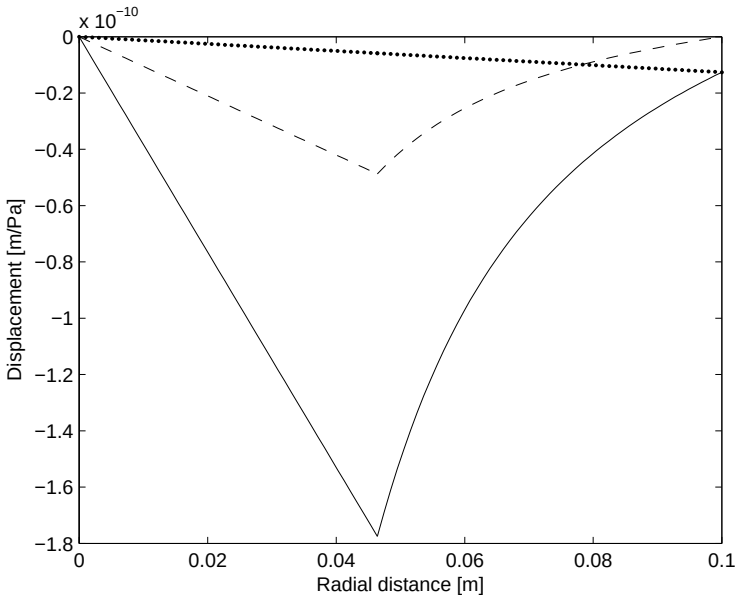

Figure 4.3: Solid (dotted curve), fluid (solid curve) and relative displacement (dashed curve) relative to the applied external pressure along the radial distance from the bubble center in the zero-frequency limit. The input parameters are as in figure 4.2.

Equation (4.44) means that in the zero-frequency limit, the total stress is constant throughout both regions and equal to the applied external radial stress. The pore pressure is also constant and a fraction of the external radial stress. From equations (4.36), (4.42) and (4.49), we find that this fraction is

$$\lim_{\omega\to 0}\frac{p}{p_{\mathrm{e}}} = \frac{1}{\gamma}\frac{(K_{\mathrm{BG}a}-K_{\mathrm{m}})(K_{\mathrm{BG}b}-K_{\mathrm{m}})}{(K_{\mathrm{BG}a}-K_{\mathrm{m}})K_{\mathrm{BG}b}+K_{\mathrm{m}}s_a(K_{\mathrm{BG}b}-K_{\mathrm{BG}a})}, \tag{4.55}$$

as also found by Dutta and Odé (1979b)[3]. In our example, the pore pressure ratio throughout the unit cell is 1.2×10^{-3} for $b = 0.1$ m. The zero-frequency limit of the displacements along the radial distance are shown in figure 4.3. We see that the solid displacement increases linearly with radial distance throughout the medium. This is also true for the fluid displacement in the gas region. Maximum fluid displacement occurs at the gas-liquid interface after which it decreases rapidly with the increasing radial distance to catch up to the solid displacement at $r = b$. Similar features were noted by Dutta and Odé (1979b).

[3]Corrected for a typo in equation (A-26) of Dutta and Odé (1979b)

4.3.2 No-flow limit

We consider the high-frequency limit of $K(\omega)$ under the assumption that the frequency is never so high as to violate $\omega \ll (\omega_{\mathrm{B}}, \omega_L)$. This case has been discussed by White (1975) and Dutta and Odé (1979b). As the frequency of the external stress becomes higher, the fluid has little time to flow. In case of the no-flow limit, the equations of motion become:

$$\frac{\partial}{\partial r}(\nabla \cdot \mathbf{u}) = 0, \tag{4.56}$$

$$\mathbf{w} = 0, \tag{4.57}$$

with the solution

$$u(r) = Ar + Br^{-2}. \tag{4.58}$$

Therefore (cf. equations (4.34)-(4.35))

$$p = -\frac{3(Q+R)}{\phi}A, \tag{4.59}$$

$$\tau(r) = 3K_{\mathrm{G}}A - \frac{4\mu}{r^3}B. \tag{4.60}$$

Again, $B_a = 0$ and the pore pressure is no longer a function of r. Three boundary conditions (4.3), (4.6), and (4.8) provide expressions for A_a, A_b, and B_b.
Continuity of total stress and solid displacement at the inner boundary yields that

$$A_a = A_b + \frac{B_b}{a^3}, \tag{4.61}$$

$$B_b = -A_b a^3 \frac{K_{\mathrm{BG}a} - K_{\mathrm{BG}b}}{H_a}. \tag{4.62}$$

Substitution of the above in the total stress condition at the outer boundary yields that

$$A_b = -\frac{p_{\mathrm{e}}}{3K_{\mathrm{BG}b} + 4\mu s_a (K_{\mathrm{BG}a} - K_{\mathrm{BG}b})/H_a}, \tag{4.63}$$

so that the effective bulk modulus in the high-frequency limit is given by

$$K_{\mathrm{BGH}} = \frac{K_{\mathrm{BG}b}H_a + \frac{4}{3}\mu s_a (K_{\mathrm{BG}a} - K_{\mathrm{BG}b})}{H_a - s_a (K_{\mathrm{BG}a} - K_{\mathrm{BG}b})}. \tag{4.64}$$

In the case of complete liquid or gas saturation, K_{BGH} reduces to $K_{\mathrm{BG}b}$ or $K_{\mathrm{BG}a}$, respectively. With a uniform frame (i.e., constant μ, K_{m}, and K_{s}) the effective bulk modulus of the medium is in exact agreement with Hill's (1963) theorem:

$$\frac{1}{K_{\mathrm{BGH}} + \frac{4}{3}\mu} = \frac{s_a}{K_{\mathrm{BG}a} + \frac{4}{3}\mu} + \frac{1 - s_a}{K_{\mathrm{BG}b} + \frac{4}{3}\mu} = \frac{s_a}{H_a} + \frac{s_b}{H_b}, \tag{4.65}$$

as Norris (1993) argued. In our example, $K_{\mathrm{BGH}} = 7.39$ GPa is the upper bound of the effective bulk modulus in figure 4.2.
We realize that although the pore pressure is constant within each phase, it is discontinuous at the inner boundary. Equations (4.42), (4.59) and (4.61)- (4.63) then give[4]:

$$\lim_{\omega\to\infty} \frac{p_a}{p_{\mathrm{e}}} = \frac{(K_{\mathrm{BG}a} - K_{\mathrm{m}})H_b}{\gamma(K_{\mathrm{BG}b}H_a + \frac{4}{3}\mu s_a(K_{\mathrm{BG}a} - K_{\mathrm{BG}b}))}, \tag{4.66}$$

$$\lim_{\omega\to\infty} \frac{p_b}{p_{\mathrm{e}}} = \frac{(K_{\mathrm{BG}b} - K_{\mathrm{m}})H_a}{\gamma(K_{\mathrm{BG}b}H_a + \frac{4}{3}\mu s_a(K_{\mathrm{BG}a} - K_{\mathrm{BG}b}))}. \tag{4.67}$$

In our example, the relative gas pressure is 8.6×10^{-5}, while the relative liquid pressure is 7.7×10^{-1}. This discontinuity at the inner boundary is due to the different physical properties of the fluids in each region. However, the total radial bulk stress is continuous, and since there is no relative fluid-flow, the inner boundary acts as if it were sealed.
In figure 4.4 we see that in the high-frequency limit, the solid and fluid displacements are equal, and the relative displacement is zero everywhere along the radial distance. Both fluid and solid move in phase, so there is no net fluid-flow across the gas-liquid interface. There is a local minimum displacement at $r = a$ and an absolute minimum displacement at $r = b$.

4.4 Generalized patchy theory in quasi-static Biot context

Johnson (2001) generalized the theory for spherical gas bubbles to gas patches of arbitrary shape. By means of high and low-frequency perturbation theory, he was able not only to define the Biot-Gassmann-Wood and Biot-Gassmann-Hill limits, but also the asymptotic behavior in both limits. The low-frequency asymptotics are described by a parameter T, whereas the high-frequency asymptotics are encompassed in a parameter G:

$$\lim_{\omega\to 0} K = K_{\mathrm{BGW}}[1 - i\omega T + ...], \tag{4.68}$$

$$\lim_{\omega\to\infty} K = K_{\mathrm{BGH}}[1 - G(-i\omega)^{-1/2} + ...]. \tag{4.69}$$

The most simple curve, obeying both low- and high-frequency asymptotics is then

[4]Corrected for a typo in equation (A-44) of Dutta and Odé (1979b)

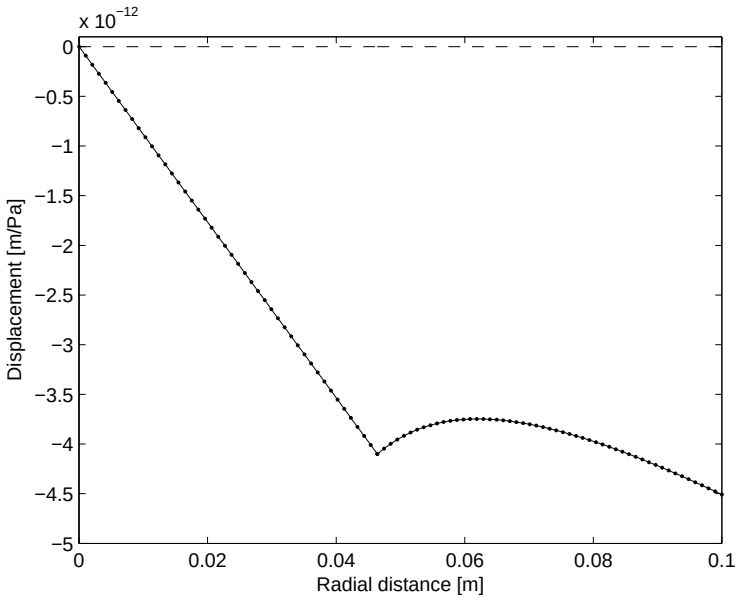

Figure 4.4: Solid (dotted curve), fluid (solid curve) and relative displacement (dashed curve) relative to the applied external pressure along the radial distance from the bubble center in the high-frequency limit. The input values are as in figure 4.2.

given by:

$$K = K_{\mathrm{BGH}} - \frac{K_{\mathrm{BGH}} - K_{\mathrm{BGW}}}{1 - \zeta + \zeta\sqrt{1 - i\omega\tau/\zeta}}, \tag{4.70}$$

where

$$\tau = \left(\frac{K_{\mathrm{BGH}} - K_{\mathrm{BGW}}}{K_{\mathrm{BGH}} G}\right)^2, \tag{4.71}$$

and

$$\zeta = \frac{(K_{\mathrm{BGH}} - K_{\mathrm{BGW}})^3}{2K_{\mathrm{BGW}}} \frac{\tau}{T}. \tag{4.72}$$

The parameter T generally depends on the geometry of the patches (sample volume V):

$$T = \frac{\phi^2}{k_0} \frac{K_{\mathrm{BGW}}}{V} \int g(\mathbf{r})\Phi(\mathbf{r}) dV, \tag{4.73}$$

with the potential $\Phi(\mathbf{r})$ [m^{2}s] the solution to

$$\nabla \cdot \left[\frac{-1}{\eta(\mathbf{r})} \nabla \Phi(\mathbf{r}) \right] = g(\mathbf{r}), \tag{4.74}$$

and $g(\mathbf{r})$ [Pa^{-1}] the compressibility function

$$g(\mathbf{r}) = \frac{\gamma(1/K_{\mathrm{W}} - 1/K_{\mathrm{f}}(\mathbf{r}))}{\gamma + \phi K_{\mathrm{m}}(1/K_{\mathrm{W}} - 1/K_{\mathrm{s}})}. \tag{4.75}$$

In the case of a gas-liquid system, $g(\mathbf{r})$ and $\eta(\mathbf{r})$ only have two distinct values, $g_{a,b}$ and $\eta_{a,b}$ in the gas bubble and the shell, respectively. In that case Johnson (2001) argued that an exact expression for T is given by

$$T = \frac{K_{\mathrm{BGW}}\phi^2}{30 k_0 b^3}(t_{aa}a^5 - t_{ab}a^3b^2 + t_{ba}a^2b^3 - t_{bb}b^5), \tag{4.76}$$

where t_{ij} are given by

$$\begin{aligned} t_{aa} &= 3\eta_b g_b^2 + 5(\eta_a - \eta_b)g_a g_b - 3\eta_a g_a^2, \\ t_{ab} &= 15\eta_b g_b(g_b - g_a), \\ t_{ba} &= 5g_b[3\eta_b g_b - (2\eta_b + \eta_a)g_a], \\ t_{bb} &= 3\eta_b g_b^2. \end{aligned} \tag{4.77}$$

Finally, the expression of the real-valued coefficient G in equation (4.71) is

$$G = \sqrt{D^*}\left[\frac{p_a - p_b}{p_{\mathrm{e}}}\right]\frac{S}{V}. \tag{4.78}$$

The pressures are given by equations (4.66)-(4.67). Expression (4.78) describes the way in which the would-be discontinuity $p_a - p_b$ is counterbalanced by a diffusive slow compressional wave which propagates away from the interface into both adjacent regions. Therefore D^* is an effective diffusivity of both phases combined, specified as

$$D^* = \left[\frac{k_0 K_{\mathrm{BGH}}}{\eta_a\sqrt{D_a} + \eta_b\sqrt{D_b}}\right]^2. \tag{4.79}$$

The diffusivity in both regions $D_{a,b}$ is given by equation (2.30). The term S/V is the ratio of the boundary area between the two phases to the sample volume.
In figure 4.2, we plotted the absolute and phase values of the generalized effective bulk modulus. We see that they are in excellent agreement with the exact curves. Small deviations do occur, however.

Johnson (2001) approximated the crossover frequency by equating the low- and high-frequency expressions for the attenuation Q^{-1}. He found that

$$\omega_c = D^* \left[\frac{2K_{\mathrm{BGW}}^2 K_{\mathrm{BGH}}^4 \zeta^2}{(K_{\mathrm{BGW}} - K_{\mathrm{BGH}})^6} \right]^{1/3} \left(\frac{p_a - p_b}{p_{\mathrm{e}}} \right)^4 \left[\frac{S}{V} \right]^2 . \tag{4.80}$$

In our example this would lead to $\omega_c/2\pi = 70$ Hz, which is on the same order of magnitude as specified by D/b^2, leading to 13 Hz (equation (4.29)). Equating the low and high-frequency asymptotes for $K(\omega)$ would yield two new cross-over values as can be seen in figure 4.2, viz. 54 Hz and 15 Hz, respectively. Again, a correct order-of-magnitude prediction is obtained setting $\omega_c = D/b^2$.

4.5 Exact patchy theory in the full Biot context

Our next aim is to obtain an expression for the effective bulk modulus in terms of the applied pressure p_{e} using the full Biot theory. Dutta and Odé (1979a) introduced expressions for the potentials of the solid displacement $u = \partial\Phi/\partial r$ in the inner sphere ($0 \leq r \leq a$) and argued that a solution to equations (2.7) and (2.8) could be written as

$$\Phi_{ja}(r) = A_j^+ j_0(k_{ja} r) + A_j^- n_0(k_{ja} r). \tag{4.81}$$

In the surrounding shell ($a \leq r \leq b$) a solution is given by

$$\Phi_{jb}(r) = B_j^+ j_0(k_{jb} r) + B_j^- n_0(k_{jb} r), \tag{4.82}$$

where j_0 and n_0 denote spherical Bessel and Neumann functions of the zeroth order and $j = 1, 2$ for the fast and slow wave. A finite displacement at $r = 0$ implies that $A_j^- = 0$.

It is understood that all field properties may vary from region a to region b. The six amplitudes A_j^+, B_j^+, and B_j^-, are determined by the boundary conditions (4.3)-(4.8).

Using equations (2.1)-(2.2), this yields in terms of the potentials

$$\sum_j \left[\frac{\partial \Phi_{ja}}{\partial r}\right]_{r=a} = \sum_j \left[\frac{\partial \Phi_{jb}}{\partial r}\right]_{r=a}, \tag{4.83}$$

$$\chi_{ja}\left[\frac{\partial \Phi_{ja}}{\partial r}\right]_{r=a} = \chi_{jb}\left[\frac{\partial \Phi_{jb}}{\partial r}\right]_{r=a}, \tag{4.84}$$

$$\lambda_{ja}\left[\frac{\partial^2 \Phi_{ja}}{\partial r^2}+\frac{2}{r}\frac{\partial \Phi_{ja}}{\partial r}\right]_{r=a} + \sum_j 2\mu\left[\frac{\partial^2 \Phi_{ja}}{\partial r^2}\right]_{r=a}$$
$$= \lambda_{jb}\left[\frac{\partial^2 \Phi_{jb}}{\partial r^2}+\frac{2}{r}\frac{\partial \Phi_{jb}}{\partial r}\right]_{r=a} + \sum_j 2\mu\left[\frac{\partial^2 \Phi_{jb}}{\partial r^2}\right]_{r=a}, \tag{4.85}$$

$$C_{ja}\left[\frac{\partial^2 \Phi_{ja}}{\partial r^2}+\frac{2}{r}\frac{\partial \Phi_{ja}}{\partial r}\right]_{r=a} = C_{jb}\left[\frac{\partial^2 \Phi_{jb}}{\partial r^2}+\frac{2}{r}\frac{\partial \Phi_{jb}}{\partial r}\right]_{r=a}, \tag{4.86}$$

$$\chi_{jb}\left[\frac{\partial \Phi_{jb}}{\partial r}\right]_{r=b} = 0. \tag{4.87}$$

$$-p_{\mathrm{e}} = \lambda_{jb}\left[\frac{\partial^2 \Phi_{jb}(b)}{\partial r^2}+\frac{2}{r}\frac{\partial \Phi_{jb}}{\partial r}\right]_{r=b} + \sum_j 2\mu\left[\frac{\partial^2 \Phi_{jb}}{\partial r^2}\right]_{r=b}. \tag{4.88}$$

Here, χ_{jn} is defined as $\phi(\beta_{jn}-1)$ for region n, and

$$\lambda_{jn}+2\mu = P_n + Q_n + \beta_{jn}(Q_n+R_n) \tag{4.89}$$

are the modified Lamé parameters of region n and β_{jn} is the fluid-solid ratio in the region. Moreover,

$$C_{jn} = \frac{Q_n+\beta_{jn}R_n}{\phi} \tag{4.90}$$

is an effective bulk modulus. Consequently, on substituting the displacement potentials in the foregoing conditions, equations (4.83)-(4.88), we can write the linear system $G\mathbf{x}=\mathbf{y}$, with

$$\mathbf{x} = (A_1^+, A_2^+, B_1^+, B_2^+, B_1^-, B_2^-)^{\mathrm{T}}, \tag{4.91}$$

and

$$\mathbf{y} = p_{\mathrm{e}}(0,0,0,0,0,1)^{\mathrm{T}}. \tag{4.92}$$

The elements of G contain the information about the properties of the matrix, liquid and gas phase and are listed in Appendix A. The solid displacement $u(b)$ at the outer boundary is

$$u(b) = \sum \frac{\partial \Phi_{jb}(b)}{\partial r} = -k_{jb}(B_j^+ j_1(k_{jb}b) + B_j^- n_1(k_{jb}b)), \tag{4.93}$$

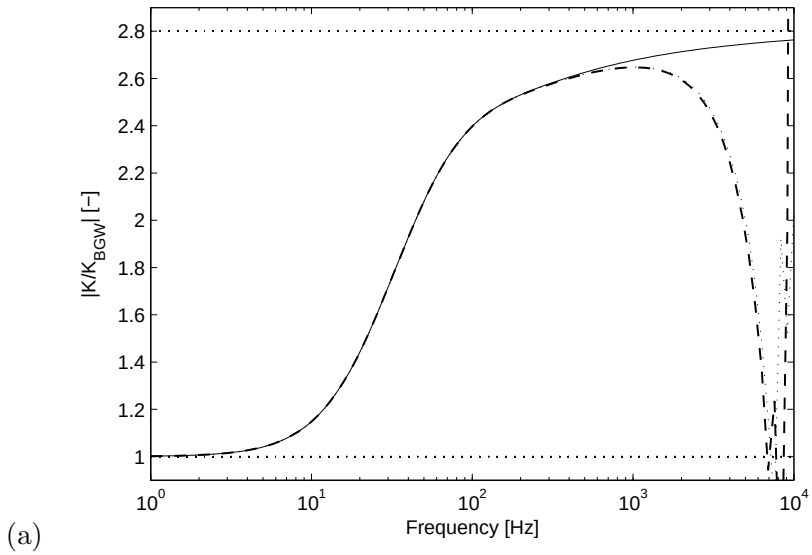

(a)

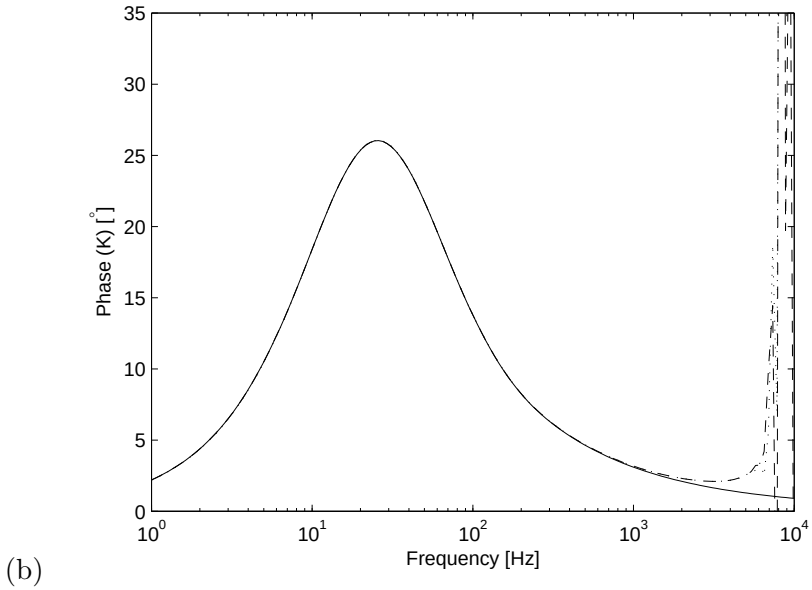

(b)

Figure 4.5: Effective bulk modulus as a function of frequency. (a) Absolute value of K/K_{BGW}. (b) Phase value. The dashed curve is the exact bulk modulus resulting from equation (4.93). The dotted curve is the approximate bulk modulus from section 4.6. The solid curve (exact quasi-static K), the horizontal dashed lines (K_{BGW} and K_{BGH}), and the input parameters are as in figure 4.2.

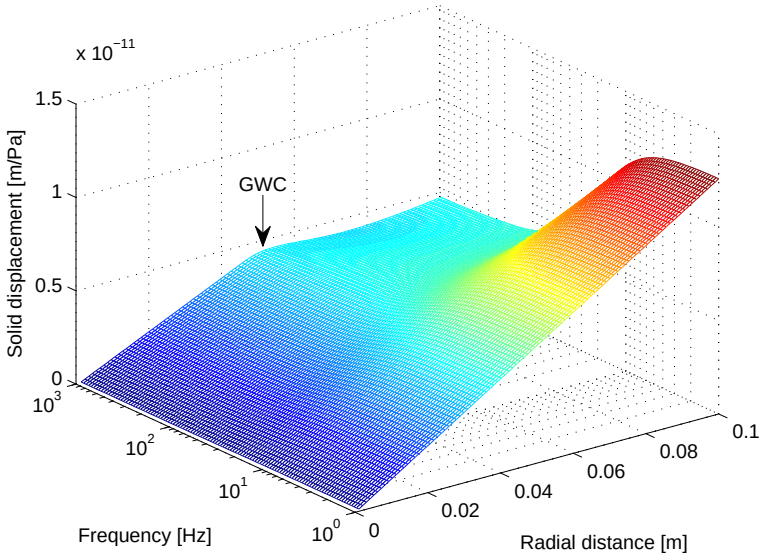

Figure 4.6: Absolute value of the solid displacement as a function of frequency and radial distance from the bubble center. The input parameters are as in figure 4.2. The gas-water contact is denoted by GWC.

where j_1 and n_1 denote spherical Bessel and Neumann functions of the first order. Finally, substitution of $u(b)$ in equation (4.9) gives the effective bulk modulus.
Using identical input values as in figure 4.2, the effective modulus using the full Biot theory is plotted in figure 4.5. Obviously, the full Biot theory gives the same results as the quasi-static Biot theory as long as the frequency is low enough. The critical Biot frequency $\omega_B/2\pi$ from equation (2.11) is 128 kHz. The frequency $\omega_L/2\pi$ in equation (4.2) is approximately 1.5 kHz (since $c_{Sa} \approx c_{S\,\mathrm{dry}} = 958$ m/s and $c_{Sb} = 893$ m/s). Above 0.4 kHz in figure 4.2a and above 1.5 kHz in figure 4.2b deviations occur, which are caused by the onset of resonance phenomena. Similar behavior is discussed in chapter 3.
In figure 4.6, the frequency-dependent solid displacement amplitude is plotted as a function of the radial distance from the gas bubble center. We observe that within the gas-saturated zone, the solid displacement increases linearly with radial distance for all frequencies. This is also true in the liquid-saturated zone at low frequencies. This is in agreement with figure 4.3 and our theoretical derivation in section 4.3.2, where we showed that the solid displacement is linearly proportional to r.

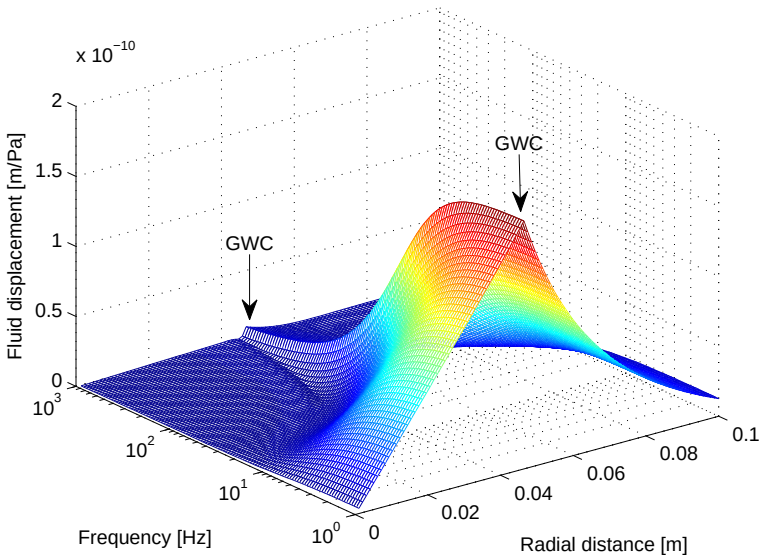

Figure 4.7: Absolute value of the fluid displacement as a function of frequency and radial distance from the bubble center. The input parameters are as in figure 4.2.

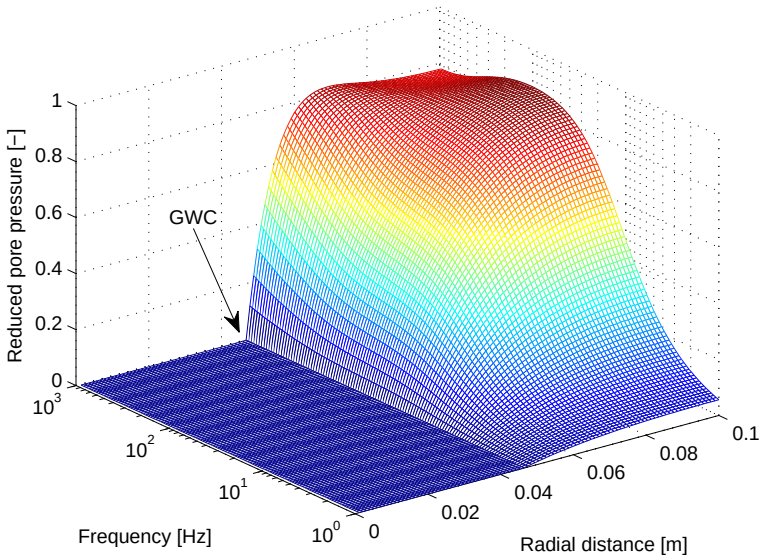

Figure 4.8: Absolute value of the reduced pore pressure as a function of frequency and radial distance from the bubble center. The input parameters are as in figure 4.2.

At high frequencies, the solid displacement has a local maximum at the gas-water contact and an absolute maximum at the external boundary. This is in accordance with figure 4.4 (note that we plot amplitudes i.e., absolute values here). The solid displacement at the gas-water contact is not very dependent on frequency.
The result for the frequency-dependent fluid displacement is given in figure 4.7. The difference in vertical scale with figure 4.6 is about a factor 10. In the gas region, the fluid displacement also increases linearly with radial distance, at low frequencies. Maximum fluid displacement is obtained at the gas-water contact for all frequencies, after which the fluid displacement rapidly decreases with increasing radial distance. This is described in section 4.3.1 for low frequencies. At the outer boundary of the shell the fluid displacement is equal to the solid displacement according to equation (4.7).
The pore pressure along the radial distance is shown in figure 4.8. The continuity of pore pressure is satisfied at the gas-water contact for all frequencies, according to equation (4.5). In the gas-saturated region, the pore pressure is approximately zero for all frequencies, due to the high compressibility of the gas phase. In the liquid-saturated region the pore pressure increases rapidly with increasing frequency, until it reaches a plateau for higher frequencies and radial distances.

4.6 Approximate patchy theory in the full Biot context

For a Helmholtz number $k_{1a}a \ll 1$, it follows that the matrix within the bubble surface may be regarded as acoustically compact, and the solid and relative fluid displacements within the bubble surface are directly proportional to the radial distance r (Lamb, 1916):

$$u_a(r) = A_a r, \tag{4.94}$$

$$w_a(r) = F_a r. \tag{4.95}$$

This means that the gas pressure is uniform within the bubble. The displacements, stresses and pressure outside the gas bubble remain given in terms of the potentials by equation (4.82). Using equations (4.34)-(4.35) and (4.94)-(4.95), the pore pressure and total stress in the gas-bearing region are

$$p_a = -\frac{3(Q_a + R_a)}{\phi} A_a - \frac{3R_a}{\phi^2} F_a, \tag{4.96}$$

$$\tau_a = 3K_{\mathrm{BG}a} A_a + \frac{3(Q_a + R_a)}{\phi} F_a. \tag{4.97}$$

Consequently, we have six unknown amplitudes $\mathbf{x} = (A_a, F_a, B_1^+, B_2^+, B_1^-, B_2^-)^{\mathrm{T}}$. The six boundary conditions are those given by equations (4.3)-(4.8). We solve

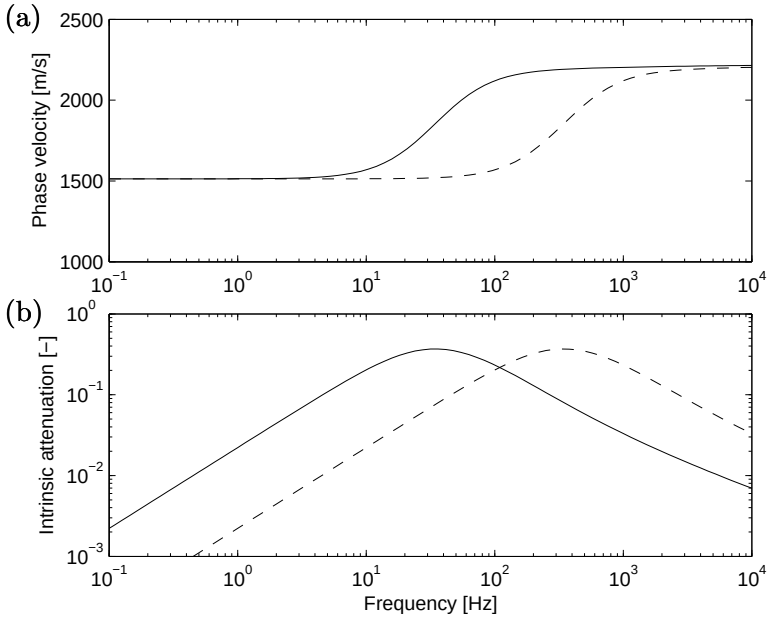

Figure 4.9: Phase velocity (a) and intrinsic attenuation (b) using permeabilities of 100 mD (solid) and 1 D (dashed).

the system $F\mathbf{x} = \mathbf{y}$ with again $\mathbf{y} = p_{\mathrm{e}}(0,\ 0,\ 0,\ 0,\ 0,\ 1)^{\mathrm{T}}$. The elements of F are given in Appendix B. The effective bulk modulus under these acoustically compact assumptions is compared with the exact solution in figure 4.5. The approximate solution is in excellent agreement with the exact solution. We even notice that the onset of oscillations is beautifully captured by this simplified theory. This proves that the resonances are affected by the scale of the representative volume b, indeed.

4.7 Dependence on medium parameters

Using the quasi-static solution of section 4.3, we analyze the dependence of the phase velocity, $c = \omega/\mathrm{Re}(k_1)$, and intrinsic attenuation, $Q^{-1} = |2\mathrm{Im}(k_1)/\mathrm{Re}(k_1)|$, on, respectively, permeability, porosity, gas bubble radius, gas fraction, and rock type in figures 4.9-4.13. We use the constituent properties of table 4.1, with a gas fraction of 0.01 and gas bubble radius of 0.01 m.

In figure 4.9, the results are shown using a permeability of 100 mD and 1 D. We observe that the velocity- and attenuation curves are shifted horizontally. This is in agreement with equation (4.29), where we see that the critical frequency increases with increasing permeability.

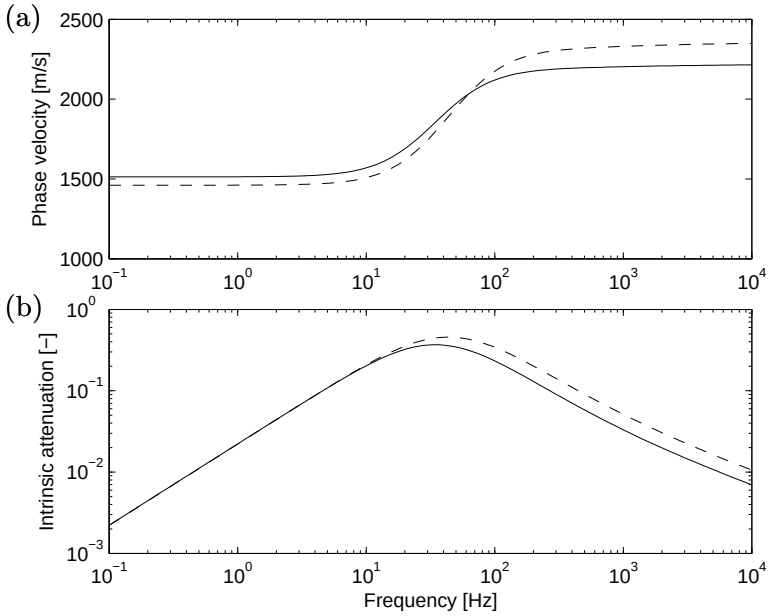

Figure 4.10: Phase velocity (a) and intrinsic attenuation (b) using porosities of 0.284 (solid) and 0.184 (dashed).

Figure 4.10 shows the results using porosities of 0.284 and 0.184. According to equation (4.29), a decrease in porosity increases the critical frequency. We see that the porosity influences both the low- and high frequency speeds. When the porosity decreases the total density increases (see equation (4.11)). Since $K_{\mathrm{f}a} \ll K_{\mathrm{f}b}$, $K_{\mathrm{BG}a}$ is much less influenced by a porosity change than $K_{\mathrm{BG}b}$, see equation (2.25). From equation (4.52), we see that $(K_{\mathrm{BG}a} - K_{\mathrm{m}})/(K_{\mathrm{BG}b} - K_{\mathrm{BG}a}) \sim 10^{-5}$, so that $K_{\mathrm{BGW}} \approx K_{\mathrm{m}}$. Therefore, the reduction in velocity at low frequencies is mainly attributed to an increase in total density. With the same reasoning, the increase in velocity at high frequencies is mainly caused by the increase in $K_{\mathrm{BG}b}$ in equation (4.65).

Any density increase is not visible in the low-frequency attenuation Q^{-1}, due to the fact that it equally affects both the imaginary and real parts of the wavenumber. At high frequencies, however, the change in total density is not the dominant term and the increase in $K_{\mathrm{BG}b}$ causes the increase in attenuation.

In figure 4.11, we increase the gas bubble radius a from 0.01 m to 0.05 m. We observe that the shift in critical frequency is in agreement with equation (4.29). We realize that $\omega_c \propto a^{-2}$, so we see that the critical frequency decreases quadratically with increasing bubble radius (for a constant gas fraction).

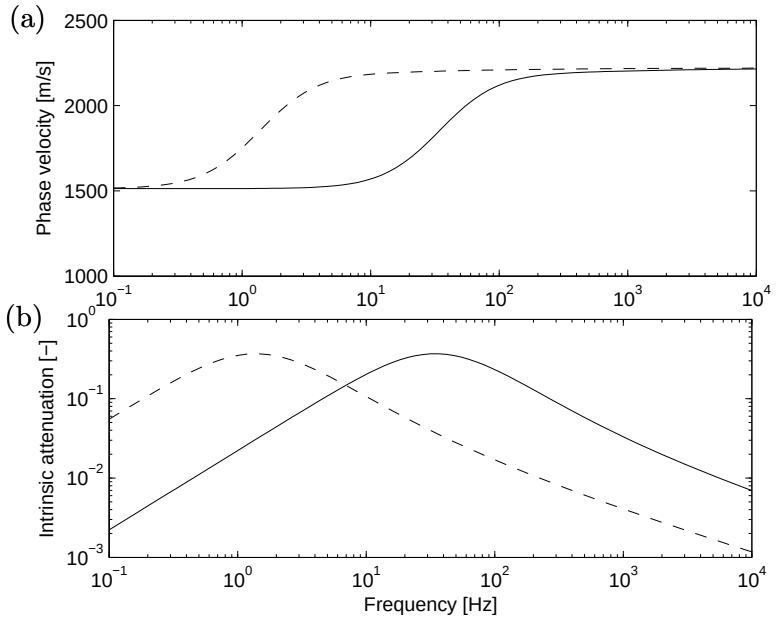

Figure 4.11: Phase velocity (a) and intrinsic attenuation (b) using gas bubble radii of 0.01 m (solid) and 0.05 m (dashed). The gas fraction is still 0.01.

The effects of an increase in gas fraction of a factor 10 is shown in figure 4.12. We see that the low-frequency velocity slightly increases due to the decrease in density ($\rho_{\mathrm{f}a} \ll \rho_{\mathrm{f}b}$). Realizing that $\omega_c \propto s_a^{2/3}$, we see that from equation (4.29), the critical frequency increases with increasing gas fraction. The maximum attenuation value for a gas fraction of 10 % is slightly less than that for 1 % gas. Similar dependence was seen earlier in figure 3.4.

We finally compare the acoustics of a weak sandstone rock with a stiffer carbonate rock. The carbonate properties are taken from White et al. (1975): $K_{\mathrm{m}} = 45.23$ GPa, $\mu = 21.19$ GPa, $\rho_{\mathrm{s}} = 2800$ kg/m^3, $K_{\mathrm{s}} = 70$ GPa, $\phi = 0.10$, $k_0 = 100$ mD. The saturating fluids and gas fraction are unaffected. The results are shown in figure 4.13, where we notice a significant difference. There is hardly any velocity dispersion for the carbonate rock. This rock has high dry rock velocities, viz. c_{P} = 5400 m/s and c_{S} = 2900 m/s. It also shows much less attenuation. This is explained by the fact that in a stiff rock $K_{\mathrm{BGW}} \approx K_{\mathrm{BGH}}$, so that the diffusive damping mechanism is effectively suppressed.

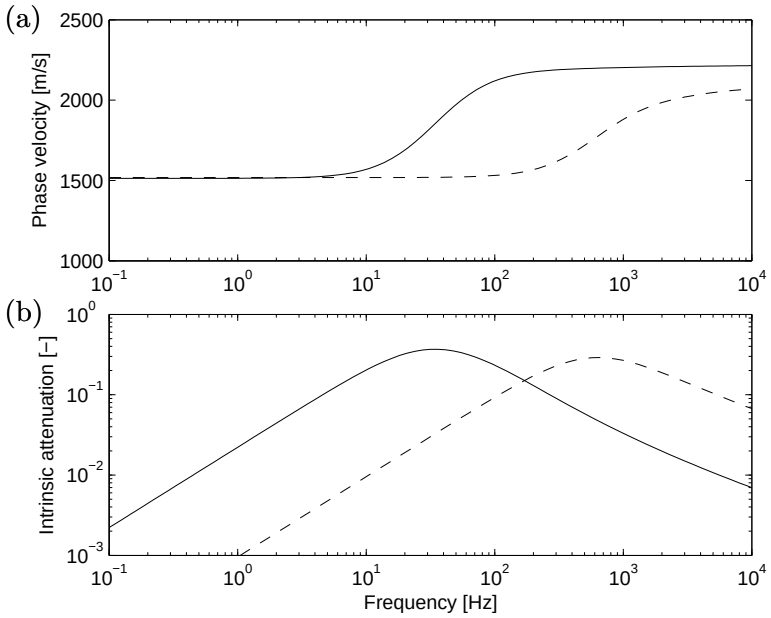

Figure 4.12: Phase velocity (a) and intrinsic attenuation (b) using gas fractions of 0.01 (solid) and 0.1 (dashed). The gas bubble radius remains 0.01 m.

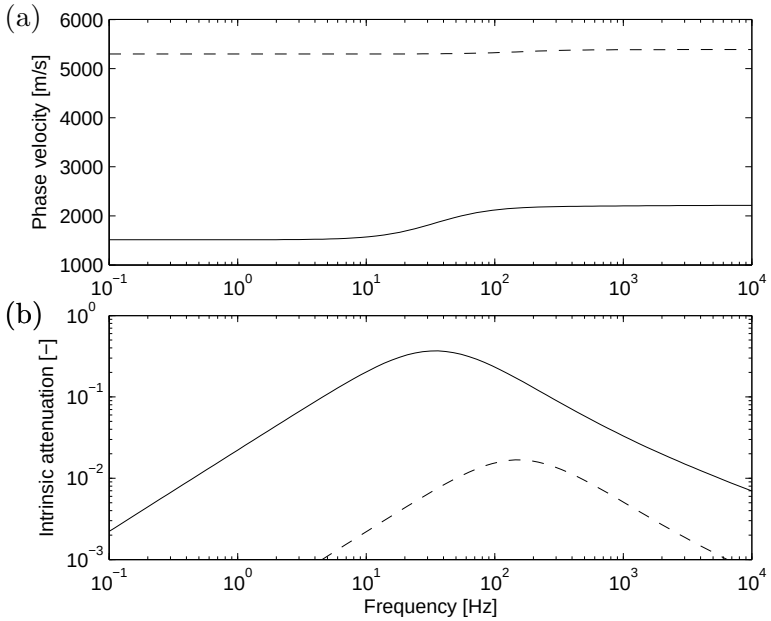

Figure 4.13: Phase velocity (a) and intrinsic attenuation (b) using a weak sandstone (solid) and a stiff carbonate rock (dashed).

4.8 Rayleigh-Plesset-Biot theory

The disadvantage of the previous class of models is that its predicts only one compressional wave on the (seismic) macro-scale thus fully ignoring the slow Biot wave. This slow wave is characteristic for saturated porous media and its existence is validated many times (Smeulders, 2005). To overcome this problem an effective Rayleigh-Plesset-Biot model was derived by Smeulders and Van Dongen (1997). The original Rayleigh-Plesset theory for linear pressure waves in bubbly liquids was applied to partially saturated porous media in a heuristic approach. Here, we present a more rigorous derivation of the model and discuss its importance for seismic attenuation by comparing it with the predictions of the generalized patchy theory, as formulated in section 4.4.

The so-called double-porosity dual-permeability model by Berryman and Wang (2000) also accounts for the slow compressional wave (in fact, two slow waves). This model is not treated here, since when reduced to an effective Biot theory (as formulated by Pride et al. (2004)) the mesoscopic heterogeneity still contains the sealed outer boundary assumption.

Consider, then, a partially saturated rock in which the solid and fluid displacements $\mathbf{u}$ and $\mathbf{U}$ are describable by the Biot equations (2.7) and (2.8). The total stress τ_{ij} and pore pressure p are related to the strains in the usual manner by equations (2.1) and (2.2).

First, consider an isolated gas bubble in an infinitely extended liquid saturating the matrix, see figure 4.8b. This geometry is essentially different from that in figure 4.8a, where the liquid shell is sealed at its outer boundary at $r = b$. When the liquid part is subjected to an oscillatory macroscopic pressure p_∞ of the seismic wave ($2\pi/k \gg b$), the mesoscopic gas bubble will act as a local sound source and dissipate energy of the seismic wave. Mesoscopic waves are excited at the gas-liquid interface, where continuity relations should be satisfied. We aim to characterize gas bubble dynamics by means of the effective compressibility of the fluid. Following Smeulders and Van Dongen (1997), we relate the change in gas volume to the liquid pressure p_∞ far away from the bubble:

$$\frac{1}{\tilde{K}_{\mathrm{f}a}} = -\frac{1}{V_a}\frac{\partial V_a}{\partial p_\infty}. \tag{4.98}$$

The effective compressibility of the gas $\tilde{K}_{\mathrm{f}a}^{-1}$ is essentially different from the usual gas compressibility, defined as

$$\frac{1}{K_{\mathrm{f}a}} = -\frac{1}{V_a}\frac{\partial V_a}{\partial p_a}, \tag{4.99}$$

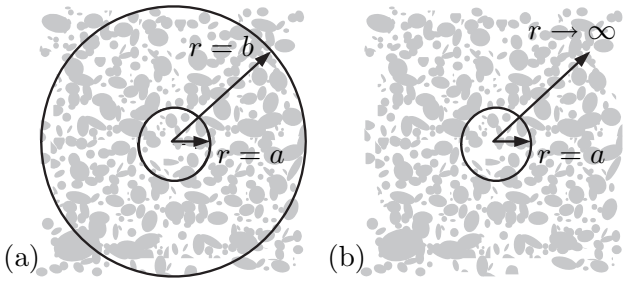

Figure 4.14: Representative geometry of a gas bubble ($r = a$) surrounded by liquid saturating a porous background material. (a) Sealed liquid outer surface. (b) Rayleigh-Plesset-Biot approach.

where p_a is the gas pressure. This gas compressibility was earlier used in, e.g., equation (4.54). It is straightforward to write an expression for the effective fluid compressibility $\tilde{K}_{\rm f}^{-1} = -\partial V_{\rm f}/(V_{\rm f}\partial p_\infty)$ in terms of the effective compressibility of the gas and the compressibility of the liquid $K_{{\rm f}b}^{-1} = -\partial V_b/(V_b\partial p_\infty)$, from purely kinematic considerations:

$$\frac{1}{\tilde{K}_{\rm f}} = \frac{s_a}{\tilde{K}_{{\rm f}a}} + \frac{s_b}{K_{{\rm f}b}}, \tag{4.100}$$

since $V_{\rm f} = V_a + V_b$ and $s_a = V_a/V_{\rm f}$. To compute $\tilde{K}_{{\rm f}a}$ within a system of spherical coordinates, it is convenient to define potential functions for the solid matrix and liquid outside the gas bubble (subscript b) as

$$\begin{aligned} u_b(r) &= \sum_{j=1,2} \nabla\Phi_{jb}, \\ U_b(r) &= \sum_{j=1,2} \nabla\Psi_{jb}. \end{aligned} \tag{4.101}$$

In this region we assume spherical waves:

$$\begin{aligned} r\Phi_{jb} &= B_j \exp(-ik_{jb}r), \\ r\Psi_{jb} &= \beta_{jb}B_j \exp(-ik_{jb}r), \end{aligned} \tag{4.102}$$

where k_{jb} are the compressional wavenumbers in region b. Equation (2.21) provides the fluid-to-solid displacement ratios β_{jb} in region b.

In the region occupied by the gas and the solid matrix, however, we assume that the pore pressure has ample time to equilibrate. The characteristic time of pressure equilibration is $\tau_{\rm c} = a^2/D_a$, where D_a is the viscous gas diffusivity, which is well approximated by $k_0 K_{{\rm f}a}/(\eta_a\phi)$, with permeability k_0 and gas viscosity η_a,

see equation (2.30). As the gas is much more compressible than the liquid, this assumption seems reasonable. Pressure and stress being uniform within the gas bubble, all displacements are linearly proportional to the radial coordinate r, see equations (4.94)-(4.95):

$$\begin{aligned} u_a(r) &= A_a r, \\ w_a(r) = \phi(U_a(r) - u_a(r)) &= F_a r, \end{aligned} \tag{4.103}$$

where A_a and F_a are arbitrary constants. We introduce the relative fluid displacement w, because it is essentially the variable that should satisfy the continuity condition over the gas-liquid interface ($r = a$). At this interface also continuity of solid displacement, total stress, and pore pressure should be satisfied. These boundary conditions are identical to the ones by Dutta and Odé (1979a), see equations (4.3)-(4.6), but are essentially different from the ones by Smeulders and Van Dongen (1997), who implicitly assumed continuity of solid velocity gradient instead of continuity of total stress. Introducing the liquid pressure variations at the bubble surface p_0, and defining $\chi_{jb} = \phi(\beta_{jb} - 1)$, we find for the boundary conditions that:

$$\begin{aligned} aA_a &= -\sum_{j=1,2} \frac{(1 + ik_{jb}a)}{a^2} B_j \exp(-ik_{jb}a), \\ aF_a &= -\sum_{j=1,2} \frac{\chi_{jb}(1 + ik_{jb}a)}{a^2} B_j \exp(-ik_{jb}a), \\ 3K_{\mathrm{BG}a}A_a + \frac{3(Q_a + R_a)}{\phi} F_a &= -\sum_{j=1,2} \frac{Z_{jb}}{a^3} B_j \exp(-ik_{jb}a), \\ \frac{3(Q_a + R_a)}{\phi} A_a + \frac{3R_a}{\phi^2} F_a &= -p_0, \end{aligned} \tag{4.104}$$

where we used the Biot-Gassmann modulus in the gas bubble region, $K_{\mathrm{BG}a}$, given by equation (2.26). The wave parameters

$$Z_{jb} = [P_b + \beta_{jb}(Q_b + R_b) + Q_b]k_{jb}^2 a^2 - 4\mu(1 + ik_{jb}a), \tag{4.105}$$

are defined in the liquid region at the gas bubble surface. From the above system it is straightforward to show that

$$\begin{aligned} B_1 &= \frac{-a_2 a^3}{a_1 b_2 - a_2 b_1} \hat{p}_0 \exp(ik_{1b}a), \\ B_2 &= \frac{a_1 a^3}{a_1 b_2 - a_2 b_1} \hat{p}_0 \exp(ik_{2b}a), \end{aligned} \tag{4.106}$$

where

$$\begin{aligned} a_j &= 3(1+ik_{jb}a)\left[K_{\mathrm{BG}a}+\frac{\chi_{jb}(Q_a+R_a)}{\phi}\right]-Z_{jb}, \\ b_j &= 3(1+ik_{jb}a)\left[\frac{(Q_a+R_a)}{\phi}+\frac{\chi_{jb}R_a}{\phi^2}\right]. \end{aligned} \tag{4.107}$$

Substituting equations (4.106) into (4.102), the wavefield in the liquid is now fully defined as a function of the dynamic pressure p_0. Next, we investigate the phase shift and amplitude difference between p_0 and the pressure p_∞ far away from the bubble. The fluid equation (2.8) is integrated over the liquid from $r = a$ to infinity:

$$\omega^2(\rho_{12}\Phi_b+\rho_{22}\Psi_b)_{|r=a}=\phi(p_0-p_\infty). \tag{4.108}$$

Substitution of the expressions for the densities and using equations (4.102) and (4.106), we find that

$$p_\infty = p_0\left(1-\rho_{\mathrm{f}b}a^2\omega^2\frac{a_1d_2-a_2d_1}{a_1b_2-a_2b_1}\right), \tag{4.109}$$

where

$$d_j=\beta_{jb}+(\beta_{jb}-1)(\tilde{\alpha}-1). \tag{4.110}$$

Equation (4.109) is a modified Rayleigh-Plesset equation, which was originally derived to describe the oscillating behavior of gas bubbles in a surrounding liquid without a porous background matrix (Van Wijngaarden, 1972). Using equations (4.98) and (4.99) yields that

$$\tilde{K}_{\mathrm{f}a}=K_{\mathrm{f}a}\left(1-\rho_{\mathrm{f}b}a^2\omega^2\frac{a_1d_2-a_2d_1}{a_1b_2-a_2b_1}\right). \tag{4.111}$$

We have implicitly used that the liquid pressure p_0 at the bubble surface equals the gas pressure inside the bubble p_a. This is not generally true, as also thermal effects (Champoux and Allard, 1991) and surface tension have to be taken into account. We choose not to consider these to allow a direct comparison with the generalized patchy model. In the limiting case of a compressible gas bubble in an incompressible liquid saturating an incompressible porous matrix, the factor $(a_1d_2-a_2d_1)/(a_1b_2-a_2b_1)$ tends to $\frac{1}{3}\tilde{\alpha}/K_{\mathrm{f}a}$, so that

$$\lim_{K_{\mathrm{f}b},K_{\mathrm{m}}\to\infty}\tilde{K}_{\mathrm{f}a}=K_{\mathrm{f}a}-\tfrac{1}{3}\tilde{\alpha}\rho_{\mathrm{f}b}a^2\omega^2. \tag{4.112}$$

With respect to the original Rayleigh-Plesset expression, the dynamic tortuosity $\tilde{\alpha}$ is added, which takes into account the viscous friction originating from the

oscillating gas bubble squeezing the incompressible liquid through the pores. The full expression (4.111) also accounts for the acoustic energy that is radiated away from the gas bubble by means of the two spherical Biot waves.

Substitution of $\tilde{K}_{\mathrm{f}a}$ into equation (4.100) yields the effective fluid modulus $\tilde{K}_{\mathrm{f}}$ of the mixture. Its absolute and phase value, together with the effective bulk modulus of the gas are shown in figure 4.15. We used the input values as in table 4.1. In the low-frequency limit $\tilde{K}_{\mathrm{f}a}$ approaches $K_{\mathrm{f}a}$, so that $\tilde{K}_{\mathrm{f}}$ is in the the Woods limit, see equation (4.54). The high-frequency limit (still maintaining $2\pi/k \gg b$) of $\tilde{K}_{\mathrm{f}}$ is $K_{\mathrm{f}b}/s_b$, which implies that the gas bubble cannot keep up with the exerted pressure variations and becomes extremely stiff. Then the gas bubble is resonating almost completely out-of-phase with respect to the effective fluid.

Following Van Wijngaarden (1972), we now assume that in a gas-liquid mixture the same relation (4.109) exists between p_0 and p_∞ as exists between the pressure in an isolated oscillating bubble and the pressure far away. We now obtain the effective poroelastic coefficients in equations (2.3), which are subsequently used in equation (2.15) to calculate the two effective compressional waves at the macroscopic level. In figure 4.16, we compare the present model with the generalized patchy model. In contrast to the generalized patchy model, the present model does predict the existence of the slow compressional Biot wave. As in the original Biot theory, the slow wave is diffusive at low frequencies and becomes propagatory at higher frequencies. The slow wave attenuation is significantly higher than that of the fast (seismic) wave. These features are in agreement with the fully-saturated curves in figure 2.1. Maximum slow wave attenuation is now reached around 0.2 Hz when the gas bubbles oscillate out-of-phase with respect to the applied liquid pressure variation p_∞.

The velocity of the seismic wave is hardly different from that predicted by the generalized patchy model. The attenuation of the seismic wave, however, is significantly higher in the seismic range (below 50 Hz). This is due to the fact that in the present theory the seismic energy is allowed to be dissipated through two spherical waves on the mesoscale, whereas in the generalized patchy model the energy is confined in the spherical shell (according boundary condition (4.8)). Apparently, upon inclusion of the slow wave in the theory on the macroscale, the signature of the fast wave changes. Dependent on the rock and fluid properties, the intrinsic attenuation is higher at low frequencies than predicted by the generalized patchy model. At higher frequencies, the predicted attenuation is comparable to that predicted by the generalized patchy model. At these frequencies, the out-of-phase motion of the gas bubbles with respect to the applied pressure diminishes. The frequency where maximum attenuation of the seismic wave is obtained, is well

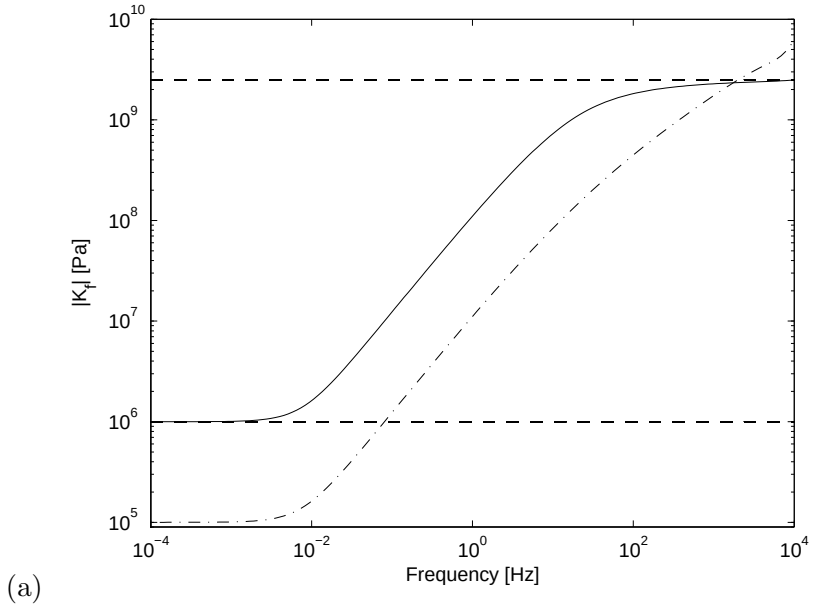

(a)

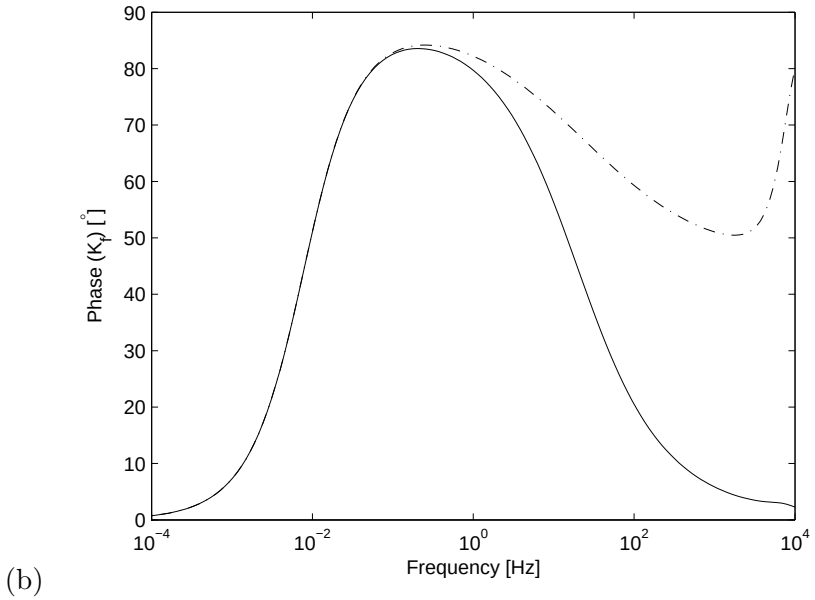

(b)

Figure 4.15: Absolute (a) and phase value (b) of the bulk modulus of the fluid. The solid curve is the effective bulk modulus of the mixture $\tilde{K}_{\mathrm{f}}$. The upper dashed line is $K_{\mathrm{f}b}/s_b$; the lower dashed line is the static limit of $\tilde{K}_{\mathrm{f}}$ (where $\tilde{K}_{\mathrm{f}a}$ equals $K_{\mathrm{f}a}$ in equation 4.100). The dashed-dotted curve is $\tilde{K}_{\mathrm{f}a}$. Gas fraction $s_a = 0.1$ and $a = 0.046$ m.

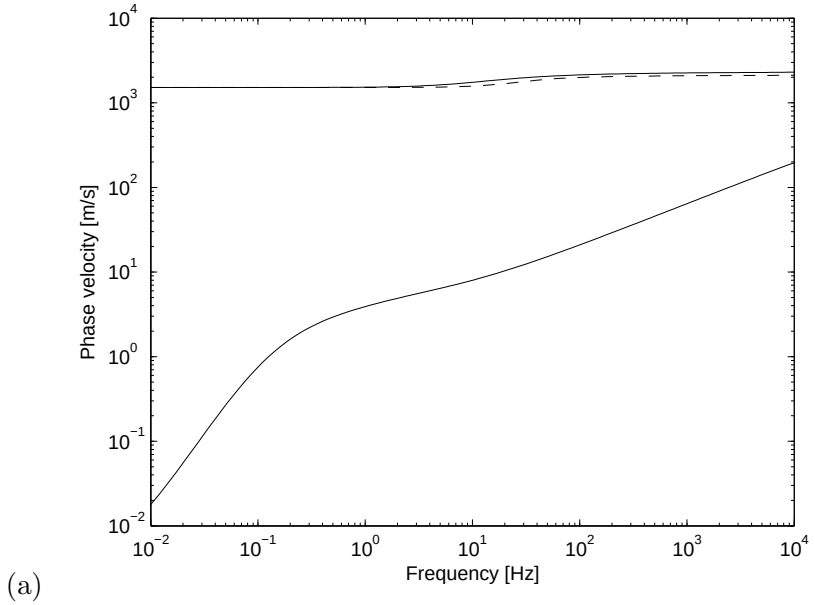

(a)

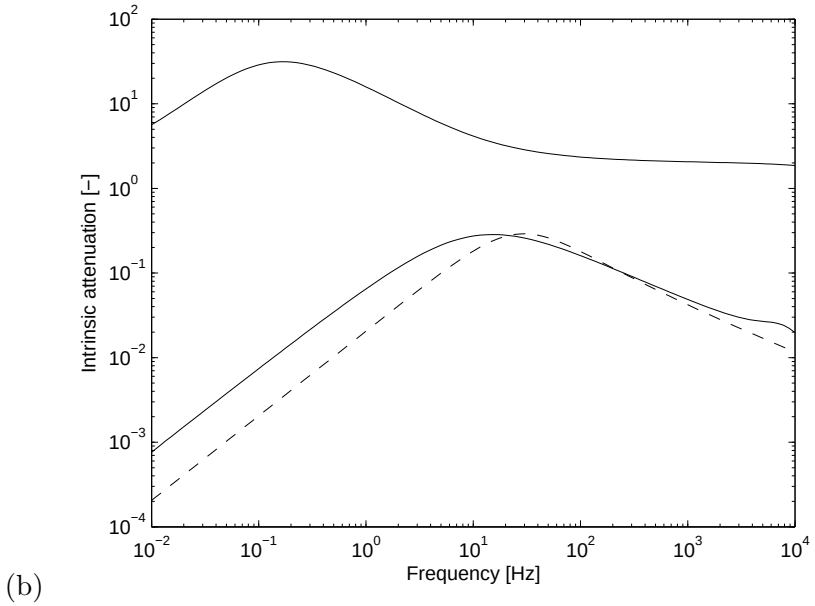

(b)

Figure 4.16: Phase velocity (a) and intrinsic attenuation (b) of the fast (seismic) and slow compressional wave. The Biot slow wave is the lower solid curve in (a) and the upper solid curve in (b). The seismic wave from the generalized patchy theory is dashed. Gas fraction $s_a = 0.1$ and $a = 0.046$ m.

approximated by $\omega_c/2\pi$ from equation 4.29.
We conclude that the present model predicts two compressional Biot waves and that the seismic attenuation is considerably higher than in the generalized patchy model, since we also take slow-wave effects on the macroscale into account.

Appendix A - Matrix elements of the exact patchy model in the full Biot context

Dutta and Odé (1979a) neglected the complex frequency-dependent viscous interaction between the solid and the fluid in both regions. We use the coefficients from the full Biot theory as treated earlier. The elements of matrix G are

$$\begin{aligned}
-g_{11} &= k_{1a} j_1(k_{1a} a), \\
-g_{12} &= k_{2a} j_1(k_{2a} a), \\
g_{13} &= k_{1b} j_1(k_{1b} a), \\
g_{14} &= k_{2b} j_1(k_{2b} a), \\
g_{15} &= k_{1b} n_1(k_{1b} a), \\
g_{16} &= k_{2b} n_1(k_{2b} a);
\end{aligned} \tag{4.113}$$

$$\begin{aligned}
g_{21} &= \chi_{1a} g_{11}, \\
g_{22} &= \chi_{2a} g_{12}, \\
g_{23} &= \chi_{1b} g_{13}, \\
g_{24} &= \chi_{2b} g_{14}, \\
g_{25} &= \chi_{1b} g_{15}, \\
g_{26} &= \chi_{2b} g_{16};
\end{aligned} \tag{4.114}$$

$$
\begin{aligned}
g_{31} &= k_{1a}^2\left(-\lambda_{1a}j_0(k_{1a}a)+2\mu_a\left(j_2(k_{1a}a)-\frac{j_1(k_{1a}a)}{k_{1a}a}\right)\right),\\
g_{32} &= k_{2a}^2\left(-\lambda_{2a}j_0(k_{2a}a)+2\mu_a\left(j_2(k_{2a}a)-\frac{j_1(k_{2a}a)}{k_{2a}a}\right)\right),\\
-g_{33} &= k_{1b}^2\left(-\lambda_{1b}j_0(k_{1b}a)+2\mu_b\left(j_2(k_{1b}a)-\frac{j_1(k_{1b}a)}{k_{1b}a}\right)\right),\\
-g_{34} &= k_{2b}^2\left(-\lambda_{2b}j_0(k_{2b}a)+2\mu_b\left(j_2(k_{2b}a)-\frac{j_1(k_{2b}a)}{k_{2b}a}\right)\right),\\
-g_{35} &= k_{1b}^2\left(-\lambda_{1b}n_0(k_{1b}a)+2\mu_b\left(n_2(k_{1b}a)-\frac{n_1(k_{1b}a)}{k_{1b}a}\right)\right),\\
-g_{36} &= k_{2b}^2\left(-\lambda_{2b}n_0(k_{2b}a)+2\mu_b\left(n_2(k_{2b}a)-\frac{n_1(k_{2b}a)}{k_{2b}a}\right)\right);
\end{aligned}
\tag{4.115}
$$

$$
\begin{aligned}
-g_{41} &= k_{1a}^2C_{1a}j_0(k_{1a}a),\\
-g_{42} &= k_{2a}^2C_{2a}j_0(k_{2a}a),\\
g_{43} &= k_{1b}^2C_{1b}j_0(k_{1b}a),\\
g_{44} &= k_{2b}^2C_{2b}j_0(k_{2b}a),\\
g_{45} &= k_{1b}^2C_{1b}n_0(k_{1b}a),\\
g_{46} &= k_{2b}^2C_{2b}n_0(k_{2b}a);
\end{aligned}
\tag{4.116}
$$

$$
\begin{aligned}
g_{51} &= 0,\\
g_{52} &= 0,\\
-g_{53} &= \chi_{1b}k_{1b}j_1(k_{1b}b),\\
-g_{54} &= \chi_{2b}k_{2b}j_1(k_{2b}b),\\
-g_{55} &= \chi_{1b}k_{1b}n_1(k_{1b}b),\\
-g_{56} &= \chi_{2b}k_{2b}n_1(k_{2b}b);
\end{aligned}
\tag{4.117}
$$

$$
\begin{aligned}
g_{61} &= 0,\\
g_{62} &= 0,\\
-g_{63} &= k_{1b}^2\left(-\lambda_{1b}j_0(k_{1b}b)+2\mu_b\left(j_2(k_{1b}b)-\frac{j_1(k_{1b}b)}{k_{1b}b}\right)\right),\\
-g_{64} &= k_{2b}^2\left(-\lambda_{2b}j_0(k_{2b}b)+2\mu_b\left(j_2(k_{2b}b)-\frac{j_1(k_{2b}b)}{k_{2b}b}\right)\right),\\
-g_{65} &= k_{1b}^2\left(-\lambda_{1b}n_0(k_{1b}b)+2\mu_b\left(n_2(k_{1b}b)-\frac{n_1(k_{1b}b)}{k_{1b}b}\right)\right),\\
-g_{66} &= k_{2b}^2\left(-\lambda_{2b}n_0(k_{2b}b)+2\mu_b\left(n_2(k_{2b}b)-\frac{n_1(k_{2b}b)}{k_{2b}b}\right)\right),
\end{aligned}
\tag{4.118}
$$

in which j_2 and n_2 are second order spherical Bessel and Neumann functions.

Appendix B - Matrix elements of the approximate patchy model in the full Biot context

The elements of F are given by:

$$\begin{aligned} f_{11} &= a, \\ f_{12} &= 0, \end{aligned} \tag{4.119}$$

$$\begin{aligned} f_{21} &= f_{12}, \\ f_{22} &= f_{11}, \end{aligned} \tag{4.120}$$

$$\begin{aligned} f_{31} &= 3K_{\mathrm{BG}a}, \\ f_{32} &= 3(Q_a + R_a)/\phi, \end{aligned} \tag{4.121}$$

$$\begin{aligned} f_{41} &= f_{32}, \\ f_{42} &= f_{32}/\gamma, \end{aligned} \tag{4.122}$$

and $f_{ij} = g_{ij}$ for $i = 1, ..., 6$ and $j = 3, ..., 6$ remain unchanged as defined in Appendix A.

Chapter 5

Rock-physical sample description

5.1 Introduction

In this chapter we experimentally determine the dry rock physical properties of 45 porous samples. The parameters needed for the models in chapters 2, 3, and 4 are: density, porosity, permeability, bulk modulus and shear modulus. We calibrate density and velocity measurements with five reference solids. The measured rock and solid properties are used in the chapters 6, 7, and 8. The measurements discussed in this chapter were acquired at the Rock Physics Laboratory of Stanford University.

5.2 Sample selection and sample preparation

For our study, we use a set of 50 samples: 45 porous samples and five reference solid samples. The reference solids are Aluminum, Teflon, PVC, Lucite, and Delrin.
The 45 porous samples comprise 38 natural rocks and seven man-made materials. The natural materials are all of sedimentary origin and consist of two chalk samples, 26 sandstone samples collected from known quarries or outcrops, and ten sandstones from an unknown location. The set of man-made materials consists of two fused glass beads samples, one brick, and four synthetic rocks of glued sand grains: two are coarsely grained (grainsize 300-350 μm) and two are finely grained (grainsize 250-300 μm). The sample identification and lithologies are given in table 5.1.

Sample ID	Lithology	ρ_{dry} [kg/m^3]	k_0 [mD]	ϕ [%]
CHK03	Chalk	1924 ± 5	1.08 ± 0.05	28.30 ± 0.01
CHK04	Chalk	1920 ± 8	1.07 ± 0.08	28.22 ± 0.01
SSA04	Berea sandstone 3 gray	2086 ± 1	362 ± 18	20.80 ± 0.01
SSA11	Berea sandstone 3 gray	2085 ± 1	310 ± 0	21.26 ± 0.02
SSB04	Berea sandstone 4 yellow	1804 ± 1	6029 ± 301	30.28 ± 0.01
SSB07	Berea sandstone 4 yellow	1847 ± 1	2748 ± 6	28.56 ± 0.01
SSB08	Berea sandstone 4 yellow	1823 ± 2	4002 ± 3	29.85 ± 0.01
SSB09	Berea sandstone 4 yellow	1854 ± 2	2650 ± 12	28.43 ± 0.01
SSC05	Boise sandstone	2317 ± 2	0.74 ± 0.04	11.75 ± 0.04
SSC06	Boise sandstone	2298 ± 1	0.95 ± 0.05	12.16 ± 0.03
SSF02	Unknown nat. sandstone	1930 ± 1	2666 ± 26	26.78 ± 0.01
SSF03	Unknown nat. sandstone	1942 ± 1	2517 ± 18	26.51 ± 0.01
SSF04	Unknown nat. sandstone	1935 ± 2	2131 ± 15	26.61 ± 0.03
SSG01	Unknown nat. sandstone	2004 ± 1	1862 ± 12	24.29 ± 0.01
SSG02	Unknown nat. sandstone	2025 ± 3	289 ± 1	23.33 ± 0.01
YBE03	Berea 5 par. to bedding	2111 ± 5	182 ± 1	18.94 ± 0.02
VIF01	Fine syn. sandstone	1603 ± 7	11928 ± 137	37.99 ± 0.02
VIF02	Fine syn. sandstone	1595 ± 9	12809 ± 753	38.33 ± 0.03
VIC05	Coarse syn. sandstone	1497 ± 10	25557 ± 2783	42.86 ± 0.03
VIC06	Coarse syn. sandstone	1517 ± 12	27743 ± 2603	41.99 ± 0.02
QUE09	Unknown nat. sandstone	2067 ± 7	2214 ± 43	21.89 ± 0.01
QUE10	Unknown nat. sandstone	2059 ± 7	2441 ± 16	22.20 ± 0.03
B1P13	Berea 1 par. to bedding	2132 ± 4	330 ± 3	20.06 ± 0.05
B1P14	Berea 1 par. to bedding	2125 ± 7	315 ± 3	20.41 ± 0.12
CAS16	Castlegate sandstone	2159 ± 2	5.51 ± 0.01	18.66 ± 0.03
CAS17	Castlegate sandstone	2135 ± 5	5.02 ± 0.02	19.54 ± 0.03
B1N20	Berea 1 norm. to bedding	2119 ± 3	205 ± 1	20.62 ± 0.01
B1N21	Berea 1 norm. to bedding	2134 ± 3	212 ± 6	19.92 ± 0.04
COL23	Colton sandstone	2338 ± 8	0.53 ± 0.00	12.04 ± 0.03
COL25	Colton sandstone	2357 ± 4	0.77 ± 0.03	11.44 ± 0.03
BEN27	Bentheimer sandstone	2010 ± 7	1151 ± 4	24.11 ± 0.02
BEN28	Bentheimer sandstone	2010 ± 2	1149 ± 21	24.13 ± 0.01
B2P30	Berea 2 par. to bedding	2144 ± 2	161 ± 1	19.52 ± 0.01
B2N32	Berea 2 norm. to bedding	2164 ± 3	92.7 ± 1.7	19.03 ± 0.02
B2N33	Berea 2 norm. to bedding	2148 ± 2	106 ± 2	19.36 ± 0.02

(continues)

(continued)

Sample ID	Lithology	ρ_{dry} [kg/m^3]	k_0 [mD]	ϕ [%]
FEL36	Felser sandstone yellow	2039 ± 4	10.1 ± 0.1	23.02 ± 0.02
FEL37	Felser sandstone yellow	2048 ± 3	9.13 ± 0.02	22.67 ± 0.04
NIV44	Nivelsteiner sandstone	1847 ± 1	6544 ± 132	30.18 ± 0.02
NIV45	Nivelsteiner sandstone	1809 ± 2	8056 ± 82	31.65 ± 0.03
UNK50	Unknown nat. sandstone	2245 ± 2	0.09 ± 0.00	15.84 ± 0.05
UNK51	Unknown nat. sandstone	2246 ± 2	0.20 ± 0.01	15.76 ± 0.06
NN356	Unknown nat. sandstone	2195 ± 3	1.50 ± 0.08	16.99 ± 0.04
NN458	Brick red	2225 ± 1	5.76 ± 0.19	15.75 ± 0.02
GL160	Glass beads 1	1884 ± 2	17935 ± 1031	34.02 ± 0.01
GL261	Glass beads 2	1895 ± 3	18324 ± 613	35.57 ± 0.01

Table 5.1: Rock physical properties of the porous materials under study obtained from independent laboratory measurements: ρ_{dry} is the density of the dry rock, k_0 is the Klinkenberg corrected permeability, and ϕ is the porosity. The error is the standard deviation of the measurements. (Nat. = natural; syn. = synthetic; par. = parallel; norm. = normal.)

The choice for this specific set was motivated by its large variety in density, porosity, permeability, and ultrasonic velocities (Heller, 2006). All samples are assumed to be of homogeneous isotropic composition (Kelder, 1998). The samples and reference solids are plane-parallel cylindrical cores, typically 3.8 cm (1.5 inch) long with a diameter of 2.5 cm (1.0 inch). The shape of the samples is dictated by the cylindrical dimensions of the sample chamber of the porosimeter and permeameter. After cutting the cores to proper length, the samples were rinsed with water and dried at room temperature. Then they were oven-dried at 85°C for two days and cooled down to room temperature in a desiccator to prevent exposure to atmospheric moisture. Density, porosity and permeability are measured directly on oven-dried samples. Several investigators found the first few percent of fluid saturation added to an ultra dry rock will lower the frame moduli (Murphy, 1982b; Knight and Dvorkin, 1992; Cadoret, 1993). Velocities calculated from ultra dry samples will be too high, because the first few mono layers of water chemically weaken the rock (Clark et al., 1980). To avoid artifacts of ultra dry rocks, the ultrasonic measurements are performed on dry samples which are acclimatized to the atmospheric humidity.

Solid	Measured values			Literature values		
	ρ [kg/m^3]	v_P [m/s]	v_S [m/s]	ρ [kg/m^3]	v_P [m/s]	v_S [m/s]
Aluminum	2714	6403	3153	2750 ± 50	6375 ± 125	3085 ± 45
Teflon	2168	1334	511	2170 ± 130	1400 ± 50	550
PVC	1383	2315	1081	1365 ± 15	2340 ± 40	1060
Lucite*	1181	2671	1334	1225 ± 45	2690 ± 80	1240 ± 120
Delrin	1421	2397	1003	1420	2430	960

*Including values for Plexiglas and Perspex.

Table 5.2: Measured material properties of reference solids compared to their literature values. The density ρ and compressional and shear wave velocities v_P and v_S are measured using the conventional techniques discussed in the text. The literature values are from Selfridge (1985), Kundu (2003), Kumar et al. (2003) and K-Mac Products (2008).

5.3 Density and porosity

The bulk densities of the dry samples and reference solids are measured by the mass-to-bulk volume ratio. The bulk volume is calculated from the sample length and diameter. The sample diameter and length are measured five times using a digital caliper. The weight is measured three times for each sample using a standard digital balance. The measured densities of the dry rock samples range from 1497 (VIC05) to 2357 kg/m^3 (COL25) as shown in table 5.1. The results for the reference solids are compared with literature values in table 5.2 and show good agreement.

The porosity of each sample is measured from the volume occupied by the grains using a standard porosimeter (Frank Jones, Tulsa, OK), see figure 5.1. The measurement is based on Boyle's law, which states that the product of pressure and volume of an ideal gas is constant at constant temperature. The set-up consists of a sample chamber connected to a high-pressure Helium cylinder. After the sample is placed in the sample chamber under atmospheric conditions, 100 psi (approximately 7 bars) Helium is released into the sample chamber until pressure equilibration. After the pressure is measured, the sample chamber is equilibrated to atmospheric pressure. This process is repeated three times for each sample (the pressure usually drops to 70 psi). From the pressure changes on the porous sample and the pressure changes on a reference plug (billet) with a known volume one can calculate the matrix volume, assuming no unconnected pore volume. The results are shown in table 5.1. The measured porosities vary from 0.11 (COL25) to 0.43

(VIC05). The relative error in porosity is less than 0.1 percent.
Figure 5.2 graphically displays the measurement set. We notice that we capture a wide range of porosity and density values. The density of the solid grains is calculated from the density of the dry sample and the measured porosity: $\rho_{\mathrm{dry}} = (1-\phi)\rho_{\mathrm{s}}$. The density of the solid grains lies between 2586 and 2683 kg/m^3 for all samples, except for the grain densities of the two glass samples, GL160 and GL261, which are 2856 and 2941 kg/m^3, respectively. The relative error in solid grain density is 0.1 percent.

5.4 Permeability

Permeability measurements are carried out using the Ultraperm-400 permeameter (Core Laboratories Instruments, Carrolton, TX), see figure 5.1. The sample is placed in an aluminum Hassler type core holder at 200 psi (approximately 14 bars) confining pressure (air). The measurement uses Darcy's law to calculate the gas (Nitrogen) permeability k_0 from the measured flow rate Q and up- and downstream pressures P_1 and P_2:

$$k_0 = \frac{2P_1 Q\eta L}{A(P_1^2 - P_2^2)}, \tag{5.1}$$

where L and A are respectively the length and cross-sectional area of the sample and η is the viscosity of Nitrogen.
Very low-permeable samples (< 1 mD) are measured using a single point, when the differential pressure over the sample length is stable with the flow over the sample area. For higher-permeable sample (> 1 mD), the so-called Klinkenberg correction is used. Klinkenberg (1941) described permeability to a gas to be dependent upon molecular free path, mean pressure and temperature. If five apparent permeabilities k_{app} are measured at various mean pressures P_{m}, the Klinkenberg factor b and the true permeability k_0 are found from the slope and extrapolated interception at infinite mean pressure ($1/P_{\mathrm{m}} = 0$) using linear regression:

$$k_{\mathrm{app}} = k_0 \left(1 + \frac{b}{P_{\mathrm{m}}}\right). \tag{5.2}$$

In figure 5.4, the Klinkenberg correction is exemplified for a typical rock (YBE03). Klinkenberg-corrected permeabilities with R^2 (coefficient of determination) lower than 0.90 are rejected. The permeability of each sample is measured three to five times. The results are shown in table 5.1. The samples cover a range from 0.09 mD (UNK50) to 28 D (VIC06). The permeameter allows for accurate determination of

permeability over the range of 0.01 mD to 15 D (Core Laboratories Instruments, 2000). Therefore, the permeabilities of VIC05, VIC06, GL160, and GL261 are considered not to be accurate. The relative error in permeability is 2.5 percent.
In figure 5.3, we show a porosity-permeability crossplot. Clearly a trend is visible, but also outlyers can be identified. There are many porosity-permeability relationships suggested in literature. Bourbié et al. (1987) discuss a form of the Carman-Kozeny relationship:

$$k_0 \propto \ell^2 \phi^n, \tag{5.3}$$

where ℓ is the characteristic grain or pore dimension (Mavko et al., 2003). In figure 5.3, we fit our data to the Carman-Kozeny relation and find that $n = 9.0$ and $\ell = 321$ μm. For our low-permeable (< 10 mD) materials the data show a large scattering and a relationship is ambiguous. The high-porosity low-permeable chalk samples clearly deviate most. A fit to high-permeable (> 10 mD) samples only gives $n = 6.6$ and $\ell = 112$ μm. Bourbié et al. (1987) observed experimentally n to vary from 3 for high porosities to 8 for low porosities on very clean Fontainebleau sandstones with a grain diameter around 250 μm.

5.5 Elastic moduli

Ultrasonic experiments are conducted to determine the bulk and shear modulus of the dry samples. Dry compressional and shear wave measurements are performed at room conditions using a standard pulse transmission bench-top set-up as shown in figure 5.5.
The experimental set-up to measure velocity consists of a pulse generator (Panametrics Pulser Receiver model 5055 PR) and a four-channel digitizing oscilloscope (Tektronix TDS 420A), connected to a computer with a PCI-GPIB cable. Using molasses to enhance the transducer-sample coupling, the set-up conducts measurements in the sample length direction. The aluminum holders of the piezoelectric transducers provide a backing of about 300 g. Two transducer pairs with a flat element diameter of 0.5 inch (Panametrics-PZT V103 and V154) allow measurements of the compressional and shear wave velocity at 1.0 and 2.25 MHz, respectively. The system delay is calibrated by face-to-face measurements of the transducers and is 380 ns for the P-wave transducers and 360 ns for the S-wave pair. Velocity calibration is accomplished by using aluminum solids of different lengths. The relative error in v_{P} and v_{S} are 0.2 % and 0.9 %, respectively, for the aluminum solids. The actual error in the velocity measurements is estimated to be 1%, because of

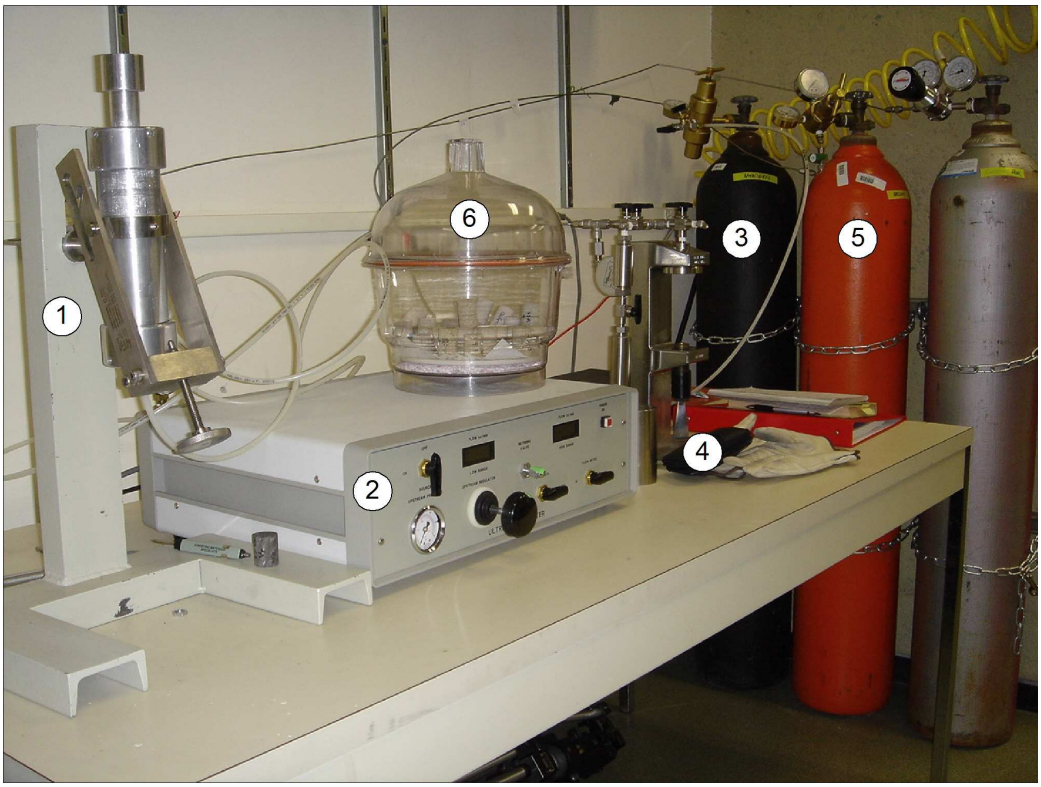

Figure 5.1: Photo of the porosimeter and permeameter. On the left is the core holder (1) of the permeameter (2). The tubes provide Nitrogen from the cylinder (3). On the right we see the set-up of the porosimeter (4), which is connected to the Helium cylinder (5). On top of the permeameter is a desiccator containing some samples (6). These set-ups are at the Rock Physics Laboratory of Stanford University.

operator error in picking the first arrival time. The velocities for the reference solids are in agreement with the values from literature, as shown in table 5.2.

The dry velocity results for the porous samples are given in table 5.3 together with the bulk and shear modulus, K_{m} and μ, respectively. The elastic moduli are calculated from the dry velocities using equations (2.5) and (2.6). In the table we observe that $v_{\mathrm{P}} > v_{\mathrm{S}}$ for all samples, while $K_{\mathrm{m}} > \mu$ for about 80 % of the samples. Similar percentages have been reported by Wisse (1999).

There is a wide variety of published $v_{\mathrm{P}}/v_{\mathrm{S}}$ relations, see Castagna et al. (1993) for a review. In general, high $v_{\mathrm{P}}/v_{\mathrm{S}}$ ratios correspond to unconsolidated sediments, while medium and low $v_{\mathrm{P}}/v_{\mathrm{S}}$ ratios correspond to dry consolidated sediments (Bourbié et al., 1987).

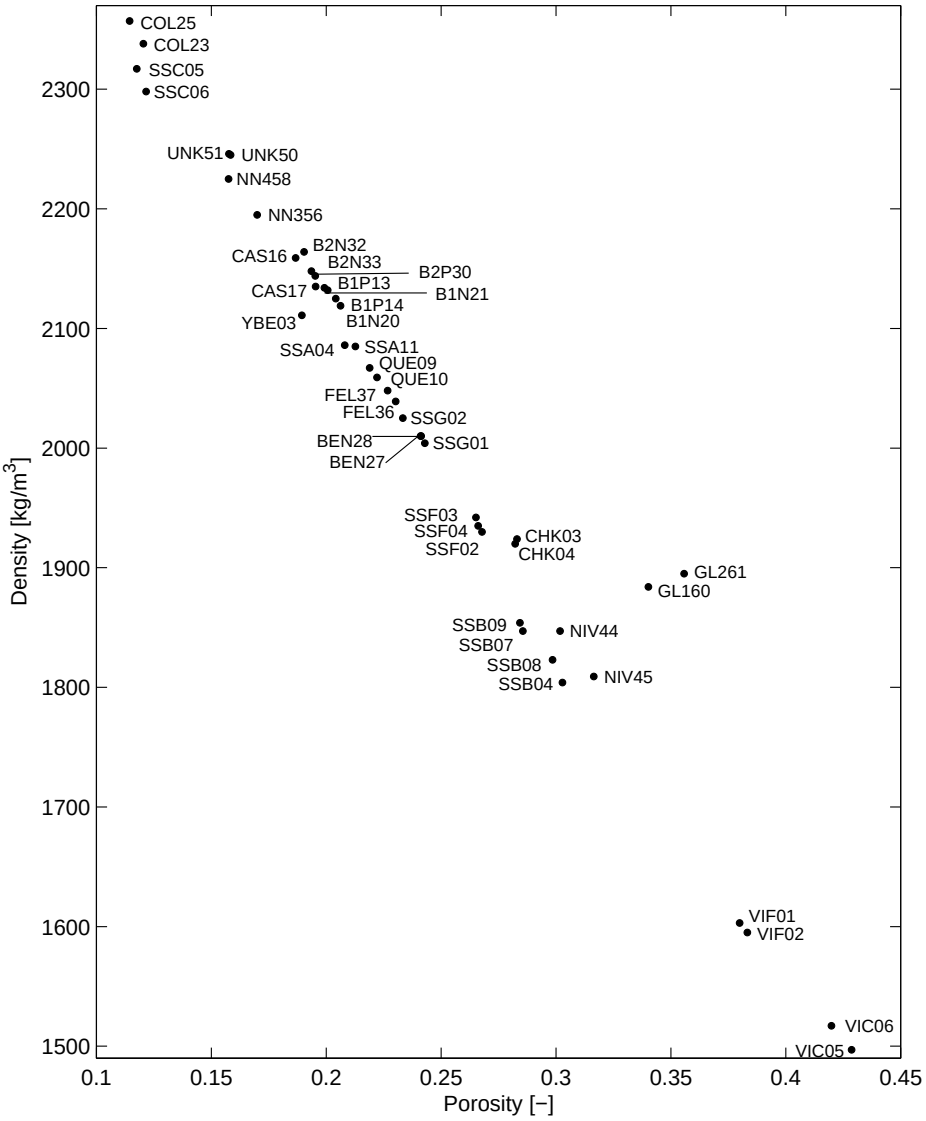

Figure 5.2: Dry bulk density versus porosity. The measured values are given in table 5.1.

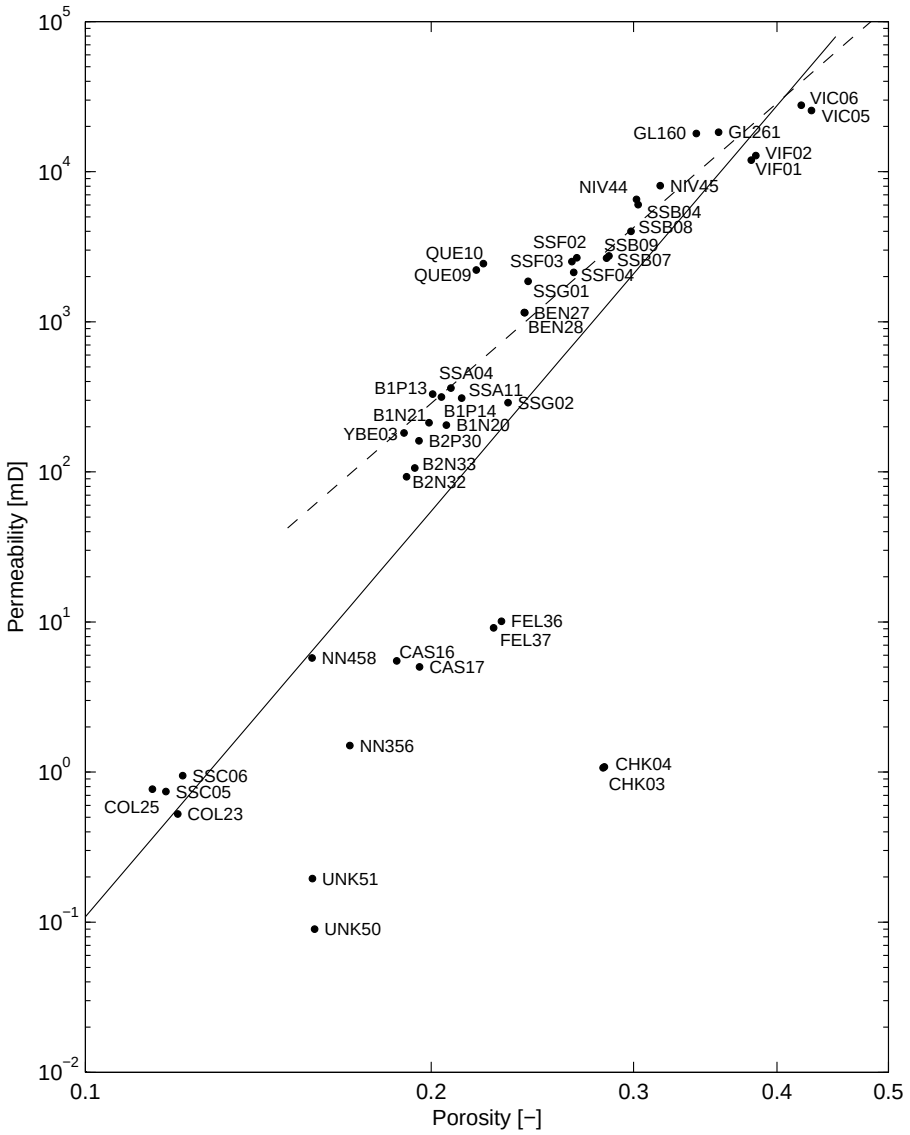

Figure 5.3: Permeability-porosity measurements and two relationships. The measured values are given in table 5.1. The solid curve is the least-squares fit to all data ($R^2 = 0.64$). The dashed curve is the fit to high-permeable (> 10 mD) samples only ($R^2 = 0.90$).

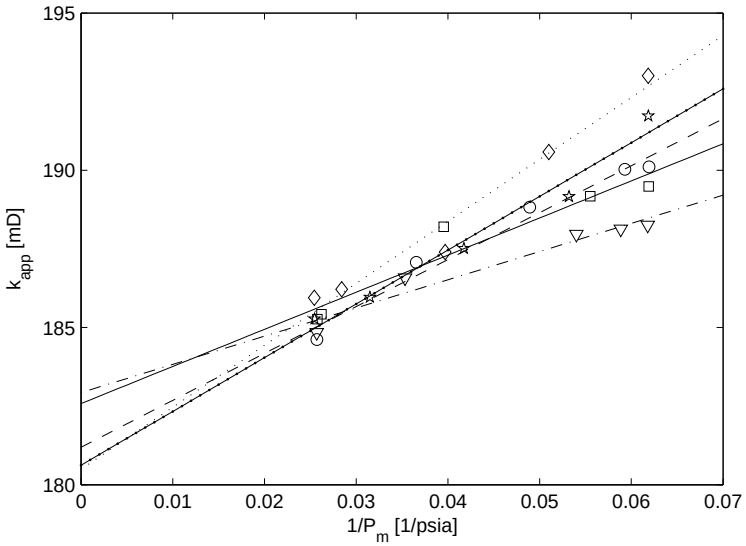

Figure 5.4: Apparent permeability k_{app} as a function of inverse mean pressure $1/P_{\mathrm{m}}$ for a Berea rock (YBE03). Each symbol denotes one experiment in which the apparent permeability is measured at five different mean pressures. The true permeability k_0 of each experiment is obtained by linear regression (fitted lines). The permeability of the sample (table 5.1) is the average of the five experiments. The dotted line is fitted to the diamonds ($R^2 = 0.97$). The solid line with dots is fitted to the stars ($R^2 = 0.97$). The dashed line to the circles ($R^2 = 0.97$). The solid line to the squares ($R^2 = 0.92$). The dashed-dotted line to the triangles ($R^2 = 0.94$). The unit 'psia' (pounds-force per square inch absolute) is the gauge pressure plus local atmospheric pressure.

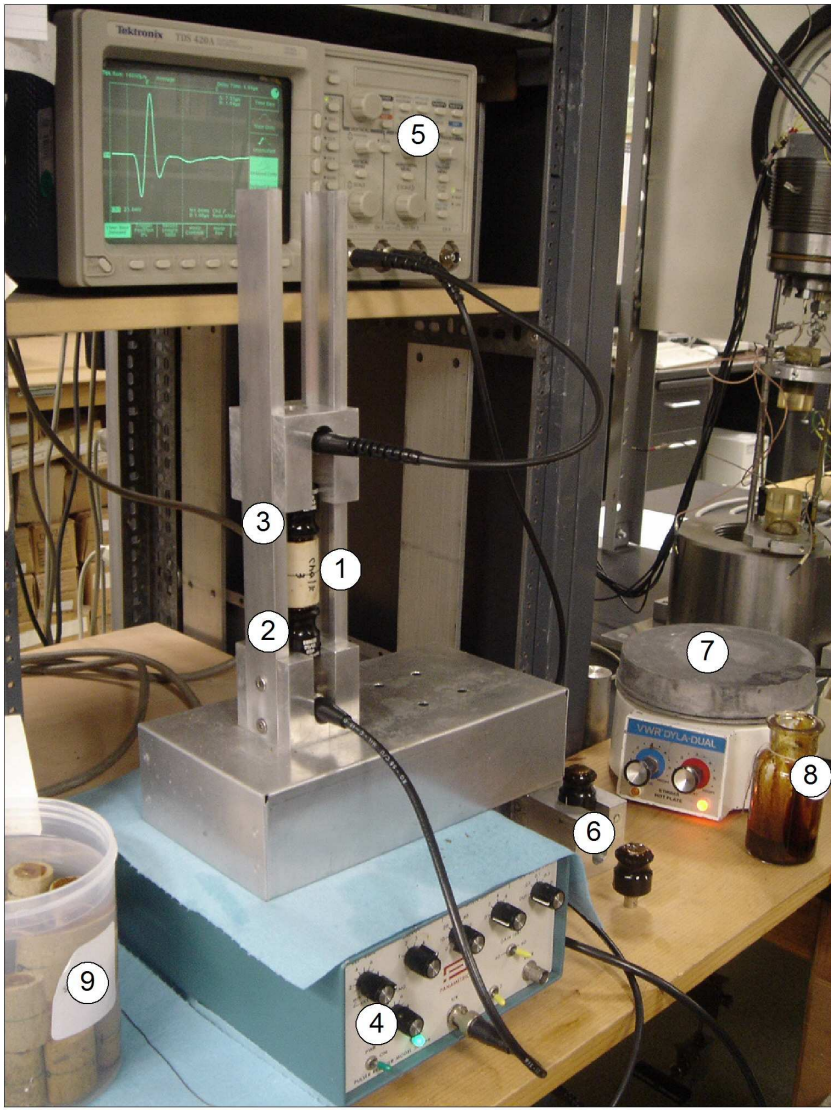

Figure 5.5: Photo of the ultrasonic bench-top set-up. A sample (1) is clamped between two identical P-wave transducers (2) and (3). The sending transducer is connected to the pulse generator (4), while the receiving transducer is connected to the oscilloscope (5). A pair of S-wave transducers (6) is visible on the table. The hot plate (7) is used to melt molasses (8), which is used to enhance transducer-sample coupling. On the left hand side we see a container with samples (9). This set-up is at the Rock Physics Laboratory of Stanford University.

Sample ID	$v_{\mathrm{P\ dry}}$ [m/s]	$v_{\mathrm{S\ dry}}$ [m/s]	K_{m} [GPa]	μ [GPa]
CHK03	4524 ± 208	2537 ± 67	22.86 ± 3.68	12.38 ± 0.65
CHK04	4499 ± 204	2519 ± 65	22.61 ± 3.59	12.19 ± 0.63
SSA04	2894 ± 86	1934 ± 39	7.06 ± 1.08	7.80 ± 0.31
SSA11	2841 ± 108	1966 ± 52	6.09 ± 1.35	8.06 ± 0.43
SSB04	3511 ± 128	2164 ± 49	10.98 ± 1.66	8.45 ± 0.38
SSB07	3928 ± 157	2417 ± 60	14.11 ± 2.34	10.79 ± 0.54
SSB08	3486 ± 125	2151 ± 48	10.90 ± 1.63	8.44 ± 0.38
SSB09	3889 ± 154	2329 ± 56	14.64 ± 2.27	10.05 ± 0.48
SSC05	3301 ± 112	1920 ± 38	13.86 ± 1.75	8.54 ± 0.34
SSC06	3199 ± 105	1926 ± 39	12.15 ± 1.58	8.53 ± 0.34
SSF02	2417 ± 60	1473 ± 23	5.69 ± 0.58	4.19 ± 0.13
SSF03	2534 ± 67	1512 ± 24	6.55 ± 0.67	4.44 ± 0.14
SSF04	2454 ± 77	1552 ± 31	5.43 ± 0.75	4.66 ± 0.19
SSG01	2822 ± 82	1801 ± 34	7.30 ± 0.96	6.50 ± 0.24
SSG02	3012 ± 93	1842 ± 35	9.21 ± 1.16	6.87 ± 0.26
YBE03	3223 ± 134	2180 ± 62	8.55 ± 1.92	10.04 ± 0.57
VIF01	2240 ± 53	1476 ± 23	3.39 ± 0.39	3.49 ± 0.11
VIF02	2298 ± 55	1513 ± 24	3.55 ± 0.42	3.65 ± 0.12
VIC05	1553 ± 26	1018 ± 11	1.54 ± 0.13	1.55 ± 0.03
VIC06	1585 ± 27	1033 ± 11	1.65 ± 0.13	1.62 ± 0.04
QUE09	2865 ± 86	1826 ± 35	7.78 ± 1.05	6.89 ± 0.26
QUE10	2766 ± 80	1799 ± 34	6.87 ± 0.95	6.67 ± 0.25
B1P13	3068 ± 98	1875 ± 37	10.08 ± 1.32	7.50 ± 0.30
B1P14	2906 ± 88	1824 ± 35	8.53 ± 1.12	7.07 ± 0.27
CAS16	2692 ± 76	1858 ± 36	5.72 ± 0.93	7.45 ± 0.29
CAS17	2728 ± 77	1864 ± 36	6.00 ± 0.94	7.41 ± 0.29
B1N20	2865 ± 86	1881 ± 37	7.40 ± 1.08	7.50 ± 0.30
B1N21	2862 ± 85	1879 ± 37	7.43 ± 1.09	7.54 ± 0.30
COL23	3155 ± 103	1919 ± 39	11.79 ± 1.57	8.61 ± 0.35
COL25	3449 ± 123	2191 ± 50	12.95 ± 2.07	11.32 ± 0.52
BEN27	3520 ± 128	2275 ± 54	11.03 ± 1.88	10.41 ± 0.50
BEN28	3517 ± 128	2273 ± 54	11.02 ± 1.87	10.39 ± 0.49
B2P30	3158 ± 104	1941 ± 40	10.62 ± 1.44	8.08 ± 0.33
B2N32	3100 ± 100	1938 ± 40	9.97 ± 1.38	8.12 ± 0.33
B2N33	3050 ± 97	1879 ± 37	9.87 ± 1.30	7.59 ± 0.30

(continues)

(continued)

Sample ID	$v_{\mathrm{P\ dry}}$ [m/s]	$v_{\mathrm{S\ dry}}$ [m/s]	K_{m} [GPa]	μ [GPa]
FEL36	3272 ± 111	2072 ± 45	10.15 ± 1.53	8.75 ± 0.38
FEL37	3271 ± 111	1963 ± 40	11.39 ± 1.52	7.89 ± 0.33
NIV44	2897 ± 88	1973 ± 41	5.92 ± 0.99	7.19 ± 0.30
NIV45	2692 ± 76	1821 ± 35	5.11 ± 0.77	6.00 ± 0.23
UNK50	3783 ± 148	2472 ± 64	13.84 ± 2.62	13.71 ± 0.71
UNK51	3662 ± 138	2457 ± 63	12.03 ± 2.38	13.56 ± 0.70
NN356	3507 ± 128	2294 ± 55	11.58 ± 2.04	11.56 ± 0.56
NN458	4437 ± 202	2912 ± 88	18.65 ± 4.14	18.86 ± 1.14
GL160	2750 ± 80	1675 ± 30	7.20 ± 0.85	5.29 ± 0.19
GL261	2908 ± 102	1720 ± 36	8.55 ± 1.15	5.60 ± 0.24

Table 5.3: Dry rock velocities and bulk moduli of the porous materials under study from ultrasonic bench-top measurements. The measured velocities $v_{\mathrm{P\ dry}}$ and $v_{\mathrm{S\ dry}}$ denote, respectively, the compressional and shear wave velocity of a dry sample. The bulk and shear modulus, K_{m} and μ, are calculated using equations (2.5) and (2.6), respectively, and the densities of table 5.1. The relative error in the velocities reflects an uncertainty of 0.4 μs in picking the first arrival times. The relative error in the elastic moduli is solely attributed to an error in the velocities.

Chapter 6

Ultrasonic measurements of oil and oil-saturated porous media

6.1 Introduction

Ultrasonic techniques are used extensively to extract material properties in such different areas as petrophysics, non-destructive testing, and echocardiography. In these techniques, the phase velocity, attenuation and the reflection and transmission coefficients are determined as a function of frequency. In the present chapter, we measure the oil-saturated acoustic bulk properties of the set of 45 samples which we described previously. First, we characterize the properties of the silicone oil (5 cSt Dow Corning 200 fluid). Then, we measure the fast compressional and shear wave velocities and fast compressional quality factor of the saturated samples and compare the results with predictions from the Biot theory of chapter 2. We use the measured rock properties of chapter 5.

6.2 Wavefield characterization

6.2.1 Introduction

Acoustic radiation from a baffled planar piston is a canonical acoustic problem already investigated by Rayleigh (1896). In this problem, a circular piston with radius a and surface S, vibrates uniformly within a rigid baffle at a radial frequency ω with normal velocity amplitude v_0 in a homogeneous fluid with a sound speed c_{f} and density ρ_{f}. The resulting radiated pressure p is given by the Rayleigh integral

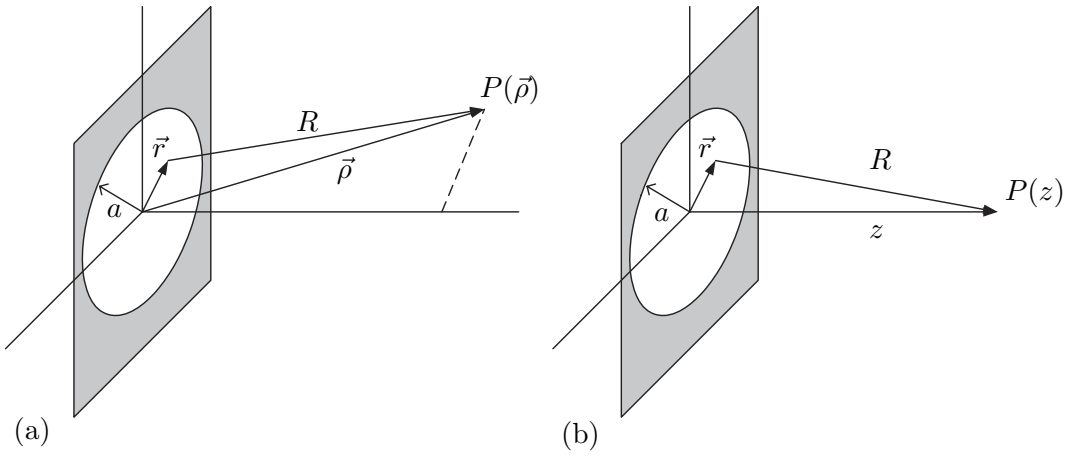

Figure 6.1: Schematic geometry and notation of the variables. A piston of radius a, centered at the origin radiates into an infinite half-space. The distance from the field point $P(\vec{\rho})$ to the surface element $d\,S(\vec{r})$ is R. (a) Off-axial field point $P(\vec{\rho})$, where $R = |\vec{\rho} - \vec{r}|$. (b) Axial field point $P(z)$, with $R = \sqrt{z^2 + r^2}$, where z is the distance along the piston symmetry axis.

of the first kind (Berkhout, 1987):

$$p(\vec{\rho}, \omega) = \frac{i\omega\rho_{\mathrm{f}} v_0}{2\pi} \int_S \frac{\exp(-ik_{\mathrm{f}} R)}{R} dS, \tag{6.1}$$

where $R = |\vec{\rho} - \vec{r}|$ is the distance from a field point $P(\vec{\rho})$ to a point on the piston surface $\vec{r}$, see figure 6.1a.
The Rayleigh integral actually represents Huygens' principle stating that every point may be considered as the source of an outgoing spherical wave, and that the field can be constructed from the superposition of these waves.

6.2.2 Transducer wavefield measured at a point

The integral (6.1) can be evaluated for the case that the field point is located on the symmetry axis z. In this case, $R = \sqrt{z^2 + r^2}$ as shown figure 6.1b, and we find that

$$\frac{p}{p_0} = \frac{ik_{\mathrm{f}}}{2\pi} \int_0^{2\pi} \int_0^a \frac{\exp(-ik_{\mathrm{f}} R)}{R} r\, dr\, d\varphi, \tag{6.2}$$

where we set $p_0 \equiv \rho_{\mathrm{f}} c_{\mathrm{f}} v_0$ and $k_{\mathrm{f}} = \omega / c_{\mathrm{f}}$ (Mast and Yu, 2005). Recognizing that $r\, dr = R\, dR$, this integral can be evaluated to give

$$\frac{p}{p_0} = \exp(-ik_{\mathrm{f}} z) - \exp(-ik_{\mathrm{f}} \sqrt{z^2 + a^2}), \tag{6.3}$$

which can be interpreted analytically. We obtain (Jocker, 2005)

$$\begin{aligned}\frac{p}{p_0} &= \exp\left(-\frac{ik_\mathrm{f}}{2}\left(\sqrt{z^2+a^2}+z\right)\right)\times \\ &\quad \left[\exp\left(\frac{ik_\mathrm{f}}{2}\left(\sqrt{z^2+a^2}-z\right)\right)-\exp\left(-\frac{ik_\mathrm{f}}{2}\left(\sqrt{z^2+a^2}-z\right)\right)\right] \\ &= 2i\,\exp\left(-\frac{ik_\mathrm{f}}{2}\left(\sqrt{z^2+a^2}+z\right)\right)\sin\left(\frac{k_\mathrm{f}}{2}\left(\sqrt{z^2+a^2}-z\right)\right), \qquad (6.4)\end{aligned}$$

so that

$$\left|\frac{p(z)}{p_0}\right| = \left|2\sin\left(\frac{k_\mathrm{f}}{2}\left(\sqrt{z^2+a^2}-z\right)\right)\right|. \qquad (6.5)$$

We plot $|p(z)/p_0|$ in figure 6.2. The near field (Fresnel zone) indicates the region close to the source where constructive and destructive interference occurs between waves emerging from different points on the surface of the radiator. The location where interference no longer occurs is the far field (Fraunhofer zone). The pattern of consecutive maxima and minima, characteristic for the Fresnel zone, is clearly visible. This pattern, as first discussed by Seki et al. (1956), is followed by a steady pressure decline in the Fraunhofer zone.

In equation (6.3), we notice that the pressure field along z is a simple plane wave modified by an edge wave with opposite polarity. For an axial observation point the travel difference between a plane wave and an edge wave is $\sqrt{z^2+a^2}-z$. The transition distance from the Fresnel to the Fraunhofer zone, z_F, is defined by this distance being equal to $\lambda/2$ or π/k_f. The position of the last maximum of $|p(z)/p_0|$ also defines this distance, which is approximated by

$$z_\mathrm{F} \approx \frac{k_\mathrm{f}a^2}{2\pi}. \qquad (6.6)$$

For a circular piston with a half-inch diameter ($a = 6.35$ mm) vibrating at its center frequency of 1 MHz in silicone oil ($c_\mathrm{f} = 979.0$ m/s, see section 6.3), z_F is 41 mm.

In figure 6.2, we also show the results of an acoustic experiment in which the wave field emitted by a flat-faced transducer (Panametrics-PZT V103) is captured by a broadband needle hydrophone (Speciality Engineering Associates, type PZT-Z44-1000). Measurements of relatively large changes in the ultrasonic signal over relatively small distances considered in the near field requires very accurate measures and stable experimental conditions. From the experimental data we observe a transition distance $z_\mathrm{F} = 49$ mm.

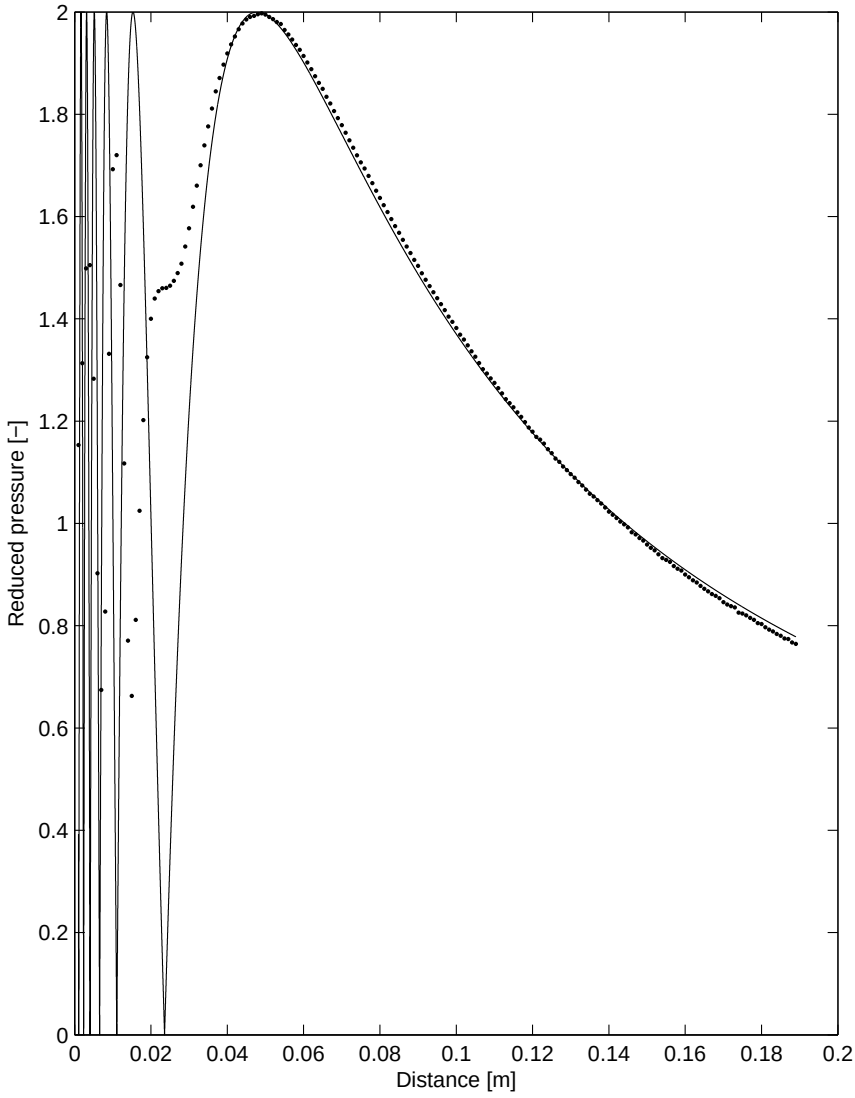

Figure 6.2: Pressure at 1 MHz as a function of the distance z in oil. The experimental data (dots) are acquired using transducer source with a radius of 6.35 mm and a needle hydrophone receiver (1 mm frontal diameter). The theoretical data (solid curve) represent the pressure emitted from a piston source with an effective radius of 6.93 mm as detected by a point receiver. The data are normalized by p_0.

The assumption that the transducers used in the experiment can be represented as an ideal piston source and an ideal point receiver in the derivation of equation (6.5) is not adequately fulfilled in practice. In reality, the surface of the transducer is clamped at the edges, so that the effective vibrating radius is not exactly the measured 6.35 mm. From z_{F} fitting, we find an effective source radius of 6.93 mm.

6.2.3 Transducer wavefield measured over a surface

The theory described heretofore dealt with ascertaining a description of the on-axial point pressure within the radiated field of a planar acoustic source. In case of a coaxially aligned source and receiver with an identical plane-circular element with radius a, the averaged received pressure is obtained by integrating the pressure over the receiving surface:

$$\langle p \rangle = \frac{1}{\pi a^2} \int_S p dS. \tag{6.7}$$

From this expression, Williams (1951) derived an expression for the acoustic pressure in terms of a plane-wave component and an edge-diffraction integral term. An approximation to Williams exact integral expression for $z > 2a$ was obtained by Bass (1958). Later, Williams (1970) extended Bass's approximate results to higher order[1]:

$$\left| \left\langle \frac{p(z)}{p_0} \right\rangle \right| = \left| \left(1 - (b_1 + b_2) e^{-i\zeta}\right) e^{-ik_{\mathrm{f}} z} \right|, \tag{6.8}$$

where

$$\begin{aligned} b_1 &= \left(1 - \frac{\eta}{2} - \frac{\eta^2}{8}\right) \left[J_0(\zeta) + i J_1(\zeta)\right], \\ b_2 &= \left(\eta + \frac{\eta^2}{4}\right) \left[\frac{J_1(\zeta)}{\zeta}\right], \end{aligned} \tag{6.9}$$

in which $\eta = (\zeta/(k_{\mathrm{f}} a))^2$, $\zeta = \frac{1}{2} k_{\mathrm{f}} \left(\sqrt{z^2 + 4a^2} - z\right)$ and J_0 and J_1 are Bessel functions of the zeroth and first order.

A simpler closed-from expression for the diffraction correction, provided that $\sqrt{k_{\mathrm{f}} a} \gg 1$, is given by Rogers and Van Buren (1974):

$$\left| \left\langle \frac{p(z)}{p_0} \right\rangle \right| = \sqrt{\left[\cos\left(\frac{k_{\mathrm{f}} a^2}{z}\right) - J_0\left(\frac{k_{\mathrm{f}} a^2}{z}\right)\right]^2 + \left[\sin\left(\frac{k_{\mathrm{f}} a^2}{z}\right) - J_1\left(\frac{k_{\mathrm{f}} a^2}{z}\right)\right]^2}, \tag{6.10}$$

[1] Corrected for a typo in Bass's (1958) result.

By differentiating equation (6.10) with respect to z, we find that $|\langle p/p_0 \rangle|$ has maxima when z is a root of $J_1(k_\mathrm{f} a^2/z) = \sin(k_\mathrm{f} a^2/z)$. The largest value of z for which $|\langle p/p_0 \rangle|$ has a maximum is approximated by:

$$z_\mathrm{F} \approx k_\mathrm{f} a^2 \frac{\pi - 1}{\pi(\pi - 1) - 1}. \tag{6.11}$$

This gives $z_\mathrm{F} = 97$ mm for a circular piston ($a = 6.35$ mm) vibrating at 1 MHz in oil. The absolute value of the normalized pressure is shown in figure 6.3 for the approximations by Williams (1970) and by Rogers and Van Buren (1974) for a circular piston set. Especially in the far field the theoretical approximations coincide, but in the near field discrepancies are visible.

From an laboratory experiment with identical half-inch diameter transducers in oil, we observe the last maximum at 82 mm in figure 6.3. The least squares difference along z between the theory of Rogers and Van Buren (1974) and the experiment is at minimum for an effective radius of 6.06 mm for both transducers.

Again, the pattern of consecutive maxima and minima though less pronounced compared with the needle measurements, is clearly visible in theory and experiment. It seems that the interference pattern in the experiment is not complete. This can be explained by the fact that the theory is based on continuous waves, while in practice we use transient signals. The steady pressure decline is also less pronounced compared to the needle measurements, due to the averaging effects over the size of the receiving transducer.

For both sets, the mismatch between theory and experiment is severe in the near field, but however in the far field the agreement is excellent. In the near field, the decrease in signal amplitude is due to interference and diffraction, whereas in the far field it is mainly caused by divergence and diffraction. Apparently, upon incorporating an effective radius, the intrinsic loss of the silicone oil is a negligible fraction of the total loss, which validates k_f to be real-valued. Similar conclusions were drawn by Jocker (2005) in an experiment with 500 kHz transducers (radius 12.7 mm) in water.

6.3 Ultrasound measurements on oil

We determine the speed of sound in silicone oil in an Ultrasound Tank (UST). The set-up is depicted in figure 6.4. The UST is an oil-filled $30 \times 40 \times 15$ cm plastic container. Two identical 1 MHz, 0.5" diameter ultrasound (US) transducers (Panametrics PZT V103) are mounted in oil on an automated positioning system,

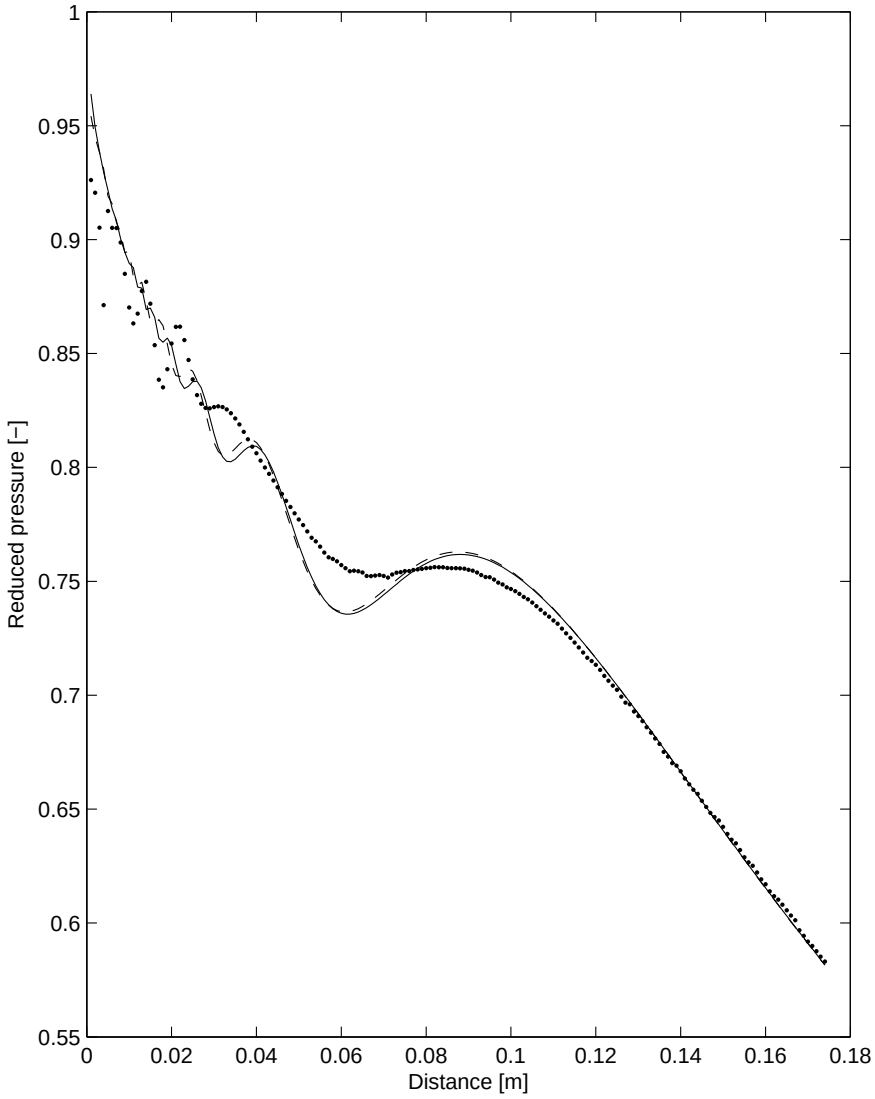

Figure 6.3: Pressure at 1 MHz as a function of the distance z in oil. The experimental data (dots) are acquired using two identical transducers with a radius of 6.35 mm. The theoretical approximations by Williams (1970) (dashed curve) and Rogers and Van Buren (1974) (solid curve) represent the pressure from a piston set with an effective radius of 6.06 mm. The data are normalized by p_0.

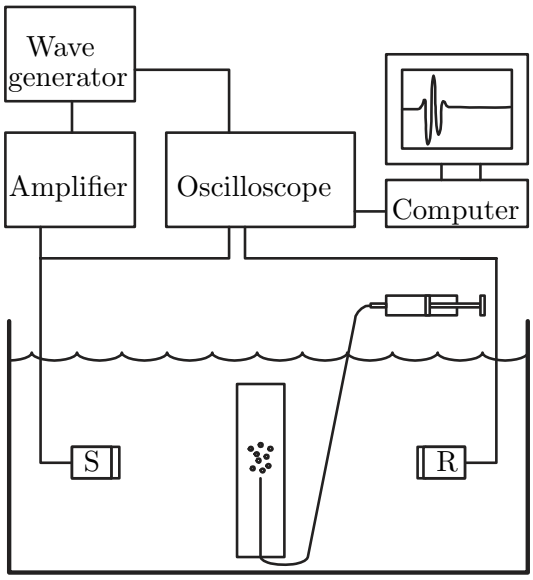

Figure 6.4: Ultrasound Tank (UST) acquisition set-up. Source and receiver are denoted by S and R, respectively. The partially saturated rock sample applies to the measurements in chapter 7.

facing each other. The distance between the transducer faces can be set within 0.1 mm accuracy.

A waveform generator (HP Agilent 33220A) generates a single 1 MHz sine wavelet burst with a peak-peak amplitude of 100 mV, which is directly fed to the US emitter. The period between two successive bursts is 10 ms, i.e. the repetition rate is 100 shots/s. A running average over 1024 bursts is captured by a digital oscilloscope (Yokogawa DL 9140) in a time window of 100 μs with a sampling interval of 2 ns. The Nyquist frequency of 250 MHz prevents aliasing within the considered bandwidth 0.5 to 1.5 MHz. The oscilloscope communicates through an USB cable with a computer, where a Labview program coordinates the triggering and saves the binary data. Each averaged trace is stored in a separate file. During the course of the experiment the variation in fluid temperature is registered by a thermocouple (Thermo Electric, The Netherlands, model IDC-420042).

Figure 6.5 shows the recorded snapshots for four different transducer distances. The duration of the experiment is less than one hour and is performed at a temperature of 17.3 $\pm$ 0.1 °C and at ambient pressure. The arrival time of the first pulse increases with increasing source-receiver distance. As expected, its amplitude decreases due to geometric spreading. The arrival time of the maximum pulse

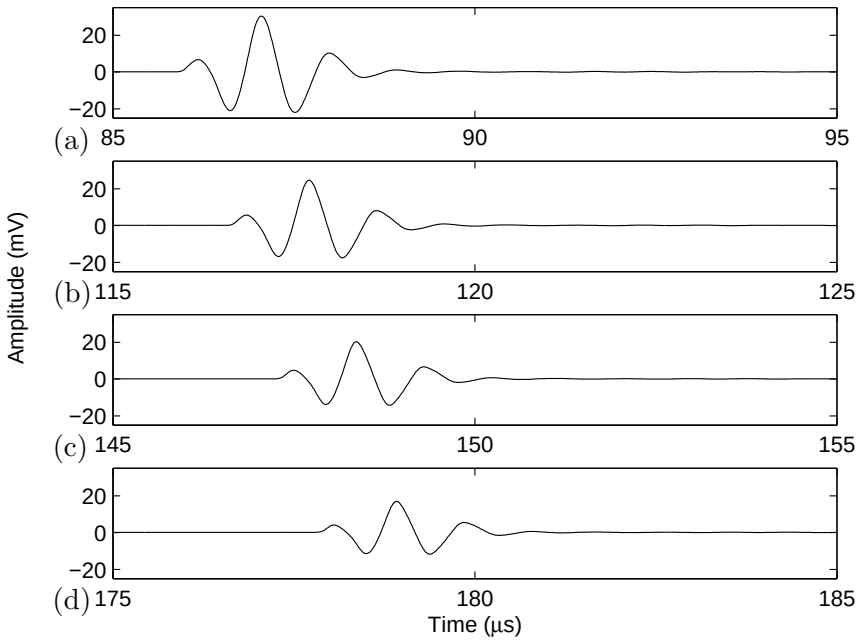

Figure 6.5: Time signals of an acoustic experiment at 1 MHz in a silicone oil liquid using four different source-receiver distances: (a) $d_0 = 85$ mm, (b) $d_1 = 115$ mm, (c) $d_2 = 145$ mm, (d) $d_3 = 175$ mm.

amplitude is automatically captured for each trace. Using the six combinations in source-receiver distance, this gives an average velocity of 979.5 ± 0.9 m/s in the silicone oil.

Another method to determine the velocity is by Spectral Ratio Data Analysis (SRDA, Toksöz et al., 1979). The Fourier transform of a zero-padded discretized time series is denoted $R(\omega)$. With a time harmonic dependence $e^{i\omega t}$ implicitly understood, the reference signal $R_0(\omega)$ received at distance d_0 from the source, is expressed in the frequency domain in terms of the source signal $S(\omega)$ as a unidirectional planar wave

$$R_0(\omega) = S(\omega) \exp(-ik_{\mathrm{f}} d_0), \tag{6.12}$$

where k_{f} is the wavenumber in oil. We consider the silicone oil non-attenuative and non-dispersive. A signal emitted by the same source after propagating over distance d_n then is

$$R_n(\omega) = S(\omega) \exp(-ik_{\mathrm{f}} d_n). \tag{6.13}$$

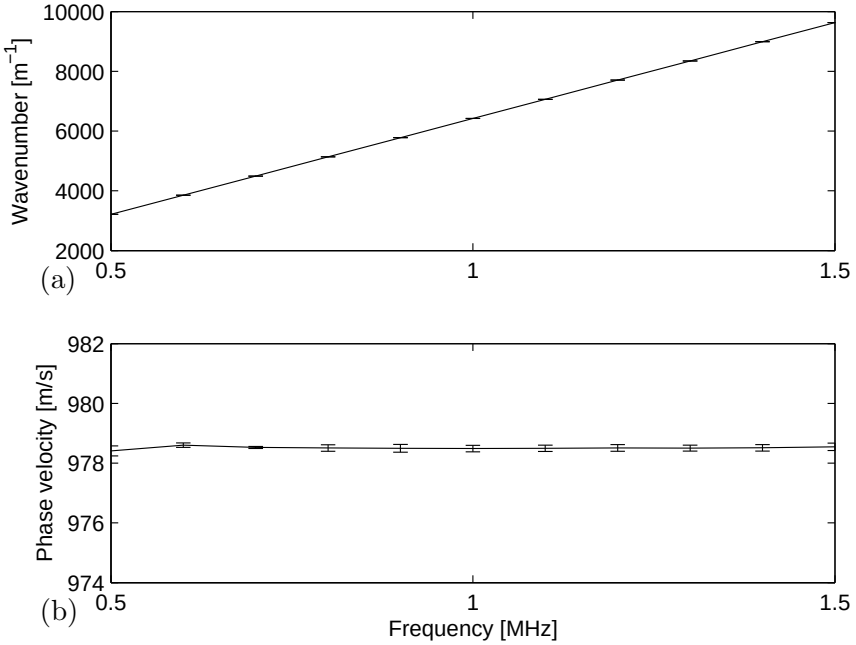

Figure 6.6: Averaged acoustic bulk properties of an acoustic experiment in a non-attenuating silicone oil liquid using four different source-receiver distances. (a) Wavenumber. (b) Phase velocity. Errors are attributable to the accuracy in the distance.

Dividing equation (6.13) by equation (6.12) yields

$$\frac{R_n(\omega)}{R_0(\omega)} = \exp\left(-ik_{\mathrm{f}}(d_n - d_0)\right). \tag{6.14}$$

Its phase gives the wavenumber k_{f}:

$$k_{\mathrm{f}}(\omega) = -\frac{1}{d_n - d_0}\mathrm{phase}\left(\frac{R_n(\omega)}{R_0(\omega)}\right). \tag{6.15}$$

Unwrapping removes the ambiguity in phase angles. The wavenumber and the phase velocity $c_{\mathrm{f}} = \omega/k_{\mathrm{f}}$ in oil, averaged over four different source-receiver distances are given in figure 6.6. The average wavenumber increases linearly with frequency from 0 to 1.5 MHz. The inaccuracies are small. Hence, the average phase velocity is constant over the frequency band that we consider. Its average value is 978.5 $\pm$ 0.1 m/s, which is in excellent agreement with the velocity obtained from the first arrival times.

6.4 Saturated rock measurements

The same samples were used as in chapter 5. The molasses was rinsed from the sample faces with water. Next, all samples were dried in the oven again and evacuated in a vacuum chamber. The vacuum chamber also holds a container filled with silicone oil. The chamber is depressurized for several hours using a vacuum pump (Welch, model 8907A). When the pressure, measured with a vacuum meter (Terranova, model 924A) is below 0.1 Torr (13 Pa), the sample is carefully immersed in the oil. Finally, the chamber is disconnected from the pump and equilibrated to atmospheric pressure.

We measure the velocity and quality factor (inverse attenuation) of the set of 45 natural and artificial rocks that are now saturated with oil. We use two different ultrasonic acquisition methods namely the conventional contact ultrasonics (CCU) of chapter 5, and non-contact ultrasonics (NCU). The former method uses the set-up described in section 5.5, where two ultrasound transducers gently clamp the sample from above and below. The difference is that now the samples are oil-saturated, whereas they were dry in section 5.5. Because of the relatively high viscosity of the oil, we assume that the samples remain fully saturated while undergoing CCU. Indeed, we noticed only minimal oil leakage from the samples. Note that no sealing or sleeving of the samples was applied. CCU measurements of the compressional and shear wave speeds are given in table 6.1 and 6.2, respectively. These data are based on first arrival detection.

In table 6.1, also NCU data are given. These are acquired in the oil-filled Ultrasound Tank (UST) depicted in figure 6.4. The transducer faces are 90.3 mm apart. We use the same electronics, burst rate, and sampling frequency as in section 6.3. The only difference is that the source signal is now pre-amplified with a broadband power amplifier (E&I 240L) at 50 dB input gain. The samples are positioned in a sample holder in between both transducers (see figure 6.4). Similar transmission set-ups have been used by, among others, Plona (1980) and Kelder and Smeulders (1997).

The experimental procedure is a two-step process: first, the acoustic properties are measured on a sample of length ℓ_0. Then, the sample is cut into two pieces of length ℓ_1 and ℓ_2, whose acoustic properties are measured as well. The lengths ℓ_1 and ℓ_2 are approximately 2/3 and 1/3 of the original length ℓ_0. The exact lengths are measured with a digital caliper.

Sample ID	Compressional wave velocity [m/s]			
	CCU-FADA	NCU-FADA	NCU-SRDA	Biot
CHK03	3414 ± 120	3461 ± 44	3461 ± 36	4393 ± 237
CHK04	3435 ± 121	3447 ± 223	3322 ± 277	4370 ± 233
SSA04	3033 ± 94	2995 ± 126	2968 ± 130	2981 ± 100
SSA11	3053 ± 125	3014 ± 294	2999 ± 272	2939 ± 130
SSB04	2908 ± 88	2806 ± 40	2746 ± 48	3435 ± 150
SSB07	3308 ± 112	3248 ± 119	3275 ± 122	3819 ± 187
SSB08	3012 ± 93	2921 ± 35	2865 ± 99	3415 ± 146
SSB09	3252 ± 108	3178 ± 37	3119 ± 31	3781 ± 180
SSC05	3484 ± 124	3529 ± 20	3505 ± 2	3396 ± 112
SSC06	3432 ± 120	3243 ± 72	3271 ± 63	3318 ± 106
SSF02	2618 ± 71	2670 ± 115	2678 ± 107	2507 ± 64
SSF03	2717 ± 77	2550 ± 6	2507 ± 121	2604 ± 70
SSF04	2578 ± 85	2490 ± 102	2507 ± 44	2545 ± 84
SSG01	2865 ± 84	2809 ± 28	2755 ± 67	2876 ± 93
SSG02	3216 ± 105	3224 ± 349	3177 ± 162	3039 ± 102
YBE03	3295 ± 140	3093 ± 150	3110 ± 119	3287 ± 173
VIF01	2324 ± 57	2190 ± 124	2174 ± 191	2292 ± 70
VIF02	2356 ± 58	2301 ± 48	2196 ± 130	2339 ± 75
VIC05	1851 ± 37	1621 ± 364	1688 ± 327	1708 ± 27
VIC06	1702 ± 31	1528 ± 352	1648 ± 442	1737 ± 28
QUE09	3003 ± 94	3088 ± 149	3121 ± 100	2934 ± 96
QUE10	2989 ± 93	2911 ± 199	2964 ± 232	2852 ± 91
B1P13	3094 ± 100	3178 ± 115	3191 ± 127	3114 ± 107
B1P14	3049 ± 97	3039 ± 181	3070 ± 149	2979 ± 97
CAS16	2773 ± 80	2615 ± 18	2665 ± 56	2844 ± 94
CAS17	2941 ± 89	2878 ± 8	2888 ± 10	2860 ± 95
B1N20	3053 ± 97	2996 ± 374	2897 ± 291	2952 ± 98
B1N21	3001 ± 94	3126 ± 19	3173 ± 36	2957 ± 97
COL23	3384 ± 119	3337 ± 151	3347 ± 125	3282 ± 105
COL25	3581 ± 133	3591 ± 162	3587 ± 133	3550 ± 132
BEN27	3588 ± 133	3466 ± 244	3612 ± 74	3489 ± 154
BEN28	3585 ± 133	3408 ± 173	3415 ± 146	3486 ± 154
B2P30	3269 ± 111	3204 ± 38	3243 ± 41	3198 ± 114
B2N32	3264 ± 111	3293 ± 136	3321 ± 147	3156 ± 111
B2N33	3208 ± 107	3232 ± 159	3248 ± 154	3107 ± 106

(continues)

(continued)

Sample ID	Compressional wave velocity [m/s]			
	CCU-FADA	NCU-FADA	NCU-SRDA	Biot
FEL36	3330 ± 115	3228 ± 36	3212 ± 36	3273 ± 128
FEL37	3271 ± 111	3189 ± 153	3180 ± 136	3265 ± 123
NIV44	3143 ± 103	3237 ± 93	3227 ± 76	2908 ± 115
NIV45	2949 ± 91	3012 ± 249	3003 ± 214	2719 ± 104
UNK50	3944 ± 161	3852 ± 88	3873 ± 81	3793 ± 176
UNK51	3811 ± 149	3784 ± 126	3795 ± 98	3697 ± 165
NN356	3442 ± 123	3499 ± 40	3500 ± 31	3541 ± 149
NN458	4334 ± 193	4168 ± 268	4171 ± 221	4382 ± 250
GL160	2393 ± 61	2115 ± 29	2195 ± 60	2737 ± 91
GL261	2461 ± 73	2382 ± 56	2426 ± 31	2866 ± 116

Table 6.1: Compressional wave velocities of natural and artificial rocks fully saturated with silicone oil. The CCU velocity is acquired using the benchtop set-up (Conventional Contact Ultrasonics). The NCU velocities are acquired in the ultrasound tank (Non-Contact Ultrasonics). The FADA velocities are obtained from First Arrival Data Analysis. The SRDA velocity is from Spectral Ratio Data Analysis at 1 MHz. The error in the CCU velocity arises from the accuracy in arrival time. The error in the NCU velocities arises from averaging over three different sample lengths. Biot velocity denotes the high-frequency limit of the Biot (1956a,b) theory. The error in the predicted Biot velocity is attributed to the uncertainty in the elastic moduli, K_m and μ, from table 5.1.

As we have now three sample lengths available, it is straightforward to compute the NCU compressional wave velocity c_P from the first arrival times:

$$\frac{1}{c_\mathrm{P}} = \frac{1}{c_\mathrm{f}} - \frac{\Delta t}{\Delta \ell}, \tag{6.16}$$

where Δt is the time lag between first arrivals of two samples having length difference $\Delta \ell$. As we know how far the transducer faces are apart, we can independently determine c_f. It was found to be 979.8 ± 0.1 m/s at 20.4 ± 0.1 °C, which is in agreement with previous first arrival time results, considering different temperatures.

Sample ID	Shear wave velocity [m/s]		Quality factor [-]	
	CCU-FADA	Biot	NCU-SRDA	Biot
CHK03	2134 ± 50	2432 ± 64	41 ± 15	2969 ± 151
CHK04	2172 ± 51	2415 ± 63	32 ± 22	3012 ± 153
SSA04	1915 ± 39	1873 ± 37	7.1 ± 0.7	705 ± 92
SSA11	1888 ± 51	1902 ± 51	5.2 ± 0.3	638 ± 116
SSB04	2068 ± 47	2072 ± 47	9 ± 1	381 ± 24
SSB07	2299 ± 57	2318 ± 58	9 ± 2	300 ± 18
SSB08	2069 ± 46	2061 ± 46	8 ± 2	339 ± 22
SSB09	2219 ± 53	2234 ± 54	13 ± 7	300 ± 18
SSC05	1980 ± 43	1882 ± 38	5.7 ± 0.2	10450 ± 1928
SSC06	1987 ± 43	1887 ± 38	4.8 ± 0.1	9137 ± 1752
SSF02	1484 ± 24	1416 ± 22	5 ± 2	911 ± 104
SSF03	1537 ± 26	1454 ± 23	5.2 ± 0.7	802 ± 85
SSF04	1585 ± 34	1493 ± 30	5 ± 2	822 ± 119
SSG01	1751 ± 33	1736 ± 32	7 ± 2	805 ± 86
SSG02	1807 ± 35	1778 ± 34	17 ± 18	333 ± 33
YBE03	2118 ± 62	2115 ± 70	8.2 ± 0.1	570 ± 112
VIF01	1464 ± 23	1406 ± 28	11 ± 1	414 ± 44
VIF02	1489 ± 24	1441 ± 30	11 ± 2	385 ± 39
VIC05	894 ± 9	969 ± 11	5 ± 3	1284 ± 215
VIC06	897 ± 9	984 ± 11	5 ± 4	1346 ± 217
QUE09	1808 ± 36	1765 ± 34	5.5 ± 0.7	1305 ± 156
QUE10	1782 ± 35	1739 ± 33	4.2 ± 0.2	1421 ± 181
B1P13	1875 ± 39	1817 ± 36	5.9 ± 0.1	651 ± 76
B1P14	1789 ± 35	1767 ± 34	6.5 ± 0.9	688 ± 87
CAS16	1858 ± 38	1804 ± 40	7 ± 2	1956 ± 405
CAS17	1882 ± 38	1808 ± 40	7.1 ± 0.5	1892 ± 349
B1N20	1862 ± 38	1822 ± 36	7 ± 2	560 ± 75
B1N21	1842 ± 37	1822 ± 36	6.7 ± 0.9	669 ± 94
COL23	1939 ± 41	1881 ± 38	7.9 ± 0.3	17862 ± 3668
COL25	2191 ± 53	2150 ± 49	9.5 ± 0.1	9840 ± 1966
BEN27	2195 ± 53	2194 ± 52	10 ± 1	451 ± 39
BEN28	2143 ± 50	2192 ± 52	10.7 ± 0.3	449 ± 39
B2P30	1961 ± 42	1883 ± 38	6.7 ± 0.4	470 ± 55
B2N32	1958 ± 42	1881 ± 38	6 ± 1	411 ± 52
B2N33	1938 ± 41	1823 ± 36	5.9 ± 0.1	423 ± 52

(continues)

(continued)

Sample ID	Shear wave velocity [m/s]		Quality factor [-]	
	CCU-FADA	Biot	NCU-SRDA	Biot
FEL36	1984 ± 43	2001 ± 44	7.0 ± 0.5	494 ± 49
FEL37	1984 ± 43	1896 ± 39	7.5 ± 0.2	536 ± 51
NIV44	1952 ± 42	1890 ± 44	32 ± 14	550 ± 53
NIV45	1821 ± 36	1743 ± 41	14 ± 2	560 ± 60
UNK50	2407 ± 64	2410 ± 63	9.4 ± 0.5	53451 ± 7089
UNK51	2394 ± 63	2396 ± 61	9.4 ± 0.5	26960 ± 3800
NN356	2186 ± 53	2233 ± 54	10.2 ± 0.3	3547 ± 468
NN458	2824 ± 88	2838 ± 86	19 ± 3	683 ± 81
GL160	1589 ± 28	1606 ± 29	8 ± 1	577 ± 42
GL261	1584 ± 32	1649 ± 35	11 ± 3	448 ± 32

Table 6.2: Shear wave velocities and quality factors of natural and artificial rocks fully saturated with silicone oil. The notation is as in table 6.1. The quality factors are measured (NCU-SRDA) and calculated (Biot) at 1 MHz.

As an example, figure 6.7 gives the recorded time signals from a Castlegate sandstone (CAS17) for three different sample lengths that are used to determine the first arrival speed. A CCU-NCU cross plot of the first arrival speeds of all samples is given in figure 6.8. We find excellent agreement.

An important advantage of the NCU measuring method over the CCU method is that the former allows Spectral Ratio Data Analysis (SRDA) as opposed to First Arrival Data Analysis (FADA), that we have used so far. SRDA not only allows the determination of the wave speeds, but also of the attenuation properties. Moreover, both the speed and attenuation are obtained as a function of frequency. SRDA proceeds as follows. Using a sample with the initial length ℓ_0, the received signal $R_0(\omega)$ at normal incidence is dependent on the source-receiver distance d, the source signal $S(\omega)$ and the transmission coefficients $T_{\text{in}}(\omega)$ and $T_{\text{out}}(\omega)$ at the oil-rock and rock-oil interface

$$R_0(\omega) = S(\omega) T_{\text{in}} \exp(-ik\ell_0) T_{\text{out}} \exp(-ik_{\text{f}}(d - \ell_0)), \tag{6.17}$$

where $k = k_r + ik_i$ is the wavenumber of the sample having real and imaginary parts k_r and k_i, respectively. We repeat the measurements on the identical sample of length ℓ_n. The received signal then is

$$R_n(\omega) = S(\omega) T_{\text{in}} \exp(-ik\ell_n) T_{\text{out}} \exp(-ik_{\text{f}}(d - \ell_n)). \tag{6.18}$$

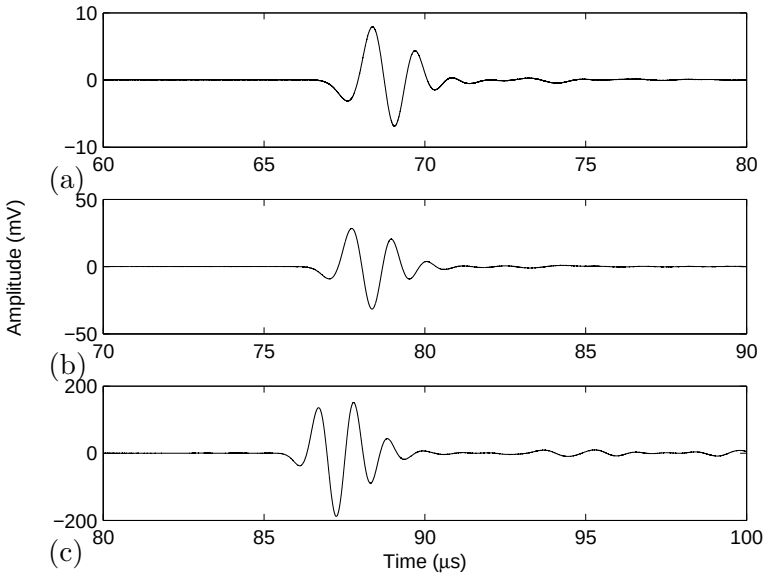

Figure 6.7: Time signals acquired from an acoustic experiment at 1 MHz on a fully saturated Castlegate rock in a silicone oil liquid using three different sample thicknesses: (a) 37.7 mm, (b) 23.9 mm, (c) 10.6 mm. Note the difference in vertical scale.

The ratio of equation (6.18) and (6.17) separates the bulk characteristics from the source term, the source-receiver distance, and transmissions coefficients:

$$\frac{R_n(\omega)}{R_0(\omega)} = \exp(k_i(\ell_0 - \ell_n)) \exp(-i(k_\mathrm{f} - k_r)(\ell_0 - \ell_n)), \tag{6.19}$$

where we considered $k_\mathrm{f} = \omega/c_\mathrm{f}$ to be the real-valued wavenumber in oil. The real and imaginary parts of the sample wavenumbers are now given by

$$k_i(\omega) = \frac{1}{\ell_0 - \ell_n} \ln \left| \frac{R_n(\omega)}{R_0(\omega)} \right|, \tag{6.20}$$

and

$$k_r(\omega) = k_\mathrm{f} - \frac{1}{\ell_0 - \ell_n} \mathrm{phase} \left(\frac{R_n(\omega)}{R_0(\omega)} \right). \tag{6.21}$$

We calculate k_i and k_r using the three possible combinations in sample length. The corresponding measured phase velocities $c_\mathrm{P} = \omega/k_r$ (equation (2.16)) and quality factors $Q = k_r/2k_i$ (cf. equation (2.17)) are shown in figure 6.9 for the

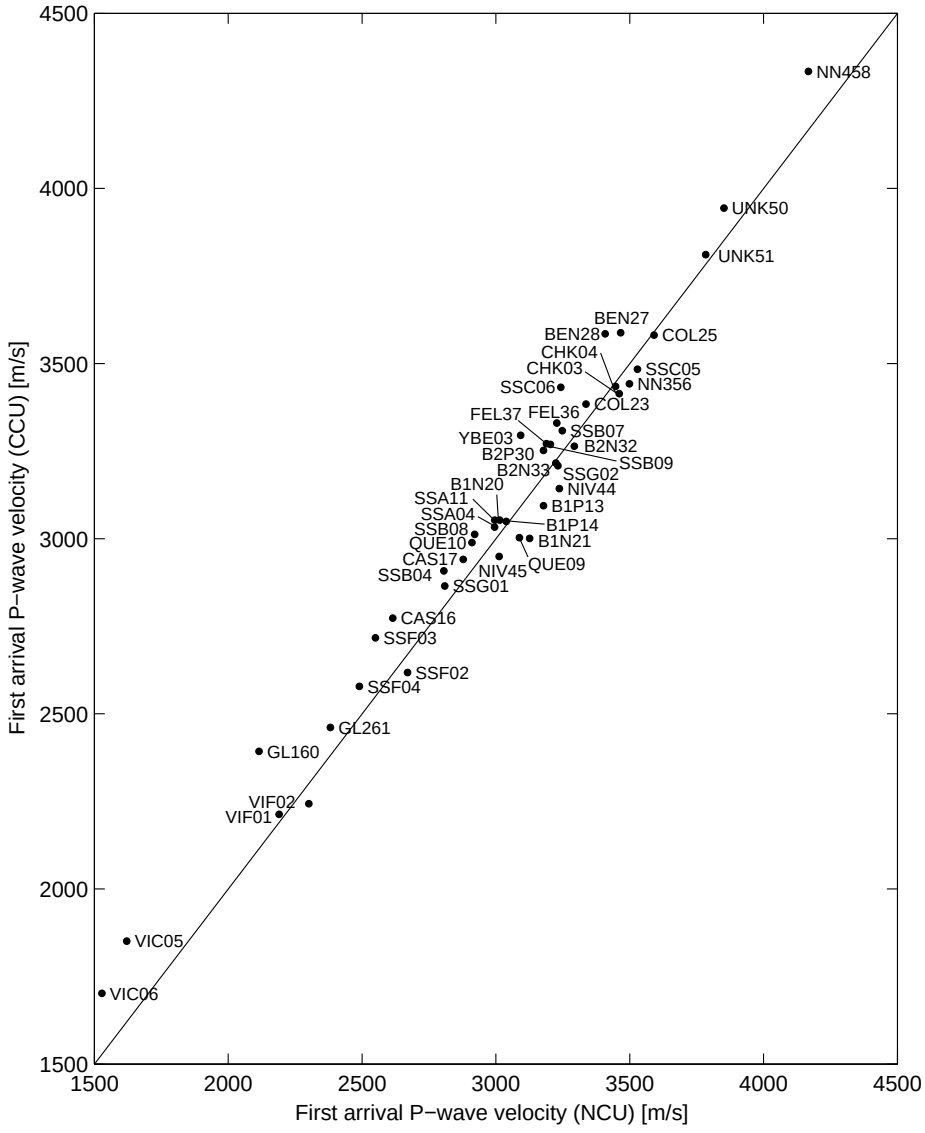

Figure 6.8: Compressional wave velocities acquired with the ultrasonic tank (NCU) versus the velocities obtained from the benchtop set-up (CCU). The velocities are determined by First Arrival Data Analysis (FADA). The velocities and errors are given in table 6.1.

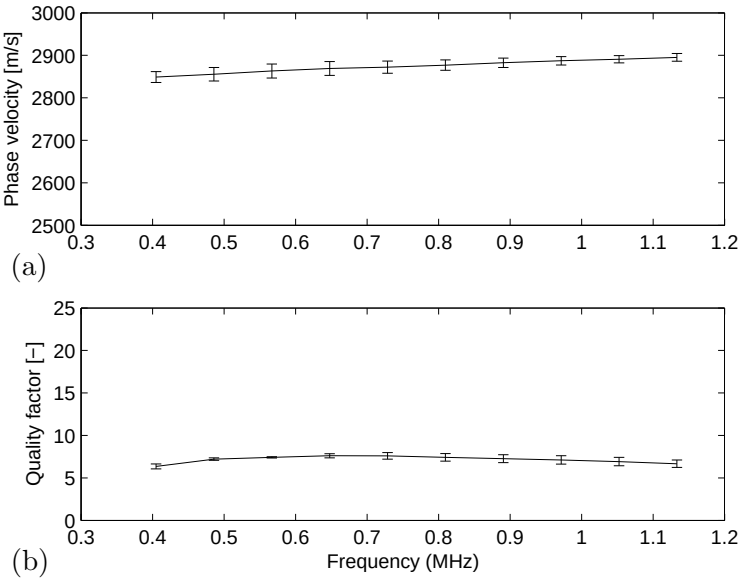

Figure 6.9: Acoustic bulk properties of a fully saturated Castlegate rock in a silicone oil liquid averaged over three different sample thicknesses. The data are acquired in the ultrasound tank with Non-Contact Ultrasound (NCU) using Spectral Ratio Data Analysis (SRDA). (a) Phase velocity. (b) Quality factor.

CAS17 sample. In the range 0.4 - 1.2 MHz, we observe that the measured speed is almost constant at 2888 ± 10 m/s. We also find that $Q = 7.1 \pm 0.5$, being virtually independent of frequency. An overview of all SRDA data is given in tables 6.1 and 6.2 as well. A cross plot of SRDA against FADA speeds is given in figure 6.10. Both data sets are from non-contact measurements in the Ultrasound Tank. Again the agreement is excellent.

We finally compare our experimental data against the Biot theory. The input data for the Biot theory are obtained from independent experiments described in chapter 5. Tortuosity α_∞ is determined from the so-called Humble equation, which is an often used version of Archie's equation for sands:

$$\alpha_\infty = a\phi^{1-m}, \tag{6.22}$$

with parameters $a = 0.62$ and $m = 2.15$ (Schön, 1996; Glover, 2009). We used here that the tortuosity α_∞ is related to the formation factor F: $\alpha_\infty = F(\phi)\phi$ (Bourbié et al., 1987). The formation factor is empirically related to porosity in brine-saturated clean (no shale) reservoir rocks: $F = \phi^{-m}$ (Mavko et al., 2003). We used these empirical values for all samples, except for our chalk samples, where

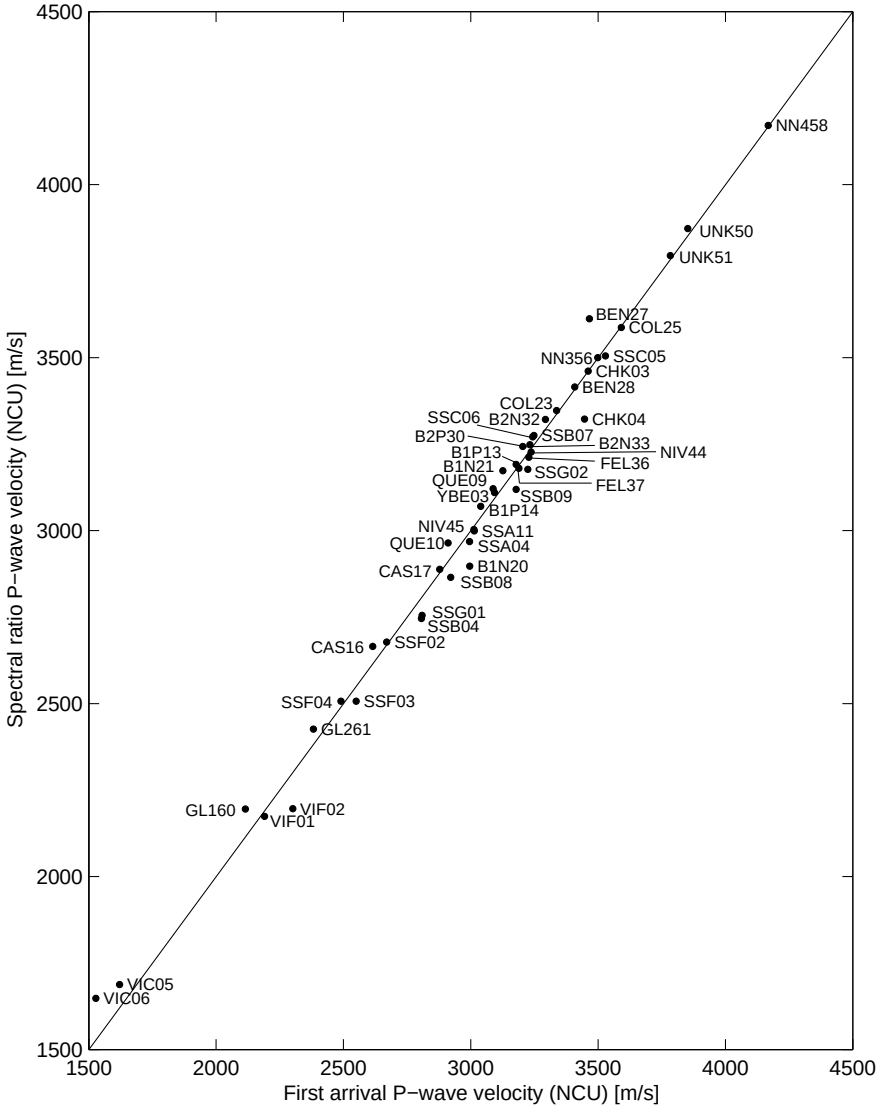

Figure 6.10: Compressional wave velocities measured from First Arrival Data Analysis (FADA) versus the velocities obtained from Spectral Ratio Data Analysis (SRDA). The velocities are acquired in the ultrasound tank with Non-Contact Ultrasound (NCU). The velocities and errors are given in table 6.1.

we use $a = 1$ and $m = 1.7$, which are mean values for chalky limestones (Schön, 1996). Mavko et al. (2003) note that carbonates show a wide range of variation and have m values as high as 5. Our derived tortuosity values are comparable to those reported from electrical resistivity experiments on natural sandstones (Kelder, 1998) and fused glass beads (Jocker, 2005). For the bulk modulus of the solid grains, K_s, we simply assume the common grain bulk moduli of calcite ($K_\mathrm{s} =$ 70 GPa) for the chalk samples and quartz ($K_\mathrm{s} = 37$ GPa) for all other samples (Mavko et al., 2003).

The viscosity of the oil is measured with a standard viscometer (Brookfield Engineering Laboratories, Stoughton, MA). We find $\eta = 6.0 \pm 0.2$ mPa s. The density of the oil is 916 ± 1 kg/m^3, measured with a standard hydrometer (Class L). The Biot predictions are listed in tables 6.1 and 6.2.

A cross plot of CCU compressional wave speeds versus theoretical values is given in figure 6.11, and a cross plot of CCU shear wave speeds versus theory is given in figure 6.12. The agreement is generally very good and within experimental error. For the compressional wave, the glass (GL160 and GL261), chalk (CHK03 and CHK04), and Berea (SSB04, 07, 08, 09) samples show distinct discrepancies between experiment and theory. For the shear wave, this is only the case for the chalk samples.

Two notes have to be made on the quality factor comparison. First, the Biot theory predicts the quality factor to be linearly dependent on frequency. This is not substantiated in our experiments (see figure 6.9 for example). We measure that the quality factor is almost constant in our frequency domain. We therefore chose to tabulate the theoretical attenuation at 1 MHz, which is the center frequency of our transducers. Second, comparing these values with the measured ones in table 6.2, we find that the attenuation is severely underestimated by Biot theory.

A cross plot of the measured and predicted attenuation is shown in figure 6.13. No agreement between measured and predicted attenuation is visible. It is well-known that the Biot theory does not adequately predict the level of attenuation measured in the practice. Similar disagreement between measured and predicted attenuation was reported by Kelder (1998) on a set of water-saturated rocks.

Mesoscale heterogeneities in the frame can be used to explain these discrepancies in terms of a double porosity model (Pride et al., 2004). As the theory is similar for frame and fluid heterogeneities, we chose to study fluid heterogeneities because they can be realized more efficiently under repeatable laboratory conditions.

Another effect that explains high attenuation at ultrasonic frequencies measured under atmospheric conditions is squirt-flow (O'Connell and Budiansky, 1974; Budiansky and O'Connell, 1976). There, the heterogeneity is at the microscopic grain

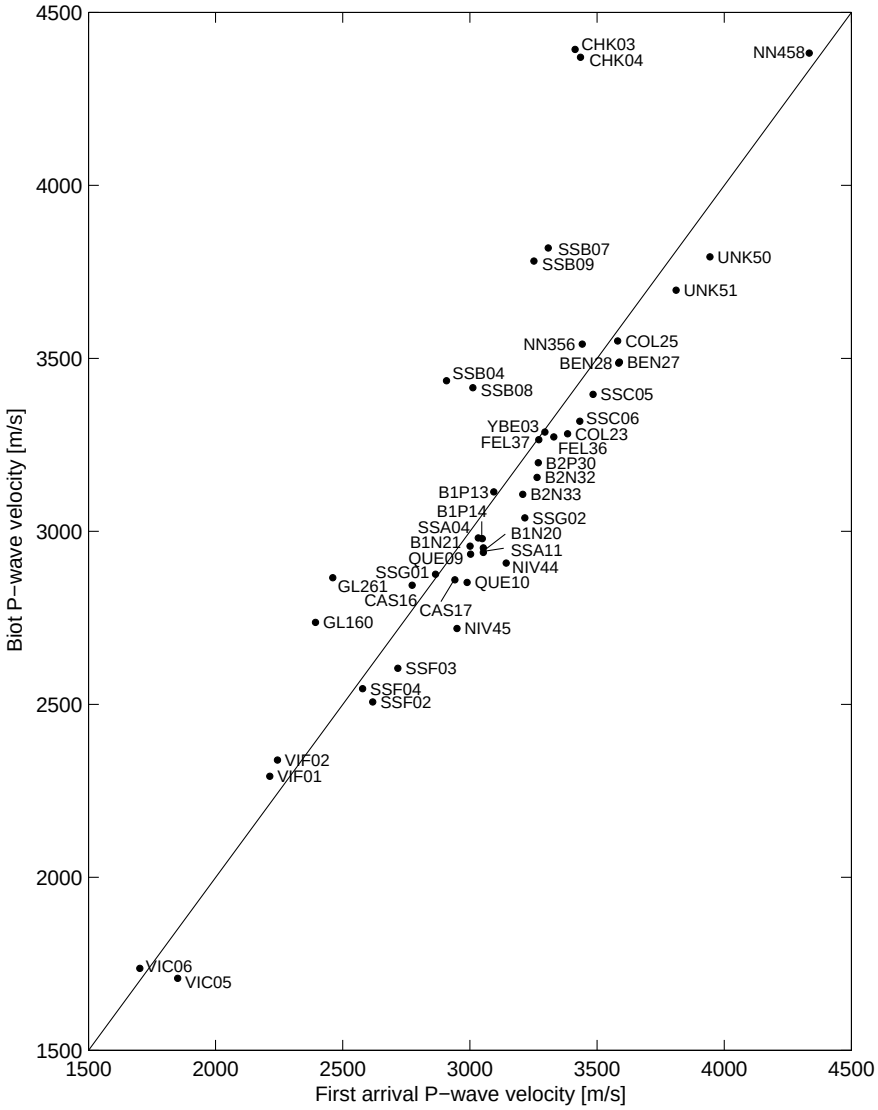

Figure 6.11: Measured compressional wave velocities from First Arrival Data Analysis using the benchtop set-up (CCU-FADA) versus the predicted velocities by the Biot (1956a,b) theory. The samples are fully saturated with silicone oil. The velocities and errors are given in table 6.1.

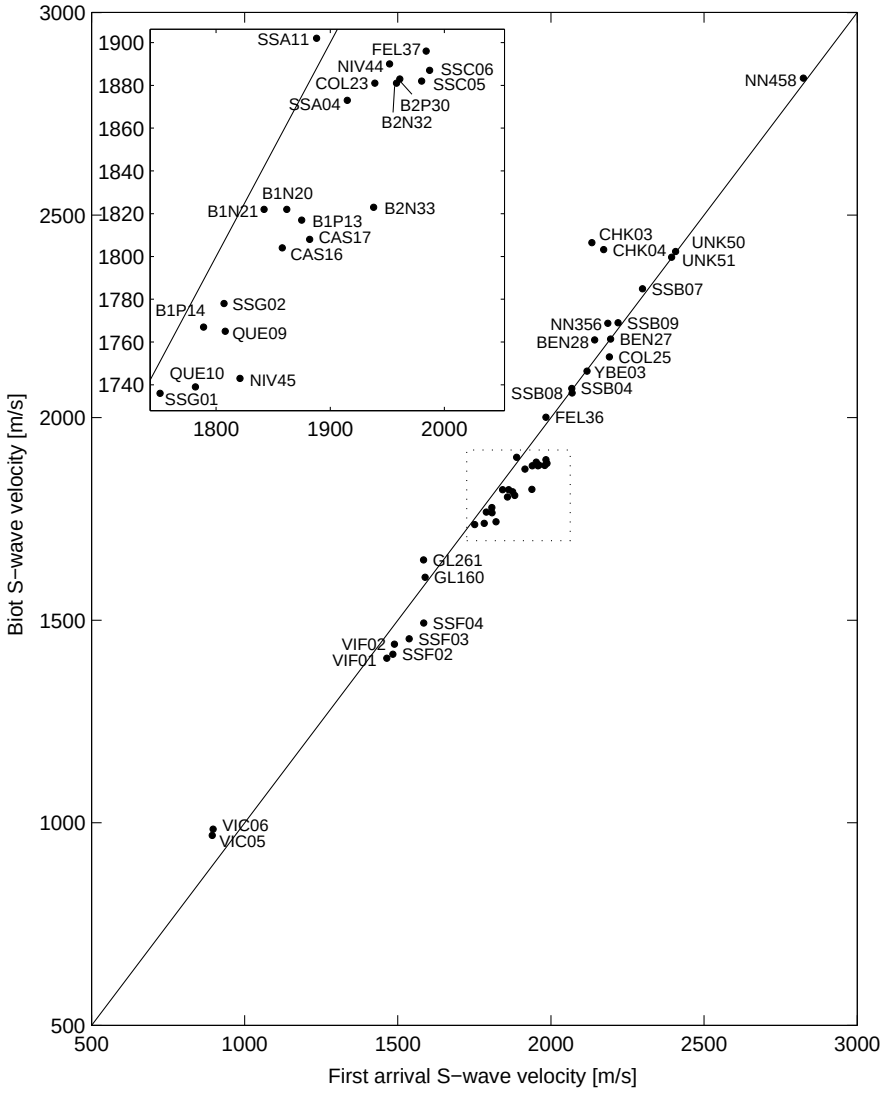

Figure 6.12: Measured shear wave velocities from First Arrival Data Analysis using the benchtop set-up (CCU-FADA) versus the predicted velocities by the Biot (1956a,b) theory. The samples are fully saturated with silicone oil. The velocities and errors are given in table 6.2.

scale, for example as broken grain contacts and/or as microcracks in the grains. When a wave squeezes a rock having such grain-scale damage, the cracks respond with a greater fluid pressure than the main pore space resulting in a flow from crack to pore (Pride et al., 2004). Microscopic heterogeneities are characterized by their crack aspect ratio, i.e., by their width and length. An independent laboratory measurement of this ratio is cumbersome, and therefore this ratio is often used in literature as a fitting parameter (Mavko et al., 2003). However, in this thesis we compare wave experiments with theoretical models based on independently measured input parameters. In the next chapter we consider fluid heterogeneities to be the dominant attenuation mechanism.

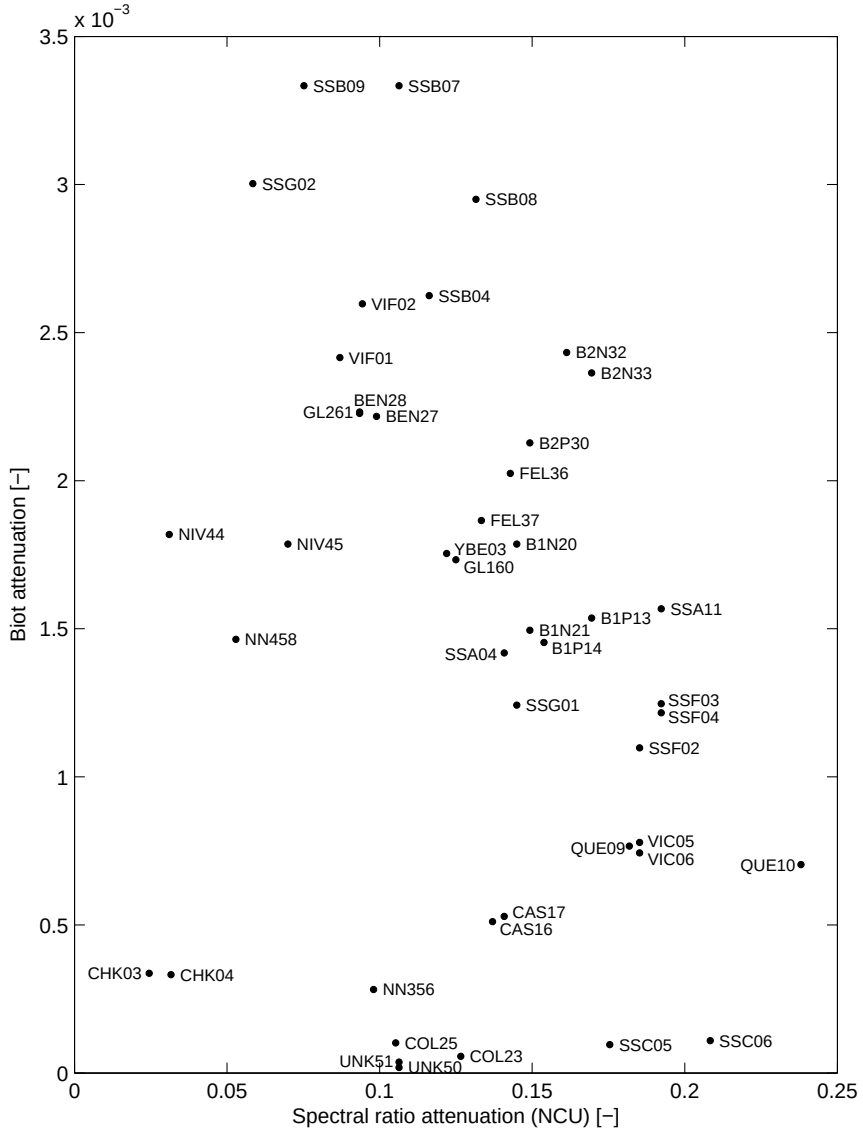

Figure 6.13: Measured compressional attenuation from Spectral Ratio Data Analysis using the ultrasound tank (NCU-SRDA) versus the predicted attenuation by the Biot (1956a,b) theory. The samples are fully saturated with silicone oil. The quality factors and errors are given in table 6.2. Note the difference in scale.

Chapter 7

Laboratory measurements on partially saturated rocks

7.1 Introduction

We experimentally show the dependence of the fast compressional wave velocity and attenuation on partial gas saturation. First, we quantify the size, shape and distribution of injected air volumes in section 7.2. In section 7.3, we measure the phase velocity and quality factor as function of ultrasonic frequency and air volume fraction and compare these with theoretical predictions of chapter 4. In section 7.4, we compare the predicted attenuation from our models (chapter 4) with resonant bar measurements from literature for a partially saturated Massillon sandstone.

7.2 Visualisation experiment on a partially saturated sample

We quantify the size, shape and distribution of injected air volumes in a visualisation experiment. We fill a perspex container with unconsolidated crushed glass. Next, this crushed glass is saturated with light mineral oil (Marcol 82, ExxonMobil). The viscosity of the oil, measured with a viscometer (Brookfield Engineering Laboratories, Stoughton, MA), is 24.2 $\pm$ 0.2 mPa·s at 23.3 °C. The measured density and sound velocity of oil at 23.3 °C are 845 $\pm$ 1 kg/m^3 and 1413 $\pm$ 1 m/s, respectively. The viscosity and density values are in agreement with the specifications provided by the manufacturer. The glass parts are angular and sifted to obtain a grain size between 1.2 - 1.6 mm. The porosity of the sample is very high at 53 $\pm$ 1 % due to the angularity of the crushed glass parts. Marcol 82 oil is

Picture No.	Diameter [mm]	V_{gas} [μl]	V_{inj} [μl]	Remark
7.1b	2.3 ± 0.2	3 ± 1	3	
7.1c	3.5 ± 0.1	12 ± 2	13	
7.1d	3.8 ± 0.1	15 ± 2	33	Breakthrough
7.1e			83	Non-spherical
7.1f			283	Non-spherical

Table 7.1: Dimensions of the injected gas pockets corresponding to the oil-saturated unconsolidated crushed glass sample in figure 7.1. The gas volume V_{gas} is calculated from the measured gas pocket diameter. The injected volume V_{inj} is read from the syringe calibration.

chosen since it has an identical refractive index (n = 1.464-1.470) as the glass, to ensure that the sample is optically transparent.

The needle of a syringe (Microlance 3) is inserted in the saturated glass sample. The outer diameter of the needle is 1.20 mm. We now inject air in the sample through the needle. The injected air volume is directly read from the syringe calibration. The results of this experiment are displayed in figure 7.1. Figure 7.1a is the state prior to air injection. Upon injecting 3 μl of air, we observe a pocket of gas at the tip of the needle, see figure 7.1b. In figure 7.1c, we inject an additional amount of 10 μl air. The gas pockets are approximately spherical in shape with an effective diameter of 2.3 ± 0.2 mm in figure b and 3.5 ± 0.1 mm in figure c. In figure 7.1d, the total amount of injected air is 33 μl. Breakthrough is observed when some air escapes upwards along the needle. The diameter of the gas pocket is now approximately 3.8 ± 0.1 mm. When another additional 50 μl air is injected, the pocket grows but looses its sphericity. In the last picture, an extra amount of 200 μl is injected. The gas pocket shrinks because the injected air and the air in place escape along the needle.

From the measured diameters and porosity, we calculate the gas volumes in place

$$V_{\text{gas}} = \tfrac{4}{3}\pi R^3 \phi. \tag{7.1}$$

The calculated gas volumes and the injected gas volumes are given in table 7.1. The difference between the calculated and injected volume is an estimate for the amount of escaped air. The difference increases with increasing injected air volume.

From the experiment we conclude that injection is an appropriate means to create a gas pocket within a liquid-saturated porous material. As a reasonable approximation, the gas pocket may be assumed spherical. This implies that the injected

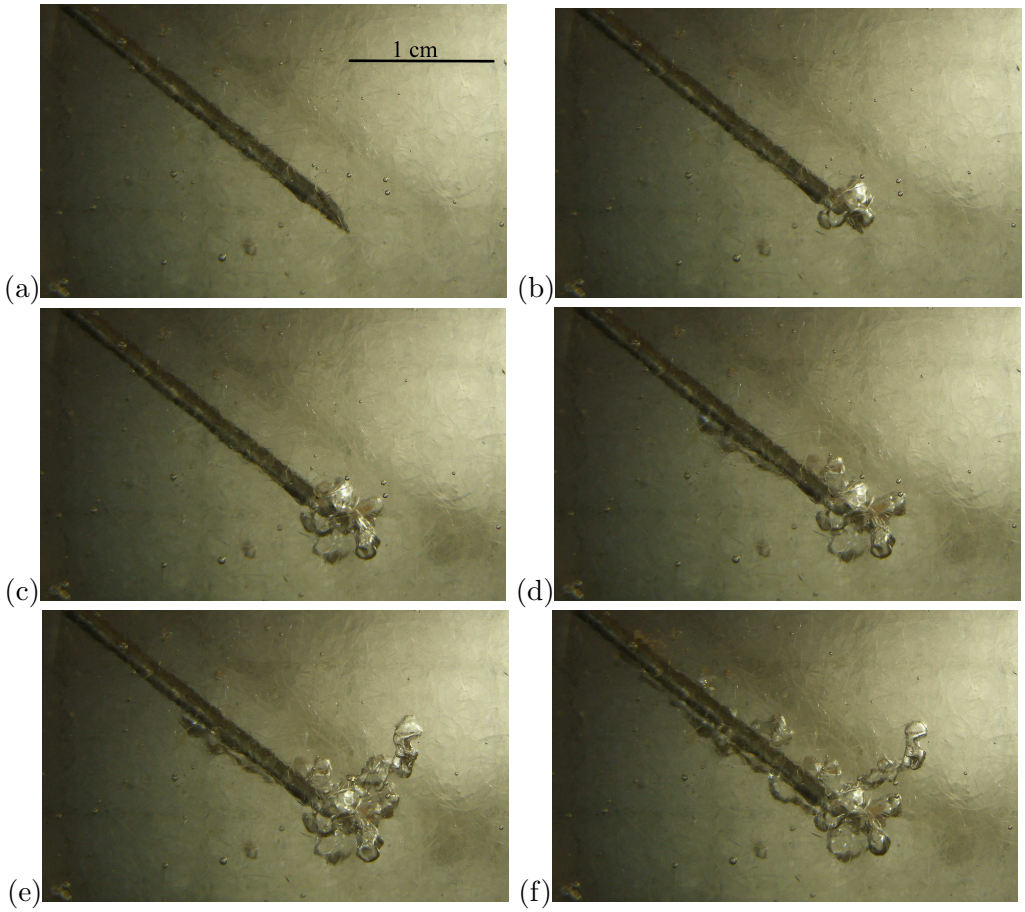

Figure 7.1: Photo gallery on air injection in a fully oil-saturated crushed glass sample. (a) Initial state (full saturation) including a length scale. The gas pocket diameter in (b) is 2.3 ± 0.2 mm, in (c) 3.5 ± 0.1 mm, and in (d) 3.8 ± 0.1 mm. The gas pockets in (e) and (f) are non-spherical.

	Matrix	Grains	Water	Air
Density ρ [kg/m^3]		2618 ± 1	998 ± 1	1.29
Bulk modulus K [Pa]	$1.60 \pm 0.13 \cdot 10^9$	$37.0 \cdot 10^9$	$2.16 \cdot 10^9$	$1.52 \cdot 10^5$
Viscosity η [Pa·s]			$1.0 \cdot 10^{-3}$	$17.1 \cdot 10^{-6}$
Porosity ϕ [-]	0.42			
Permeability k_0 [m^2]	$26.7 \pm 2.7 \cdot 10^{-12}$			
Shear modulus μ [Pa]	$1.58 \pm 0.04 \cdot 10^9$			
Tortuosity α_∞ [-]	1.66 ± 0.01			

Table 7.2: Constituent properties of a partially saturated synthetic sandstone. The matrix and grain properties are from the values of VIC05 and VIC06 as measured in chapter 5. The density and wave speed of water are measured. The viscosity of water and the values for air are from literature (Verbeek et al., 1986).

air volume gives a reasonable estimate for the bubble diameter. Care has to be taken to avoid gas breakthrough.

7.3 Ultrasonic measurements on a partially saturated rock

We apply Spectral Ratio Data Analysis (SRDA) on the signals measured on a partially saturated sample, which is cut from the coarse-grained synthetic sandstone block from which also samples VIC05 and VIC06 are obtained, see chapter 5. Because of the small variability in the properties of samples VIC05 and VIC06, we can assume the synthetic sandstone to be reasonably homogeneous.
Sample preparation and saturation procedure are similar as described in sections 5.2 and 6.4. The initial sample length ℓ_0 is 26.3 ± 0.1 mm; the shorter sample length ℓ_1 is 14.6 ± 0.1 mm; the diameter is 39.0 ± 0.1 mm. A one-millimeter hole is drilled from the cylindrical edge to the sample's center in which a 40 mm syringe (Microlance 3) is glued with a silicone elastomer (CAF 4, Rhodia Group). The outer diameter of the needle is again 1.20 mm.
The experimental set-up is identical to the one described in section 6.4. Here, we use flat one-inch transducers (Panametrics-PZT V301) with a center frequency of 500 kHz. The source-receiver distance d is 158.7 ± 0.1 mm. The saturating fluid is tap water. The velocity in water averaged over four first arrival times is 1471.7 $\pm$ 0.3 m/s at a temperature of 21.0 ± 0.2 °C. This velocity value is in agreement with literature (Del Grosso and Mader, 1972).
The measured time signals acquired on the fully water-saturated synthetic sand-

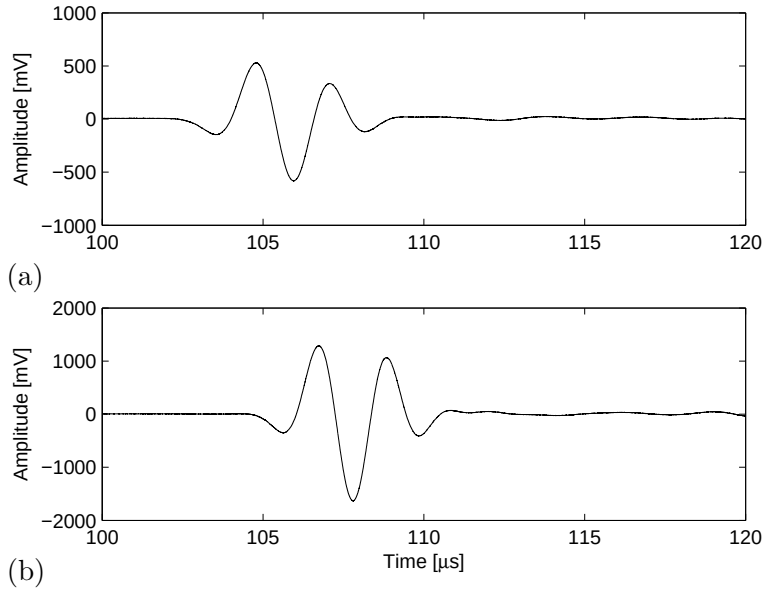

Figure 7.2: Time signals acquired from an acoustic experiment at 500 kHz on a fully saturated sandstone in water using two different sample thicknesses. (a) 26.3 mm and (b) 14.6 mm.

stone over the two different lengths are given in figure 7.2. We measure the arrival times of the signal maxima and minima. This gives an average velocity of 1937 ± 23 m/s.

Denoting the initial sample length ℓ_0 and the shorter length ℓ_1, the real and imaginary parts of the wavenumber for the fully water-saturated sample are computed through SRDA. The corresponding phase velocities and quality factors are shown in figure 7.3. The phase velocity is almost constant over the shown frequency band with a value of 1926 ± 11 m/s, which is in good agreement with the first arrival measurements. Hence, the wavelength at 500 kHz is 3.9 mm in the fully-saturated sample. The quality factor shows to be dependent on frequency with a value of 8.2 ± 0.2 at 500 kHz. The errors reflect the accuracy in sample lengths. Using the dry rock properties of table 7.2, the high-frequency limit of the Biot theory predicts a velocity of 2044 ± 50 m/s, which is slightly higher than the experimental values.

We now carefully inject different amounts of air in the fully water-saturated sandstone sample. In steps, we inject the cumulative gas volumes 0.3 ml, 0.6 ml, 1.0 ml, 2.0 ml, 3.0 ml and 5.0 ml. Breakthrough is not observed at injected volumes of 0.3 ml, 0.6 ml, and 1.0 ml. With a porosity of 42 % for the sandstone, we calculate

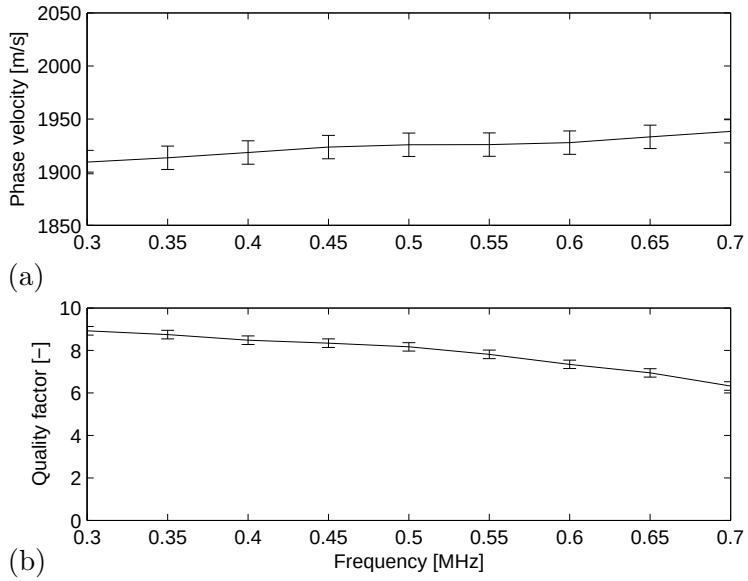

Figure 7.3: Acoustic bulk properties of a fully water-saturated synthetic sandstone in water measured over two different sample thicknesses. (a) Phase velocity. (b) Quality factor. The error bars arise from averaging over the shown frequencies.

the bubble radii from equation (7.1). The calculated air bubble radii in the partially saturated sandstone are given in table 7.3, where also the corresponding gas fractions are summarized. The gas fraction is defined as the gas-to-pore volume ratio. As in the visualisation experiments, we only consider the situations prior to gas breakthrough properly described by spherical pockets.
With the gas pocket in place, acoustic transmission experiments are performed.

V_{inj} [ml]	a [mm]	s_{g} [-]	Remarks
0.3	5.3	0.02	
0.6	6.8	0.04	
1.0	8.2	0.07	
2.0			Breakthrough
3.0			Breakthrough
5.0			Breakthrough

Table 7.3: Radii and gas fractions of the injected air bubbles in the partially water-saturated sandstone. As before, it is not likely that the gas pockets will retain a spherical shape upon breakthrough.

The effect of partial air saturation in the time domain signals is obvious in figure 7.4. We observe that upon air injection the signal amplitude decreases. The most significant decrease occurs from 0.6 to 1.0 ml injected air volume.
We assume that the transmission coefficients at the water-rock and the rock-water interface are not altered by the presence of gas located in the center of the sample. We write for the received signal $R_0'(\omega)$ through a partially saturated sample with length ℓ_0:

$$R_0'(\omega) = S(\omega) T_{\text{in}} e^{-ik'\ell_0} T_{\text{out}} e^{-ik_{\text{f}}(d-\ell_0)}, \tag{7.2}$$

where $k' = k_r' + ik_i'$ is the wavenumber of the partially saturated sample and k_{f} is obviously the wavenumber in water. The source term S, the source-receiver distance d, the transmission coefficients T, the trajectory through the water, and any effect due to the presence of the syringe are identical to the fully saturated case and are eliminated by taking the ratio of the fully and partially saturated signals:

$$\frac{R_0'(\omega)}{R_0(\omega)} = e^{\ell_0(k_i'-k_i)} e^{-i\ell_0(k_r'-k_r)}, \tag{7.3}$$

The wavenumbers in the partially saturated rock are then given by

$$k_i'(\omega) = k_i(\omega) + \frac{1}{\ell_0} \ln \left| \frac{R_0'(\omega)}{R_0(\omega)} \right|, \tag{7.4}$$

and

$$k_r'(\omega) = k_r(\omega) - \frac{1}{\ell_0} \text{phase} \left(\frac{R_0'(\omega)}{R_0(\omega)} \right), \tag{7.5}$$

where k_i and k_r are the fully saturated wavenumbers determined from equations (6.20)-(6.21).
The phase velocities of the partially saturated rock ω/k_r' are shown in figure 7.5. The phase velocities of all partially saturated samples are slightly higher than that of the fully saturated sample. The quality factors $k_r'/2k_i'$ are shown in figure 7.6. The quality factor decreases with increasing gas fraction, as expected from figure 4.12. The quality factor also varies with the frequency. For the first three gas fractions there is a peak attenuation at approximately 500 kHz. For the latter three gas injections, the quality factor gradually increases with increasing frequency. At low frequencies the quality factor is significantly more affected by an increasing air volume than at higher frequencies.
We finally compare in figure 7.7 the experimental results with predictions of the generalized quasi-static patchy model and of the Rayleigh-Plesset-Biot model as

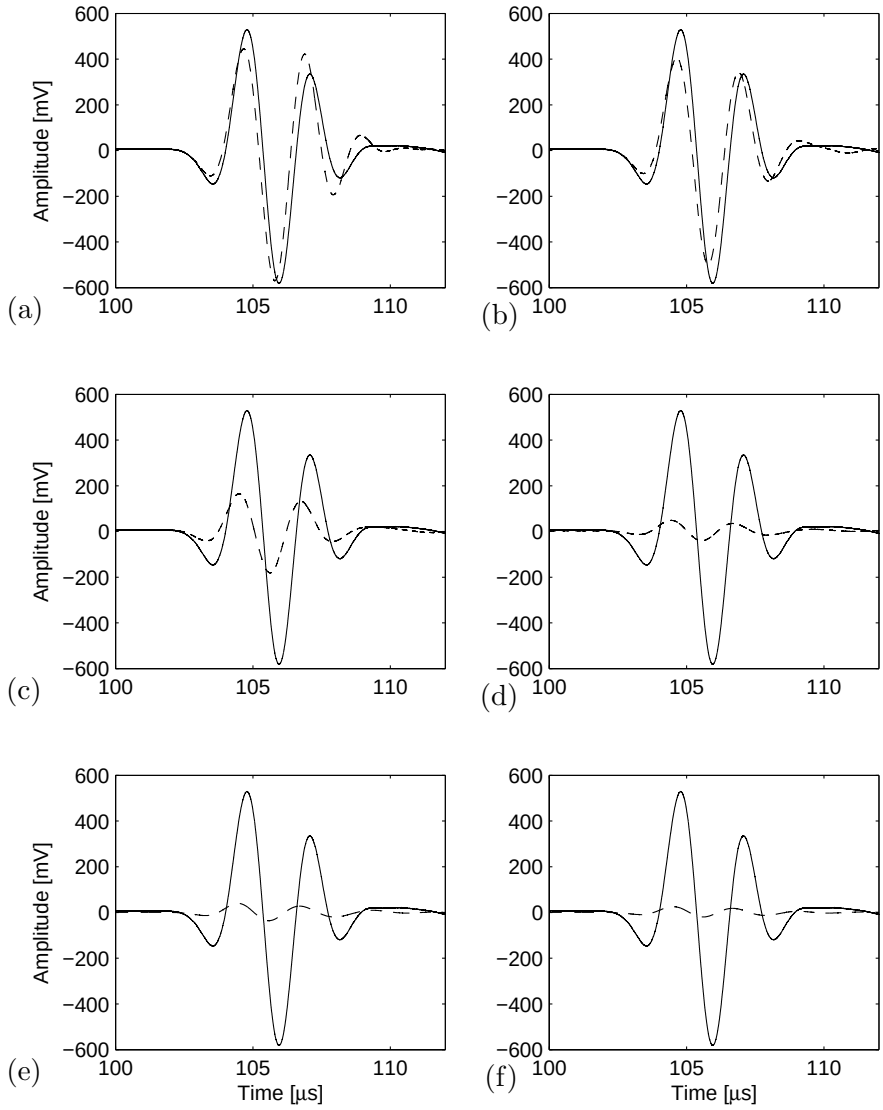

Figure 7.4: Time signals acquired from an acoustic experiment at 500 kHz on a partially saturated sandstone. The solid curve denotes the fully water-saturated measurement. The dashed curves denote the partial gas-saturated state with cumulative injected air volumes of (a) 0.3 ml. (b) 0.6 ml. (c) 1.0 ml. (d) 2.0 ml. (e) 3.0 ml. (f) 5.0 ml.

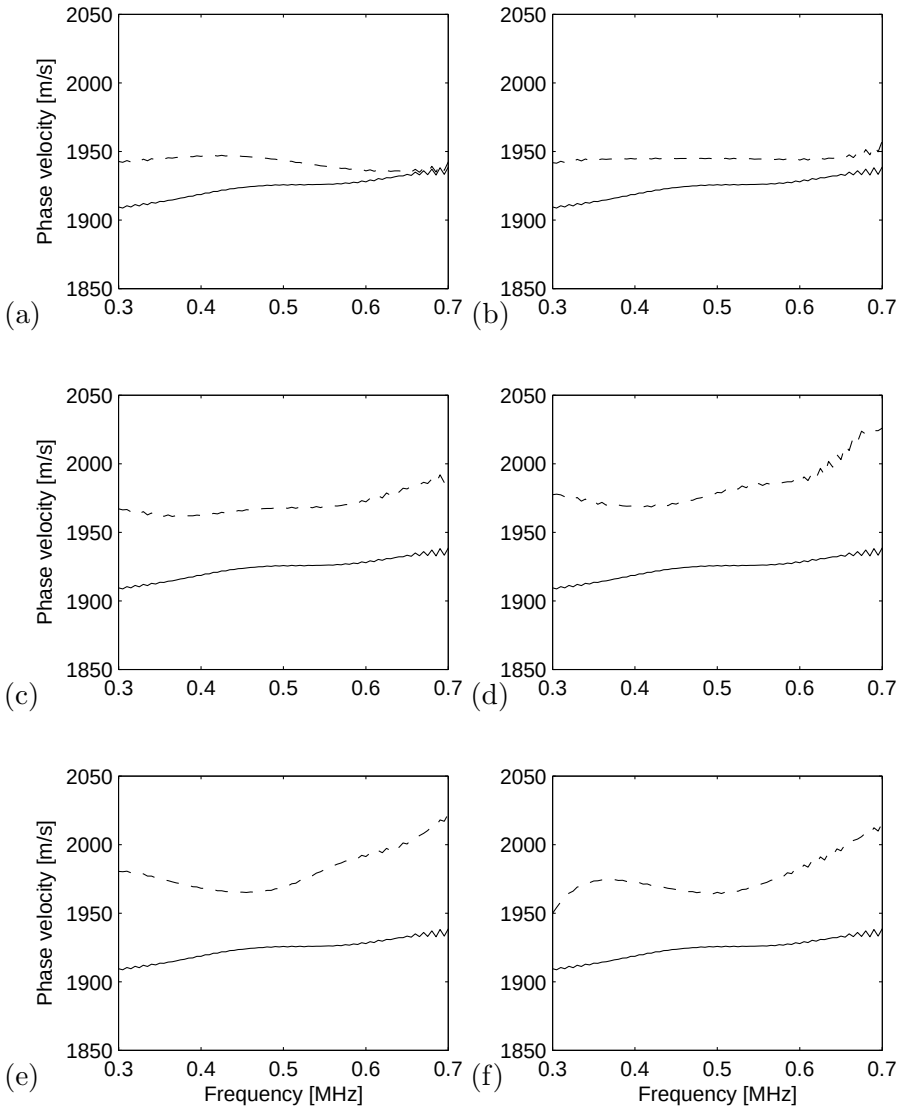

Figure 7.5: Phase velocities calculated from an acoustic experiment on a partially saturated sandstone. The solid curve is the fully saturated measurement. The dashed curves denote the partial gas saturated state with cumulative injected air volumes of (a) 0.3 ml. (b) 0.6 ml. (c) 1.0 ml. (d) 2.0 ml. (e) 3.0 ml. (f) 5.0 ml.

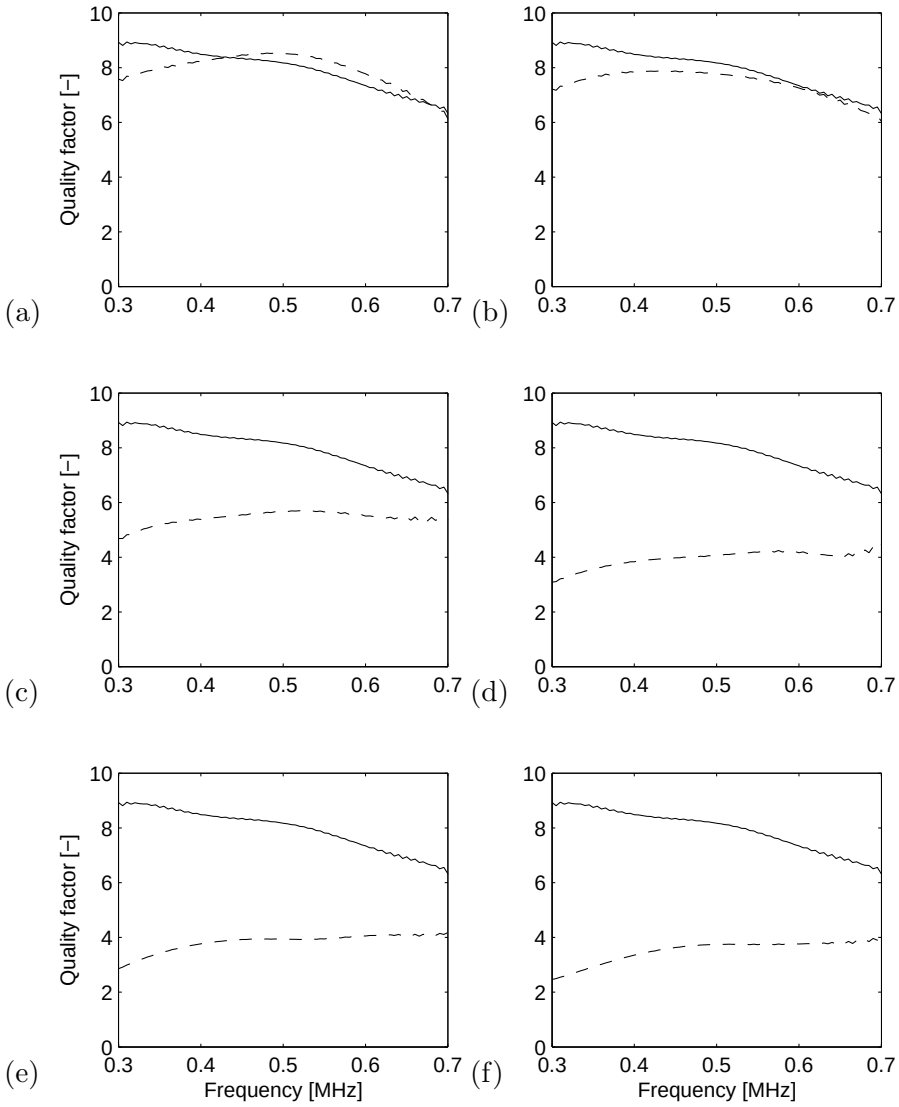

Figure 7.6: Quality factors calculated from an acoustic experiment on a partially saturated sandstone. The solid curve is the fully saturated measurement. The dashed curves denote the partial gas saturated state with cumulative injected air volumes of (a) 0.3 ml. (b) 0.6 ml. (c) 1.0 ml. (d) 2.0 ml. (e) 3.0 ml. (f) 5.0 ml.

	Matrix	Grains	Water	Air
Density ρ [kg/m^3]		2660	997	1.1
Bulk modulus K [Pa]	$9.26 \cdot 10^9$	$35.0 \cdot 10^9$	$2.25 \cdot 10^9$	$0.8 \cdot 10^6$
Viscosity η [Pa·s]			$1.0 \cdot 10^{-3}$	$17.1 \cdot 10^{-6}$
Porosity ϕ [-]	0.23			
Permeability k_0 [m^2]	$737 \cdot 10^{-15}$			
Shear modulus μ [Pa]	$6.14 \cdot 10^9$			

Table 7.4: Constituent properties of a partially saturated Massillon sandstone (Murphy, 1982a,b, 1984; Lumley et al., 1997).

described in sections 4.4 and 4.8, respectively. Only measurements prior to gas breakthrough are shown. It is interesting to note that the generalized model and the Rayleigh-Plesset-Biot model predict opposite velocity trends for increasing saturation, at 500 kHz. The measured data are more or less independent of saturation. Overall, the generalized model gives a slightly better estimate for the velocities. This is definitely true for the quality factor. The predictions of the generalized model are in excellent agreement with the laboratory data, whereas the Rayleigh-Plesset-Biot model predictions are much too high, i.e. this model predicts too low attenuation at ultrasonic frequencies. We note, however, that the wavelength is on the order of the inhomogeneity, so that additional attenuation mechanisms might contribute.

7.4 Literature data on partially saturated rocks

An extensive experimental study on wave attenuation in partially saturated media was published by Murphy (1982a). The Massillon rock samples in Murphy's study are medium-grained high-porosity sandstones. These rock and fluid properties, measured with standard techniques, are given in table 7.4.

The extensional attenuation is measured by Murphy using a resonant bar technique described in detail by Winkler and Nur (1982). A horizontal rock cylinder is made to resonate using electromagnets at both ends while being supported at the center. Signal detection is through two crystal phonograph pickups. The driving voltage is set at resonant frequency. After cutting the voltage, the vibration decay with time is analysed. A frequency range of 0.6 to 6 kHz is obtained using bars of various lengths and by exciting higher harmonics. The water saturation is controlled within an accuracy of 2% by a drying procedure in a humidity chamber.

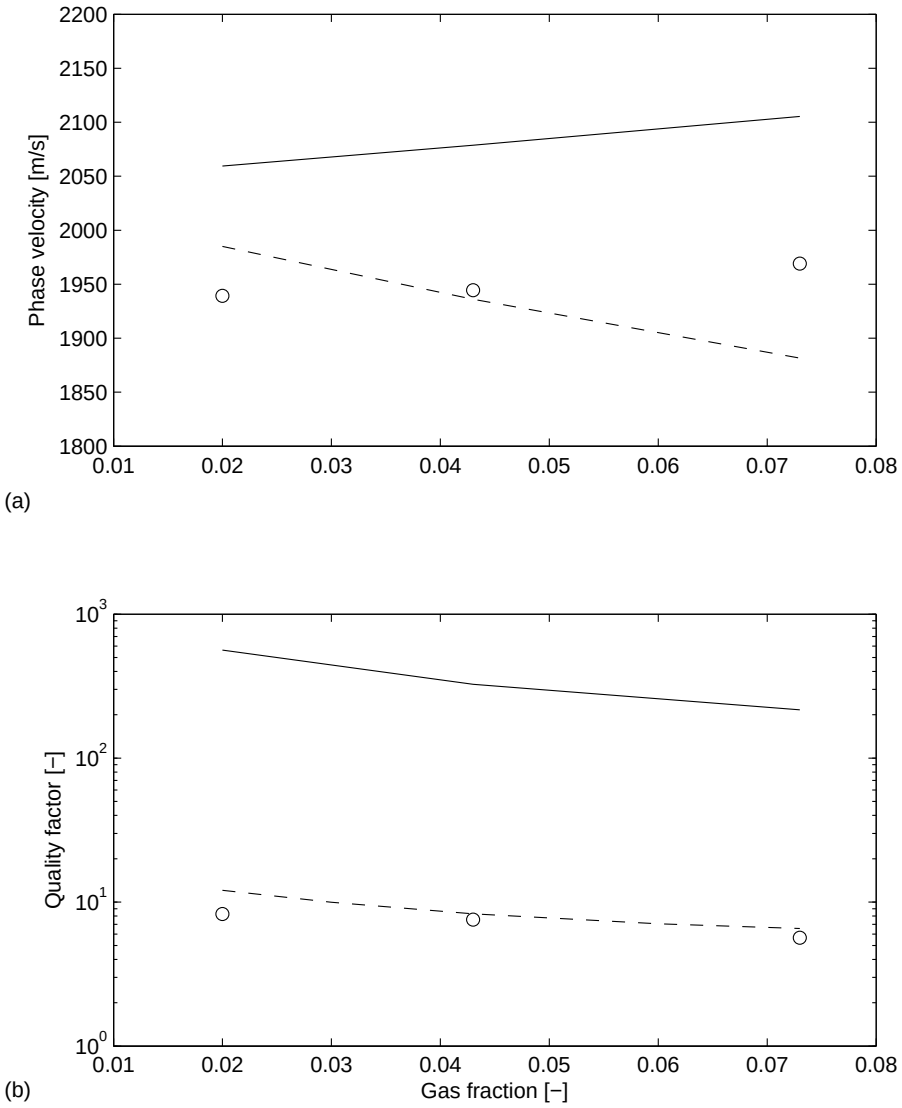

Figure 7.7: Comparison of the theoretical and experimentally measured acoustic bulk properties of a partially saturated sandstone at 500 kHz. (a) Phase velocity. (b) Quality factor. The experimental data (circles) are from figures 7.5 and 7.6 for the different gas fractions of table 7.3. The input values of the Rayleigh-Plesset-Biot partially saturation model (solid curves) and generalized quasi-static patchy model (dashed curves) are given in table 7.2.

Murphy reported signal-to-noise problems with combinations of high loss, higher harmonics, and high frequency (> 4 kHz). He estimated the inaccuracy of the attenuation measurements to be 10%.
Murphy's attenuation results are reproduced for gas fractions of 9% in figure 7.8a and of 25% in figure b and compared with our theoretical models of chapter 4. Unfortunately, in Murphy's paper no gas bubble radius was given. We therefore use this as a fitting parameter. For a gas fraction of 9%, this yields a gas bubble radius of 1.1 cm for the Rayleigh-Plesset-Biot model and 1.6 cm for the generalized patchy model. It appears that the Rayleigh-Plesset-Biot model works better in predicting attenuation at sonic frequencies.
For a gas fraction of 25%, the best fit yields a gas bubble radius of 2.0 cm for the Rayleigh-Plesset-Biot model and 4.2 cm for the generalized model. Here it can be seen that the generalized model is not able to predict the measured attenuation. Changing the gas bubble radius does not affect the amplitude of the attenuation, as also illustrated in figure 4.11, so in this model it is impossible to obtain a better fit. The Rayleigh-Plesset-Biot model, however, is significantly better. Most values are accurately matched, and the deviation at higher frequencies is small.
For the shown cases, it appears that the Rayleigh-Plesset-Biot model is quite accurate in the sonic frequency range, whereas the generalized model is better for much higher frequencies (see section 7.3).

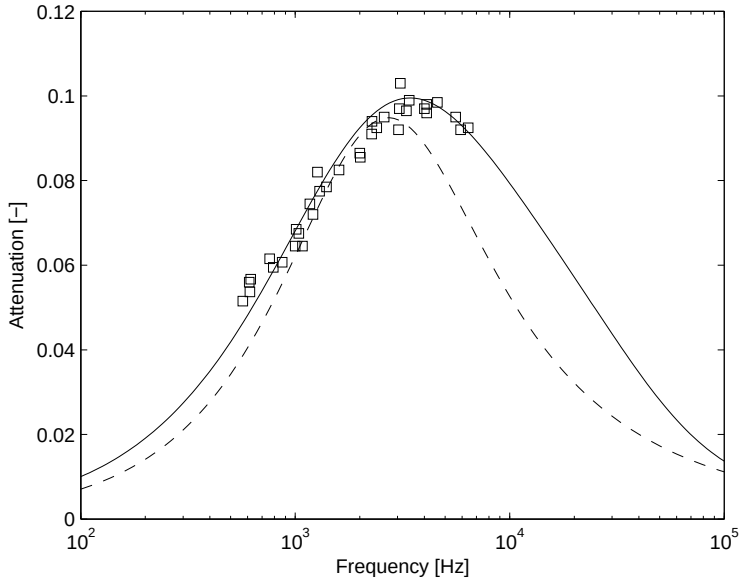

(a)

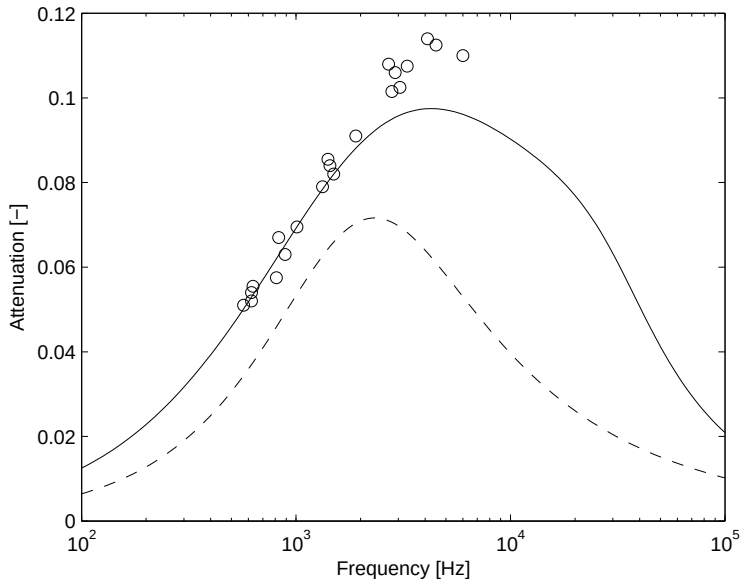

(b)

Figure 7.8: Comparison of the theoretical and experimentally measured attenuation of a partially saturated Massillon sandstone. The gas fraction is 9 % in (a) and 25 % in (b). The experimental data are from Murphy (1982a) using a resonant bar technique. The predicted attenuations are least-squares fits to the Rayleigh-Plesset-Biot model (solid curves) and to the generalized model (dashed curves). The input values are given in table 7.4.

Chapter 8

DARS measurements

8.1 Introduction

Acoustic Resonance Spectroscopy is an established methodology, that is used by the National Bureau of Standards to measure the velocity and quality factor of fluids (Harris, 1996). Harris (1996) proposed to adapt this method to measure the velocity and quality factor of sound in rocks in the sonic frequency range.

The Differential Acoustic Resonance Spectroscopy (DARS) is an experimental method based on the change in the acoustic resonance frequency of a fluid-filled tube due to the introduction of a foreign object in a tube. The resonance frequency of the fluid-filled tube is proportional to the ratio of the sound velocity in the surrounding medium and the length of the cylinder. For example, for liquids with velocities in the order of 1000 to 1500 m/s, the resonance frequency of a 0.5 m open-ended cylinder is 1000 - 1500 Hz. For gases, the same cylinder resonates at approximately 300 Hz.

Applications of this experimental method involve the estimation of the acoustic attenuation of porous rocks by Harris et al. (2005), the estimation of the flow properties of porous rocks by Xu et al. (2006) and Xu (2007), and the determination of the physical mechanism responsible for the measured compressibility by Vogelaar et al. (2008).

The purpose of this chapter is to demonstrate that the DARS set-up provides a complementary technique to measure the sample bulk modulus at low frequencies (1 kHz). The DARS measurements discussed in this chapter were acquired at the Seismic Wave Physics Laboratory of Stanford University.

8.2 Laboratory set-up and acquisition procedure

The length of the tube and the sound velocity determine the resonance frequency of the system. In our experiment, we use 5 cSt Dow Corning 200 silicone oil to fill the tube. The density and viscosity of the oil are independently measured to be 916 ± 1 kg/m^3 and 6.0 ± 0.2 mPa·s, see chapter 6. We measure the temperature (Springfield, Precisetemp) in the oil prior to every resonance experiment. The average temperature over 119 experiments is 23.7 ± 0.4 °C. During the course of an experiment, temperature variations were always below 0.1 °C. Variations in temperature influence the velocity, density and viscosity of the oil. We apply a linear relationship between temperature and velocity c_0 [m/s] and temperature and density ρ_0 [kg/m^3], inferred from the silicone oil information sheet (Clearco Products, 2006)

$$\begin{aligned} c_0 &= -3.00T + 1046.7, \\ \rho_0 &= -0.975T + 937.6, \end{aligned} \tag{8.1}$$

where T is the oil temperature in °C. We remark that the velocity-temperature relationship is not in agreement with the one by Xu (2007), who used a slope of -2.81 and an offset of 1051.8. Using equations (8.1), we have a direct relationship between fluid temperature and fluid compressibility (inverse bulk modulus)

$$\kappa_0 = (-8.8T^3 + 15 \times 10^3 T^2 - 7.0 \times 10^6 T + 1.0 \times 10^9)^{-1}. \tag{8.2}$$

Using $T = 23.7 \pm 0.4$ °C yields an average oil compressibility of $1.149 \pm 0.003 \times 10^{-9}$ Pa^{-1}.

The oil fills 64 cm of a 23 × 23 × 70 cm tank (inner dimensions) having 13 mm thick perspex walls. The cylinder is composed of solid Aluminum and has a length of 38.1 cm, an inner radius of 3.9 cm, and a wall thickness of 8 mm.

A schematic lay-out of the laboratory equipment is shown in figure 8.1. Explanatory photographs of the DARS set-up and the cylinder in detail are shown in figures 8.2 and 8.3.

Two piezoelectric ceramic frequency discs (Sensor Technology Ltd.) are used to excite vibrations in the oil. The sources are embedded in the wall in the middle of the cylinder facing each other. The sources are connected to a source amplifier (Krohn-Hite, model 7500).

A small calibrated hydrophone (Brüel & Kjær, type 8103) is used to measure the pressure. The receiver can be attached to the inner surface of the cylinder in the source plane at 90° from the sources. The received signal is amplified by a high-sensitivity charge amplifier (Brüel & Kjær, type 2635) with a gain of 31.6 dB.

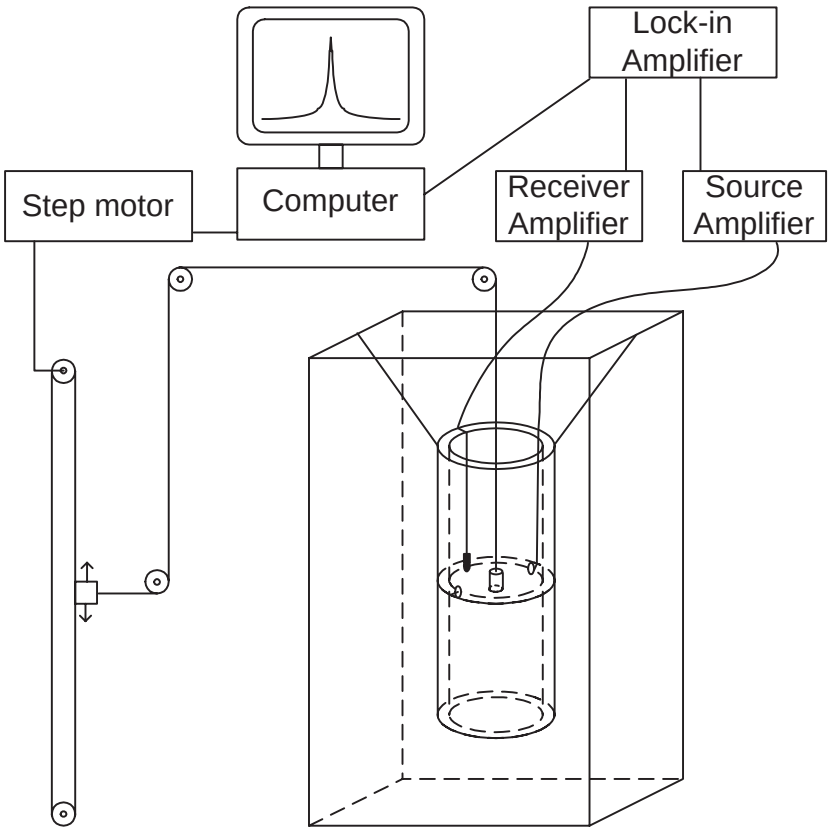

Figure 8.1: Schematic lay-out of the DARS set-up. The rectangular box is the oil-filled container in which a hollow cylinder is hung. The two sources are drawn as two opposite open circles in the cylinder wall, whereas the receiver is schematized as a bullet at 90° from the sources. The test object (small cylindrical sample) is hung on a thin nylon wire in the sources-receiver plane (the so-called pressure antinode), but can be moved vertically along the axis of the cylinder using the step motor. The data acquisition equipment is described in the text. The drawing is not to scale.

Both the amplifier of the sources and of the receiver are connected to a lock-in amplifier (Stanford Research Systems, model SR850 DSP). A lock-in amplifier is a phase-sensitive detector that singles out the component of the signal at a specific reference frequency and phase. Noise and background signals at frequencies other than the reference frequency are suppressed. The internal oscillator of the lock-in amplifier is also used as a function generator to excite the sources.

The settings of the lock-in amplifier are controlled and automated by a computer program (Labview National Instruments). The lock-in amplifier covers a frequency

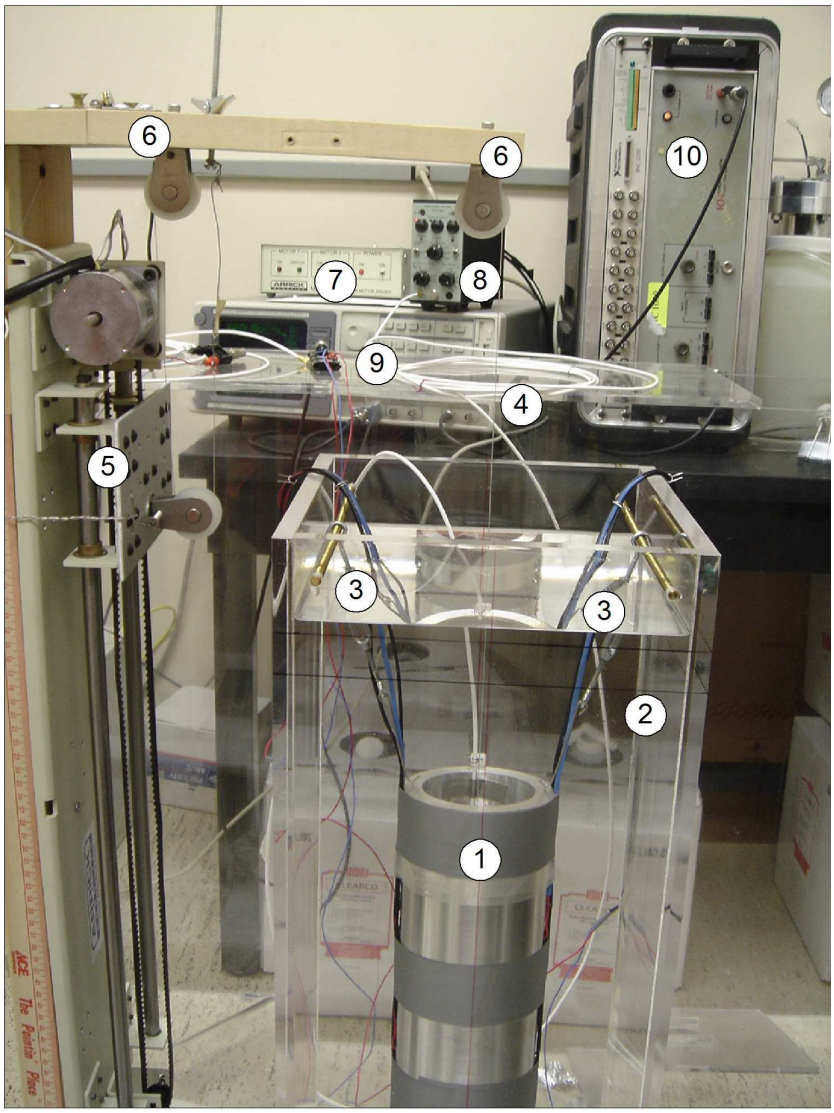

Figure 8.2: Photo of the DARS set-up. In front we observe the hollow cylinder (1) submerged in the oil-filled perspex container (2). The blue and black cables (3) provide power to the frequency discs (sources not visible); the curly white cable (4) is connected to the hydrophone (receiver not visible). On the most left is the step motor frame (5) visible including the nylon wire over the pulley sheaves (6). At the back, we observe the stepper motor apparatus (7) and the charge amplifier (8) on top of the lock-in amplifier (9); on the right is the source amplifier (10). This set-up is at the Seismic Wave Physics Laboratory of Stanford University.

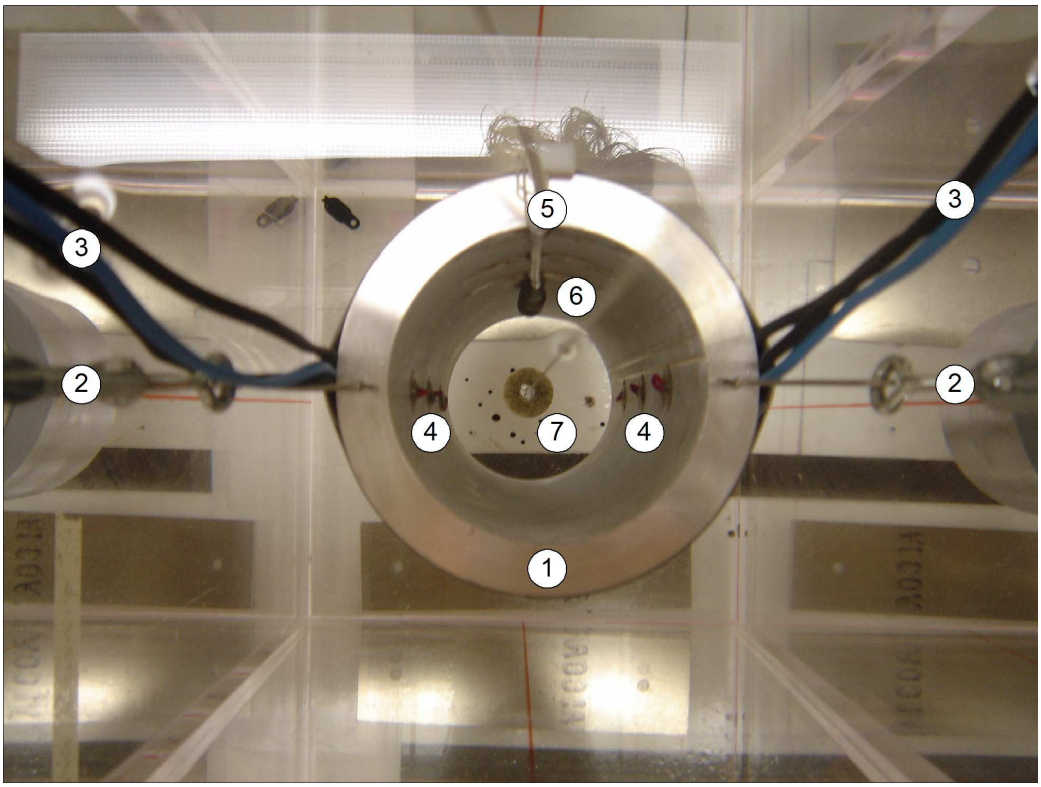

Figure 8.3: Top-view photo of the cylindrical resonator. We observe the submerged cylinder (1), including the connections (2) attached to the perspex container. The blue and black source cables (3) provide power to the frequency discs (4), of which only the center ones are operative in our experiment. The white cable (5) is connected to the hydrophone (6), which is attached to the cylinder's inner wall. A rock sample (7) is hung at the nylon wire along the axis of the cylinder. This set-up is at the Seismic Wave Physics Laboratory of Stanford University.

sweep from 1035 to 1135 Hz with a sample rate of 128 shots/s and a scan length of 30 s to select the resonance curve of the first mode. Hence, 3840 data points are acquired each time.

The tested sample is moved vertically along the axis of the cylinder by the step motor (Arrick Robotics, model MD-2A). The step motor is computer-controlled (Labview) and provides an accurate and repeatable positioning of the sample. A typical measurement covers 93 sample positions along the axis of the cylinder, sampled at 70 mm intervals from above the bottom of the container to below the oil-atmosphere surface, in such a way that the 47^{th} position is exactly in the middle

of the cylinder.
The first measurement is over the empty, fluid-filled, cylinder. In this way, we build for each tested sample a data file containing 94×3840 data points. Clearly, the typical output is the pressure as a function of frequency and sample position.

8.3 Tube resonance

In the following we derive a theoretical approximation of the pressure field within the tube, which we compare with the one acquired by the laboratory experiment. The experiment is illustrated by the photo of figure 8.4. We move the hydrophone through the cylinder from the bottom of the container to the top and measure the acoustic pressure at 1 cm intervals along the cylinder's axis. At each position, the acoustic pressure is measured as a function of the frequency.
The ceramic discs generate vibrations in the fluid with a velocity amplitude V_0. For symmetry reasons, only half of the tube has to be taken into account. The tube's half-length is denoted L. Assuming that the tube is filled with an attenuative fluid (complex-valued velocity c_0 and density ρ_0), the pressure and velocity distribution over the tube can be written as

$$\hat{p} = P^+ \exp(-ik_\mathrm{f}x) + P^- \exp(ik_\mathrm{f}x), \tag{8.3}$$

$$\rho_0 c_0 \hat{v} = P^+ \exp(-ik_\mathrm{f}x) - P^- \exp(ik_\mathrm{f}x), \tag{8.4}$$

with x the axial coordinate having its origin at the symmetry plane, and k_f the wavenumber of the quasi-1D wave in the tube.
Substitution of the boundary conditions $\hat{v} = V_0$ at $x = 0$ and $\hat{p} = 0$ at $x = L$ (pressure release surface) yields that

$$\hat{p} = i\rho_0 c_0 V_0 \frac{\sin k_\mathrm{f}(L-x)}{\cos k_\mathrm{f} L}, \tag{8.5}$$

This means that the pressure in the symmetry plane $x = 0$ can be written as

$$\frac{\hat{p}_0}{\rho_0 c_r V_0} = \left(1 + \frac{ic_\mathrm{i}}{c_r}\right) \frac{\exp(ik_\mathrm{f}L) - \exp(-ik_\mathrm{f}L)}{\exp(ik_\mathrm{f}L) + \exp(-ik_\mathrm{f}L)}, \tag{8.6}$$

where c_i and c_r are the imaginary and real parts of c_0, respectively. For non-attenuative media ($c_i = 0$), it is easy to show that system resonance will occur at $f_n = (2n+1)c_r/4L$, for $n = 0, 1, 2, \ldots$. For our system this would mean that $f_0 = 1280.3$ Hz. However, in the laboratory we measure a resonance frequency of 1086.1 Hz. The difference is caused by the fact that the boundary condition $\hat{p} = 0$ at $x = L$ is not met exactly. Following Pierce (1989), the simplest end correction

is to take the pressure release surface at $x = L + \Delta L$. From our experiments, we find that $\Delta L = 3.4$ cm.
Figure 8.5 gives a typical resonance curve. The theoretical line is from equation (8.6), where L is replaced by $L + \Delta L$, so that the resonance frequency is now in agreement with the measured resonance frequency. A small amount of damping ($c_i = 3.1$ m/s) is added to obtain a perfect match between theory and experiment. Interestingly, the introduction of damping does not change the resonance frequency, which is only determined by the non-attenuative part c_r, and the length of the tube.
We now investigate equation (8.6) more closely. Applying Taylor expansion in frequency to $k_\mathrm{f}L$ yields that $k_\mathrm{f}L = k_{\mathrm{f}0}L + \Delta k_\mathrm{f}L$ is equal to

$$k_\mathrm{f}L = 2\pi f_0 L \left(\frac{c_r - ic_i}{|c_0|^2}\right)\left(1 + \frac{\Delta f}{f_0}\right), \tag{8.7}$$

where $f = f_0 + \Delta f$. As we expand around $f_0 = c_r/4L$, it is easily found that

$$k_\mathrm{f}L \approx \tfrac{1}{2}\pi \left(1 - \frac{ic_i}{c_r}\right)\left(1 + \frac{\Delta f}{f_0}\right), \tag{8.8}$$

for $c_i \ll c_r$. This implies that in first order approximation $k_{\mathrm{f}0}L = \frac{1}{2}\pi(1 - ic_i/c_r)$ and $\Delta k_\mathrm{f}L = \frac{1}{2}\pi\Delta f/f_0$.
Taylor expansion of equation (8.6) yields that

$$\frac{\hat{p}_0}{\rho_0 c_r V_0} \approx \left(1 + \frac{ic_\mathrm{i}}{c_r}\right)\frac{(1 + 2i\Delta k_\mathrm{f}L)\exp(2ik_{\mathrm{f}0}L) - 1}{(1 + 2i\Delta k_\mathrm{f}L)\exp(2ik_{\mathrm{f}0}L) + 1}. \tag{8.9}$$

Subsequent substitution of the expressions for $k_{\mathrm{f}0}L$ and $\Delta k_\mathrm{f}L$ yields that

$$\frac{\hat{p}_0}{\rho_0 c_r V_0} \approx \left(1 + \frac{ic_\mathrm{i}}{c_r}\right)\frac{1 + i\pi\Delta f/f_0 + \exp(-\pi c_i/c_r)}{1 + i\pi\Delta f/f_0 - \exp(-\pi c_i/c_r)}. \tag{8.10}$$

For $\Delta f = 0$, we find that

$$\left|\frac{\hat{p}_0}{\rho_0 c_r V_0}\right| \approx \left|1 + \frac{ic_\mathrm{i}}{c_r}\right|\frac{2 - \pi c_i/c_r}{\pi c_i/c_r} \approx \frac{2 - \pi c_i/c_r}{\pi c_i/c_r}. \tag{8.11}$$

Denoting this value the amplitude A, we find that

$$\left|\frac{\hat{p}_0}{\rho_0 c_r V_0}\right|^2 \approx \frac{A^2 + \left(\frac{\Delta f}{f_0}\frac{c_r}{c_i}\right)^2}{1 + \left(\frac{\Delta f}{f_0}\frac{c_r}{c_i}\right)^2}. \tag{8.12}$$

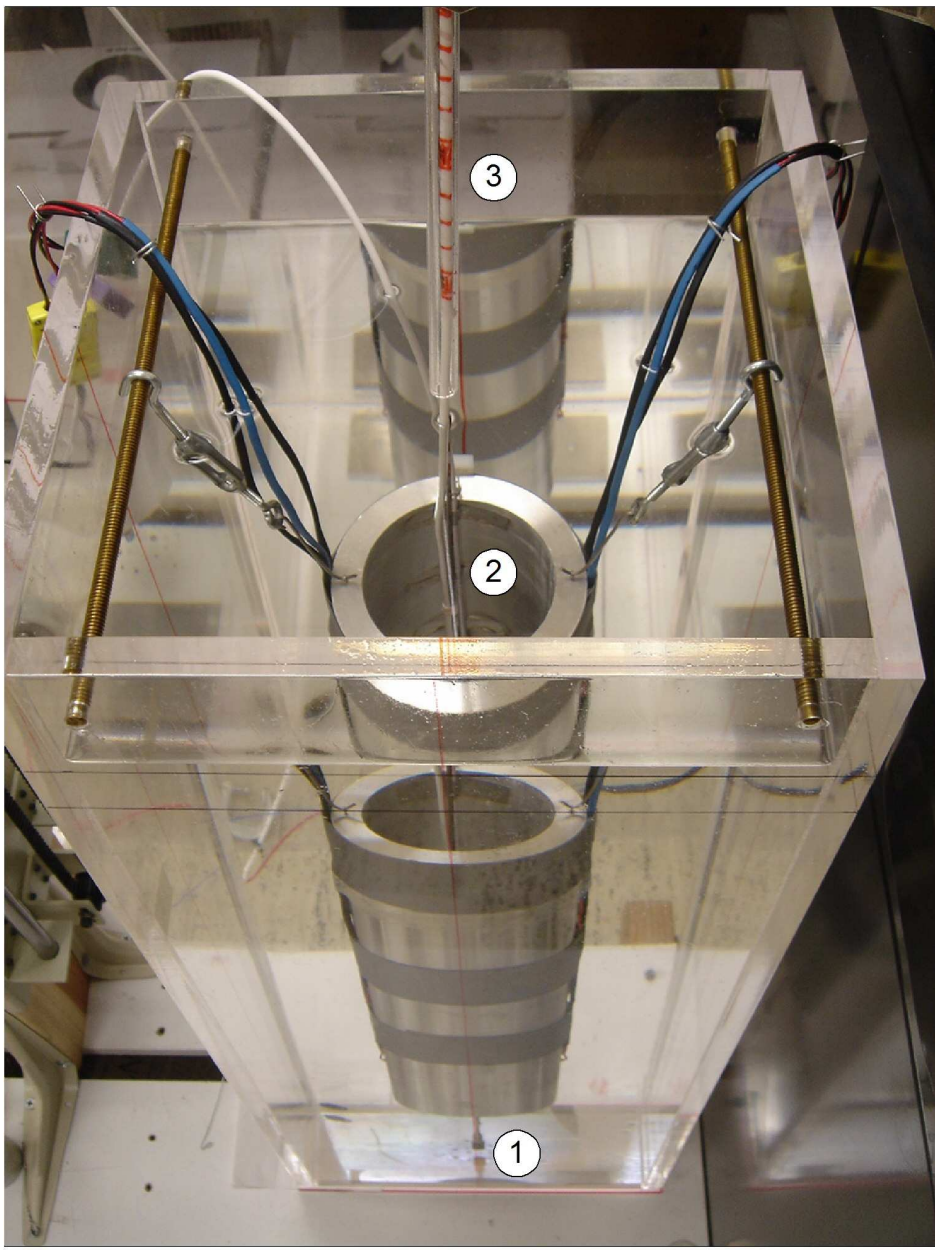

Figure 8.4: Photo of the cylindrical resonator and hydrophone. The tip of the hydrophone (1) is visible at the bottom end of the container. Its white cable (2) is along the axis of the cylinder. The hydrophone is carefully guided upward through the plastic sleeve (3) with intervals of 1 cm. The remaining features are discussed in figures 8.2 and 8.3. This set-up is at the Seismic Wave Physics Laboratory of Stanford University.

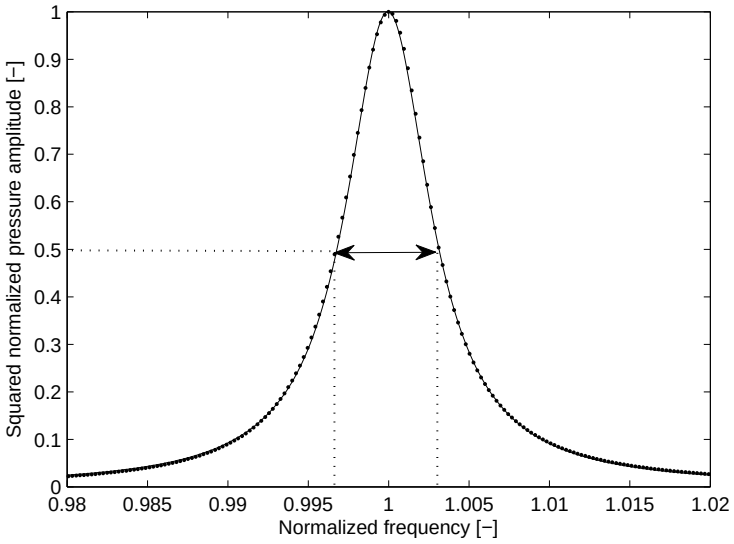

Figure 8.5: Squared sound pressure at a pressure antinode ($x = 0$) in the vicinity of the resonant frequency. The solid curve is the theoretical response of a system given by equation (8.6) using $c_r = 975.6$ m/s and $c_i = 3.1$ m/s. The dots are the experimentally measured responses of an oil-filled DARS system. The length of the arrow is the width of the curve at half power $2\Delta f/f_0$ or attenuation Q^{-1}. The two vertical dotted lines are at $1 \pm \Delta f/f_0$. Both pressures are normalized by their maximum amplitude. The frequency is normalized by the resonance frequency.

We note that for $\Delta f c_r = f_0 c_i$, we have that

$$\left| \frac{\hat{p}_0}{\rho_0 c_r V_0} \right|^2 \approx \tfrac{1}{2} A^2, \tag{8.13}$$

for large A. The width of the curve at $|\hat{p}_0/\rho_0 c_r V_0|^2 = \frac{1}{2}A^2$ equals $2c_i/c_r$, which is by definition equal to $1/Q$. The quality factor Q of our oil-filled system is then approximately 157. We note that this set-up is excellently suited to measure the quality factor of the resonator.

Next, we measure the pressure over the tube length at resonant frequency. In figure 8.6 we show the theoretical and measured responses at resonance frequency (1086 Hz). The theoretical curve is computed from equation (8.5), with L replaced by $L + \Delta L$. Note that the measurements were extended outside the tube. In the tube, discrepancies between theory and experiment exist. Most notable is the symmetry disturbance of the experiments. This is probably due to the hydrophone

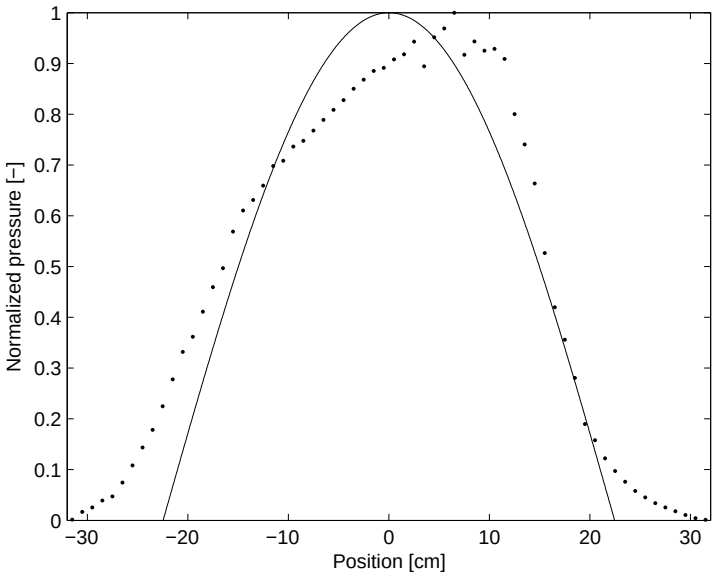

Figure 8.6: Pressure along the axis of the cylinder at resonant frequency (1086 Hz). The solid curve is the theoretical response of a system given by equation (8.5). The dots are the experimentally measured response of an oil-filled DARS system. Both responses are normalized by their maximum value. The actual ends of the cylinder are at $x = \pm 19$ cm.

cable that is completely outside the tube at $x = 19$ cm and completely inside at $x = -19$ cm.

The combined dependence of the experimental and theoretical pressure fields on position and frequency is shown by the iso-bar contours (pressure amplitudes) in figure 8.7. In figure 8.7a, the maximum pressure for a certain position is always at resonance frequency. The iso-bar contours from the experiment in figure 8.7b are somewhat distorted. The maximum pressure for a certain position varies slightly with frequency as shown by the dots. This means that not only the symmetry in position is disturbed, but also the frequency symmetry.

8.4 Pressure perturbation

Morse and Ingard (1968) derived an expression for the perturbed normal mode due to the scattering of a small object of volume V_S within a resonator of volume V_0. The foreign object has density ρ_S and compressibility κ_S, different from the values

in the surrounding medium ρ_0 and κ_0, respectively. The perturbed resonance frequency is determined by the rms pressure-amplitude distribution p and the velocity-amplitude distribution v over the sample (Morse and Ingard, 1968; Harris, 1996; Xu, 2007)

$$\frac{\omega_S^2 - \omega_0^2}{\omega_0^2} \simeq -\frac{1}{\Lambda}\frac{V_S}{V_0}\left[\delta_\kappa \langle p\rangle^2 + \delta_\rho \langle \rho_0^2 c_0^2 v^2\rangle\right], \qquad V_S \ll \lambda^3 \tag{8.14}$$

where Λ is a calibration coefficient. The brackets around a quantity define the averaging operator

$$\langle f\rangle = \frac{1}{V_S}\iiint_{V_S} f dV. \tag{8.15}$$

One part of the change in resonance frequency in equation (8.14) is proportional to the difference in compressibility δ_κ:

$$\delta_\kappa = \frac{\kappa_S - \kappa_0}{\kappa_0}. \tag{8.16}$$

The other term is proportional to the difference in density δ_ρ:

$$\delta_\rho = \frac{\rho_S - \rho_0}{\rho_S}. \tag{8.17}$$

If the object is heavier and stiffer than the displaced fluid, $\rho_S > \rho_0$ and $\kappa_S < \kappa_0$, the first term on the right-hand-side in equation (8.14) tends to increase the resonance frequency and the second term tends to decrease the resonance frequency. When the measurements are performed at a pressure antinode ($x = 0$), the second term on the right-hand-side of equation (8.14) may be neglected and we write

$$\frac{\omega_S^2 - \omega_0^2}{\omega_0^2} \simeq -\frac{\langle p\rangle^2}{\Lambda}\frac{V_S}{V_0}\delta_\kappa. \tag{8.18}$$

Introducing a sample in the tube at a pressure antinode will thus change the resonance frequency. An example is given in figure 8.8, where a cylindrical Aluminum sample is used with a length of 3.7 cm and a diameter of 2.5 cm. The pressures are measured with the hydrophone mounted at the wall. We notice that the resonance frequency shifts from 1083 Hz to 1092 Hz due to the introduction of the sample. The change in frequency is related to the change in compressibility of the system, while the change in half-power line width is related to the change in quality factor of the system.

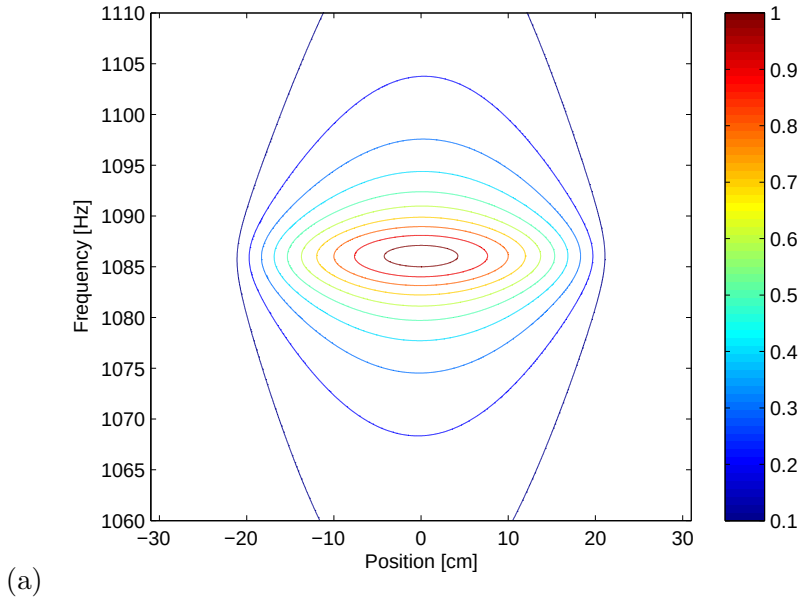

(a)

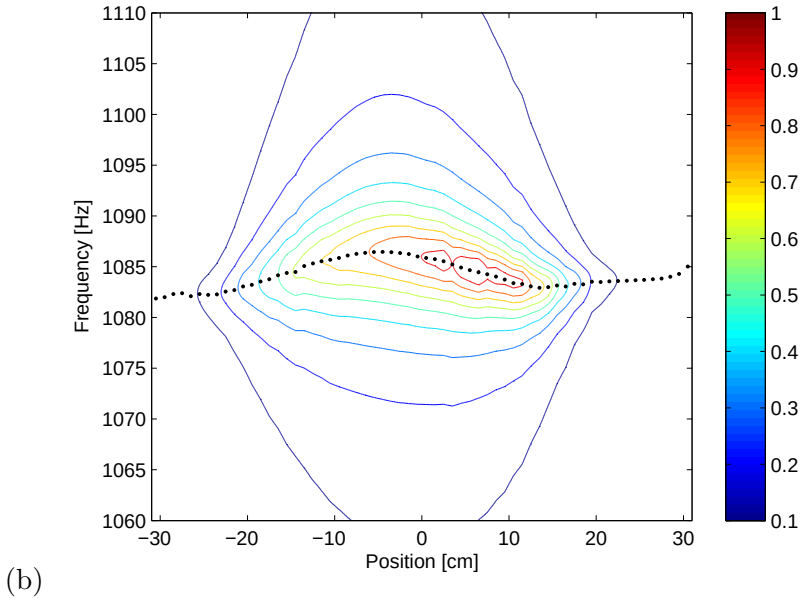

(b)

Figure 8.7: Iso-bar contours (pressure amplitudes) as a function of position and frequency. (a) The theoretical pressure is given by equation (8.5). (b) The experimental pressure is the measured response of an oil-filled DARS system. The dots represent the measured position-dependent resonant frequency (maximum pressure). Both responses are normalized by their maximum value.

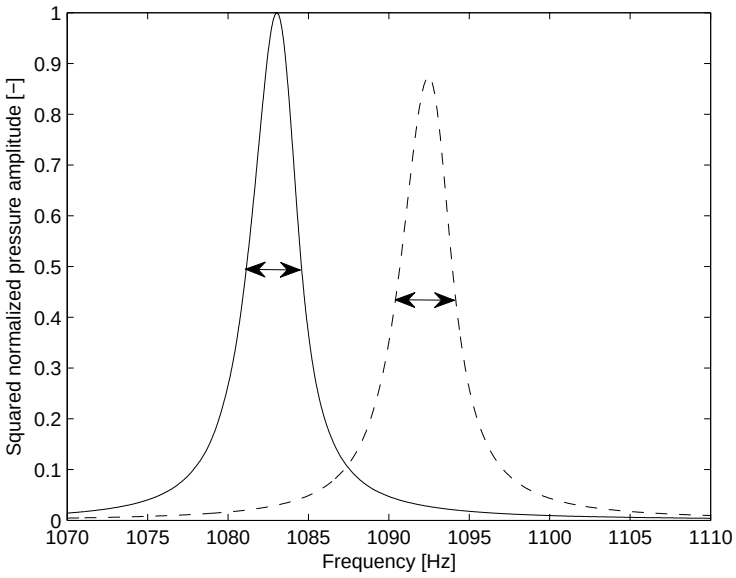

Figure 8.8: Squared acoustic response at $x = 0$ due to the presence of an Aluminum cylinder in the center of the tube $x = 0$ (dashed curve). The unperturbed pressure (solid curve) is the measured response at $x = 0$ in an oil-filled cylinder. Both pressures are normalized by the unperturbed peak amplitude, which has an absolute value of 58 mV at 1083 Hz. The absolute value of the perturbed peak is 54 mV at 1092 Hz. The arrows denote the width of the curves at half-power.

Equation (8.18) means that a linear dependence between $(\omega_S^2 - \omega_0^2)/\omega_0^2$ and V_S may be expected, where the sample size rather than the sample shape is involved. This is tested for a series of Aluminum and Lucite samples with different dimensions, tabulated in table 8.1. These measurements were performed by Xu (2007). In figure 8.9, the relative squared resonance frequency is plotted as a function of the sample volume of these solids. Obviously, the slopes are different due to the difference in compressibility.

In the figure, we observe a strong linear correlation for both samples, indeed. We see that the sample volume rather than the sample shape determines the resonant frequency. We infer from this observation that the average acoustic pressure over the sample surface is approximately constant. Xu (2007) concluded that the small fluctuations around the trend line for samples with fixed diameter but varying lengths, indicate that the pressure distribution over the sample body is slightly varying with sample length. In addition, the results for samples with fixed length

L_S [cm]	D_S [cm]	V_S [cm^3]	$\omega_{Alu}/2\pi$ [Hz]	$\omega_{Luc}/2\pi$ [Hz]
5.08	2.54	25.74	1096	1094
5.08	2.79	31.15	1098	1096
5.08	3.05	37.07	1101	1098
5.08	3.30	43.50	1105	1101
5.08	3.56	50.45	1108	1103
5.08	3.81	57.92	1113	1107
2.54	3.81	28.96	1098	1095
3.05	3.81	34.75	1100	1098
3.56	3.81	40.54	1103	1100
4.06	3.81	46.33	1106	1102
4.57	3.81	52.12	1109	1104

Table 8.1: Values of the dimensions and resonant frequency of two reference solids. The samples lengths L_S and diameters D_S are measured. Subscript S denotes sample. The volume-dependent resonant frequencies at $x = 0$ for Aluminum and Lucite are $\omega_{Alu}/2\pi$ and $\omega_{Luc}/2\pi$, respectively. The resonant frequency of the oil-filled cylinder $\omega_0/2\pi$ is here 1083 Hz. The measurements are acquired by Xu (2007).

but varying diameter indicate that the pressure variation in the radial direction can be ignored. The slopes of the fitted lines through the origin are estimates for the value $\delta_\kappa \langle p \rangle^2/\Lambda$ in equation (8.18).

We also investigate the dependence on sample stiffness of five different solids. Their properties are given in table 5.2. Prior to each measurement of the resonant frequency of the tested samples, we measure the resonant frequency of the oil-filled cylinder. The resulting frequencies are shown in table 8.2.

We now calculate the compressibility of the solids predicted by the DARS method. Rewriting equation (8.16) using equation (8.18) gives

$$\kappa_S = (1 + A_\kappa \xi_S)\kappa_0, \tag{8.19}$$

where

$$\xi_S = \frac{\omega_S^2 - \omega_0^2}{\omega_0^2}\frac{V_0}{V_S}, \tag{8.20}$$

is the measured volume-normalized frequency perturbation for sample S. Coefficient A_κ is equal to $-\Lambda/\langle \hat{p} \rangle^2$. Using the five solid reference samples we find that $A_\kappa = -0.594 \pm 0.004$.

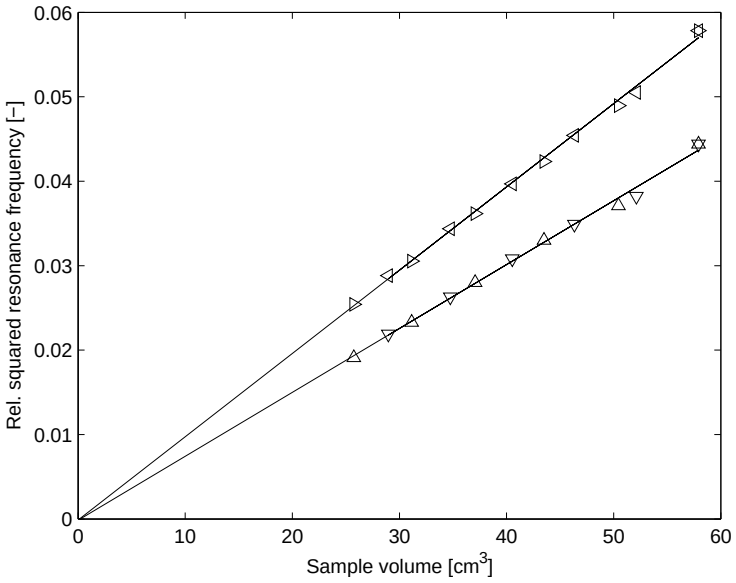

Figure 8.9: Relative squared resonance frequency at $x = 0$ as a function of the sample volume and sample shape for two reference solids: Aluminum ($\triangleright$ (fixed length) and $\triangleleft$ (fixed diameter)) and Lucite ($\triangle$ (fixed length) and $\triangledown$ (fixed diameter)). The lengths, diameters, volumes and resonant frequencies are tabulated in table 8.1. The lines are linear least-squares fits to all data points, yielding R^2 statistics of 0.999 for Aluminum and 0.998 for Lucite, respectively.

Solid	$\omega_0/2\pi$ [Hz]	$\omega_S/2\pi$ [Hz]	V_S [cm^3]	κ_{DARS} [GPa^{-1}]	κ_{US} [GPa^{-1}]
Alum	1083.0	1092.4	19.27 ± 0.01	0.006 ± 0.007	0.013 ± 0.001
Teflon	1083.8	1090.2	19.20 ± 0.01	0.367 ± 0.005	0.345 ± 0.017
PVC	1082.7	1090.5	19.21 ± 0.01	0.190 ± 0.006	0.190 ± 0.009
Lucite	1082.9	1090.8	19.17 ± 0.02	0.179 ± 0.007	0.178 ± 0.009
Delrin	1083.3	1091.2	19.16 ± 0.01	0.172 ± 0.007	0.160 ± 0.008

Table 8.2: Experimental results of the reference solids. The resonant frequencies ω_0 and ω_S are the oil-filled and sample-loaded values at the pressure antinode, respectively. The volume of the resonating cylinder V_0 is 1855 cm^3. The ultrasonic compressibilities κ_{US} are calculated from table 5.2. The DARS compressibilities κ_{DARS} are calculated using equation (8.19). Errors are attributed to the uncertainty in A_κ.

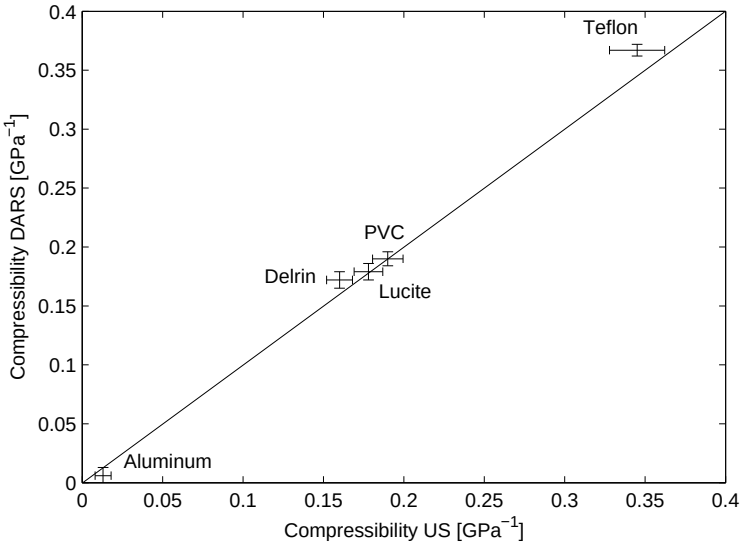

Figure 8.10: Compressibilities of the reference solids calculated by the DARS method and by ultrasound. The values are given in table 8.2.

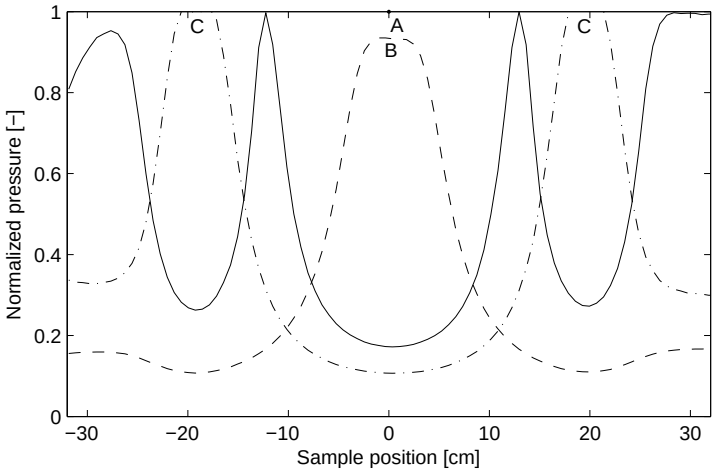

Figure 8.11: Acoustic pressure at $x = 0$ as a function of the sample position at a fixed frequency: 1083 Hz (solid curve), 1092 Hz (dashed curve), and 1078 Hz (dashed-dotted curve). All pressures are normalized by the unperturbed resonant pressure at $x = 0$, i.e. 1083 Hz. The tested sample is an Aluminum solid. Point A at (0, 1) refers to the unperturbed pressure. Point B is the perturbed pressure at $x = 0$. Points C are the perturbed pressures at $x = \pm 19$ cm.

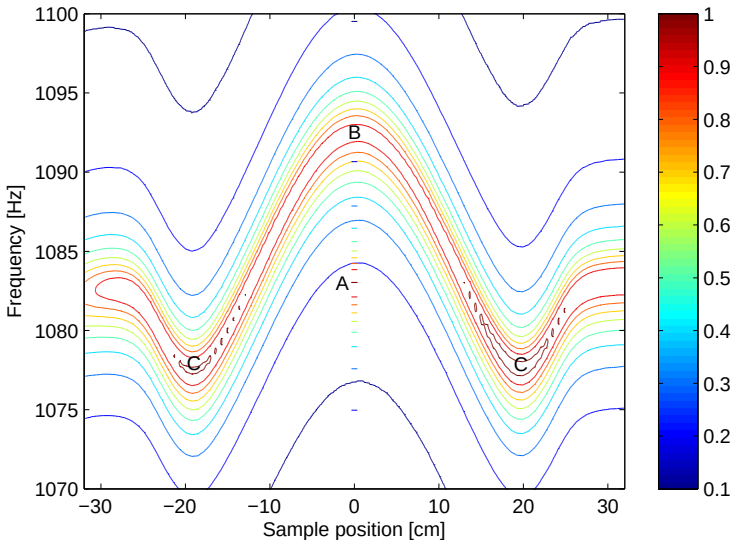

Figure 8.12: Iso-bar plot of the change of the resonance frequency due the position of the sample in a resonant experiment. The unperturbed frequency response (empty measurement) is represented by the short segments at $x = 0$. The unperturbed maximum pressure is denoted with point A at (0, 1083). The perturbed frequency for an Aluminum sample moved over $x = \pm 32$ cm is represented by the remaining contours. Both pressures are normalized by the unperturbed pressure peak. Point B is the antinode at 1092 Hz. Points C are the perturbed pressure nodes at 1078 Hz.

The DARS compressibility values and the compressibilities determined by ultrasound are given in table 8.2 and cross-plotted in figure 8.10. Within the measurement accuracy, the compressibilities for all solids determined by the two methods are in excellent agreement, indicating that the experimental resonant set-up, acquisition procedure, and corresponding theory are capable to estimate the compressibility for the tested nonporous materials.

In the next section, we apply these findings to porous samples.

8.4.1 Dependence on sample location

Next, we determine the pressure dependency at $x = 0$ on the sample position. From equation (8.14), we see that if the sample is near a pressure maximum for the unperturbed standing wave, the compressibility perturbation δ_κ predominates the shift in resonant frequency (Morse and Ingard, 1968). Then, $\hat{p} \gg \rho_0 c_0 \hat{v}$ and

$\omega_S > \omega_0$. If the sample is near a pressure node, where $\rho_0 c_0 \hat{v} \gg \hat{p}$, the density perturbation δ_ρ predominates the shift in resonant frequency and $\omega_S < \omega_0$.

The perturbed pressure plot of an Aluminum sample is shown in figure 8.11 for several frequencies. The pressures are normalized by the unperturbed pressure. The pressure at $x = 0$ measured at the unperturbed resonance frequency (1083 Hz) drops dramatically when the sample is introduced at $x = 0$. If the frequency is set at 1092 Hz, a new maximum is obtained (point B), which is slightly lower than the unperturbed maximum (point A). If measured at a lower frequency (1078 Hz), the pressure at $x = 0$ decreases even more. Next, if the sample is moved through the cylinder at constant frequency, a typical pattern of minima and maxima occurs.

The combined picture is given in figure 8.12. We plot the pressure as a function of the sample position and frequency. The maximum pressure of the unperturbed measurement is denoted by point A. We see from figure 8.12 that the pressure denoted by point B, is a local minimum, since two absolute maxima, denoted by points C, are seen at the ends of the tube at $(\pm 19, 1078)$. These absolute maxima correspond to the pressure nodes.

We finally plot the change in resonant frequency between each empty and Aluminum sample-loaded measurement $(\omega_S^2 - \omega_0^2)/\omega_0^2$ in figure 8.13 as a function of the sample position. In the middle of the cylinder, $x = 0$, the sample's smaller compressibility leads to a positive shift in frequency. At the ends of the cylinder, $x = \pm 19$, the sample's higher density results in a negative frequency shift. This is in accordance with equation (8.14), where the pressure or the velocity dominates. In addition, we observe that the stiff solids (e.g. Aluminum) produce systematically a larger shift in resonant frequency than the softer ones (e.g. Teflon).

8.5 Porous medium compression

We derive the quasi-static expression for the bulk modulus of a saturated spherical sample with open pores due to an external fluid pressure $\hat{p}_e$. This is done to predict the DARS measurements on porous samples. The bulk modulus of the sample is (cf. equation (4.9))

$$K(\omega) = -\frac{a}{3\hat{u}(a)}\hat{p}_e, \tag{8.21}$$

where $\hat{u}(a)$ is the radial solid displacement at the sample's surface having radius a. The equations for the solid displacement $\hat{u}$, pore pressure $\hat{p}$, and total stress $\hat{\tau}$

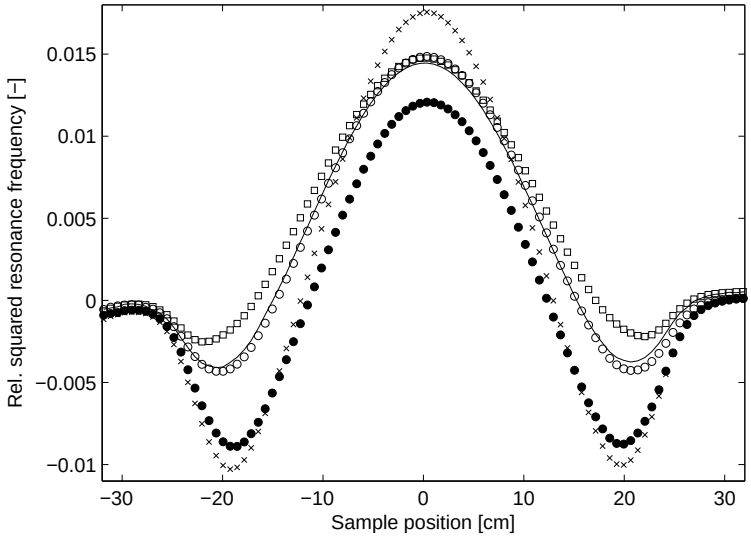

Figure 8.13: Relative squared resonance frequency as a function of the position of the sample in a resonant experiment. The frequency change is between an oil-filled ω_0 and sample-loaded measurement ω_S as given in table 8.2. The cylinder is located between ±19 cm. The tested solids, Aluminum (×), Delrin (○), Lucite (□), PVC (−), and Teflon (●) have the measured properties of table 5.2.

are simply retrieved from equations (4.14):

$$\hat{u}(r) = Ar + (Q+R)Fj_1(k_2r), \tag{8.22}$$

$$\hat{p}(r) = -\frac{3(Q+R)}{\phi}A + \frac{(PR-Q^2)}{\phi}k_2Fj_0(k_2r), \tag{8.23}$$

$$\hat{\tau}(r) = 3K_{\mathrm{BG}}A - \frac{4\mu(Q+R)}{r}Fj_1(k_2r). \tag{8.24}$$

There are two arbitrary constants: A and F. The two boundary conditions at the open porous surface ($r = a$) are $\hat{p}(a) = \hat{p}_{\mathrm{e}}$ and $\hat{\tau}(a) = -\hat{p}_{\mathrm{e}}$, which yields

$$-\frac{3(Q+R)}{\phi}A + \frac{(PR-Q^2)}{\phi}k_2Fj_0(k_2a) = \hat{p}_{\mathrm{e}}, \tag{8.25}$$

$$3K_{\mathrm{BG}}A - \frac{4\mu(Q+R)}{r}Fj_1(k_2a) = -\hat{p}_{\mathrm{e}}. \tag{8.26}$$

Adding both equations gives

$$A = \frac{4\mu(Q+R)j_1(k_2a)/a - (PR-Q^2)k_2j_0(k_2a)/\phi}{3K_{\mathrm{BG}} - 3(Q+R)/\phi}F. \tag{8.27}$$

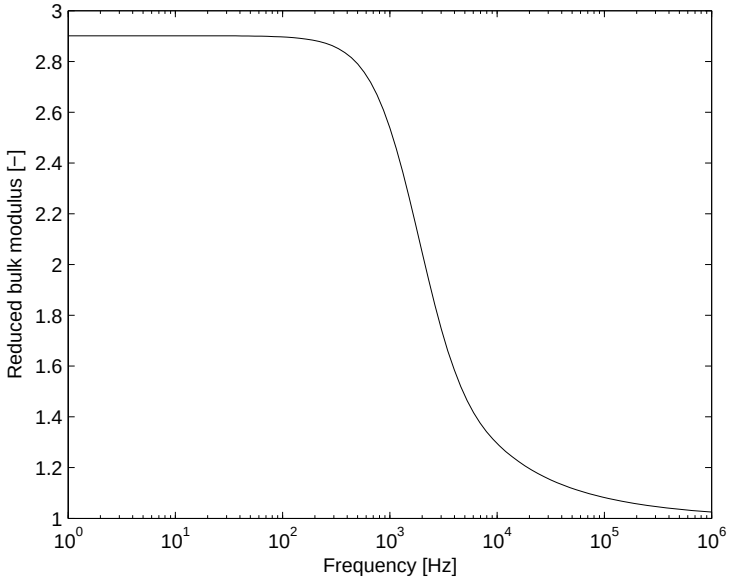

Figure 8.14: Frequency-dependent bulk modulus for a Bentheimer sandstone sample (BEN27). The bulk modulus is normalized by the Biot-Gassmann modulus.

Subsequent substitution into equation (8.25) yields

$$F = \frac{Q + R - K_{\mathrm{BG}}\phi}{4\mu(Q+R)^2 j_1(k_2 a)/a - (PR - Q^2)K_{\mathrm{BG}}k_2 j_0(k_2 a)}\hat{p}_{\mathrm{e}}. \tag{8.28}$$

Substitution of these constants into equation (8.22) gives for equation (8.21)

$$K(\omega) = \frac{(PR - Q^2)K_{\mathrm{BG}}k_2 a j_0(k_2 a) - 4\mu(Q+R)^2 j_1(k_2 a)}{(PR - Q^2)k_2 a j_0(k_2 a) - 3(Q+R)(H\phi - Q - R)j_1(k_2 a)}. \tag{8.29}$$

The frequency-dependent bulk modulus is shown in figure 8.14 for an arbitrary sample (BEN27). From the measured properties in chapter 5 we have $K_{\mathrm{BG}} = 12.75$ GPa. The sample radius is approximated by $a = \sqrt[3]{3V_{\mathrm{S}}/4\pi}$.
From the figure we infer that at low frequencies the bulk modulus of the sample goes to the bulk modulus of the solid grains $K_{\mathrm{s}} = 37$ GPa. At high frequencies the compressibility of the sample goes to the Biot-Gassmann modulus K_{BG}.
Xu (2007) followed an alternative approach to predict the DARS measurements on porous samples. He considered micro-scale fluid flow through the surface of the sample to release the differential pressure across the surface boundary. Accordingly, he described this dynamic flow phenomenon as a quasi-static diffusion

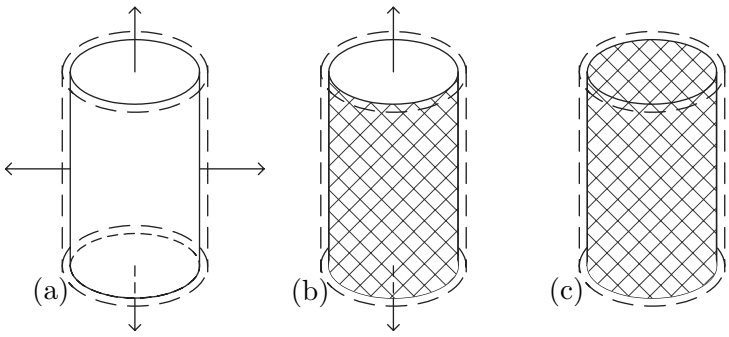

Figure 8.15: Schematic representation of the dependency of the fluid flux on sample surface conditions under loading. The dashed contours represent the initial size of the compressible porous sample prior to loading. The arrows indicate the pore-fluid flow direction under pressure load. (a) Porous sample with open outer pores. The pore fluid is free to move in radial and longitudinal direction in the surrounding fluid. (b) Porous sample with cylindrically sealed outer surface. The pore fluid is free to move in longitudinal direction only. (c) Completely sealed porous sample. Fluid flow is restricted.

process. He found that effective compressibility of a fluid-saturated porous material under periodic loading is the superposition of the wet-frame compressibility (inverse Gassmann modulus) and a contribution from the amount of fluid flowing in and out of the sample.

8.6 DARS results porous samples

The set of investigated porous samples is the variety of consolidated natural and artificial rocks, studied in chapter 5 and 6. Their rock physical properties, measured with the conventional methods are given in tables 5.1 and 5.3. All samples are fully saturated with 5cSt silicone oil, which is identical to the fluid filling the container. For the purpose of this experiment, the pores of the tested samples are initially open, so that the pore-fluid can communicate with the surrounding fluid, see figure 8.15a.

We compare the data from the DARS technique with the conventional ultrasonic method from which the dry and saturated ultrasonic bulk moduli are calculated (see chapters 5 and 6). In addition, the Biot-Gassmann modulus K_{BG} is calculated using Gassmann's equation (2.26). The results are listed in table 8.3.

We first measure the resonant frequency of the empty cylinder, followed by the equidistant measurements of the sample-loaded cylinder at various positions along

the cylinder's axis. The empty and sample-loaded frequency at the middle position are used to calculate ξ_S from equation (8.20), where the V_S is the bulk volume of the porous sample.

We apply equation (8.19) with temperature-corrected κ_0 to calculate the DARS bulk modulus of the porous samples. The results are shown in the first column of table 8.3. We observe a large variety in bulk moduli.

The bulk moduli estimated using the DARS method are compared with the dry ultrasonic bulk moduli in figure 8.16a. From the figure it is obvious that the bulk moduli calculated by the two methods are generally in disagreement.

It can be argued that the disagreement is attributable to the saturated state of the DARS-measured samples. The cross plot of the measured wet ultrasonic bulk moduli in figure 8.16b now shows that the distance off the 45° line is even larger than for the dry ultrasonic bulk moduli. In the figure, we observe that the DARS bulk modulus is higher than the measured wet ultrasonic bulk modulus for all samples.

Xu et al. (2006) estimated the flow properties in porous media with a model for dynamic diffusion and related the effective compressibility (measured with DARS) to permeability. He found that the permeability of the sample greatly influences the DARS-compressibility.

To further investigate this claim, we carefully seal the outer cylindrical surface of the porous samples by means of an exopy resin (Devcon 2-Ton Clear Epoxy). The top and bottom of the sample are left open, see figure 8.15b.

DARS-measurements on these partially sealed porous samples show a higher bulk modulus K_{part} than DARS-measurements on the samples with open pores K_{open}. Obviously, partially sealed samples are stiffer than samples with open outer pores. The partially-sealed bulk modulus is plotted against the dry-rock and, respectively, the oil-saturated ultrasonic bulk modulus in figure 8.17.

Finally, we completely seal several porous samples. The bulk moduli of these completely sealed samples are also given in table 8.3. The relations to the dry and wet ultrasonic bulk modulus are shown in figure 8.18.

There is a reasonable agreement between K_{seal} and K_{wet}. The agreement between K_{seal} and K_{BG} is even better. With reference to section 8.5, we note that the measured bulk moduli by DARS are generally not close to K_s. This is probably because the bulk modulus is described by the relative fluid displacement instead of the solid displacement: $\phi\hat{U}(a) + (1-\phi)\hat{u}(a)$, where $\hat{U}(a)$ is the radial fluid displacement at the sample's surface.

Apparently, the bulk modulus measured with DARS is dependent on whether or not the pore fluid is allowed to communicate with the surrounding fluid. The fluid

flux is illustrated in figure 8.15. The mechanism responsible for the bulk modulus measured with the DARS set-up is a combination of bulk modulus of the saturated frame and fluid flow, while the dry bulk modulus measured by ultrasound is a direct measure of the bulk modulus of the frame.
Future work on DARS should concentrate on verifying the validity of the relative fluid displacement assumption and quantifying the quality factor of porous samples.

Sample ID	K_{open} [GPa]	K_{part} [GPa]	K_{seal} [GPa]	K_{wet} [GPa]	K_{BG} [GPa]
CHK03	10.9 ± 2.4	12.6 ± 3.4	42.6 ± 23.4	12.2 ± 0.6	24.2 ± 1.2
CHK04	11.6 ± 2.8	19.3 ± 6.8		12.0 ± 0.6	24.0 ± 1.1
SSA04	4.1 ± 0.4	6.8 ± 1.0	8.7 ± 1.6	9.8 ± 0.5	9.6 ± 0.5
SSA11	4.9 ± 0.5	7.8 ± 1.3		10.4 ± 0.5	8.8 ± 0.4
SSB04	2.7 ± 0.1	3.4 ± 0.2		5.7 ± 0.3	12.4 ± 0.6
SSB07	3.0 ± 0.2	4.2 ± 0.4	14.3 ± 4.0	8.2 ± 0.4	15.3 ± 0.7
SSB08	2.9 ± 0.2	3.9 ± 0.3		7.1 ± 0.3	12.3 ± 0.6
SSB09	3.0 ± 0.2	4.6 ± 0.4		8.5 ± 0.4	15.7 ± 0.7
SSC05	10.2 ± 2.2	13.0 ± 3.4	17.6 ± 5.8	16.8 ± 0.8	16.5 ± 0.8
SSC06	6.3 ± 0.9	11.9 ± 2.9		15.7 ± 0.7	15.1 ± 0.7
SSF02	2.9 ± 0.2	4.1 ± 0.4	6.9 ± 1.0	8.5 ± 0.4	7.9 ± 0.4
SSF03	2.7 ± 0.1	4.3 ± 0.4		9.3 ± 0.4	8.7 ± 0.4
SSF04	3.1 ± 0.2	4.6 ± 0.5		7.2 ± 0.3	7.7 ± 0.4
SSG01	3.3 ± 0.2	5.4 ± 0.6	10.1 ± 2.1	9.2 ± 0.4	9.5 ± 0.5
SSG02	3.4 ± 0.2	5.3 ± 0.6		13.4 ± 0.6	11.2 ± 0.5
YBE03	5.6 ± 0.7	8.0 ± 1.4	11.0 ± 2.5	11.1 ± 0.5	11.1 ± 0.5
VIF01	2.3 ± 0.1	2.7 ± 0.1	6.0 ± 0.8	5.0 ± 0.2	5.2 ± 0.2
VIF02	2.2 ± 0.1	2.7 ± 0.1		5.1 ± 0.2	5.4 ± 0.3
VIC05	1.9 ± 0.1	2.4 ± 0.1	3.7 ± 0.3	4.5 ± 0.2	3.4 ± 0.2
VIC06	1.9 ± 0.1	2.2 ± 0.1		3.5 ± 0.2	3.5 ± 0.2
QUE09	3.3 ± 0.2	5.2 ± 0.6	10.3 ± 2.2	10.6 ± 0.5	10.1 ± 0.5
QUE10	4.3 ± 0.4	4.6 ± 0.5		10.6 ± 0.5	9.3 ± 0.4
B1P13	5.5 ± 0.6	7.2 ± 1.1	9.8 ± 2.0	11.3 ± 0.5	12.3 ± 0.6
B1P14	5.4 ± 0.6	6.3 ± 0.9		11.6 ± 0.6	10.9 ± 0.5
CAS16	9.3 ± 1.8	11.0 ± 2.5	9.1 ± 1.8	7.2 ± 0.3	8.8 ± 0.4
CAS17	7.3 ± 1.2	8.8 ± 1.7		9.1 ± 0.4	8.9 ± 0.4
B1N20	4.3 ± 0.4	6.5 ± 0.9	8.2 ± 1.4	10.8 ± 0.5	9.9 ± 0.5
B1N21	4.3 ± 0.4	7.2 ± 1.1		10.4 ± 0.5	10.1 ± 0.5
COL23	9.1 ± 1.8	10.3 ± 2.2	13.0 ± 3.4	15.8 ± 0.8	14.8 ± 0.7
COL25	9.7 ± 2.0	11.9 ± 2.9		15.8 ± 0.8	15.9 ± 0.8
BEN27	3.4 ± 0.2	5.9 ± 0.8	13.6 ± 3.7	14.4 ± 0.7	12.7 ± 0.6
BEN28	3.4 ± 0.2	5.9 ± 0.8		15.0 ± 0.7	12.7 ± 0.6
B2P30	5.5 ± 0.7	7.7 ± 1.3	9.7 ± 2.0	12.9 ± 0.6	12.8 ± 0.6
B2N32	6.2 ± 0.8	9.6 ± 2.0	11.5 ± 2.7	13.0 ± 0.6	12.3 ± 0.6
B2N33	5.5 ± 0.7	10.2 ± 2.2		12.3 ± 0.6	12.1 ± 0.6

(continues)

(continued)

Sample ID	K_{open} [GPa]	K_{part} [GPa]	K_{seal} [GPa]	K_{wet} [GPa]	K_{BG} [GPa]
FEL36	6.4 ± 0.9	6.8 ± 1.0	9.2 ± 1.8	13.1 ± 0.6	12.1 ± 0.6
FEL37	6.0 ± 0.8	6.6 ± 0.9		12.3 ± 0.6	13.2 ± 0.6
NIV44	3.2 ± 0.2	3.3 ± 0.2	12.1 ± 3.0	10.2 ± 0.5	7.9 ± 0.4
NIV45	2.8 ± 0.1	3.4 ± 0.2		9.0 ± 0.4	7.1 ± 0.3
UNK50	8.5 ± 1.5	12.9 ± 3.4	14.1 ± 3.9	18.7 ± 0.9	15.9 ± 0.8
UNK51	8.9 ± 1.7	12.7 ± 3.2		16.4 ± 0.8	14.4 ± 0.7
NN356	9.3 ± 1.8	9.3 ± 1.8	12.9 ± 3.3	12.9 ± 0.6	13.9 ± 0.7
NN458	13.6 ± 3.7	15.5 ± 4.6	18.3 ± 6.2	19.3 ± 0.9	20.0 ± 1.0
GL160	2.5 ± 0.1	2.9 ± 0.2	5.0 ± 0.5	5.2 ± 0.2	8.8 ± 0.4
GL261	2.5 ± 0.1	2.9 ± 0.2	5.6 ± 0.7	6.0 ± 0.3	10.0 ± 0.5

Table 8.3: Bulk moduli of the fully-saturated samples. Moduli K_{open}, K_{part}, and K_{seal} are determined using the DARS method with different surface conditions. Their error reflects the uncertainty in coefficient A_κ. Moduli K_{wet} and K_{BG} are determined from ultrasonic measurements.

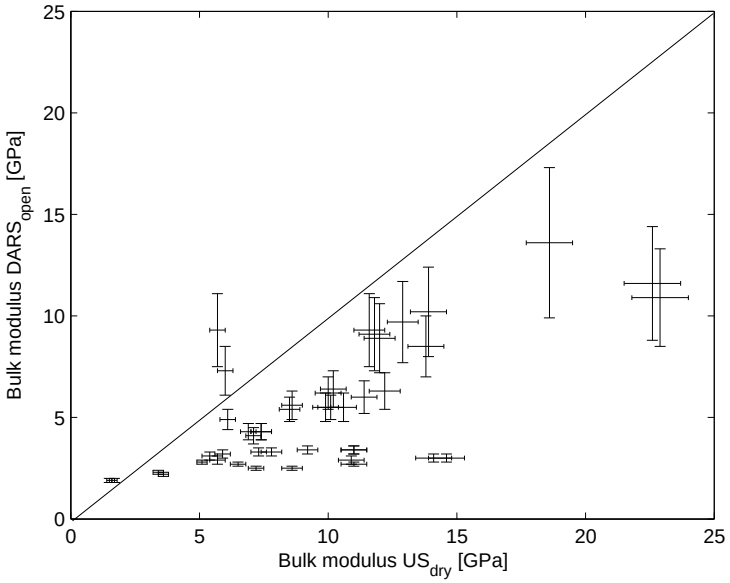

(a)

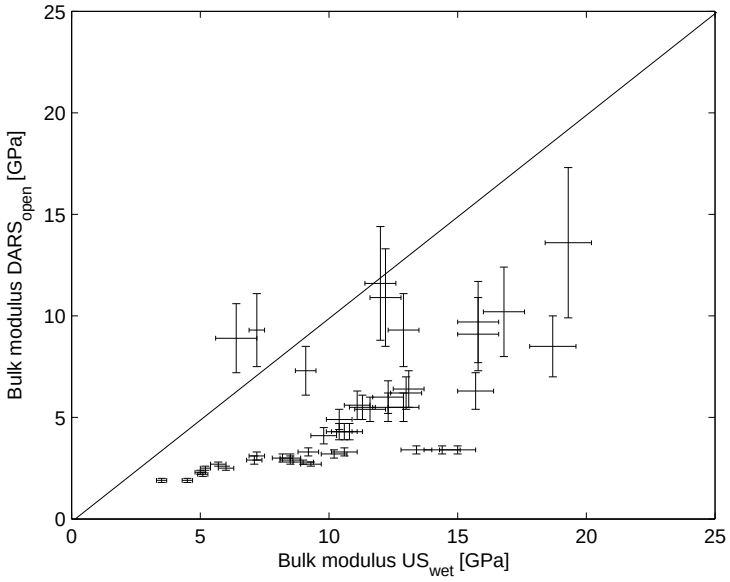

(b)

Figure 8.16: Cross-plots of the bulk moduli of the open porous samples estimated by the DARS method and by ultrasound. (a) Dry ultrasonic bulk modulus K_{m}. (b) Oil-saturated ultrasonic bulk modulus K_{wet}.

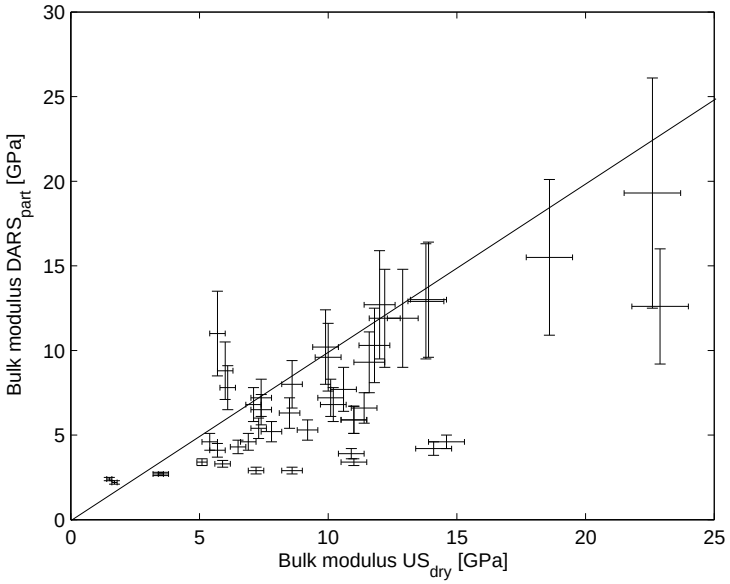

(a)

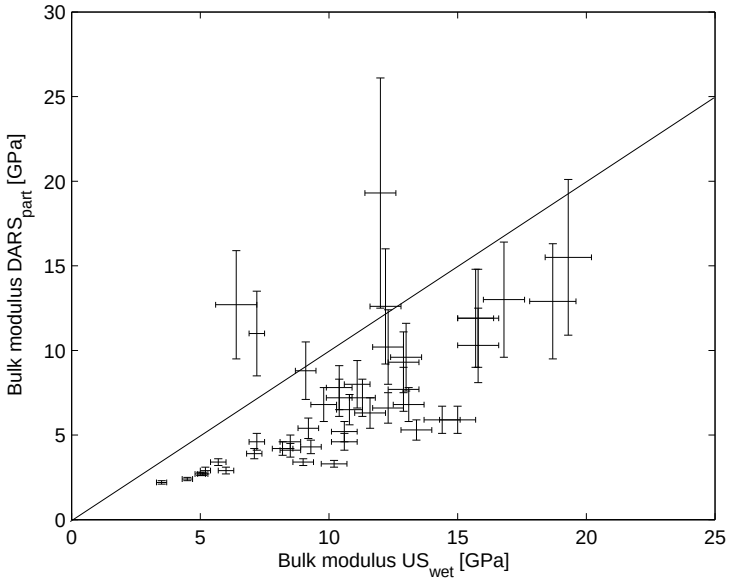

(b)

Figure 8.17: Cross-plots of the bulk moduli of the partially sealed porous samples estimated by the DARS method and by ultrasound. (a) Dry ultrasonic bulk modulus K_{m}. (b) Oil-saturated ultrasonic bulk modulus K_{wet}.

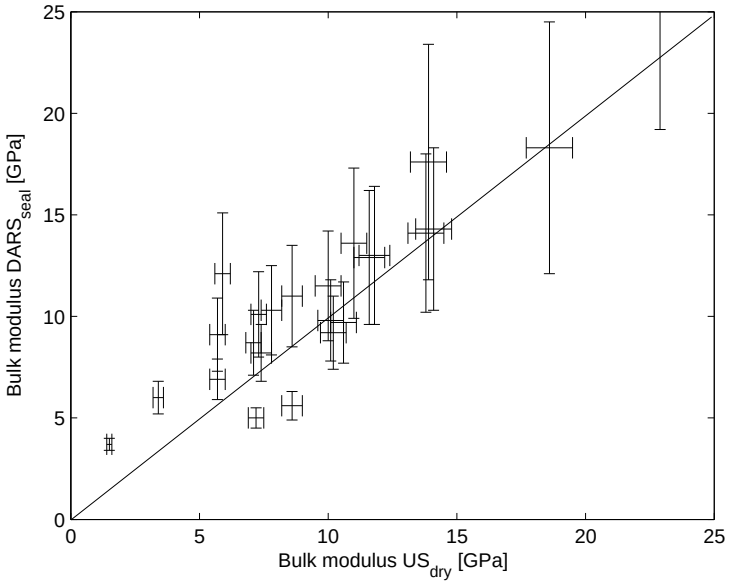

(a)

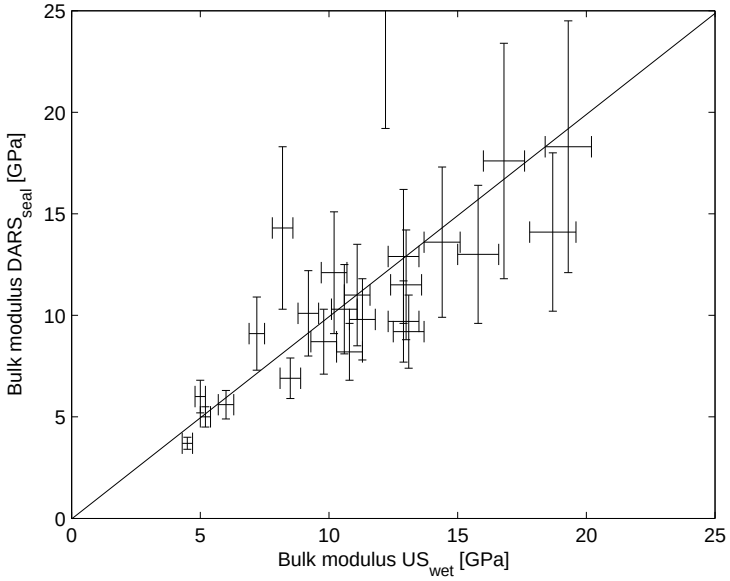

(b)

Figure 8.18: Cross-plots of the bulk moduli of the sealed porous samples estimated by the DARS method and by ultrasound. (a) Dry ultrasonic bulk modulus K_{m}. (b) Oil-saturated ultrasonic bulk modulus K_{wet}. The value of CHK03 falls outside the scales.

Chapter 9

Conclusions

The aim of this research was to extend the Biot concept of wave propagation in fluid-saturated porous media to heterogeneous porous media with special attention to attenuation in the seismic frequency band. This thesis focuses on fluid inhomogeneities, i.e., partially saturated porous media. The inhomogeneities are on the mesoscopic scale, i.e., larger than the typical pore size but smaller than the wavelength. Frame inhomogeneities are not considered. The conclusions are as follows:

1. Local pressure differences due to the passing of a sound wave in a fluid-saturated porous medium with a mesoscale contrast in constituent properties are counterbalanced by fluid flow (White theory). We extended White's theory for layered inhomogeneities in porous media to higher frequencies. This extended theory is then comparable to Dutta-Odé's theory for spherical gas fractions in porous media. It was found that resonance effects become important when the size of the inhomogeneity has the order of magnitude of the wavelength. This behavior was fully neglected in the White's original papers. However, when the frequency is smaller than the critical Biot frequency, and the wavelength larger than the size of the inhomogeneity, low-frequency Biot theory can effectively be applied. It is assumed that the frequencies are so low that the dynamic permeability is equal to the Darcy permeability. Moreover, all acceleration terms in the Biot equations can safely be neglected. In this way it is possible to determine an effective dynamic bulk modulus. Following Johnson, it can be shown that the so-called patchy saturation theory describes the transition from low-frequency Wood-like behavior toward high-frequency Hill-like behavior. We demonstrated that our exact analytical solution to patchy saturation in the quasi-static

Biot context is in exact agreement with the generalized (Johnson) model.

2. The problem with the patchy saturation model is that it is based on the assumption of sealed boundary conditions. These are imposed because of the inherent assumption of regular unit cell distributions. For dilute gas-liquid mixtures the so-called Rayleigh-Plesset-Biot approach is more suited. Here it is assumed that in first order approximation the gas bubbles do not interact and that they radiate energy into the infinitely extended surrounding liquid. We modified the Rayleigh-Plesset-Biot assumption for porous media, and we compared the outcome of the computations with the patchy saturation model. We found that the attenuation of the fast Biot wave was significantly larger than predicted by the patchy saturation model, for relevant seismic frequencies, gas saturations, and gas bubble radii. Moreover, the second, slow Biot wave is naturally incorporated in the Rayleigh-Plesset-Biot approach, which is not the case for the patchy saturation model.

3. Applying the Rayleigh-Plesset-Biot model to the literature data of Murphy, we were able to get a very good match between the reported attenuation values and the theoretical predictions. This was not the case for the patchy saturation model. The frequency range in Murphy's data was from 0.6 to 6 kHz.

4. Using a gas-injection technique, we measured the ultrasound velocity and attenuation of partially saturated porous rocks. The effectiveness of the injection technique was tested in an independent visualization set-up. For the determination of the phase velocities and the attenuation coefficients, the Spectral Ratio Data Analysis technique was used. Under our experimental conditions, conducted at 500 kHz, we found that the patchy saturation model gave a better prediction of the measured attenuation values than the Rayleigh-Plesset-Biot approach. We note, however, that squirt-flow mechanisms may play an important additional role in this frequency range. This mechanism was not taken into account here.

5. By means of ultrasound experiments in oil using either a needle hydrophone or a transducer receiver, we successfully validated far and near-field wave theory when an effective source radius is introduced. This accounts for non-planar behavior of the piston source, and for transient effects. As the theory is based on the continuous wave assumption, discrepancies are bound to occur as the wavelets simply do not have enough time for complete diffraction. Still, the agreement between experiment and theory is not sufficiently close to be

able to determine the intrinsic losses in the silicone oil. Using Spectral Ratio Data Analysis (SRDA), however, it is possible to exactly determine the wave speed in the oil. For this, two identical planar transducers are used as source and receiver.

6. Differential Acoustic Resonance Spectroscopy (DARS) experiments on non-porous samples confirm the perturbation theory. DARS can thus be used successfully to determine the compressibility of those samples at tube resonance frequencies (around 1 kHz). The compressibility of porous samples, however, is determined by the relative fluid motion at the sample outer wall. If the sample is sealed, the closed-pore boundary conditions apply, and the Gassmann modulus of the sample is measured. This leaves open the question whether DARS can be used for measuring sample attenuation, and whether reservoir properties, such as permeability and gas volume content, can be extracted from seismically measured attenuation.

Bibliography

Anderson, A. L. and L. D. Hampton (1980a). Acoustics of gas-bearing sediments. 1. Background. *Journal of the Acoustical Society of America 67*(6), 1865–1889.

Anderson, A. L. and L. D. Hampton (1980b). Acoustics of gas-bearing sediments. 2. Measurements and models. *Journal of the Acoustical Society of America 67*(6), 1890–1903.

Arntsen, B. and J. M. Carcione (2001). Numerical simulation of the Biot slow wave in water-saturated Nivelsteiner sandstone. *Geophysics 66*(3), 890–896.

Bass, R. (1958). Diffraction effects in the ultrasonic field of a piston source. *Journal of the Acoustical Society of America 30*(7), 602–605.

Batzle, M. L., D. H. Han, and R. Hofmann (2006). Fluid mobility and frequency-dependent seismic velocity - direct measurements. *Geophysics 71*(1), N1–N9.

Bedford, A. and M. Stern (1983). A model for wave-propagation in gassy sediments. *Journal of the Acoustical Society of America 73*(2), 409–417.

Berkhout, A. J. (1987). *Applied seismic wave theory*. Elsevier, Amsterdam.

Berryman, J. G. (1999). Origin of Gassmann's equations. *Geophysics 64*(5), 1627–1629.

Berryman, J. G., L. Thigpen, and R. C. Y. Chin (1988). Bulk elastic wave-propagation in partially saturated porous solids. *Journal of the Acoustical Society of America 84*(1), 360–373.

Berryman, J. G. and H. F. Wang (1995). The elastic coefficients of double-porosity models for fluid transport in jointed rock. *Journal of Geophysical Research-Solid Earth 100*(B12), 24611–24627.

Berryman, J. G. and H. F. Wang (2000). Elastic wave propagation and attenuation in a double-porosity dual-permeability medium. *International Journal of Rock Mechanics and Mining Sciences 37*(1-2), 63–78.

Best, A. I., Q. J. Huggett, and A. J. K. Harris (2001). Comparison of in situ and laboratory acoustic measurements on Lough Hyne marine sediments. *Journal of the Acoustical Society of America 110*(2), 695–709.

Best, A. I., C. McCann, and J. Sothcott (1994). The relationships between the velocities, attenuations and petrophysical properties of reservoir sedimentary-rocks. *Geophysical Prospecting 42*(2), 151–178.

Biot, M. A. (1956a). Theory of propagation of elastic waves in a fluid-saturated porous solid: I. Low frequency range. *Journal of the Acoustical Society of America 28*, 168–178.

Biot, M. A. (1956b). Theory of propagation of elastic waves in a fluid-saturated porous solid: II. High frequency range. *Journal of the Acoustical Society of America 28*, 179–191.

Biot, M. A. (1962a). Generalized theory of acoustic propagation in porous dissipative media. *Journal of the Acoustical Society of America 34*(9), 1254–1264.

Biot, M. A. (1962b). Mechanics of deformation and acoustic propagation in porous media. *Journal of Applied Physics 33*(4), 1482–1498.

Biot, M. A. and D. G. Willis (1957). The elastic coefficients of the theory of consolidation. *Journal of Applied Mechanics 24*, 594–601.

Birch, F. (1975). Velocity and attenuation from resonant vibrations of spheres of rock, glass, and steel. *Journal of Geophysical Research 80*(5), 756–764.

Bourbié, T., O. Coussy, and B. Zinszner (1987). *Acoustics of Porous media*. Institut Francais du Petrole Publications, Gulf Publishing Co.

Bourbie, T. and B. Zinszner (1985). Hydraulic and acoustic properties as a function of porosity in Fontainebleau sandstone. *Journal of Geophysical Research-Solid Earth and Planets 90*(NB13), 1524–1532.

Brajanovski, M., B. Gurevich, and M. Schoenberg (2005). A model for P-wave attenuation and dispersion in a porous medium permeated by aligned fractures. *Geophysical Journal International 163*(1), 372–384.

Brandt, H. (1960). Factors affecting compressional wave velocity in unconsolidated marine sand sediments. *Journal of the Acoustical Society of America 32*(2), 171–179.

Brie, A., F. Pampur, A. Marsala, and O. Meazza (1995). Shear sonic interpretation in gas-bearing sands. *Society of Petroleum Engineers - Annual Technical Conference, Paper 30595*, 701–710.

Budiansky, B. and R. J. O'Connell (1976). Elastic-moduli of a cracked solid. *International Journal of Solids and Structures 12*(2), 81–97.

Cadoret, T. (1993). *Effet de la saturation eau/gaz sur les propriétés acoustiques des roches - Étude aux fréquences sonores et ultrasonores*. Thèse, Université de Paris VII.

Cadoret, T., D. Marion, and B. Zinszner (1995). Influence of frequency and fluid distribution on elastic-wave velocities in partially saturated limestones. *Journal of Geophysical Research - Solid Earth 100*(6), 9789–9803.

Cadoret, T., G. M. Mavko, and B. Zinszner (1998). Fluid distribution effect on sonic attenuation in partially saturated limestones. *Geophysics 63*(1), 154–160.

Carcione, J. M. (1998). Viscoelastic effective rheologies for modelling wave propagation in porous media. *Geophysical Prospecting 46*(3), 249–270.

Carcione, J. M., B. Gurevich, and F. Cavallini (2000). A generalized Biot-Gassmann model for the acoustic properties of shaley sandstones. *Geophysical Prospecting 48*(3), 539–557.

Carcione, J. M., H. B. Helle, and N. H. Pham (2003). White's model for wave propagation in partially saturated rocks: Comparison with poroelastic numerical experiments. *Geophysics 68*(4), 1389–1398.

Carcione, J. M. and S. Picotti (2006). P-wave seismic attenuation by slow-wave diffusion: Effects of inhomogeneous rock properties. *Geophysics 71*(3), O1–O8.

Castagna, J. P., M. L. Batzle, and T. K. Kan (1993). *Rock physics: The link between rock properties and AVO response*. Number 8. J. P. Castagna and M. Backus, eds., Offset-dependent reflectivity: Theory and practice of AVO analysis, Investigations in Geophysics.

Castagna, J. P., S. Sun, and R. W. Seigfried (2003). Instantaneous spectral analysis: detection of low-frequency shadows associated with hydrocarbons. *The Leading Edge 22*(2), 120–127.

Champoux, Y. and J.-F. Allard (1991). Dynamic tortuosity and bulk modulus in air-saturated porous-media. *Journal of Applied Physics 70*(4), 1975–1979.

Chandler, R. N. and D. L. Johnson (1981). The equivalence of quasistatic flow in fluid-saturated porous-media and Biot's slow-wave in the limit of zero frequency. *Journal of Applied Physics 52*(5), 3391–3395.

Chapman, M., E. R. Liu, and X. Y. Li (2006). The influence of fluid-sensitive dispersion and attenuation on AVO analysis. *Geophysical Journal International 167*(1), 89–105.

Clark, V. A., B. R. Tittmann, and T. W. Spencer (1980). Effect of volatiles on attenuation (Q^{-1}) and velocity in sedimentary rocks. *Journal of Geophysical Research 85*(10), 5190–5198.

Clearco Products (2006). *Product information sheet, Figure 1 - Viscosity-temperature relationships*. www.clearcoproducts.com.

Core Laboratories Instruments (2000). *Technical Specifications Ultraperm-400 permeameter*.

Del Grosso, V. A. and C. W. Mader (1972). Speed of sound in pure water. *Journal of the Acoustical Society of America 52*(5), 1442–1446.

Deresiewicz, H. and R. Skalak (1963). On uniqueness in dynamic poroelasticity. *Bulletin of the Seismological Society of America 53*, 783–788.

Diallo, M. S., M. Prasad, and E. Appel (2003). Comparison between experimental results and theoretical predictions for P-wave velocity and attenuation at ultrasonic frequency. *Wave Motion 37*(1), 1–16.

Domenico, S. N. (1976). Effect of brine-gas mixture on velocity in an unconsolidated sand reservoir. *Geophysics 41*(5), 882–894.

Dutta, N. C. and H. Odé (1979a). Attenuation and dispersion of compressional waves in fluid-filled porous rocks with partial gas saturation (White model). 1. Biot theory. *Geophysics 44*(11), 1777–1788.

Dutta, N. C. and H. Odé (1979b). Attenuation and dispersion of compressional waves in fluid-filled porous rocks with partial gas saturation (White model). 2. Results. *Geophysics 44*(11), 1789–1805.

Dutta, N. C. and A. J. Seriff (1979). White model of attenuation in rocks with partial gas saturation. *Geophysics 44*(11), 1806–1812.

Dvorkin, J., G. M. Mavko, and A. Nur (1995). Squirt flow in fully saturated rocks. *Geophysics 60*(1), 97–107.

Dvorkin, J. and A. Nur (1993). Dynamic poroelasticity - A unified model with the squirt and the biot mechanisms. *Geophysics 58*(4), 524–533.

Ebrom, D. (2004). The low frequency gas shadow on seismic sections. *The Leading Edge 23*(8), 772–775.

Frenkel, J. (1944). On the theory of seismic and seismo-electric phenomena in a moist soil. *Journal of Physics USSR 8*(4), 230–241.

Gardner, G. H. F., M. R. J. Wyllie, and D. M. Droschak (1964). Effects of pressure + fluid saturation on attenuation of elastic waves in sands. *Journal of Petroleum Technology 16*(2), 189–193.

Garg, S. K. and A. H. Nayfeh (1986). Compressional wave-propagation in liquid and or gas saturated elastic porous-media. *Journal of Applied Physics 60*(9), 3045–3055.

Gassmann, F. (1951). Über die Elastizität poröser Medien. *Vierteljahresschrift Naturforschenden Gesellschaft Zürich 96*, 1–23.

Gei, D. and J. M. Carcione (2003). Acoustic properties of sediments saturated with gas hydrate, free gas and water. *Geophysical Prospecting 51*(2), 141–157.

Gelinsky, S., S. A. Shapiro, T. M. Müller, and B. Gurevich (1998). Dynamic poroelasticity of thinly layered structures. *International Journal of Solids and Structures 35*(34), 4739–4751.

Gist, G. A. (1994a). Fluid effects on velocity and attenuation in sandstones. *Journal of the Acoustical Society of America 96*(2), 1158–1173.

Gist, G. A. (1994b). Interpreting laboratory velocity-measurements in partially gas-saturated rocks. *Geophysics 59*(7), 1100–1109.

Glover, P. (2009). What is the cementation exponent? A new interpretation. *The Leading Edge 28*(1), 82–85.

Goloshubin, G. M. and V. A. Korneev (2000). Seismic low-frequency effects from fluid-saturated reservoir. *Expanded Abstracts, 70th SEG Annual Meeting*, 1–4.

Gregory, A. R. (1976). Fluid saturation effects on dynamic elastic properties of sedimentary-rocks. *Geophysics 41*(5), 895–921.

Gurevich, B. and S. L. Lopatnikov (1995). Velocity and attenuation of elastic-waves in finely layered porous rocks. *Geophysical Journal International 121*(3), 933–947.

Harris, J. M. (1996). *Differential Acoustical Resonance Spectroscopy.* Seismic Tomography Project Annual Report, Paper F, Stanford University.

Harris, J. M., Y. Quan, and C. Xu (2005). Differential Acoustical Resonance Spectroscopy: An experimental method for estimating acoustic attenuation in porous media. *Expanded Abstracts, 75th SEG Annual Meeting Houston 24*, 1569–1572.

Helle, H. B., N. H. Pham, and J. E. M. Carcione (2003). Velocity and attenuation in partially saturated rocks: poroelastic numerical experiments. *Geophysical Prospecting 51*(6), 551–566.

Heller, H. K. J. (2006). *Personal correspondence.*

Hill, R. (1963). Elastic properties of reinforced solids - Some theoretical principles. *Journal of the Mechanics and Physics of Solids 11*(5), 357–372.

Hornby, B. E. and W. F. Murphy (1987). v_p/v_s in unconsolidated oil sands - Shear from Stoneley. *Geophysics 52*(4), 502–513.

Jocker, J. (2005). *Ultrasonic wave propagation in heterogeneous elastic and poroelastic media.* Dissertation, Delft University of Technology.

Jocker, J., D. M. J. Smeulders, G. G. Drijkoningen, C. van der Lee, and A. Kalfsbeek (2004). Matrix propagator method for layered porous media: Analytical expressions and stability criteria. *Geophysics 69*(4), 1071–1081.

Johnson, D. L. (2001). Theory of frequency dependent acoustics in patchy-saturated porous media. *Journal of the Acoustical Society of America 110*(2), 682–694.

Johnson, D. L., J. Koplik, and R. Dashen (1987). Theory of dynamic permeability and tortuosity in fluid-saturated porous-media. *Journal of Fluid Mechanics 176*, 379–402.

Johnston, D. H., M. N. Toksöz, and A. Timur (1979). Attenuation of seismic waves in dry and saturated rocks. Part 2. Mechanisms. *Geophysics 44*(4), 691–711.

Jones, T. D. (1986). Pore fluids and frequency-dependent wave-propagation in rocks. *Geophysics 51*(10), 1939–1953.

Jones, T. D. and A. Nur (1983). Velocity and attenuation in sandstone at elevated-temperatures and pressures. *Geophysical Research Letters 10*(2), 140–143.

K-Mac Products (2008). *Product information sheet*. www.k-mac-plastics.com.

Kelder, O. (1998). *Frequency-dependent wave propagation in water-saturated porous media*. Dissertation, Delft University of Technology.

Kelder, O. and D. M. J. Smeulders (1997). Observation of the Biot slow wave in water-saturated Nivelsteiner sandstone. *Geophysics 62*(6), 1794–1796.

King, M. S., J. R. Marsden, and J. W. Dennis (2000). Biot dispersion for P- and S-wave velocities in partially and fully saturated sandstones. *Geophysical Prospecting 48*(6), 1075–1089.

Kjartansson, E. (1979). Constant Q-wave propagation and attenuation. *Journal of Geophysical Research 84*(NB9), 4737–4748.

Klimentos, T. and C. McCann (1990). Relationships among compressional wave attenuation, porosity, clay content, and permeability in sandstones. *Geophysics 55*(8), 998–1014.

Klinkenberg, L. J. (1941). The permeability of porous media to liquids and gases. *Drilling and Production Practice, American Petroleum Institute*, 200–213.

Knight, R. and J. Dvorkin (1992). Seismic and electrical-properties of sandstones at low saturations. *Journal of Geophysical Research-Solid Earth 97*(B12), 17425–17432.

Knight, R., J. Dvorkin, and A. Nur (1998). Acoustic signatures of partial saturation. *Geophysics 63*(1), 132–138.

Knight, R. and R. Nolen-Hoeksema (1990). A laboratory study of the dependence of elastic wave velocities on pore scale fluid distribution. *Geophysical Research Letters 17*(10), 1529–1532.

Korneev, V. A., G. M. Goloshubin, T. M. Daley, and D. B. Silin (2004). Seismic low-frequency effects in monitoring fluid-saturated reservoirs. *Geophysics 69*(3), 522–532.

Kumar, A., T. Jayakumar, B. Raj, and K. Ray (2003). Correlation between ultrasonic shear wave velocity and Poisson's ratio for isotropic solid materials. *Acta Materialia 51*, 2417–2426.

Kundu, T. (2003). *Ultrasonic Nondestructive Evaluation: Engineering and Biological Material Characterization*. CRC Press, Florida, USA.

Lamb, H. (1916). *Statics*. Reprinted by Cambridge University Press, Cambridge, United Kingdom, 1960.

Lebedev, M., J. Toms, B. Clennell, M. Pervukhina, V. Shulakova, L. Paterson, T. M. Müller, B. Gurevich, and F. Wenzlau (2009). Direct laboratory observation of patchy saturation and its effects on ultrasonic velocities. *The Leading Edge 28*(1), 24–27.

Lockner, D. A., J. B. Walsh, and J. D. Byerlee (1977). Changes in seismic velocity and attenuation during deformation of granite. *Journal of Geophysical Research 82*(33), 5374–5378.

Lopatnikov, S. L. and P. Y. Gorbachev (1987). Propagation and attenuation of longitudinal-waves in a partially gas-saturated porous-medium. *Izvestiya Akademii Nauk SSSR Fizika Zemli* (8), 78–86.

Lucet, N. and B. Zinszner (1992). Effects of heterogeneities and anisotropy on sonic and ultrasonic-attenuation in rocks. *Geophysics 57*(8), 1018–1026.

Lumley, D., D. Bevc, J. Ji, and S. Talas (1997). *Lab measurements of elastic velocities in dry and saturated Massillon sandstone*. Stanford Exploration Project, Stanford University.

Mason, W. P., K. J. Marfurt, D. N. Beshers, and J. T. Kuo (1978). Internal friction in rocks. *Journal of the Acoustical Society of America 63*(5), 1596–1603.

Masson, Y. J., S. R. Pride, and K. T. Nihei (2006). Finite difference modeling of Biots poroelastic equations at seismic frequencies. *Journal of Geophysical Research 111*(1), B10305.1–B10305.13.

Mast, T. D. and F. Yu (2005). Simplified expansions for radiation from a baffled circular piston. *Journal of the Acoustical Society of America 118*(6), 3457–3464.

Mavko, G. M. (1979). Frictional attenuation - Inherent amplitude dependence. *Journal of Geophysical Research 84*(9), 4769–4775.

Mavko, G. M., T. Mukerji, and J. Dvorkin (2003). *The rock physics Handbook: Tools for Seismic Analysis in Porous Media*. Cambridge University Press, New York.

Mavko, G. M. and A. Nur (1979). Wave attenuation in partially saturated rocks. *Geophysics 44*(2), 161–178.

Miksis, M. J. (1988). Effects of contact line movement on the dissipation of waves in partially saturated rocks. *Journal of Geophysical Research - Solid Earth and Planets 93*(6), 6624–6634.

Mochizuki, S. (1982). Attenuation in partially saturated rocks. *Journal of Geophysical Research 87*, 8598–8604.

Morse, P. M. and K. U. Ingard (1968). *Theoretical acoustics*. McGraw-Hill Inc., New, York.

Müller, T. M. and B. Gurevich (2004). One-dimensional random patchy saturation model for velocity and attenuation in porous rocks. *Geophysics 69*(5), 1166–1172.

Müller, T. M. and B. Gurevich (2005a). A first-order statistical smoothing approximation for the coherent wave field in random porous random media. *Journal of the Acoustical Society of America 117*(4), 1796–1805.

Müller, T. M. and B. Gurevich (2005b). Wave-induced fluid flow in random porous media: Attenuation and dispersion of elastic waves. *Journal of the Acoustical Society of America 117*(5), 2732–2741.

Murphy, W. F. (1982a). *Effects of microstructure and pore fluids on the acoustic properties of granular sedimentary materials*. Dissertation, Stanford University.

Murphy, W. F. (1982b). Effects of partial water saturation on attenuation in Massilon sandstone and Vycor porous-glass. *Journal of the Acoustical Society of America 71*(6), 1458–1468.

Murphy, W. F. (1984). Acoustic measures of partial gas saturation in tight sandstones. *Journal of Geophysical Research 89*(NB13), 1549–1559.

Murphy, W. F., K. W. Winkler, and R. L. Kleinberg (1984). Frame modulus reduction in sedimentary-rocks - The effect of adsorption on grain contacts. *Geophysical Research Letters 11*(9), 805–808.

Murphy, W. F., K. W. Winkler, and R. L. Kleinberg (1986). Acoustic relaxation in sedimentary-rocks - Dependence on grain contacts and fluid saturation. *Geophysics 51*(3), 757–766.

Nagy, P. B., L. Adler, and B. B. P. (1990). Slow wave propagation in air-filled porous materials and natural rocks. *Applied Physics Letters 56*(25), 2504–2506.

Norris, A. N. (1993). Low-frequency dispersion and attenuation in partially saturated rocks. *Journal of the Acoustical Society of America 94*(1), 359–370.

O'Connell, R. J. and B. Budiansky (1974). Seismic velocities in dry and saturated cracked solids. *Journal of Geophysical Research 79*(35), 5412–5426.

Palmer, I. D. and M. L. Traviolia (1980). Attenuation by squirt flow in undersaturated gas sands. *Geophysics 45*(12), 1780–1792.

Pham, N. H., J. M. Carcione, H. B. Helle, and B. Ursin (2002). Wave velocities and attenuation of shaley sandstones as a function of pore pressure and partial saturation. *Geophysical Prospecting 50*(6), 615–627.

Pierce, A. D. (1989). *Acoustics: An introduction to its physical principles and applications* (2^{nd} ed.). Acoustical Society of America, Woodbury, New York.

Plona, T. J. (1980). Observation of a 2nd bulk compressional wave in a porous-medium at ultrasonic frequencies. *Applied Physics Letters 36*(4), 259–261.

Pride, S., J. Harris, D. Johnson, A. Mateeva, K. Nihei, R. Nowack, J. Rector, H. Spetzler, R. Wu, T. Yamamoto, J. Berryman, and M. Fehler (2003). Permeability dependence of seismic amplitudes. *The Leading Edge 6*, 518–525.

Pride, S. R. and J. G. Berryman (2003a). Linear dynamics of double-porosity dual-permeability materials. I. Governing equations and acoustic attenuation. *Physical Review E 68*(3), 036603.01–036603.10.

Pride, S. R. and J. G. Berryman (2003b). Linear dynamics of double-porosity dual-permeability materials. II. Fluid transport equations. *Physical Review E 68*(3), 036604.01–036604.10.

Pride, S. R., J. G. Berryman, and J. M. Harris (2004). Seismic attenuation due to wave-induced flow. *Journal of Geophysical Research 109*(1), B01201.01–B01201.19.

Pride, S. R. and Y. J. Masson (2006). Acoustic attenuation in self-affine porous structures. *Physical Review Letters 97*(18).

Pride, S. R., E. Tromeur, and J. G. Berryman (2002). Biot slow-wave effects in stratified rock. *Geophysics 67*(1), 271–281.

Rayleigh, J. W. S. (1896). *The theory of sound*, Volume 2. Reprinted by Dover, New York, 1945.

Rogers, P. H. and A. L. Van Buren (1974). Exact expression for Lommel diffraction correction integral. *Journal of the Acoustical Society of America 55*(4), 724–728.

Rutherford, S. R. and R. H. Williams (1989). Amplitude-versus-offset variations in gas sands. *Geophysics 54*(6), 680–688.

Sams, M. S., J. P. Neep, M. H. Worthington, and M. S. King (1997). The measurement of velocity dispersion and frequency-dependent intrinsic attenuation in sedimentary rocks. *Geophysics 62*(5), 1456–1464.

Savage, J. C. and H. S. Hasegawa (1967). Evidence for a linear attenuation mechanism. *Geophysics 32*(6), 1003–1014.

Schön, J. H. (1996). *Physical properties of rocks: fundamentals and principles of petrophysics*, Volume 18. Handbook of Geophysical Exploration. Elsevier Science Ltd, Oxford, UK.

Seki, H., A. Granato, and R. Truell (1956). Diffraction effects in the ultrasonic field of a piston source and their importance in the accurate measurement of attenuation. *Journal of the Acoustical Society of America 28*(2), 230–238.

Selfridge, A. R. (1985). Approximate material properties in isotropic materials. *IEEE Transactions on Sonics and Ultrasonics 32*(3), 381–394.

Shapiro, S. A. and T. M. Müller (1999). Seismic signatures of permeability in heterogeneous porous media. *Geophysics 64*(1), 99–103.

Smeulders, D. M. J. (2005). Experimental evidence for slow compressional waves. *Journal of Engineering Mechanics 131*(9), 908–917.

Smeulders, D. M. J. and M. E. H. Van Dongen (1997). Wave propagation in porous media containing a dilute gas-liquid mixture: Theory and experiments. *Journal of Fluid Mechanics 343*, 351–373.

Stoll, R. D. (1985). Marine sediment acoustics. *Journal of the Acoustical Society of America 77*(5), 1789–1799.

Stoll, R. D. and G. M. Bryan (1970). Wave attenuation in saturated sediments. *Journal of the Acoustical Society of America 47*(5), 1440–1447.

Tittmann, B. R., V. A. Clark, J. M. Richardson, and T. W. Spencer (1980). Possible mechanism for seismic attenuation in rocks containing small amounts of volatiles. *Journal of Geophysical Research 85*(10), 5199–5208.

Toksöz, M. N., C. H. Cheng, and A. Timur (1976). Velocities of seismic-waves in porous rocks. *Geophysics 41*(4), 621–645.

Toksöz, M. N., D. H. Johnston, and A. Timur (1979). Attenuation of seismic waves in dry and saturated rocks. Part 1: Laboratory measurements. *Geophysics 44*(4), 681–690.

Toms, J., T. M. Müller, R. Ciz, and B. Gurevich (2006). Comparative review of theoretical models for elastic wave attenuation and dispersion in partially saturated rocks. *Soil Dynamics and Earthquake Engineering 26*(6-7), 548–565.

Toms, J., T. M. Müller, and B. Gurevich (2007). Seismic attenuation in porous rocks with random patchy saturation. *Geophysical Prospecting 55*(5), 671–678.

Turgut, A. and T. Yamamoto (1988). Synthetic seismograms for marine-sediments and determination of porosity and permeability. *Geophysics 53*(8), 1056–1067.

Verbeek, G., J. B. Broens, W. Kranendonk, F. J. Van de Puijl, J. L. Sikkema, and C. W. Stam (1986). *Binas*. Wolters-Noordhoff Groningen.

Vogelaar, B. B. S. A. and D. M. J. Smeulders (2007). Extension of White's layered model to the full frequency range. *Geophysical Prospecting 55*(5), 685–695.

Vogelaar, B. B. S. A., D. M. J. Smeulders, and J. M. Harris (2008). Differential Acoustic Resonance Spectroscopy (DARS) measurements. *Extended Abstracts, 70th EAGE Conference Rome*, I038.

White, J. E. (1975). Computed seismic speeds and attenuation in rocks with partial gas saturation. *Geophysics 40*(2), 224–232.

White, J. E., N. Mikhaylova, and F. Lyakhovitskiy (1975). Low-frequency seismic-waves in fluid-saturated layered rocks. *Izvestija Academy of Sciences USSR, Physics of Solid Earth 11*, 654–659.

Wijngaarden van, L. (1972). One-dimensional flow of liquids containing small gas bubbles. *Annual Review of Fluid Mechanics 4*, 369–395.

Williams, A. O. (1951). The piston source at high frequencies. *Journal of the Acoustical Society of America 23*(1), 1–6.

Williams, A. O. (1970). Integrated signal on circular piston receiver centered in a piston beam. *Journal of the Acoustical Society of America 48*(1), 285–289.

Winkler, K. W. (1979). *The effects of pore fluids and frictional sliding on seismic attenuation.* Dissertation, Stanford University.

Winkler, K. W. (1983). Frequency-dependent ultrasonic properties of high-porosity sandstones. *Journal of Geophysical Research 88*(NB11), 9493–9499.

Winkler, K. W. (1985). Dispersion analysis of velocity and attenuation in Berea sandstone. *Journal of Geophysical Research-Solid Earth and Planets 90*(NB8), 6793–6800.

Winkler, K. W. (1986). Estimates of velocity dispersion between seismic and ultrasonic frequencies. *Geophysics 51*(1), 183–189.

Winkler, K. W. and W. F. Murphy (1995). *Rock physics and phase relations - A handbook of physical constants.* American Geophysical Union.

Winkler, K. W. and A. Nur (1979). Pore fluids and seismic attenuation in rocks. *Geophysical Research Letters 6*(1), 1–4.

Winkler, K. W. and A. Nur (1982). Seismic attenuation - Effects of pore fluids and frictional sliding. *Geophysics 47*(1), 1–15.

Winkler, K. W., A. Nur, and M. Gladwin (1979). Friction and seismic attenuation in rocks. *Nature 277*(5697), 528–531.

Wisse, C. J. (1999). *On frequency dependence of acoustic waves in porous cylinders.* Dissertation, Delft University of Technology.

Xu, C. (2007). *Estimation of effective compressibility and permeability of porous materials with Differential Acoustic Resonance Spectroscopy.* Dissertation, Stanford University.

Xu, C., J. M. Harris, and Y. Quan (2006). Estimating flow properties of porous media with a model for dynamic diffusion. *Expanded Abstracts, 76th SEG Annual Meeting New Orleans 25*, 1831–1835.

Yamamoto, T. and A. Turgut (1988). Acoustic-wave propagation through porous-media with arbitrary pore-size distributions. *Journal of the Acoustical Society of America 83*(5), 1744–1751.

Yin, C.-S., M. L. Batzle, and B. J. Smith (1992). Effects of partial liquid/gas saturation on extensional wave attenuation in Berea sandstone. *Geophysical Research Letters 19*, 1399–1402.

Zwikker, C. and C. W. Kosten (1941). Extended theory of the absorption of sound by compressible wall-coverings. *Physica (Amsterdam) 8*(9), 968–978.

Samenvatting

De eigenschappen van de porievloeistof en de vaste stof beïnvloeden de voortplanting van geluidsgolven door poreuze materialen. Geluidssnelheid en reistijden worden veel gebruikt voor de beeldvorming van de ondergrond en voor het voorspellen van de petrofysische eigenschappen, zoals porositeit, vloeistoftype en verzadigingsgraad. De demping (het verlies van golfenergie) wordt echter zelden toegepast bij deze voorspellingen.
In dit proefschrift wordt verslag gelegd van de invloed van vloeistofheterogeniteiten (gasbellen) op de golfdemping in vloeistofverzadigde poreuze materialen. Het is duidelijk dat de Biot theorie de snelheden op seismische en 'crosswell' frequenties (1-1000 Hz) nauwkeurig kan voorspellen, terwijl de demping in hoge mate onderschat wordt. Deze afwijking is hoofdzakelijk toe te schrijven aan heterogeniteiten op mesoschaal in de vaste stof (bijvoorbeeld kleilaagjes) en in de vloeistof (bijvoorbeeld gasbellen of gaslagen). De term mesoschaal moet gezien worden als zijnde groter dan de karakteristieke porieschaal maar kleiner dan de seismische golflengte. De heterogeniteiten kunnen als groep in zijn geheel worden beschreven met drukvereffeningsmodellen. De passerende seismische golf veroorzaakt plaatselijke drukverschillen tussen gas en vloeistof. Deze drukverschillen worden geëgaliseerd door vloeistof- en gasstroming op de mesoschaal. Voor heterogeniteiten in de vaste stof staan deze modellen bekend als 'double-porosity' modellen, terwijl ze voor heterogeniteiten in de vloeistof 'patchy saturation' modellen heten.
'Patchy saturation' modellen nemen de langzame Biotgolf op de mesoschaal mee in de beschouwingen aangezien het vereffenen van drukverschillen een diffusief proces is. Echter op de macroschaal komt de langzame Biotgolf niet meer voor in de modellen. Op deze schaal planten de seismische golven zich voort en wordt de demping bepaald door visceuze vloeistofstroming onder invloed van drukverschillen op de schaal van de golflengte. We hebben de invloed van de frequentie in 'patchy saturation' modellen onderzocht voor gaslaagjes in poreuze materialen. We hebben gevonden dat voor lagere frequenties dan de kritische Biot frequentie

de traagheidstermen kunnen worden verwaarloosd en dat de dynamische permeabiliteit [illegible]aderd door de Darcy permeabiliteit. Het systeem gaat resoneren bij hogere frequenties. Het 'patchy saturation' model beschrijft de overgang van laagfrequent gedrag zoals beschreven door Wood (volledige drukvereffening) naar hoogfrequent gedrag zoals beschreven door Hill, waarbij deze hoge frequenties wel lager dienen te worden verondersteld dan de kritische Biotfrequentie. In deze frequentielimiet is er geen massa-uitwisseling mogelijk tussen de vloeistoffen de gasfase, omdat er eenvoudigweg niet voldoende tijd is om een drukevenwicht tot stand te brengen ('frozen situation').

Een alternatief voor het 'patchy saturation' model is het Rayleigh-Plesset-Biot concept. Hierbij wordt op de macroschaal nog steeds onderscheid gemaakt tussen het fluïdum en de vaste stof, omdat er alleen een middeling plaatsvindt over het fluïdum. Dit fluïdum bestaat dan uit de vloeistof en de gasbelletjes. Het Rayleigh-Plesset-Biot model voorspelt twee drukgolven op de seismische schaal, terwijl het pachy saturation model er maar een voorspelt. Ook vonden we dat de seismische golf sterker gedempt wordt dan in het patchy saturation model. Een uitstekende overeenkomst tussen de theoretisch en experimenteel verkregen demping werd gevonden voor een uit de literatuur bekend resonantie-experiment met poreuze gesteentemonsters tussen de 0.6 en 6 k

accenten op 'een'

trema op tweede e

Door middel van een gasinjectietechniek hebben we in een met olie verzadigd poreus monstertje een enkele gasbel gecreeërd. De procedure is getest door middel van het aanbrengen van een vloeistof in de poriën met gelijke brekingsindex als die van de vaste stof. We vonden in dit geval dat het patchy saturation model bij 500 kHz een beter voorspelling gaf dan het Rayleigh-Plesset-Biot model. Echter, stroming op een veel kleinere microschaal (zogenaamde 'squirt flow') kan ook bijdragen aan de demping bij deze frequenties. De dempingsmetingen werden uitgevoerd met behulp van spectraalanalyse, waarbij in het experiment gebruik werd gemaakt van twee overigens identieke monstertjes van verschillende lengte. De fasesnelheden van 45 natuurlijke gesteenten en synthetische poreuze materialen, die ook op deze manier werden gemeten, werden gekalibreerd met de standaard ultrasone metingen gebaseerd op eerste aankomsttijd. We hebben gevonden dat voor de fasesnelheden de Biottheorie nauwkeurig is, maar dat deze voor de demping onjuiste waarden voorspelt. Bij deze frequenties spelen heterogeniteiten op mesoschaal waarschijnlijk geen noemenswaardige rol, omdat de heterogeniteiten op de veel kleinere microschaal (haarscheurtjes in de korrels of gebroken cementatiecontacten) overheersen. Dit vraagstuk ligt echter buiten het kader van dit proefschrift.

Dezelfde 45 monstertjes zijn ook gebruikt bij 'Differential Acoustic Resonance

Spectroscopy' (DARS) metingen. De samendrukbaarheid van een monstertje wordt in deze experimenten bepaald door de verandering in resonantiefrequentie van een buis als gevolg van het inbrengen van het monstertje. DARS experimenten aan niet-poreuze monstertjes bevestigden de verstoringstheorie van Morse en Ingard. We vonden een goede overeenkomst tussen de Gassmann en DARS modulus voor afgedichte poreuze monstertjes. Voor monstertjes met open poriën, kon de DARS modulus niet worden geïnterpreteerd in termen van de vaste stof- en vloeistof-modulus, omdat de samendrukbaarheid wordt gegeven door de relatieve vloeistofbeweging aan de rand van het monstertje. Het kwantificeren van de demping van de poreuze monstertjes gebaseerd op realistische in-situ omstandigheden (samengeperste multi-componenten monstertjes) volgens de DARS methode moet in de toekomst leiden tot een betere toepassing van de gemeten demping van seismische signalen voor de beschrijving van het reservoir.

Acknowledgments

From experience I know that most readers who receive this thesis first scroll to current pages and start searching their valuable name.
During the course of this research I have benefited greatly from the creative ideas and physical insights of David Smeulders through plentiful discussions. Since the day we met, I am impressed by his animated way of presenting such tough subjects as rock physics. I am still impressed by his competence to keep his ghastly houseplant alive. Together with his lab crew Karel, Jan, and retired Andre, they manage to create a warm and excellent technical support. Their cumulative years of experience in the lab exceed a century.
It is a privilege to have Kees Wapenaar as supervisor. Being SEG editor he can even turn noise in an impact factor into signal. The members of the doctoral examination committee are acknowledged for their involvement and their readiness to improve the quality of this text. I am especially grateful to Rini van Dongen, Jerry Harris, Max Peeters, and René-Edouard Plessix for making several critical suggestions concerning the content of the manuscript.
For my visit at Stanford University, I express my appreciation to Jerry Harris and Chuntang Xu for their willingness to share their cutting-edge facilities at the Seismic Wave Physics Laboratory. Jerry, I feel so honored that you offered me a postdoc position at Stanford. Gary Mavko and Tiziana Vanori are acknowledged to let me use their Rock Physics Laboratory. I enjoyed the tours guided by Steve Pride in the Lawrence Berkeley National Laboratory and in his wine yard.
I thank my 'focal point' at Shell René-Edouard Plessix for his mathematical perspectives on our 'soft' Earth-scientific problems. You were always interested in my progress and the latest experimental results. I thank Andreas Bauer and Christian Lehr for the well-suited position at Shell before we move to Stanford.
Despite the prosperous use of ultrasound contrast agents as a diagnostic tool in the human arteries, the mutual efforts with the Thorax Medical Center of the Erasmus University Rotterdam to apply medical bubbles in porous rocks were not successful. Nico de Jong and Jeroen Borsboom are accredited for their cooperation.

I kindly acknowledge the financial support of Shell in their FOM-project "Physics of fluids and sound propagation". I enjoyed the 'Management Business Course' at Nyenrode University and the Summerschool at Imperial College London.
I feel flattered that I was invited to the selected group of, among others, the minister of Education, the president of the Board of Governors (CvB), the Rector Magnificus, and the mayor of Delft, during the opening of our new laboratory.
I enjoyed the atmosphere at the Dietz laboratory and later in the 'Kunstgebittengebouw', and I look forward to collaborate with my former colleagues in the future. Thank you: Jeroen, Patrick, Yufei, Tanguy, Chistiaan, Menne, Jelke (for the crushed glass and oil), Hein, Koen, Roald, Bert-Rik, Willem-Jan, Saikat, Rouhi, Hamid, Daria, Elmer, Nihed, Karel, Tristan, Bobby, and Orion. I appreciate the efforts of our management support-, technical support-, and IT-staff.
A special mention goes to my sisters Inez and Anne-Sophie who took so great care of my dad after my mom went to heaven just some months before the beginning of my PhD research. Being our teacher she would have been proud to see all of us doing so well.
Finally, I thank Saint Barbara for her protection and the god of love Cupid for shooting his bow. I am so lucky with my wife Dorien and our kids Rosalie and Olivier for their incredible sweetness every sun rising day.

Acta est fabula,

Bouko Vogelaar. Utrecht, September 2008.

About the author

In 2001, Bouko Vogelaar obtained his MSc degree in Exploration Geophysics and Seismology at Utrecht University. During his studies, he was teaching-assistant in mathematics, mechanics, and seismology. He did an internship at the OYO Corporation and worked part-time as site surveyor offshore Egypt. He was a board member in several student societies. After graduating, he was offered a full-time appointment at Georesources Consulting, where he provided geophysical services in such countries as Norway, UK, Italy, Egypt, and Turkmenistan. The practice of acquisition, processing, interpretation, and reporting of geophysical data triggered his interest in the importance of seismic research.

This interest was pursued by accepting a Shell/FOM-funded PhD position in the group of Applied Geophysics and Petrophysics at Delft University of Technology in 2004. During his PhD, the author contributed to conferences in Austin, Madrid, London, San Antonio, and Rome. Bouko is member of DPS, EAGE, SEG, and SPE. He was founding President of the Delft University of Technology Geophysical Society. The PhD work, which resulted in this dissertation, was partly performed at the Wave Physics Laboratory at Stanford University, where Bouko is currently working as a postdoctoral researcher.